Topological Properties of Aperiodic Tilings and Fractals

Yaroslav Don

Topological Properties of Aperiodic Tilings and Fractals

Research thesis

In partial fulfillment of the requirements
for the degree of Doctor of Philosophy

Yaroslav Don

Submitted to the Senate of the Technion – Israel Institute of Technology

Adar, 5781 Haifa March, 2021

The Research Thesis was done under the supervision of
Professor Eric Akkermans in the Department of Physics

The generous financial help of Irwin and Joan Jacobs Fellowship
and the Technion is gratefully acknowledged

List of Publications

Some results in this thesis have been published as articles by the author and research collaborators in conferences and journals during the course of the author's doctoral research period, the most up-to-date versions of which are listed below.

[i] O. Shpielberg, Y. Don, and E. Akkermans, "Numerical study of continuous and discontinuous dynamical phase transitions for boundary-driven systems," Phys. Rev. E **95**, 032137 (2017).

[ii] E. Akkermans, Y. Don, E. Levy and D. Gitelman, "Topological properties of some quasi-periodic tilings – From structure to spectrum, in Spectral Structures and Topological Methods" in Mathematical Quasicrystals, Workshop ID: 1740, M. Baake, D. Damanik, J. Kellendonk and D. Lenz (eds.), Mathematisches Forschungsinstitut Oberwolfach (2017).

[iii] O. Ovdat, Y. Don and E. Akkermans, "Vacancies in graphene: Dirac physics and fractional vacuum charges," Phys. Rev. B **102**, 075109 (2020).

[iv] E. Akkermans, Y. Don, J. Rosenberg and C. L. Schochet, "Relating Diffraction and Spectral Data of Aperiodic Tilings: Towards a Bloch theorem," (accepted, 2021) arXiv: 2007.15961 [math-ph].

Acknowledgments

I wish to express my sincerest gratitude to my advisor, Prof. Eric Akkermans, for inspiring me to pursue a clean and precise academic research; for his myriad of ideas and immeasurable knowledge – an ideal to which I aspire; and for being more than a mentor and a friend.

I am especially grateful to my collaborators: Ohad Shpielberg, Eli Levi, Dor Gitelman, Omrie Ovdat, Jonathan Rosenberg, Chaim Schochet and Eric Akkermans, who helped me to manifest my thoughts and schemes into concrete compositions.

I would also like to thank my colleagues: Ohad Shpielberg, Dor Gitelman, Omrie Ovdat, Boris Rotstein, Barak Katzir, Tom Shindelman and Ariane Soret for the many hours of fruitful discussions and the interesting ideas.

Lastly, I salute my family for their infinite patience and support.

To my late grandfather,
Antsel Fridman

Contents

List of Figures

List of Tables

Abstract

Structural and spectral properties of periodic tilings are well understood in the framework of the Bloch theorem. For quasiperiodic tilings generated by the Cut and Project (C&P) algorithm, we show how to relate structure and spectrum of $1d$ tilings by means of topological numbers originated in windings of phases that we define. These winding numbers are associated with Bragg peak locations in the reciprocal space and with spectral gap labeling for the structure and spectrum, respectively, suggesting a novel extension of the Bloch theorem for $1d$ C&P tilings. We investigate and classify general non-C&P tilings using cohomology groups, and implement these ideas with dual tilings and scattering theory. We analyze the diffraction spectrum of $1d$ tilings, and illustrate how to establish structural features based on these groups. We then present an extension of the Bloch theorem based on certain groups in dimensions ≤ 3, and discuss its application in both C&P and non-C&P cases.

Furthermore, we apply ideas from tiling theory to fractals embedded in a $2d$ space, and suggest a gap labeling formula in fractal systems. Immersing fractals into a non-uniform magnetic flux, we demonstrate topological phase transitions using the flux as an order parameter. Finally, we present and analyze topological phase transitions inside randomized substitution tilings adapting the aforementioned cohomology groups.

Abbreviations and Notation

Abbreviations

AC	Absolutely continuous
Aper	Aperiodic
BZ	Brillouin zone
C&P	Cut and Project
DOM	Density of modes
DOS	Density of states
Fibo	Fibonacci
Fibo^2	Fibonacci squared
FLC	Finite local complexity
Fr	Fractal
GLT	Gap Labeling Theorem
IDOS	Integrated density of states / modes
PD	Period Doubling
PE	Pattern Equivariant / Pattern Equivarience
Per	Periodic
Pisot	Pisot-Vijayaraghavan property
PP	Pure-point
RS	Rudin-Shapiro
SC	Singularly continuous
Sier	Sierpiński
TH	Top-hat
TM	Thue-Morse
TPT	Topological Phase Transition

const	Constant
h.c.	Hermitian conjugate
N/A	Not applicable
w.r.t.	With respect to

Notation

$\star$	Autocorrelation binary operator
$*$	Convolution binary operator
$\oplus$	Direct sum binary operator
$[\cdot\,,\cdot]$	Commutator binary operator
$\langle\cdots\rangle_r$	Average with respect to r
$\lvert\cdot\rangle\,,\langle\cdot\rvert$	Ket and Bra brackets
$\langle\cdot\,,\cdot\rangle$	Nearest neighbors
$\langle\langle\cdot\,,\cdot\rangle\rangle$	Next nearest neighbors
$\cdot \overset{n}{\sim} \cdot$	Neighbors of order n
$\doteq$	"Defined as" binary relation
$\mapsto$	"Maps to" binary relation
$\mathbb{D}$	Dyadic numbers
$\mathbb{D}_r$	r-adic numbers
$\mathbb{N}$	Natural numbers
$\mathbb{Q}$	Rational numbers
$\mathbb{R}$	Real numbers
$\mathbb{T}^2$	Torus
$\mathbb{Z}$	Integer numbers
$\mathbb{Z}\,[c]$	The ring $\mathbb{Z}$ with c adjoined
$\triangle$	Upward plaquette (triangle)
$\triangledown_m$	Downward plaquette (triangle) of depth m
$\boldsymbol{A}$	Vector potential

$A, B, \ldots$	$1d$ tiles (letters)
α	Chiral phase
α	Scaling exponent for diffraction measure
α_{ij}	Magnetic (Peierls) phase
A_*^{T}	Inflation matrices
$\boldsymbol{B}$	Magnetic field
$\mathcal{B}, \mathcal{B}_T$	Non-commutative Brillouin zone
β_n	Betti number of H_n
b	Flux basis of growth
C	Autocorrelation
$C(t)$	Heat capacity
$c^\dagger, c$	Creation and annihilation operators
C	Chern number
c_N	Slope numerator approximation of order N
d	Space dimension
d_h	Hausdorff dimension
d_s	Spectral dimension
d_w	Walk dimension
∇^2	Continuous Laplacian
Δ	Discrete Laplacian
$\delta(k)$	Total phase shift
$\delta(x)$	Delta function
d_N	Slope denominator approximation of order N
∂	Boundary operator
δ	Coboundary operator
$D(\cdot, \cdot)$	Tiling metric
E	Energy
E_F	Fermi energy
$E_\parallel$	Physical space
$E_\perp$	Internal space

$F(t)$	Free energy
F_N	Generalized substitution numbers of order N
$\hat{\mathcal{F}}, \hat{\mathcal{F}}_x$	Fourier transform with respect to x
Φ	Magnetic flux
Φ_0	Magnetic flux quantum
$\boldsymbol{G}$	Reciprocal lattice
G	Planar graph
G_n	Bratteli graph for length-n letters
γ	Asymmetrical phase
γ	Scaling exponent for diffraction peaks
Γ_n	Alphabet of length-n letters
γ_n	Shift map for length-n letters
γ_{ij}	Geometric angle
γ	Zak phase, Berry phase
G, g	Diffraction amplitude
$\mathcal{H}$	Continuous Hamiltonian
$\check{H}^*$	Integral Čech cohomology
$\check{H}^*(\Omega_T, G)$	Čech cohomology over Ω_T with coefficients in $G = \mathbb{Z}, \mathbb{R}$
H_n^*	Simplicial cohomology of G_n
η	IDOS as a measure
H	Discrete Hamiltonian
H_L, H_A	Linear and Area model Hamiltonians
H_P	Peierls Hamiltonian
I	Inverse Participation Ratio
k	Wavevector
K_0	The K_0 group.
k_0	Singularly continuous peak location in k-space
k_B	Bragg (pure-point) peak location in k-space
L	L-system
l	Letter

L_A, L_B	Tile length
$\mathbf{\Lambda}$	Miller indices
λ_*, λ_1	Leading eigenvalue
M	Occurrence matrix
μ	Positive diffraction measure
$\mu_{\mathrm{PP}}, \mu_{\mathrm{AC}}, \mu_{\mathrm{SC}}$	Pure-Point, Absolotely Continuous and Singularly Continuous measures
$\mathcal{N}, \eta$	Integrated density of states / modes
n	Refraction index
ν	Index
P	Band projections
ϕ	Phason
π	L-system rule
$\pi_{\parallel}$	Projection onto the physical space
$\pi_{\perp}$	Projection onto the internal space
ρ	Atomic density
ϱ	Density of states / modes
ρ_A, ρ_B	Tile density (probability)
r	Ratio between the fluxes in $\triangle$ and $\triangledown_1$
$\vec{r}, \overleftarrow{r}$	Rightwards and Leftwards reflection coefficients
$\mathcal{S}$	Scattering matrix
S	Diffraction intensity
s	C&P slope
$S\,(t)$	Entropy
σ, σ_T	Substitution rule on tiling T
Σ_0	Default shift matrix
Σ_1	Permuted shift matrix
Σ_2	Continuous shift matrix
$\sigma_{T_2}^{T_1}$	Random substitution rule between tilings T_1 and T_2
$\sigma_x, \sigma_y, \sigma_z$	Pauli matrices
s_N	Slope approximation of order N

$\mathcal{S}^{\boldsymbol{x}}$	C&P permutation operator
$\mathcal{T}$	Translation operator
T	Tiling
t	Tile
τ	Golden ratio
$\tau_*^{\check{H}}$	Trace on the $\check{H}^1$ group.
τ_*, τ_*^K	Trace on the K_0 group.
θ	Normalized flux
Θ, θ	Diffraction argument
t	Transmission coefficient
$T, \mathcal{T}$	Transfer matrix
$U\,(t)$	Internal energy
$\boldsymbol{u}_*, \boldsymbol{u}_1$	Right leading eigenvector
$\boldsymbol{v}_*, \boldsymbol{v}_1$	Left leading eigenvector
W	Winding number
w	Word
w_∞	Infinite word
$\mathcal{W}_\phi$	Winding operator with respect to the phason
Ξ	Relative winding
χ	Characteristic function
$x_n, \boldsymbol{x}_n$	Atomic positions
ψ_n	Eigenvector
$\psi_{\boldsymbol{k}}$	Eigenfunction
$u_{\boldsymbol{k}}$	Bloch Eigenfunction
Z	Neighbor matrix
$\zeta\,(z)$	Zeta function
$\zeta_H\,(t)$	Thermodynamic zeta function
$\zeta\,(s, \gamma)$	Spectral zeta function
$Z\,(t)$	Heat kernel
Ω, Ω_T	Tiling space

Chapter 1

Introduction

1.1 Context and Motivation

Periodic systems are of utmost significance in physics. They give rise to a plethora of phenomena in 1, 2 and 3 dimensions. Some are structural, such as crystallographic arrangement, diffraction, rigidity etc. [1]; others are spectral like bandgap, mobility and Chern numbers [1–4]. In addition, time periodicity causes Floquet Hamiltonians or time crystals. Combining structural and spectral properties, one arrives at the celebrated Bloch theorem [1] relating structural symmetries with those of the Hamiltonian wavefunctions.

Departing from periodic systems, one seeks close-to-periodic setups. A common scheme is a perturbative approach inserting a small disorder to a periodic system; another is introducing a topological defect such as a vacancy [5, 6], color center [7, 8] or a fracture; a different concept is hyperuniform materials [9, 10], which are disordered but sharing many properties with periodic systems. What we seek are almost-periodic systems that are, on the one hand, deterministic without any disorder or perturbation; but, on the other hand, are not periodic despite sharing features with them. The answer to that are aperiodic tilings, on which we focus in this thesis especially in $1d$.

Aperiodic tilings appear in many fields in condensed matter physics, dynamical systems, statistical mechanics, material science and optics among others. They answer the question: "is there a deterministic but non-periodic tiling of the plane using a finite set of tiles?". Initially conjectured positively by Wang [11] and confirmed by Berger using Wang tiles [12], this scheme was later generalized into Local Matching Rules. Soon many more tilings were found. Penrose [13, 14] showed a 5-fold rotational symmetry tiling of the plane known today as Penrose tiling using substitution rules. In $1d$, substitution rules of tilings are equivalent to spatial arrangements of letters above an alphabet [15, 16]. Later, de Bruijn explained how to obtain an aperiodic tiling by projecting from a higher-dimensional space [17, 18] established nowadays as the Cut and Project (C&P) scheme [15, 19]. To this day, these three methods, Local Matching Rules, Substitutions and C&P, are the main techniques to create aperiodic tilings.

A celebrated family of aperiodic tilings is that of quasiperiodic tilings being the closest (almost) periodic [20–22]. Tilings of this family exhibit Bragg peak diffraction; their spectral characteristics (of propagating waves, tight-binding Hamiltonians, etc.) display highly lacunar fractal energy spectrum with infinitely many gaps [23–26]. The Gap Labeling Theorem (GLT) [27, 28] makes it possible to classify these gaps

with integer numbers different from the usual Chern number classification of periodic tilings expressed in terms of Berry curvature [4, 29–31]. Those integer numbers cannot be represented in curvature terms of commutative geometries [27, 32]. These numbers can be given both a topological character and invariance properties via Čech cohomology. However, most of these features remain uncharted and inaccessible to experimental verification save notable exceptions [33–38]. Therefore, the topological content of aperiodic tilings, namely, the aforementioned integer numbers, has not been considered to be of physical relevance [39–41]. We demonstrate how to characterize these topological numbers in quasiperiodic tilings using winding numbers and connect them to known experiments.

Strolling outside the quasiperiodic realm, tilings become more exotic. Quasiperiodic tilings exhibit Bragg peaks that can be enumerated in the reciprocal space similar to Miller indices of periodic tilings. However, general aperiodic tilings have different combinatorics and thus cannot be enumerated in this manner. Additional physical properties, such as the spectrum of Hamiltonians defined on aperiodic tilings, are also affected by this change in combinatorics. We present the main mathematical tools required to identify and describe aperiodic tilings emphasizing Čech cohomology. We then show the physical consequences and present new calculations arising by using this description.

One main attribute of tilings is their diffraction spectrum characterizing their structural properties. A diffraction experiment on periodic tilings yields a picture consisting of Bragg peaks only in the reciprocal space implying a long-range correlation. Likewise, quasiperiodic tilings produce Bragg peaks in the reciprocal space, but have a dense diffraction spectrum and no Brillouin zone. From a physical point of view, the existence of Bragg peaks is a necessary (but not sufficient) trait for a tiling to be quasiperiodic. In general, however, the diffraction spectrum may be Lebesgue decomposed into Bragg, absolutely continuous and singularly continuous components. Notable examples are the Rudin-Shapiro tiling with an absolutely continuous diffraction spectrum, and the Thue-Morse tiling with a singularly continuous one. We analyze these diffraction components and show how to calculate the diffraction in some cases using methods derived from the calculation of the Čech cohomology.

If Bloch theorem is the central aspect of periodic tilings connecting the location of Bragg diffraction peaks to spectral gaps, then how does it manifest in aperiodic tilings? In quasiperiodic tilings, Bloch theorem is known to hold similarly to periodic tilings. In aperiodic tilings, however, it is typically not the case. We first formulate Bloch theorem in quasiperiodic tilings. Furthermore, we show that in $1d$ quasiperiodic tilings, there is an additional relation between structural windings over the phase of Bragg peaks and spectral windings over the chiral phase of the scattering matrix. We then show that in the more general case of finite local complexity (FLC) tilings in dimensions $d \leq 3$, only traces over the Čech cohomology and K_0 group keep the equivalence between structural and spectral properties, respectively.

We have established the integral Čech cohomology as the major topological invariant in aperiodic tilings in low dimensions. Therefore, a transition between two tilings with different Čech cohomologies infers a topological phase transition. To show it, however, is not a simple matter. In a first approach, we detour via fractals to show that for the Sierpiński gasket immersed in a magnetic flux, a topological phase transition occurs. We then present additional transport properties and analyze several index theorems on these fractals. In a second approach, we use randomized substitution rules to derive topological phase transitions between regular aperiodic tilings and demonstrate analogous thermodynamic properties therein.

1.2 Organization

This thesis is organized as follows.

In Chapter 2, we show simple quasiperiodic tilings created with the Cut and Project procedure and some of their characteristics using continued fractions. We investigate winding numbers, diffraction spectrum and Wannier diagrams. Finally, we show affinity with other quasiperiodic tilings created with substitution procedure.

In Chapter 3, we introduce the mathematical background used to describe general aperiodic tilings with an emphasis on substitution tilings. We then discuss physical topological features of aperiodic tilings using tools from scattering theory.

In Chapter 4, we analyze the diffraction spectrum using the Thue-Morse tiling as an example. We then show how to calculate diffraction in some cases with new mathematical tools.

In Chapter 5, we present the generalized Bloch theorem to quasiperiodic and aperiodic tilings.

In Chapter 6, we demonstrate fractals as an extension of tilings using L-systems. Adding magnetic flux, we indicate the gap labeling theorem and topological phase transitions. We finish with topological numbers and index formulae defined in such systems.

In Chapter 7, we illustrate topological phase transitions made between aperiodic tilings linked with random-rule order parameter, and shows analogous thermodynamic relations thereby derived.

In Chapter 8, we summarize the thesis and outline future prospects.

Chapter 2

Cut and Project Tilings and Windings

Aperiodic tilings contain topological information. Yet, at times, it is difficult to extract these topological attributes and connect them to physical features that can be measured in the laboratory. In the following, we show that winding numbers are a manifestation of the topological attributes.

2.1 Introduction

In this section, we introduce the main tools for the remainder of the chapter.

2.1.1 Cut and Project Scheme

The canonical Cut and Project (C&P) $2d \longrightarrow 1d$ procedure is defined as follows [42].

Cut.

1. Start with a 2-dimensional space $R = \mathbb{R}^2$.
2. Insert "atoms" on the integer lattice $Z = \mathbb{Z}^2$.
3. Divide R into a *physical space* (line) $E_\parallel$ and an *internal space* (line) $E_\perp$ such that $E_\parallel \oplus E_\perp = R$ and $E_\parallel \cap E_\perp = \{\boldsymbol{c}\}$ with $\boldsymbol{c} \in R$ defined below.
4. To resolve ambiguity for $E_\parallel$, choose an initial location $\boldsymbol{c} \in R$ such that $E_\parallel$ passes through $\boldsymbol{c}$. There is no such requirement for $E_\perp$.

Project.

1. Inspect the square $\mathbb{I}_2 = [-0.5, 0.5)^2$.
2. The *window* is its projection on the internal space $W = \pi_\perp(\mathbb{I}_2)$.
3. The *strip* is the product with the physical space $S = W \otimes E_\parallel$.
4. Choose only the points inside the strip $S \cap Z$, and project them onto the physical space, $Y = \pi_\parallel(S \cap Z)$.
5. The *atomic density* is given by $\rho(\boldsymbol{x}) \doteq \rho_{\boldsymbol{c}}(\boldsymbol{x}) = \sum_{\boldsymbol{y} \in Y} \delta(\boldsymbol{x} - \boldsymbol{y})$ with $\boldsymbol{x} \in E_\parallel$. Note the implicit dependence of Y on $\boldsymbol{c}$.

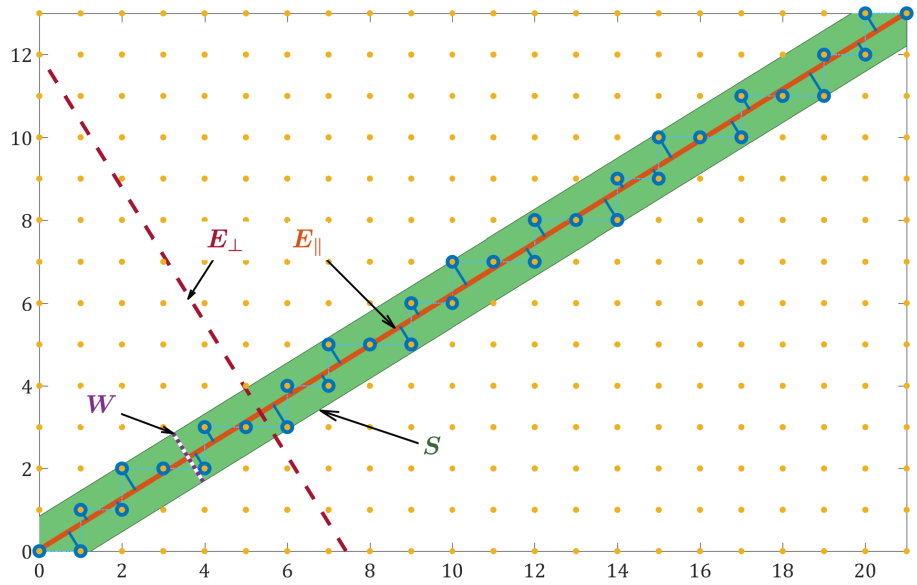

Figure 2.1: The Cut and Project (C&P) scheme. The red line is the cut line $E_\parallel$ with $y = x \tan\alpha + c$. Additionally $E_\perp$, W and S, as well as the points Z can the projections are indicated within.

The C&P scheme for $2d \to 1d$ is depicted in Figure 2.1. Here, there are only 2 possible distances between neighboring atoms, L_A, L_B. This gives us the notion of a *tiling* of the letters A and B. Another way to create this tiling is by moving in a stairway fashion on the atoms inside the strip: we assign A to a rightwards movement and B to the upward one.

This scheme is naturally generalized to any n-dimensional tiling as presented in Section 5.2.1.

2.1.2 Substitutions

For completion, we describe the substitution process in $1d$ [15, 43, 44]. Let $\Gamma_1 \doteq \{A, B, C, \ldots\} = \{l_1, l_2, \ldots\}$ be a set of letters and $w = l^{(1)} l^{(2)} \ldots l^{(m)} \in \Gamma_1^m$ be a word of size m made by concatenation. We define a substitution $\sigma : \Gamma_1 \to \Gamma_1^{\mathbb{N}}$ by replacing a letter $l_i \in \Gamma_1$ by some word. The action of σ on some word w is also made by concatenation $\sigma(w) = \sigma\left(l^{(1)}\right) \sigma\left(l^{(2)}\right) \ldots \sigma\left(l^{(m)}\right)$. Consecutive applications of σ are denoted by $\sigma^n(w)$. We denote by $w_\infty \doteq \sigma^\infty(l)$ the infinite word, where $\sigma^\infty \doteq \lim_{n\to\infty} \sigma^n$ assuming the limit exists.

The occurrence matrix M is defined by counting the number of letters in σ, namely, $M_{ij} = \left\{\#\text{ of } l_j \text{ in } \sigma(l_i)\right\}$. For example, a binary substitution σ with $\sigma(A) = A^\alpha B^\beta$ and $\sigma(B) = A^\gamma B^\delta$ has an occurrence matrix $M = \begin{pmatrix} \alpha & \beta \\ \gamma & \delta \end{pmatrix}$.

We typically demand that σ be:

Primitive. There exists some N such that all elements of M^N are strictly positive.

- It also means that $\sigma^N(l_i) \ni l_j$ for all l_i, l_j.
- The infinite word w_∞ are the same for all l_i [45].

Pisot. For spec $M = \{\lambda_1, \lambda_2, \ldots\}$ the eigenvalues of M have $\lambda_* \doteq \lambda_1 > 1$ and $|\lambda_{n\geq 2}| < 1$.

- The right eigenvector $\boldsymbol{u}_*$ of M has strictly positive elements, which denote the tile lengths $u_i^* = L_i$ for all $l_i \in \Gamma_1$ [43].
- The left eigenvector $\boldsymbol{v}_*$ of M has strictly positive elements and normalized by $\sum_i v_i^* = 1$. It corresponds to tile densities (probabilities) $v_j^* = \rho_j$ in w_∞ for all $l_j \in \Gamma_1$ [43].

Using M, we set $t = \operatorname{Tr} M$ and $p = \det M$, and define the sequence F_N for binary substitutions by

$$F_{N+1} = tF_N - pF_{N-1}, \quad F_0 = 0, F_1 = 1. \tag{2.1}$$

Example. For the Fibonacci substitution $\sigma_{\text{Fib}}(A) = AB$ and $\sigma_{\text{Fib}}(B) = A$, we obtain $M_{\text{Fib}} = \left(\begin{smallmatrix} 1 & 1 \\ 1 & 0 \end{smallmatrix}\right)$ so that $\lambda_{1,\text{Fib}} = \tau = (\sqrt{5}+1)/2$, $t_{\text{Fib}} = 1$, $p_{\text{Fib}} = -1$ and F_N are the Fibonacci numbers.

2.1.3 Windings

In the following, we shall use C&P tilings. More details are in Section 2.4 and Appendix 2.A.1. Consider a characteristic function [37, 38]

$$\chi(n, \phi) = \operatorname{sign}\left[\cos(2\pi n\, s + \phi) - \cos(\pi s)\right], \tag{2.2}$$

taking $n = 0 \ldots d_N - 1$ (where d_N are the *denominators* of the continued fraction of s, as explained in Section 2.4), and $\phi \in [0, 2\pi]$ being the phason. This characteristic function is equivalent to C&P (see Appendix 2.A.1). We make ϕ discrete by taking $\phi_\ell = 2\pi d_N^{-1}\, \ell = \Delta\phi\, \ell$ for $\ell = 0 \ldots d_N - 1$. In this case, only two neighboring letters change each $\Delta\phi$. This is in comparison with the C&P picture: as we move in the ϕ direction, namely in $E_\perp$, we hit a single "atom" each $\Delta\phi$ for a rational slope s_N. Therefore a single pair of letters changes: $AB \leftrightarrow BA$.

We take the discrete Fourier transform of $\chi(n, \phi)$ with respect to n,

$$g(\xi, \phi) = \sum_{n=0}^{d_N - 1} \omega^{-\xi n} \chi(n, \phi), \quad \omega = \mathrm{e}^{2\pi \mathrm{i}/d_N}. \tag{2.3}$$

The normalized structure factor is given by

$$S(\xi, \phi) = |g(\xi, \phi)|^2. \tag{2.4}$$

It is ϕ-independent as will be shown later (see Figure 2.2), and its phase of g is given by

$$\theta(\xi, \phi) = \arg g(\xi, \pi). \tag{2.5}$$

Here, one can define the winding number at some ξ_0 by

$$W_{\xi_0} = \frac{1}{2\pi} \int_0^{2\pi} \frac{\partial \theta(\xi = \xi_0, \phi)}{\partial \phi}\, \mathrm{d}\phi. \tag{2.6}$$

All the numerical results are given in Figure 2.2.

Claim. The winding $W = 1$ lies at position $\xi_0 = c_N$ with c_N the *numerators* of the continued fraction of s (see Section 2.4). This results from the formula of the Bragg peak locations for quasiperiodic sequences,

$$k_{p,q} = p + qs \pmod 1. \tag{2.7}$$

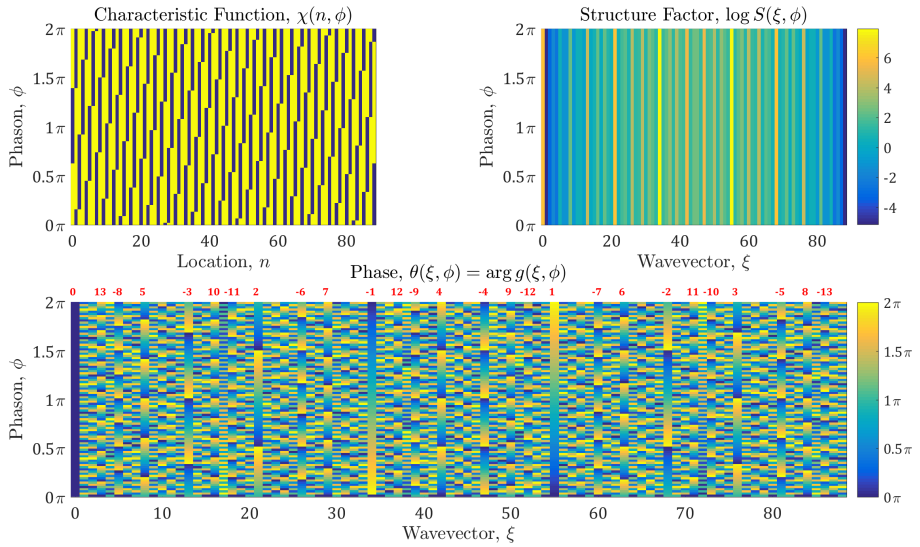

Figure 2.2: Characteristic function (top left) and its Fourier transform (top right) for the Fibonacci sequence. The phase θ is shown on the bottom panel. The winding numbers for $|W| \leq 13$ are indicated by red numbers. Here, $d_N = 89$ points were taken.

For the discrete case with a word of size d_N, one has

$$\begin{aligned} \xi_{p,q} = d_N k_{p,q} &\simeq p d_N + q c_N \pmod{d_N} \\ &= q c_N \pmod{d_N}, \end{aligned} \tag{2.8}$$

and identifying q with the winding. The details are in the following sections.

2.2 Analytic Calculation of Windings

In the following, we show how to define and calculate the winding numbers. We investigate the structural properties and show that the Fourier transform contains additional information with regard to these topological features.

2.2.1 Calculation of the Structural Phase

Let $s_0(n) = \chi(n, 0)$ be the first row of χ of size d_N. Let $\mathcal{T}$ be a translation operator such that $\mathcal{T}[s_0(n)] = s_0(n+1)$. Let Σ_0 be a vertical concatenation of such words,

$$\Sigma_0 = \begin{pmatrix} s_0 \\ \mathcal{T}[s_0] \\ \vdots \\ \mathcal{T}^{d_N-1}[s_0] \end{pmatrix} \implies \Sigma_0(n,\ell) = \mathcal{T}^{\ell}[s_0(n)]. \tag{2.9}$$

Note that Σ_0 is a $d_N \times d_N$ matrix (see Figure 2.3).

Consider now the matrices $\tilde{\Sigma}_r$, which are row-permuted Σ_0:

$$\tilde{\Sigma}_r = U_r \Sigma_0, \qquad U_r(m,\ell) = \delta_{\ell,\, m\, r\, c_N}. \tag{2.10}$$

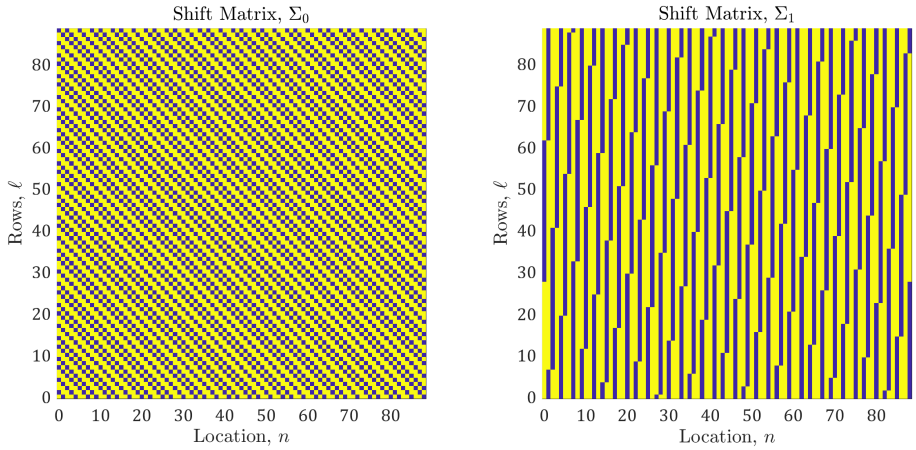

Figure 2.3: Shift matrices Σ_0 and Σ_1 for the Fibonacci sequence. Here, $d_N = 89$ points were taken.

Equivalently,

$$\tilde{\Sigma}_r(n,\ell) = \mathcal{T}^{m(\ell,r)}\left[s_0(n)\right], \tag{2.11}$$

with $m(\ell,r) = \ell\, r^{-1}\, c_N^{-1} \pmod{d_N}$. Henceforth, we shall remove the tilde $\tilde{\Sigma}_r \to \Sigma_r$ to simplify notations. We are interested in Σ_1 (see Figure 2.3).

Claim. For $\phi = 2\pi\ell/d_N$ with $n, \ell = 0 \ldots d_N - 1$ one has $\chi(n,\phi) = \Sigma_1(n,\ell)$. This is shown in Appendix 2.A.2.

Building on this equivalence, we take the discrete Fourier transform of Σ_1 with respect to n to have

$$\begin{aligned} G_N(\xi,\ell) \doteq \sum_{n=0}^{d_N-1} \omega^{-\xi n}\, \Sigma_1(n,\ell) &= \sum_{n=0}^{d_N-1} \omega^{-\xi n}\, \mathcal{T}^{m(\ell)}\left[s_0(n)\right] \\ &= \sum_{n=0}^{d_N-1} \omega^{-\xi n}\, s_0(n + m(\ell)) \\ &= \omega^{m(\ell)\xi} \sum_{n=0}^{d_N-1} \omega^{-\xi n}\, s_0(n) \\ &= \omega^{m(\ell)\xi}\, \varsigma_0(\xi)\,. \end{aligned} \tag{2.12}$$

Here, $\varsigma_0(\xi)$ is the discrete Fourier transform of $s_0(n)$.

Next, we identify $|\varsigma_0(\xi)|^2$ with the structure factor $S(\xi,\phi)$, since it holds the absolute-value information of $G(\xi,\ell)$. It is ϕ-independent as expected—its phase is constant with ϕ—and thus does not contribute to the windings.

To analyze the phase of $G(\xi,\ell)$, we inspect the $\omega^{m(\ell)\xi}$ part:

$$\begin{aligned} \Theta_N(\xi,\ell) \doteq \arg \omega^{m(\ell)\xi} &= \frac{2\pi}{d_N}\, m(\ell)\ \xi \pmod{2\pi} \\ &= \frac{2\pi}{d_N}\, \ell\, \frac{\xi}{c_N} \pmod{2\pi}. \end{aligned} \tag{2.13}$$

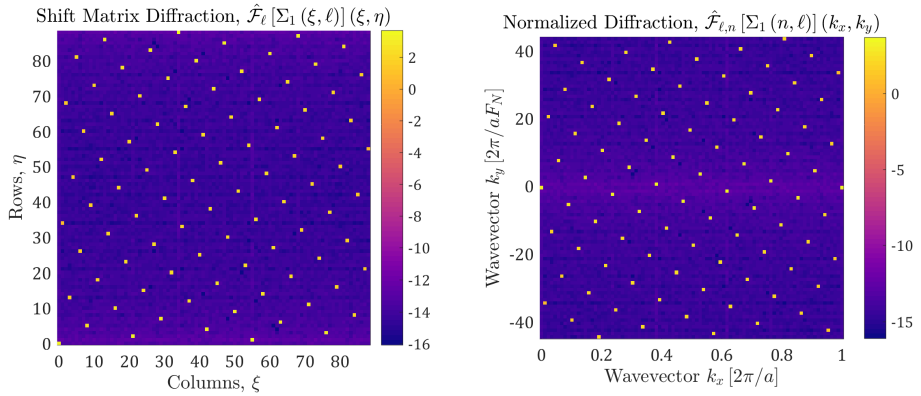

Figure 2.4: The double Fourier transform of Σ_1 for the Fibonacci sequence. Here, $d_N = 89$ points were taken. The images are in a logarithmic scale. (Left) The Shift matrix diffraction; (Right) same but with axes of $\left(k_x, k_y\right)$ with $a = 1$. Note that the last column in (b) is repeated for convenience.

Now, for $\xi_1 = 1 \cdot c_N$ one has $\Theta\left(\xi_1, \ell\right) = 2\pi d_N^{-1}\, \ell \times (+1)$, which leads to $W_{\xi_1} = +1$. This is our initialization condition. Generally, for any $\xi_q = q c_N$ one has

$$\Theta_N\left(\xi_q, \ell\right) = \frac{2\pi}{d_N}\, \ell\, q \pmod{2\pi} \implies W_{\xi_q} = q. \tag{2.14}$$

The result for the entire ξ axis is taken by the limit of N, namely,

$$\Theta\left(\xi, \ell\right) \doteq \lim_{N\to\infty} \Theta_N\left(\xi, \ell\right). \tag{2.15}$$

2.2.2 Fourier Transform of Σ_1

In the diffraction experiments of [38], a laser beam was shined through a mask having the shape of Σ_1 (see Figure 2.3), where a yellow pixel means a solid wall, and a blue one – a vacancy. Then, its diffraction pattern was inspected.

We inspect the discrete Fourier transform of $\Sigma_1\left(n, \ell\right)$ with respect to both n and ℓ. Note that it is the discrete Fourier transform of $G\left(\xi, \ell\right)$ with respect to ℓ:

$$\hat{\mathcal{F}}_\ell\left[\hat{\mathcal{F}}_n\left[\Sigma_1\left(n,\ell\right)\right]\left(\xi\right)\right]\left(\eta\right) = \hat{\mathcal{F}}_\ell\left[d_N\, G_N\left(\xi,\ell\right)\right]\left(\eta\right). \tag{2.16}$$

Thus,

$$\begin{aligned} E\left(\xi,\eta\right) &\doteq \hat{\mathcal{F}}_{\ell,n}\left[\Sigma_1\left(n,\ell\right)\right]\left(\xi,\eta\right) \\ &= \hat{\mathcal{F}}_\ell\left[d_N\, \varsigma_0\left(\xi\right)\, \omega^{m(\ell)\xi}\right]\left(\eta\right) \\ &= \hat{\mathcal{F}}_\ell\left[d_N\, \varsigma_0\left(\xi\right)\, \omega^{\ell\xi/F_{N-1}}\right]\left(\eta\right) \\ &= d_N^2\, \varsigma_0\left(\xi\right)\, \delta\left(\eta - \xi c_N^{-1}\right), \end{aligned} \tag{2.17}$$

where the argument of $\delta\left(\cdot\right)$ is taken modulo d_N.

Note that the strength is only dependent on $\varsigma_0\left(\xi\right)$. Additionally, one has Bragg peaks at $\xi = \eta c_N \pmod{d_N}$ (see Figure 2.4a). To normalize to the results of [38], transform the axes such that $k_x = -\xi/d_N$ and $k_y = \eta - \lceil d_N/2 \rceil$ (see Figure 2.4b).

Claim. We use c_N and d_N of the continued fraction, as explained in Section 2.4, but for substitution systems, we may use instead F_{N-1} and F_N. The latter case works only for quasiperiodic tilings, and specifically for the Fibonacci substitution. In the general quasiperiodic metallic or alloy case, compare to the results of Section 2.5.

Remark. Henceforth, we shall omit the subscript N in Θ_N and G_N for simplicity, as we are dealing with finite sequences.

2.3 Diffraction Spectrum of an Atomic Chain

Thus far, we have only examined the diffraction of a tiling, namely, assigning different values for tiles A/B. Next, we put atoms on the *boundaries* between the tiles and inspect their Fourier transform. This corresponds to two different possible diffraction experiments: the former was using a mask, and the latter is from a lattice.

2.3.1 Diffraction Spectrum

Consider atoms put on boundaries between tiles. We assign widths $l_{A/B}$ for layers A/B, respectively, for a tiling of size d_N, so that the total distance reads

$$y_n = \sum_{m=0}^{n} l_m. \tag{2.18}$$

Thus, the positions can be written—after proper normalization—as

$$x_n = y_n - \overline{y}, \tag{2.19}$$

with

$$\overline{y} = \frac{1}{d_N} \sum_{i=0}^{d_N-1} y_i = \frac{1}{d_N} \sum_{m=0}^{d_N-1} (d_N - m)\, l_m, \tag{2.20}$$

so that $\sum_n x_n = 0$.

The atomic density is given by

$$\rho(x) = \sum\nolimits_n \delta(x - x_n), \tag{2.21}$$

and its Fourier transform is

$$g(k) = \hat{\rho}(k) \doteq \sum\nolimits_n \mathrm{e}^{-\mathrm{i}x_n k}. \tag{2.22}$$

Correspondingly to the previous section, the diffraction spectrum reads

$$\acute{S}(k) = \frac{1}{d_N} |g(k)|^2, \tag{2.23}$$

where the factor $1/d_N$ accounts for the normalization. The structural phase is

$$\vartheta(k) = \arg g(k). \tag{2.24}$$

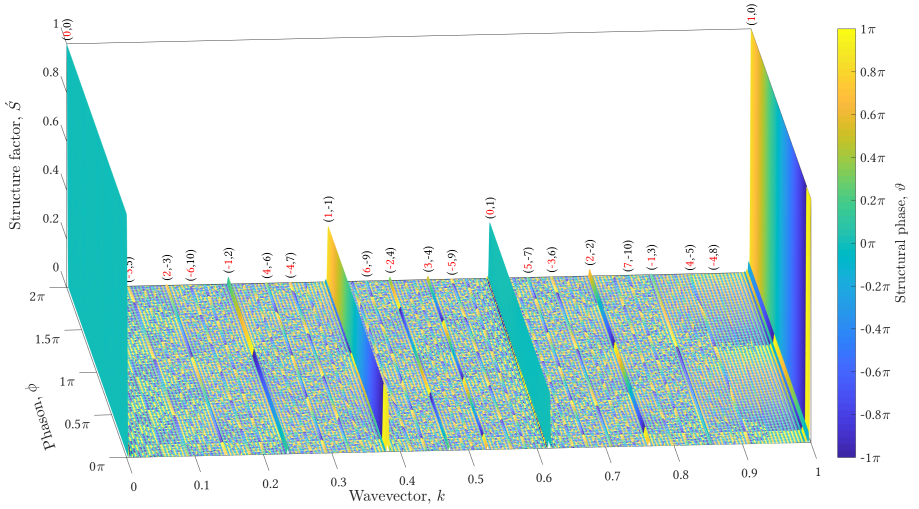

Figure 2.5: The atomic Fourier transform for the Fibonacci sequence with $\{l_A, l_B\} = \{2, 1\}$ and $d_N = 233$. The height represents the structure factor $\acute{S}/d_N$, and the color the structural phase ϑ. The pairs (p, q) for the first few Bragg peaks $k_0 = p + q/\tau$ are shown, and their corresponding winding number $\acute{W}$ is emphasized in red.

2.3.2 Adding the Phason

In order to make the structural phase ϕ dependent $\vartheta(k) \longrightarrow \vartheta(k, \phi)$, we consider the widths $l_{n,\ell}$ taken from Σ_1 above by

$$l_{n,\ell} = \frac{1 + \Sigma_1(n, \ell)}{2}(l_A - l_B) + l_B. \tag{2.25}$$

Next, the atomic positions are given by

$$x_n = \bar{l}n + (l_A - l_B)\, u_n, \qquad \bar{l} = \lim_{n\to\infty} \frac{x_n}{n}, \tag{2.26}$$

with $\bar{l}$ the mean length and u_n fluctuations. The relation between u_n and l_n (for any ℓ) is given by

$$l_n = (l_A - l_B)(u_n - u_{n-1}) \doteq (l_A - l_B)\,\epsilon_n. \tag{2.27}$$

We will sometimes consider ϵ_n instead of l_n.

Next, we find the relations between the Fourier transforms of u_n and ϵ_n. Recall that for a discrete Fourier transform,

$$\hat{\mathcal{F}}_n[f](\xi) \doteq \hat{f}(\xi) = \sum\nolimits_n \omega^{-\xi n} f(n), \tag{2.28}$$

with $\omega = e^{2\pi i/d_N}$, one obtains equation for the derivative

$$\hat{\mathcal{F}}_n[\Delta f](\xi) \doteq \sum\nolimits_n \omega^{-\xi n}(f(n) - f(n-1)) = \left(1 - \omega^{-\xi}\right)\hat{f}(\xi). \tag{2.29}$$

Thus,

$$\hat{\epsilon}_{\xi,\ell} = \frac{\hat{l}_{\xi,\ell}}{l_A - l_B} = \left(1 - \omega^{-\xi}\right)\hat{u}_{\xi,\ell}. \tag{2.30}$$

Table 2.1: Diophantine relations between (l_A, l_B) and $\left(n_p, n_q\right)$ in (2.32) for selected substitution sequences.

Name	Rule	M_1	n_p	n_q
Fibonacci	$\substack{A\mapsto AB\\B\mapsto A}$	$\left(\begin{smallmatrix}1&1\\1&0\end{smallmatrix}\right)$	$l_A - l_B$	$2l_B - l_A$
Fibonacci^2	$\substack{A\mapsto ABA\\B\mapsto AB}$	$\left(\begin{smallmatrix}2&1\\1&1\end{smallmatrix}\right)$	$l_B - l_A$	$3l_B - 2l_A$
Silver	$\substack{A\mapsto AAB\\B\mapsto A}$	$\left(\begin{smallmatrix}2&1\\1&0\end{smallmatrix}\right)$	$l_B - l_A$	$3l_A - 2l_B$

2.3.3 Phase Windings of Bragg Peaks

The Fourier transform $\hat{u}_{\xi,\ell}$ is *not* equivalent to $\hat{\rho}_{k,\ell} = g\left(k, \ell\right)$ in the limit $N \to \infty$. This is because u_n represents a step function, whilst $\rho\left(x\right)$ are the atomic positions. Nevertheless, by using simulations, we calculate $g\left(x, \ell\right)$ as in (2.22). The winding number is given, as before, by

$$\acute{W}_{k_0} = \frac{1}{2\pi} \int_0^{2\pi} \frac{\partial \vartheta\left(k = k_0, \phi\right)}{\partial \phi} \, \mathrm{d}\phi. \tag{2.31}$$

Figure 2.5 shows such results for the Fibonacci sequence for $\{l_A, l_B\} = \{2, 1\}$. Here, the winding number $\acute{W}_{p,q}$ of the Bragg peak $k_0 = p + q/\tau$ is given by its p value (instead of q). These results extend beyond the first quasi-Brillouin zone shown in Figure 2.5.

A numerical analysis shows that $\acute{W}$ obeys the following Diophantine equation in p, q for quasiperiodic substitution sequences,

$$\acute{W} = n_p p + n_q q, \qquad n_p, n_q \in \mathbb{Z}, \tag{2.32}$$

such that $n_{p,q}$ fulfill a linear Diophantine relation in $l_A, l_B \in \mathbb{Z}$. The results are given in Table 2.1. Note, however, that it works only for selected pairs of (l_A, l_B).

Remark. There cannot be a q-dependent only winding (that is, $p = 0$). In that case, $l_A = l_B$, as seen in Table 2.1, and there would be no aperiodic diffraction pattern.

2.4 Continued Fractions

The winding numbers obtained by Σ_1 do not work for any tiling length L_n, but only for the lengths of the tiling approximants T_N by consecutive orders N. For a general slope $s \in [0, 1]$, we inspect the continued fraction of s, which consists of the best rational approximations to s. These approximations produce the correct lengths d_N for Σ_1. This natural expansion is shown below (see also [46, 47]).

2.4.1 Expansion via Continued Fractions

Every number $s \in \mathbb{R}$ can be written in a continued fraction form

$$s = a_0 + \cfrac{1}{a_1 + \cfrac{1}{a_2 + \cfrac{1}{a_3 + \ldots}}} \doteq \left[a_0; a_1, a_2, a_3, \ldots\right], \tag{2.33}$$

where $a_0 \in \mathbb{Z}$ is an integer and $a_{i\geq 1} \in \mathbb{N}$ natural numbers.

- If the expansion is finite—that is $\exists n_0$ such that $\forall n > n_0$ one has $a_n = 0$—then $x \in \mathbb{Q}$ is rational.
- If the expansion becomes periodic—that is $\exists n_0, d$ such that $\forall n > n_0,\ a_{n+d} = a_n$—then s is algebraic. For example, the golden ratio reads

$$\tau^{-1} = \cfrac{1}{1 + \cfrac{1}{1 + \cfrac{1}{1 + \ldots}}} \doteq [0; 1, 1, 1, \ldots] . \tag{2.34}$$

- If there is no period, then the number s is transcendental. For example, for $s = 1/\pi$,

$$\pi^{-1} = [0; 3, 7, 15, 1, 292, 1, 1, 1, 2, 1, 3, 1, 14, 2, 1, 1, 2, 2, 2, \ldots] . \tag{2.35}$$

Next, we consider the sequence s_N, the finite expansion up to the N^{th} number a_N,

$$s_N = \cfrac{1}{a_1 + \cfrac{1}{a_2 + \cfrac{1}{\ddots + \frac{1}{a_N}}}} = [0; a_1, a_2, \ldots, a_N] . \tag{2.36}$$

It is a rational approximation to s (that is $s_N \in \mathbb{Q}$), where

$$\lim_{N\to\infty} s_N = s. \tag{2.37}$$

For example, for $s = 1/\pi$,

$$\{s_N\}_{N=0}^{\infty} = \left\{ \frac{0}{1}; \frac{1}{3}, \frac{7}{22}, \frac{106}{333}, \frac{113}{355}, \frac{33102}{103993}, \frac{33215}{104348}, \frac{66317}{208341}, \frac{99532}{312689}, \ldots \right\} . \tag{2.38}$$

We consider the sequences c_N the numerators and d_N denominators of s_N. For instance, for $s = 1/\pi$,

$$\begin{aligned} c_N &= \{0; 1,\ \ 7, 106, 113,\ \ 33102,\ \ 33215,\ \ 66317,\ \ 99532, \ldots\} , \\ d_N &= \{1; 3, 22, 333, 355, 103993, 104348, 208341, 312689, \ldots\} . \end{aligned} \tag{2.39}$$

We list below several lemmas and corollaries, proofs of which can be found in standard textbooks [48].

Lemma. *These sequences are minimal in the sense that for any $c \le d \le d_N$ approximating s by $s \simeq c/d$, the distance $\delta = |ds - c|$ is minimal for $c = c_N$ and $d = d_N$.*

Corollary. *The sequence s_N constitutes the best rational approximations to s.*

Lemma. *For the N^{th} convergent $s_N = c_N/d_N$, the following holds,*

$$d_N c_{N-1} - d_{N-1} c_N = (-1)^N . \tag{2.40}$$

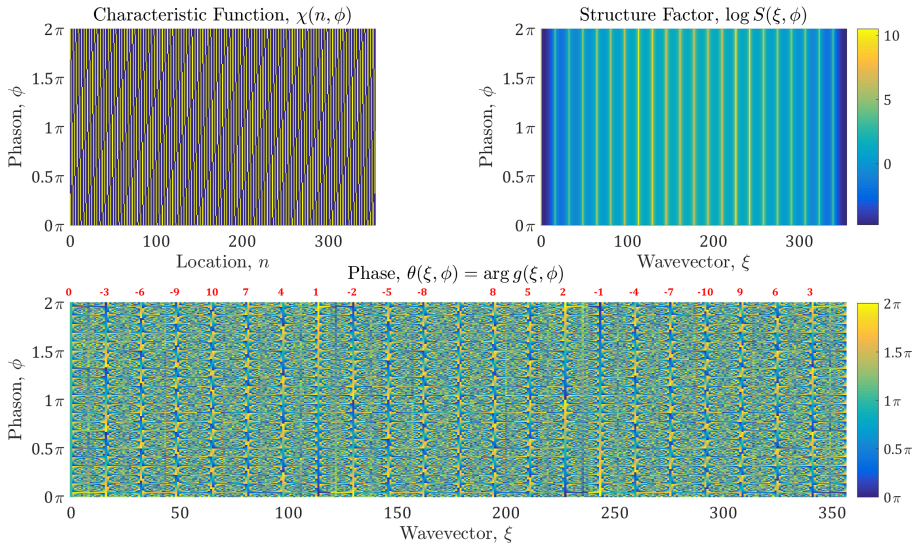

Figure 2.6: Characteristic function (top left) and its Fourier transform (top right) for $s = 1/\pi$. he phase θ is shown on the bottom panel. The winding numbers for $|W| \leq 10$ are indicated by red numbers. Here, $d_N = 355$ is the period and $c_N = 113$ the first Bragg peak location.

Corollary. *For periodic continued fractions using the lemma above,*

$$c_N^2 = \pm 1 \pmod{d_N}. \tag{2.41}$$

Remark. The s_N numbers in (2.36) can be generalized so that $\tilde{s}_N = [0; a_1, a_2, \ldots, a_N - 1]$ is also a good approximation. In other words, any partial rational approximation,

$$\tilde{s}_N^{(j)} = [0; a_1, a_2, \ldots, a_N - j], \qquad a_N > j \geq 0, \ j \in \mathbb{Z}, \tag{2.42}$$

holds *all* the properties of $s_N \doteq \tilde{s}_N^{(0)}$ above. For instance, it has generalized c_N and d_N.

2.5 Affinity between C&P and Substitution Tilings

Cut and Project and substitution methods usually create incongruous tilings. For instance, the π^{-1} tiling has no substitution counterpart, whereas σ_3 (see (3.46)) cannot be created by a C&P procedure. In the following section, we shall show the differences and similarities between both.

2.5.1 Quasiperiodic Sequences in C&P

Cut and Project tilings are the closest to periodic. In fact, in 1d they are equivalent to Sturmian sequences [49]. There are uncountably many ones [50], as the slope $s \in [0, 1] \subset \mathbb{R}$. We shall use the following.

Proposition (Quasiperiodic C&P). *A quasiperiodic tiling in* 1d *made by C&P method has an irrational slope, namely,* $s \in \mathbb{R} \setminus \mathbb{Q}$.

This excludes all periodic tilings, but does not exclude transcendental ones. The latter have non-algebraic slopes, e.g., $s = \pi^{-1}$. To connect to substitution sequences we must have *algebraic* quasiperiodic C&P sequences.

The diffraction (Bragg) spectrum of a $1d$ C&P tiling is given by

$$k_0 \in \mathbb{Z} + s\mathbb{Z}. \tag{2.43}$$

It is equivalent to the Hamiltonian spectrum by the location of the gaps

$$\mathcal{N} \in (\mathbb{Z} + s\mathbb{Z}) \cap [0, 1)\,. \tag{2.44}$$

This implies a Bloch theorem for these tilings.

2.5.2 Quasiperiodic Sequences in Substitutions

Consider again 2-letter substitution rule σ and its associated occurrence matrix M_1 as in Section 2. We inspect only *primitive, irreducible* matrices with *Pisot property.* The leading *left* eigenvector of M (namely, the one corresponding to the largest—Pisot—eigenvalue λ_*) portrays the tile densities ρ_i (in the infinite word w_∞) by

$$\boldsymbol{v}_1 = \begin{pmatrix} \rho_A & \rho_B \end{pmatrix}, \qquad \rho_A + \rho_B = 1. \tag{2.45}$$

For substitutions with $\det M = \pm 1$, the Bragg peaks are located at [43],

$$k_0 \in \mathbb{Z} + \rho_B\mathbb{Z}, \tag{2.46}$$

with the gaps placed at [27],

$$\mathcal{N} \in (\mathbb{Z} + \rho_B\mathbb{Z}) \cap [0, 1)\,. \tag{2.47}$$

This is reminiscent of the C&P tilings above implying a connection between both.

The leading *right* eigenvector $\boldsymbol{w}_1 = \begin{pmatrix} l_A & l_B \end{pmatrix}^{\mathsf{T}}$ expresses the tile lengths. There are two natural normalizations.

1. One of the tiles is of unit length 1,

$$\min\{l_A, l_B\} = 1. \tag{2.48}$$

2. The ratio of the tiles converges to a fixed point [43],

$$\xi_* \doteq \frac{l_A}{l_B} = \frac{\beta}{\lambda_* - a} = \frac{\lambda_* - \delta}{\gamma}. \tag{2.49}$$

This corresponds to a C&P scheme with slope s and angle θ,

$$\frac{l_A^{\text{C\&P}}}{l_B^{\text{C\&P}}} \doteq \frac{1/\cos\theta}{1/\sin\theta} = \tan\theta = \frac{1}{s^{-1} - 1}. \tag{2.50}$$

Both normalizations can be generalized to higher dimensions or larger tile sets (with the first one simpler to implement).

We consider next the following substitutions.

Definition (Common unimodular substitution)**.** A substitution σ is called *unimodular* if it is *primitive, irreducible,* with *Pisot property,* and *unimodular* ($\det M = \pm 1$). It is called *common unimodular* if it additionally has *common prefix* (or *suffix*) [51].

Theorem. *Common unimodular substitution tilings have a pure-point spectrum [43, 51].*

We inspect substitutions with *common prefix*, that is $\sigma(l)$ starts with the same letter l_0 for all $l \in \{A, B\}$. We consider *metallic* and *alloy* substitutions

$$\sigma_m^{\text{metal}} : \begin{matrix} A \mapsto A^m B \\ B \mapsto A \end{matrix} \qquad m \geq 1, \tag{2.51a}$$

$$\sigma_m^{\text{alloy}} : \begin{matrix} A \mapsto A^{m-1} B^{m-2} \\ B \mapsto AB \end{matrix} \qquad m \geq 3. \tag{2.51b}$$

Their occurrence matrices are

$$M_m^{\text{metal}} = \begin{pmatrix} m & 1 \\ 1 & 0 \end{pmatrix}, \tag{2.52a}$$

$$M_m^{\text{alloy}} = \begin{pmatrix} m-1 & m-2 \\ 1 & 1 \end{pmatrix}, \tag{2.52b}$$

having the characteristic polynomials

$$p_m^{\text{metal}}(z) = z^2 - mz - 1, \tag{2.53a}$$

$$p_m^{\text{alloy}}(z) = z^2 - mz + 1, \tag{2.53b}$$

with the Perron-Frobenius eigenvalues

$$\lambda_m^{\text{metal}} = \left(m + \sqrt{m^2 + 4}\right)/2, \tag{2.54a}$$

$$\lambda_m^{\text{alloy}} = \left(m + \sqrt{m^2 - 4}\right)/2. \tag{2.54b}$$

Remark. The metallic and alloy substitutions (with internal permutations) span all quasiperiodic substitutions [51], since all monic quadratic polynomials over the integers $p(x) = x^2 + a_1 x + a_0$ with $a_0 = \pm 1$ are either $p_m^{\text{metal}}(\pm x)$, $p_m^{\text{alloy}}(\pm x)$ or $r(x) = x^2 \pm 1$.

Proposition. *The spectrum of the metallic and alloy substitutions is given by [51]*

$$\mathcal{N} \in \mathbb{Z}[v_1] \cap [0, 1), \tag{2.55}$$

so that

$$\mathcal{N}^{metal} \in \frac{1}{\lambda_m + 1} (\mathbb{Z} + \lambda_m \mathbb{Z}) \cap [0, 1), \tag{2.56a}$$

$$\mathcal{N}^{alloy} \in \frac{m-2}{\lambda_m + m - 3} \left(\mathbb{Z} + \frac{\lambda_m - 1}{m-2} \mathbb{Z}\right) \cap [0, 1). \tag{2.56b}$$

These can be rewritten as

$$\mathcal{N}^{metal} \in \frac{1}{m} (\mathbb{Z} + \lambda_m \mathbb{Z}) \cap [0, 1), \tag{2.57a}$$

$$\mathcal{N}^{alloy} \in \frac{1}{\lambda_m + m - 3} (\mathbb{Z} + \lambda_m \mathbb{Z}) \cap [0, 1). \tag{2.57b}$$

Remark. The metal and alloy substitutions are not unique in creating the characteristic polynomials (2.53). Another option may be

$$M_m^{\text{metal}^*} = \begin{pmatrix} m-2 & 1 \\ m-1 & 1 \end{pmatrix}, \tag{2.58a}$$

$$M_m^{\text{alloy}^*} = \begin{pmatrix} m-1 & 1 \\ m-2 & 1 \end{pmatrix}. \tag{2.58b}$$

2.5.3 Connection between C&P and Substitution Tilings

2.5.3.1 Tile Frequencies.

Recall (2.77), where

$$s = \rho_A \qquad \text{or} \qquad s = \rho_B, \tag{2.59}$$

where the two options are symmetric. Now,

$$\rho_B^{\text{metal}} = \frac{1}{\lambda_m^{\text{metal}} + 1} \tag{2.60a}$$

$$\rho_B^{\text{alloy}} = \frac{m-2}{\lambda_m^{\text{alloy}} + m - 3}, \tag{2.60b}$$

implying that (2.43) corresponds to (2.56).

2.5.3.2 Atomic Spectra.

Another connection is given by [43]. There the authors claim that only substitutions of the form

$$\sigma_r^{\text{ore}} : \begin{array}{l} A \mapsto (BA^r)^r A \\ B \mapsto BA^r, \end{array}, \tag{2.61}$$

with

$$M_r^{\text{ore}} = \begin{pmatrix} r^2+1 & r \\ r & 1 \end{pmatrix}, \tag{2.62}$$

are quasiperiodic. The leading eigenvalue and eigenvector of M_r^{ore} are

$$\lambda_r^{\text{ore}} = \frac{r^2 + 2 + r\sqrt{r^2+4}}{2}, \tag{2.63}$$

$$\boldsymbol{v}_r^{\text{ore}} = \frac{1}{\lambda_r^{\text{ore}} - 1 + r}\left(\lambda_r^{\text{ore}} - 1, \quad r\right). \tag{2.64}$$

After some algebra, one obtains,

$$\mathcal{N}^{\text{ore}} \in \frac{1}{r^4}\left(\mathbb{Z} + \lambda_r^{\text{ore}}\mathbb{Z}\right) \cap [0,1). \tag{2.65}$$

This class, however, excludes the simple Fibonacci substitution (but includes its square).

On top of that, [43] quantify substitutions of the same occurrence matrix by their fluctuations $\Delta_u(\sigma)$, namely, distance from the mean tiling length

$$\Delta_u = \lim_{n\to\infty} \sup u_n - \lim_{n\to\infty} \inf u_n, \tag{2.66}$$

where $u_n = x_n - \bar{l}n$ with x_n atomic positions and $\bar{l} = \lim_{n\to\infty} x_n/n$. These substitutions are thus distributed into families. The quasiperiodic family is given by $\Delta_u = 1$ with the normalization of l_A, l_B as in (2.49).

Proposition. *Quasiperiodic substitutions are common unimodular substitutions with* $\Delta_u = 1$.

Remark. Quasiperiodic substitutions can be defined only by $\Delta_u = 1$. The necessary common unimodular condition comes to reduce the search space.

COMPLEMENT 2.A Equivalence Calculations

We have shown three ways to create quasiperiodic sequences: C&P, characteristic function and Σ_1. In the following Appendix, we shall show that all three are, indeed, equivalent.

2.A.1 Equivalence between Cut and Project and Characteristic Function

The quasiperiodic sequence [43]

$$x_k = ka + (l_A - l_B)\, u_k, \tag{2.67}$$

can be identified with Cut and Project [43]

$$x_k = \frac{1}{\sin\alpha + \cos\alpha} k + (\cos\alpha - \sin\alpha)\, g\,(ks)\,, \quad \begin{cases} a = (\sin\alpha + \cos\alpha)^{-1} \\ l_A = \cos\alpha \\ l_B = \sin\alpha. \end{cases} \tag{2.68}$$

The fluctuations $u_k = g\,(ks)$ are given by [43]

$$g\,(x) = \mathrm{frac}\,(x) - 1, \tag{2.69}$$

with $\mathrm{frac}\,(x) = x \pmod 1 = x - \lfloor x \rfloor$ the fractional part, and

$$s \doteq \lim_{k\to\infty} \frac{L_B^k}{L_A^k + L_B^k} = \frac{\sin\alpha}{\sin\alpha + \cos\alpha} = \frac{1}{1 + \cot\alpha}, \tag{2.70}$$

is the generalized slope, where $L_{A/B}^k \doteq \lfloor k \cdot l_{A/B} \rfloor$ the number of A-s or B-s up to the k^{th} letter. Note that $s \in [0, 1]$.

Now, we are interested in the difference,

$$\epsilon_k = u_k - u_{k-1} = g\,(sk) - g\,(s\,(k-1))\,, \tag{2.71}$$

which can have only two values (l_A and l_B). This is the tiling. Rephrasing, one has $\epsilon_k = f\,(ks)$ with [43]

$$f\,(x) = g\,(x) - g\,(x-s) = \mathrm{frac}\,(x) - \mathrm{frac}\,(x-s) = \begin{cases} s, & 1 > \mathrm{frac}\,(x) > s; \\ s-1, & s > \mathrm{frac}\,(x) > 0. \end{cases} \tag{2.72}$$

Note that $f\,(x)$ is 1-periodic function that can have only two values

$$\begin{array}{rl} f(x): & \\ x: & \underset{0}{|}\overset{1-s}{\text{———}}\underset{s}{|}\overset{s}{\text{———}}\underset{1}{|}. \end{array} \tag{2.73}$$

Another function behaving similarly is

$$h\,(x) = \mathrm{sign}\,[\cos\,(2\pi x) - a]\,. \tag{2.74}$$

It is one periodic and can only have two values (± 1).

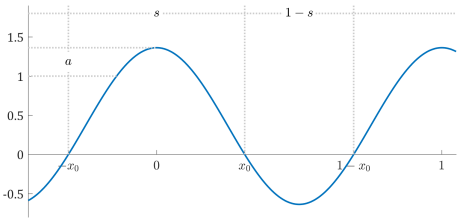

Figure 2.7: The cosine function inside $h\,(x)$. Here, the period is 1, where the widths are indicated above. The constant a is indicated on the left.

We therefore only need to find a such that $h(x)$ is weighted appropriately. Looking at Figure 2.7 it is clear we only need to find the first zero $x_0 = s/2$. It lies at $x_0 = \cos^{-1}(a)/2\pi$. Thus,

$$h(x) = \text{sign}\left[\cos(2\pi x) - \cos(\pi s)\right]. \tag{2.75}$$

We set $x = ns + \phi/2\pi$ to reproduce the characteristic function

$$\chi(n,\phi) = h(ns + \phi/2\pi) = \text{sign}\left[\cos(2\pi ns + \phi) - \cos(\pi s)\right]. \tag{2.76}$$

We thus finish our proof of equivalence between $f(x)$ and $\chi(n,\phi)$. ⊠

Remark. According to [43]

$$s = \rho_B = \frac{\lambda_1 - \alpha}{\lambda_1 - \alpha + \gamma} = \frac{\beta}{\lambda_1 + \beta - \delta}, \tag{2.77}$$

with the usual notation $M = \begin{pmatrix} \alpha & \beta \\ \gamma & \delta \end{pmatrix}$. The choice of $s = \lambda_1^{-1}$ is consistent only for Fibonacci substitutions. For the general case, read Section 2.5.3.

2.A.2 Equivalence between Characteristic Function and Σ_1

In the previous section, we showed the equivalence between the C&P $f(x)$ function and the characteristic $\chi(n,\phi) = h(ns + \phi/2\pi)$. To show $\chi(n,\phi) \cong \Sigma_1(n,\ell)$, all we have to show is the equivalence

$$\Sigma_1(n,\ell) \cong f_{n,\ell}(x) = f(ns + \phi_\ell/2\pi). \tag{2.78}$$

Now, Σ_1 is defined by translations $\mathcal{T}^m$, meaning,

$$\text{row}_\ell\, \Sigma_1 = \mathcal{T}^{m(\ell)}\, \text{row}_0\, \Sigma_1. \tag{2.79}$$

Thus, we need to show that $f(x)$ is also invariant under translations by any $x_\ell = \phi_\ell/2\pi = \ell d_N$ such that $\exists m$, where

$$f(ns + x_\ell) = f((n+m)s) = f(ns + ms). \tag{2.80}$$

The condition above can be rephrased as

$$\text{frac}(x_\ell) = \text{frac}(ms) \iff \ell\, d_N^{-1} = ms \pmod 1. \tag{2.81}$$

In the finite approximation we use, $s \simeq c_N/d_N$ (or, F_{N-1}/F_N for Fibonacci). Hence, we have

$$m\, c_N = \ell \pmod{d_N}, \tag{2.82}$$

which is the exact definition of m in Σ_1. ⊠

Remark. There is a small discrepancy between $\chi(n,\phi)$ and $\Sigma_1(n,\ell)$. From Section 3.1.5, we know that there are $d_N + 1$ different words of size d_N. All of these words are seen in $\chi(n,\phi)$, when $\phi \in [0, 2\pi)$ is a continuous parameter. Yet, only d_N such words exist in $\Sigma_1(n,\ell)$ by definition; the extra word lies in the small cycle, as explained in Section 3.1.6.

The equivalence above between χ and Σ_1 holds only for $\phi \mapsto \phi_\ell$ being a *discrete* parameter and a proper choice of the initial condition ϕ_0. It does not, however, change our understanding of the toroidal topology of Σ_1.

Chapter 3

Substitution Tilings

In the previous sections, we showed how the C&P scheme can generate winding numbers for any slope s. In this section, we shall investigate substitution sequences, and how they generate windings.

3.1 Mathematical Background

In this section, we give the mathematical background and tools required for the latter parts. Mainly, we focus on the Gap Labeling theorem and the Čech cohomology.

3.1.1 Tilings

Tilings are a natural generalization of $1d$ sequences to higher dimensions. It is, therefore, the main tool we employ throughout this work.

Let us set up the main definitions for tilings we use [45, 52, 53].

1. A tiling T in $\mathbb{R}^n$ is a subdivision of $\mathbb{R}^n$ into tiles.
2. A tile t is a polytope (interval in $1d$; polygon in $2d$; polyhedron in $3d$; etc.).
3. There are only a finite number of file types up to Euclidean translation.

Definition. A tiling T that satisfies the above is called a "simple tiling".

4. A patch S is a finite subset of tiles in T.
5. A patch S_R is said to be of radius R if contains a ball of radius R (namely, $S_R \supseteq B_R$).
6. A tiling has finite local complexity (FLC) if for any fixed R there can only be a finite number of patches of radius R.

Claim. A simple tiling, whose tiles meet edge-to-edge, is FLC [52].

7. FLC tilings in $\mathbb{R}^n$ carry a metric [52, 54]

$$D(T,T') \doteq \inf\left\{\tfrac{1}{r+1} \mid \exists \boldsymbol{x},\boldsymbol{x}' \in \mathbb{R}^n,\ |\boldsymbol{x}|,|\boldsymbol{x}| \leq \tfrac{1}{r} : B_r \cap (T-\boldsymbol{x}) = B_r \cap (T'-\boldsymbol{x}')\right\}, \tag{3.1}$$

where B_r is a ball of radius r around the origin, and $B_r \cap (T-\boldsymbol{x})$ a patch of $T-\boldsymbol{x}$ containing B_r. In simple words, two tilings are $\frac{1}{r+1}$-close if they agree on a ball of radius r (up to translations of $\frac{1}{r}$ or less) taking the supremum such r.

8. The Hull Ω_T is the orbit closure of T with respect to the metric (3.1), $\Omega_T \doteq \overline{\{T - \boldsymbol{x} \mid \boldsymbol{x} \in \mathbb{R}^n\}}$. It is compact if T is a simple tiling [52].

Remark. Throughout this work, we only deal with FLC tilings. Other tilings, such as non-edge-to-edge [55] or the Kakutani sequences [56, 57], will not be considered.

In $1d$ we can consider tiles as letters, patches as words, and tilings as infinite words. We therefore can employ tools from dynamical systems analysis [50].

3.1.2 Gap Labeling Theorem

When the spectrum of an operator contains gaps, they manifest as plateaus in the IDOS $\mathcal{N}(E)$. For certain operators, such as Hamiltonians built using aperiodic tilings, these plateaus can be labeled by integer numbers. They are called "gap labels". In this section, we present succinctly how to calculate the gap labels in aperiodic Hamiltonians according to the gap labeling theorem.

3.1.2.1 The Gap Labeling Formula

For a $1d$ aperiodic substitution σ with occurrence matrix M, the possible gaps in the spectrum are given by [27],

$$\mathcal{N}_{\text{gap}} \in \tau_* \left[K_0 \left(\mathcal{B}_T \right) \right], \tag{3.2}$$

where the K_0 group is taken over the non-commutative Brillouin zone $\mathcal{B}_T$, and τ_* is its trace. The gap labeling theorem states that all open gaps must abide (3.2), but it does not force the existence of such gaps. The non-commutative Brillouin zone is given by

$$\mathcal{B}_T = \mathcal{B}\left(\Omega_T\right) \doteq C^*\left(\mathbb{R}^d \times \Omega_T\right) \cong C\left(\Omega_T\right) \rtimes \mathbb{R}^d \tag{3.3}$$

where $C^*(X)$ and $C(X)$ are the C^*-algebra and continuous real functions on X, respectively, and $\rtimes$ a semidirect product. (see [58] and definitions within). Note that $\mathcal{B}$ is a separable C^*-algebra and hence $K_*(\mathcal{B})$ is a countable abelian group.

To put the abstract $K_0(\mathcal{B}_T)$ group into concrete terms, there exists a direct formula for $\mathcal{N}_{\text{gap}}$. For $1d$ substitution tilings, these spectral gaps are explicitly calculated as [27]

$$\mathcal{N}_{\text{gap}} = \frac{1}{a} \frac{k}{\lambda_*^N} \pmod 1, \quad k, N \in \mathbb{N}, \tag{3.4}$$

where $\mathcal{N}$ is the integrated density of states of some tight-binding Hamiltonian or wave equation built using aperiodic tilings, a is the normalization factor and λ_* is the leading (largest) eigenvalue of M. The calculation of a is given in Section 3.1.2.2 below. For $d = \det(M) \neq 0$, (3.4) can be rewritten as

$$\mathcal{N}_{\text{gap}} = \frac{1}{a} \frac{p + q/\lambda_*}{d^N} \pmod 1, \quad p, q \in \mathbb{N}. \tag{3.5}$$

We call such tilings "limit-quasiperiodic" [43].

For $1d$ C&P tilings with slope s, the gaps are given by

$$\mathcal{N}_{\text{gap}} = p + qs \pmod 1, \quad p, q \in \mathbb{Z}. \tag{3.6}$$

Let us present some intuition behind the GLT. The possible existence of a gap at some $\mathcal{N}$ requires an infinite number of appearances of some word w (similarly to

periodic tilings). It therefore corresponds to its density $\mathcal{N}_w = \varrho_w$. For instance, in a $1d$ tiling, A and B tiles imply gaps on $\mathcal{N}_A = \varrho_A = 1 - \varrho_B$ and $\mathcal{N}_B = \varrho_B$. For substitution tilings, one requires an updated rule $\sigma_n : \Gamma_n \to \Gamma_n$ with its occurrence matrix M_n for each n. For primitive substitutions, the leading eigenvalue λ_* is the same for all M_n, and the densities are given by the leading eigenvector $\boldsymbol{v}_{*,n}$. The eigenvectors $\boldsymbol{v}_*$ and $\boldsymbol{v}_{*,2}$ together with λ_* suffice to span all other densities [50]. Thus, the GLT is given by (3.4). In $1d$ C&P tilings, the densities of all $w_n \in \Gamma_n$ are integral linear combinations of 1 and s thus inferring (3.6).

3.1.2.2 Calculation of the Normalization Factor

Let us introduce letter doublets $L_k = l_i l_j$, where $l_i l_j$ are all *possible neighbors* in w_∞. We then rewrite w_∞ in terms of L_k denoting it w_∞^2. We denote the set of all doublets as $\Gamma_2 = \{L_k\} = \{\alpha, \beta, \gamma, \ldots\}$.

The next step is to define a substitution $\sigma_2 : \Gamma_2 \to \Gamma_2^{\mathbb{N}}$. It is done as follows for each letter $L \in \Gamma_2$ [50].

(a) Translate back to $L = l_1 l_2 \ldots l_m$ where $l_i \in \Gamma_1$;

(b) Apply $\sigma(L) = \sigma(l_1 l_2 \ldots l_m) = \ell_1 \ell_2 \ldots \ell_n$;

(c) Calculate the length $d = |\sigma(l_1)|$;

(d) Define $S = \ell_1 \ell_2 \ldots \ell_{d+1}$;

(e) Translate $S = L_1 \ldots L_d$ in terms of Γ_2.

Then, the definition of σ_2 reads

$$\sigma_2(L) = S, \quad \forall L \in \Gamma_2. \tag{3.7}$$

We then define the occurrence matrix M_2 similarly to M. The eigenvalues of M_2 contain all eigenvalues of M. Specifically, they have the same leading eigenvalue λ_*.

Next, we calculate a as follows. We take the respective leading left-eigenvectors $\boldsymbol{v}_*^L$ and $\boldsymbol{v}_{*,2}^L$ and inspect all their entries v_i. The least common multiplier of all v_i (removing factors of λ_*) is a^{-1}.

Example. In the Fibonacci substitution, $\Gamma_2 = \{\alpha = AA, \beta = AB, \gamma = BA\}$. Using the algorithm above, we obtain

$$\sigma_2^{\text{Fib}} : \begin{cases} \alpha \mapsto \beta\gamma, \\ \beta \mapsto \beta\gamma, \\ \gamma \mapsto \alpha; \end{cases} \tag{3.8}$$

with the occurrence matrix

$$M_2^{\text{Fib}} = \begin{pmatrix} 0 & 1 & 1 \\ 0 & 1 & 1 \\ 1 & 0 & 0 \end{pmatrix}. \tag{3.9}$$

Additionally, $\lambda_*^{\text{Fib}} = (\sqrt{5}+1)/2 \doteq \tau$ and $a_{\text{Fib}} = 1$.

3.1.2.3 Primitivity Condition

The primitivity of M and M_2 ensures that

(a) the leading eigenvalue λ_* is unique, real and positive;

(b) the leading eigenvectors $\boldsymbol{v}_*^L$ and $\boldsymbol{v}_{*,2}^L$ have strictly positive entries v_i [59, 60].

These v_i are interpreted as corresponding letter l_i frequencies in the infinite word w_∞ [43]. They are used as probability measures in the calculation of GLT [27]. The Perron-Frobenius theorem above also holds for a general non-strictly-upper-triangular nonnegative matrix M (see Thm. 2.20 in [59]) up to the uniqueness of λ_*.

3.1.3 Bratteli Diagrams

Let us reinspect the simplicial complexes Γ_n created by the n-letter words of the substitution σ. Note that in $1d$, these complexes are also $1d$, namely, graphs. Explicitly,

$$\Gamma_n = \{w \in w_\infty : |w| = n\}, \qquad w_\infty = \sigma^\infty(A). \tag{3.10}$$

We set for completion $\Gamma_0 = \emptyset$. Next, we define the shift-map $\gamma_n : \Gamma_n \longrightarrow \Gamma_n$ by

$$\gamma_n(w_i) = w_j \quad \text{if } w_j \text{ follows } w_i \text{ in } w_\infty. \tag{3.11}$$

The tuple $G_n = (\Gamma_n, \gamma_n)$ constitutes the Bratteli diagrams. We may view them as simplicial complexes c_k for each n .

Next, we define the *boundary* operators on the simplicial complexes c_k,

$$\begin{aligned} \partial_0(a) &= 0 \\ \partial_1(ab) &= b - a, \end{aligned} \qquad a, b \in \Gamma_n \tag{3.12}$$

with $\partial_k : C_k \longrightarrow C_{k-1}$ (here, C_k is the free abelian group on the set of k-simplices c_k), and represent them as a matrix in the basis of nodes and edges. The *coboundary* δ_* is given by [53]

$$\left(\delta^k \alpha^k\right)(c_{k+1}) = \alpha^k(\partial_{k+1} c_{k+1}), \tag{3.13}$$

for a $(k+1)$-chain c_{k+1}, and a k-cochain α^k. Setting $C^k \doteq \mathrm{Hom}(C_k, \mathbb{Z})$, the coboundary operator is defined on $\delta^k : C^k \longrightarrow C^{k+1}$. In the simplices G_n above, its matrix representation abides,

$$\delta^* = \partial_*^{\mathsf{T}}. \tag{3.14}$$

The (simplicial) cohomology groups are thus defined by

$$H_n^k \doteq H^k(\Gamma_n) = \frac{\ker \delta^k}{\mathrm{im}\, \delta^{k+1}} = \frac{\mathrm{coker}\, \partial_k}{\mathrm{coim}\, \partial_{k+1}}, \tag{3.15}$$

where their Betti numbers are given by

$$\beta_n^k \doteq \beta_k(\Gamma_n) = \dim_{\mathbb{R}}\left(H^k(\Gamma_n, \mathbb{R})\right) \tag{3.16}$$

where $H^k(X, \mathbb{R})$ is defined just like $H^k(X, \mathbb{Z})$ except we use real coefficients. The Betti numbers of the Thue-Morse substitution are shown in Figure 3.1.

Remark. If the complex X is 1-dimensional, then $H^k(\Gamma_n, \mathbb{Z}) \otimes \mathbb{R} \cong H^k(\Gamma_n, \mathbb{R})$ but this fails if X is of higher dimension.

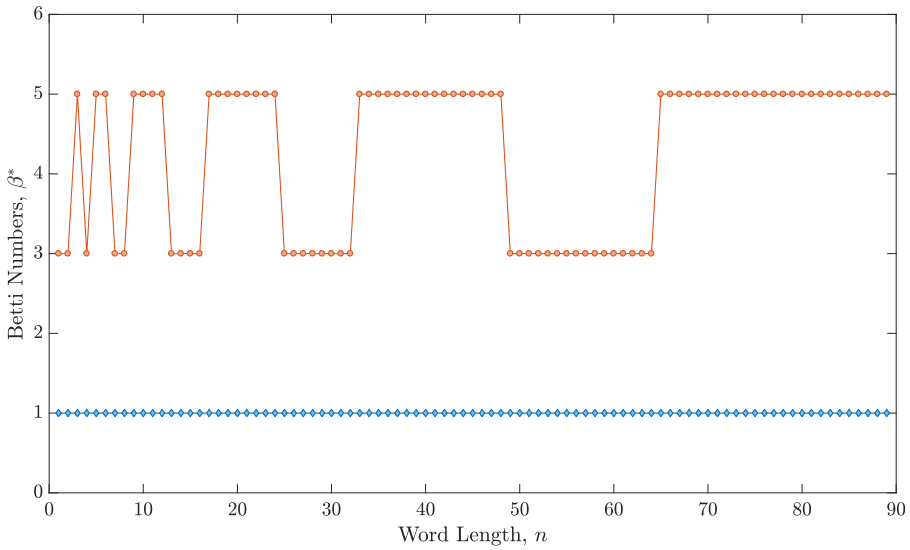

Figure 3.1: The Betti numbers β_n^* of the Thue-Morse substitution. In blue are β_n^0, and in red are β_n^1. Inspecting $\check{H}^1(\Omega_{\mathrm{TM}}) \simeq \mathbb{Z}\oplus\mathbb{Z}\left[\frac{1}{2}\right]$, the subgroup $\mathbb{Z}\left[\frac{1}{2}\right]$ may be implied from $\beta_n^1 = 5$: the length of each contiguous sequence grows as 2^k, but a proper calculation is required to confirm it.

Example. For the Fibonacci substitution,

$$\begin{aligned}\Gamma_1^{\mathrm{Fib}} &= \{A, B\}\\ \Gamma_2^{\mathrm{Fib}} &= \{AA, AB, BA\}\\ \Gamma_3^{\mathrm{Fib}} &= \{AAB, ABA, BAA, BAB\}\\ &\cdots\end{aligned} \tag{3.17}$$

so that

$G_0^{\mathrm{Fib}} =$ 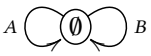

$G_1^{\mathrm{Fib}} =$ 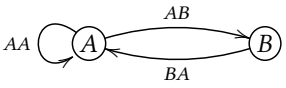

$G_2^{\mathrm{Fib}} =$ 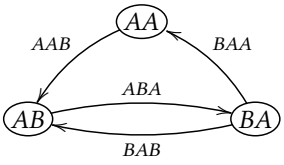

(3.18)

$\cdots$

Note that each G_n^{Fib} as 2 independent cycles, thus $\beta_n = 2$ and $H_n^1 \cong \mathbb{Z}^2$ for all n. Since H_n^0 counts the connected components, $H_n^0 \cong \mathbb{Z}$ for all n.

3.1.4 Čech Cohomology

In the above example, we used a calculation based on the boundary operators, namely, the homology groups. So long as we are dealing with finite approximations, the homol-

ogy and cohomology groups are equivalent up to the distinction that cohomologies describe *functions* acting on the Bratteli simplex. However, we do not want to constrict ourselves to the approximants Γ_n, but rather inspect the entire tiling space Ω and find its topological groups.

The problem arises when we try to take the limit to infinity, since Ω is connected but not path-connected, and path components are contractible [52]. Therefore, the standard candidates for topological groups do not work: (a) homology counts connected components so that $H_0(\Omega)$ is of infinite rank, and $H_1(\Omega) = \{0\}$; (b) homotopy is dependent on the initial location so that the limit is non-unique; (c) similarly, simplicial, singular and cellular cohomology all fail [52]. Simply put, since the tiling space is compact metric but not a finite complex that the best-behaved cohomology theory is Čech theory [61]. Therefore, we use the *Čech cohomology*.

3.1.4.1 Calculation of the Čech Cohomology

Define the Čech cohomology by [45, 52]

$$\check{H}^*(\Omega) = \varinjlim H^*(\Gamma_n), \tag{3.19}$$

where $\varinjlim$ is the direct limit [45, 52, 53].

Remark. When the acting group is omitted, the notation of the Čech cohomology reads $\check{H}^*(\Omega) \doteq \check{H}^*(\Omega, \mathbb{Z})$, since it is typically defined over the integers in tiling spaces Ω.

To calculate the Čech cohomology, we compute how the inflation map $\sigma^\star$ acts on $\check{H}^*(\Omega)$,

$$\begin{aligned} \sigma &: \Omega \to \Omega, \\ \sigma^\star &: \check{H}^*(\Omega) \leftarrow \check{H}^*(\Omega). \end{aligned} \tag{3.20}$$

Knowing the Betti numbers β_n^* is not enough, as we need to know the inflation rule.

Since Ω is connected, $\check{H}^0(\Omega) = \mathbb{Z}$, but to calculate $\check{H}^1(\Omega)$ we need to work some more. The easiest way is to inspect the collared complex G_2 [45] and calculate the action of σ on its nodes and edges, namely, $\sigma(G_2)$. It is done as follows.

(1) Apply σ_{n+1} on the edges of G_n.
   - The calculation of σ_n is a generalization of the procedure in Section (3.1.2.2) from Γ_2 to Γ_n. Explicitly, we redefine $S = \ell_1 \ell_2 \dots \ell_{d+n-1}$ in step (d).
   - A slightly different version of σ_n appears in [45, 52] based on "collared tiles" (see the definition below). For σ_3, we denote $e = |\sigma(l_2)|$ and set $S = \ell_d \ell_{d+1} \dots \ell_{d+e+1}$ in step (d).

(2) Deduce the nodes as the heads and tails of relevant edges in $\sigma(G_n)$.

(3) Compute the inflation matrices $A_0 : \Gamma_n \to \Gamma_n$ and $A_1 : \Gamma_{n+1} \to \Gamma_{n+1}$ by identifying the transformation of the nodes and edges, respectively.

Definition. A collared tiling ($\bar{T}$ in $\mathbb{R}^n$) is a renaming of the tiles in T such that each "renamed" tile contains the original tile with all its neighbors [45, 52]. In $1d$, it is equivalent to defining T by Γ_3.

To calculate $\check{H}^k$, we compute A_0 and A_1 of G_2, whose edges are the collared tiles of the tiling in $1d$. It is required to obtain the correct Čech cohomology for aperiodic tilings. Although G_0 (whose edges are the regular tiles in Γ_1) may also work in some cases,

such as quasiperiodic tilings, in general it misses some of the structure. For example, the Thue-Morse tiling has $\check{H}^1 \cong \mathbb{Z} \oplus \mathbb{Z}\left[\frac{1}{2}\right]$ for the full tiling, but only the $\mathbb{Z}\left[\frac{1}{2}\right]$ part if calculated with G_0 only [52] (cf. Section 3.1.4.2 below).

The inflation $\sigma^\star$ on $\check{H}^*(\Omega)$ is represented by A_1^T modulo the eigenvalues of A_0^T. Thus, we need to inspect the characteristic polynomials

$$\frac{q_1(x)}{q_0(x)} \doteq \frac{\det\left(Ix - A_1^\mathsf{T}\right)}{\det\left(Ix - A_0^\mathsf{T}\right)}. \tag{3.21}$$

Letting $z = x^{-1}$ and inverting the last equation, we obtain the ζ-function of [45, 62, 63],

$$\zeta(z) = \frac{\det\left(I - zA_0^\mathsf{T}\right)}{\det\left(I - zA_1^\mathsf{T}\right)} \doteq \frac{p_0(z)}{p_1(z)}. \tag{3.22}$$

with the polynomials $p_0 = 1 - z$, and p_1 reduced so that $1 - z$ remains in the numerator of (3.22).

The Čech cohomology can be deduced from $p_k(z)$ by decomposing it to its irreducible components over the integers. Namely, if

$$p_k(z) = \prod_{i=1}^{I}(1 - c_i z) \prod_{j=1}^{J}\left(1 - d_j z - e_j z^2\right), \tag{3.23}$$

with $c_i, d_j, e_j \in \mathbb{Z}$, then

$$\begin{aligned} \check{H}^k &\cong \bigoplus_{i=1}^{I} \mathbb{Z}\left[1/c_i\right] \;\oplus\; \bigoplus_{j=1}^{J} \mathbb{Z}^2\left[1/e_j\right] \\ &= \mathbb{Z}\left[c_1^{-1}\right] \oplus \cdots \oplus \mathbb{Z}\left[c_I^{-1}\right] \;\oplus\; \mathbb{Z}^2\left[e_1^{-1}\right] \oplus \cdots \oplus \mathbb{Z}\left[e_J^{-1}\right], \end{aligned} \tag{3.24}$$

with $\mathbb{Z}[1/c] = \{n/c^m \mid n, m \in \mathbb{Z}\}$ the ring $\mathbb{Z}$ with $1/c$ adjoined. Irreducible polynomials of higher orders are naturally generalized.

Example. In the Fibonacci substitution, G_2^{Fib} and $\sigma\left(G_2^{\text{Fib}}\right)$ read,

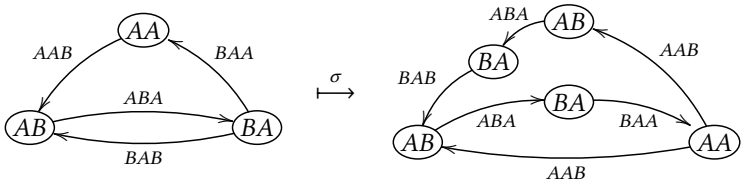

(3.25)

Comparing G_2^{Fib} with $\sigma\left(G_2^{\text{Fib}}\right)$ allows us to write the inflation matrices for edges A_1^T and nodes A_0^T [45],

$$A_1^\mathsf{T} = \begin{pmatrix} 0 & 1 & 0 & 1 \\ 0 & 1 & 1 & 0 \\ 1 & 0 & 0 & 0 \\ 1 & 0 & 0 & 0 \end{pmatrix}, \quad A_0^\mathsf{T} = \begin{pmatrix} 0 & 1 & 0 \\ 0 & 1 & 0 \\ 1 & 0 & 0 \end{pmatrix}. \tag{3.26}$$

Therefore,

$$\zeta_{\text{Fib}}(z) = \frac{1 - z}{1 - z - z^2}, \tag{3.27}$$

so that

$$\check{H}^0_{\text{Fib}} \cong \mathbb{Z} \tag{3.28a}$$

$$\check{H}^1_{\text{Fib}} \cong \mathbb{Z}^2. \tag{3.28b}$$

Example. For the Thue-Morse substitution,

$$\zeta_{\mathrm{TM}}(z) = \frac{1-z}{(1+z)(1-2z)}. \tag{3.29}$$

Therefore, $\check{H}^1(\Omega_{\mathrm{TM}}) \cong \mathbb{Z} \oplus \mathbb{Z}\left[\frac{1}{2}\right]$ and $\check{H}^0(\Omega_{\mathrm{TM}}) \cong \mathbb{Z}$. Other examples are shown in Table 3.1.

Remark. If $\deg p_1 < |\Gamma_1| = m$, it implies one of the eigenvalues of q_1 is 0 (equivalently, $c_m = 0$ in p_1). Therefore, (3.24) is no longer valid. These are periodic substitutions; we therefore set $\check{H}^1 \cong \mathbb{Z}$ in this case.

Remark. $\check{H}^0 \cong \mathbb{Z}$ for all substitutions since they are path connected.

Remark. The above procedure is for $1d$ tilings. In $2d$ tilings, the calculation of $\check{H}^0$, $\check{H}^1$ and also $\check{H}^2$ is more convoluted (due to torsion and other effects), and $\zeta(z)$ is not sufficient. The exact details appear in [45, 52].

Remark. There are other, equivalent, ways to calculate $\sigma^\star$ and $\check{H}^1$, for instance, using the Barge-Diamond complex [52, 64].

3.1.4.2 Čech Cohomology and Counting

The most straightforward usage for Čech cohomology is for counting tiles on the infinite tiling. Let us show how it is done using a simple example [52, 53].

Consider the Thue-Morse tiling $A \mapsto AB$, $B \mapsto BA$. Its Čech cohomology is given by $\mathbb{Z} \oplus \mathbb{Z}\left[\frac{1}{2}\right]$ (see [45, 52, 64]). Let us show what exactly $\mathbb{Z}$ and $\mathbb{Z}\left[\frac{1}{2}\right]$ count.

First, let us show the origin of $\mathbb{Z}\left[\frac{1}{2}\right]$. We take a supertile t_N of size 2^N. We choose a special (say, the leftmost) tile, and define a 1-cochain α_N that evaluates 1 on this tile (edge) as shown in (3.30a). Now we choose its right neighbor and define the 1-cochain β_N that evaluates 1 on this neighbor as shown in (3.30b). Observe that α_N and β_N are cohomologous, since $\alpha_N - \beta_N = \iota_N$, where ι_N is the 0-cochain that evaluates 1 on the boundary (node) between these tiles as shown in (3.30c).

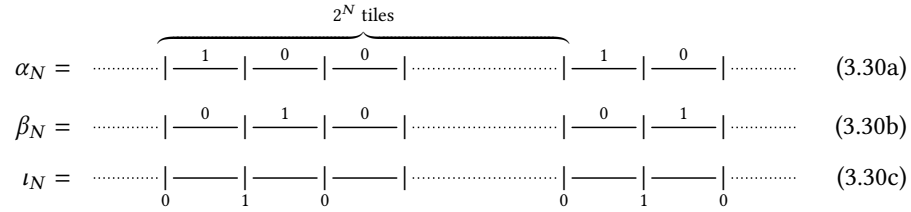

Hence, the cohomology class of α_N does not depend on the choice of the special tile. Next, we inspect $2^N\alpha_N$. It is cohomologous to the sum of all 2^N choices of the special tiles. But it evaluates 1 to the entire tiling, and thus corresponds to 1. Therefore, α_N represents $1/2^N$. Thus the class $a/2^N \in \mathbb{Z}\left[\frac{1}{2}\right]$ is generated by a 1-cochain that evaluates a each 2^N tiles and 0 everywhere else.

To see the origin of $\mathbb{Z}$, we inspect the doublets AB. Let γ be a 1-cochain that evaluates 1 on these doublets. Since the density of AB is $\varrho_{AB} = \frac{1}{3}$, then γ corresponds to $\frac{1}{3}$ on the entire tiling. However, because $\frac{1}{3}$ is not a finite linear combination of $a/2^N$, γ cannot be generated by α_N cochains. Hence, γ is the generator of $\mathbb{Z}$.

An analogous calculation can be done for Period Doubling substitution, and trivially implemented on other substitution tilings with integer λ_*. For substitution tilings with

Table 3.1: Summary of various properties of $1d$ substitution tilings.

Name	Substitution		Substitution on Doublets		Self Properties		Čech Cohomology		Zeta Function	Gap Labeling Theorem		Properties	
	Rule σ_1	Occurrence M_1	Rule σ_2	Occurrence M_2	Eigenvalue λ_1	Char. Polynomial	$\check{H}^0(\Omega,\mathbb{Z})$	$\check{H}^1(\Omega,\mathbb{Z})$	$\zeta(z)$			Pisot char.	Periodicity
Fibonacci	$\begin{smallmatrix}0\mapsto 01\\1\mapsto 0\end{smallmatrix}$	$\left(\begin{smallmatrix}1&1\\1&0\end{smallmatrix}\right)$	$\begin{smallmatrix}a\mapsto bc\\b\mapsto bc\\c\mapsto a\end{smallmatrix}$	$\left(\begin{smallmatrix}0&1&1\\0&1&1\\1&0&0\end{smallmatrix}\right)$	τ	$\lambda^2-\lambda-1=0$	$\mathbb{Z}^1$	$\mathbb{Z}^2$	$\frac{1-z}{1-z-z^2}$	$p+q\cdot\tau$	$p,q\in\mathbb{Z}$	Pisot	quasiperiodic
Cantor Set	$\begin{smallmatrix}0\mapsto 010\\1\mapsto 111\end{smallmatrix}$	$\left(\begin{smallmatrix}2&1\\0&3\end{smallmatrix}\right)$	$\begin{smallmatrix}a\mapsto aba\\b\mapsto ccb\\c\mapsto ccc\end{smallmatrix}$	$\left(\begin{smallmatrix}2&1&0\\0&1&2\\0&0&3\end{smallmatrix}\right)$	3	$\lambda^2-5\lambda+6=0$	$\mathbb{Z}^1$	$\mathbb{Z}\left[\frac{1}{2}\right]\oplus\mathbb{Z}\left[\frac{1}{3}\right]$	$\frac{1-z}{(1-2z)(1-3z)}$	$\frac{k}{3^N}$	$k,N\in\mathbb{Z}$	not primitive	limit-quasiperiodic
Non-Pisot	$\begin{smallmatrix}0\mapsto 0001\\1\mapsto 011\end{smallmatrix}$	$\left(\begin{smallmatrix}3&1\\1&2\end{smallmatrix}\right)$	$\begin{smallmatrix}a\mapsto aabc\\b\mapsto aabc\\c\mapsto bdc\\d\mapsto bdc\end{smallmatrix}$	$\left(\begin{smallmatrix}2&1&1&0\\2&1&1&0\\0&1&1&1\\0&1&1&1\end{smallmatrix}\right)$	$\tau+2$	$\lambda^2-5\lambda+5=0$	$\mathbb{Z}^1$	$\mathbb{Z}^2\left[\frac{1}{5}\right]$	$\frac{1-z}{1-5z+5z^2}$	$\frac{p+q\cdot\tau}{5^N}$	$p,q,N\in\mathbb{Z}$	non-Pisot	limit-quasiperiodic
Periodic	$\begin{smallmatrix}0\mapsto 01\\1\mapsto 01\end{smallmatrix}$	$\left(\begin{smallmatrix}1&1\\1&1\end{smallmatrix}\right)$	$\begin{smallmatrix}a\mapsto ab\\b\mapsto ab\end{smallmatrix}$	$\left(\begin{smallmatrix}1&1\end{smallmatrix}\right)$	2	$\lambda^2-2\lambda=0$	$\mathbb{Z}^1$	$\mathbb{Z}$	$\frac{1-z}{1-2z}$	$\frac{k}{2}$	$k\in\mathbb{Z}$	Pisot	periodic
Thue-Morse	$\begin{smallmatrix}0\mapsto 01\\1\mapsto 10\end{smallmatrix}$	$\left(\begin{smallmatrix}1&1\\1&1\end{smallmatrix}\right)$	$\begin{smallmatrix}a\mapsto bc\\b\mapsto bd\\c\mapsto ca\\d\mapsto cb\end{smallmatrix}$	$\left(\begin{smallmatrix}0&1&1&0\\0&1&0&1\\1&0&1&0\\0&1&1&0\end{smallmatrix}\right)$	2	$\lambda^2-2\lambda=0$	$\mathbb{Z}^1$	$\mathbb{Z}\oplus\mathbb{Z}\left[\frac{1}{2}\right]$	$\frac{1-z}{(1-2z)(1+z)}$	$\frac{k}{3\cdot 2^N}$	$k,N\in\mathbb{Z}$	Pisot	aperiodic
Period Doubling	$\begin{smallmatrix}0\mapsto 01\\1\mapsto 00\end{smallmatrix}$	$\left(\begin{smallmatrix}1&1\\2&0\end{smallmatrix}\right)$	$\begin{smallmatrix}a\mapsto bc\\b\mapsto bc\\c\mapsto aa\end{smallmatrix}$	$\left(\begin{smallmatrix}0&1&1\\0&1&1\\2&0&0\end{smallmatrix}\right)$	2	$\lambda^2-\lambda-2=0$	$\mathbb{Z}^1$	$\mathbb{Z}\oplus\mathbb{Z}\left[\frac{1}{2}\right]$	$\frac{1-z}{(1-2z)(1+z)}$	$\frac{k}{3\cdot 2^N}$	$k,N\in\mathbb{Z}$	non-Pisot	limit-quasiperiodic
Circle Sequence	$\begin{smallmatrix}0\mapsto 202\\1\mapsto 02302\\2\mapsto 01202\end{smallmatrix}$	$\left(\begin{smallmatrix}1&0&2\\2&0&3\\2&1&2\end{smallmatrix}\right)$	$\begin{smallmatrix}a\mapsto dbd\\b\mapsto dbd\\c\mapsto bcdbd\\d\mapsto acdbc\\e\mapsto acdbd\end{smallmatrix}$	$\left(\begin{smallmatrix}0&1&0&2&2&0\\0&1&0&2&2&0\\0&2&0&2&2&1\\1&1&1&1&1&1\\1&1&1&2&2&0\end{smallmatrix}\right)$	τ^3	$\lambda^3-3\lambda^2-5\lambda-1=0$	$\mathbb{Z}^1$	$\mathbb{Z}\oplus\mathbb{Z}^2$	$\frac{1-z}{(1+z)(1-4z-z^2)}$	$\frac{1}{2}(p+q\cdot\tau)$	$p,q\in\mathbb{Z}$	Pisot	quasiperiodic
Rudin-Shapiro	$\begin{smallmatrix}0\mapsto 02\\1\mapsto 32\\2\mapsto 01\\3\mapsto 31\end{smallmatrix}$	$\left(\begin{smallmatrix}1&0&1&0\\0&0&1&1\\1&1&0&0\\0&1&0&1\end{smallmatrix}\right)$	$\begin{smallmatrix}a\mapsto bf\\b\mapsto bc\\c\mapsto hc\\d\mapsto hf\\e\mapsto ag\\f\mapsto ad\\g\mapsto gd\\h\mapsto gc\end{smallmatrix}$	$\left(\begin{smallmatrix}0&1&0&0&0&1&0&0\\0&1&0&0&1&0&0&0\\0&0&0&0&1&0&0&1\\0&0&0&0&1&0&1&0\\1&0&1&0&0&0&0&0\\1&0&0&1&0&0&0&0\\0&0&0&1&0&0&1&0\\0&0&1&0&0&0&1&0\end{smallmatrix}\right)$	2	$\lambda^4-2\lambda^3-2\lambda^2+4\lambda=0$	$\mathbb{Z}^1$	$\mathbb{Z}\oplus\mathbb{Z}\left[\frac{1}{2}\right]\oplus\mathbb{Z}^2\left[\frac{1}{2}\right]$	$\frac{1-z}{(1-2z)(1-2z^2)(1+z)}$	$\frac{k}{2^N}$	$k,N\in\mathbb{Z}$	non-Pisot	aperiodic
Luck Ternary #1	$\begin{smallmatrix}0\mapsto 01\\1\mapsto 02\\2\mapsto 012\end{smallmatrix}$	$\left(\begin{smallmatrix}1&1&0\\1&0&1\\1&1&1\end{smallmatrix}\right)$	$\begin{smallmatrix}a\mapsto ac\\b\mapsto ac\\c\mapsto bc\\d\mapsto bc\\e\mapsto ade\end{smallmatrix}$	$\left(\begin{smallmatrix}1&0&1&0&0\\1&0&1&0&0\\0&1&0&0&1\\0&1&0&0&1\\1&0&0&1&1\end{smallmatrix}\right)$	2.247	$\lambda^3-2\lambda^2-\lambda+1=0$	$\mathbb{Z}^1$	$\mathbb{Z}^3$	$\frac{1-z}{1-2z-z^2+z^3}$	$p+q\cdot\lambda_1+r\cdot\lambda_1^2$	$p,q,r\in\mathbb{Z}$	Pisot	quasiperiodic
Luck Ternary #2	$\begin{smallmatrix}0\mapsto 2\\1\mapsto 0\\2\mapsto 12\end{smallmatrix}$	$\left(\begin{smallmatrix}0&0&1\\1&0&0\\0&1&1\end{smallmatrix}\right)$	$\begin{smallmatrix}a\mapsto c\\b\mapsto a\\c\mapsto be\\d\mapsto bc\\e\mapsto bd\end{smallmatrix}$	$\left(\begin{smallmatrix}0&0&1&0&0\\1&0&0&0&0\\0&1&0&0&1\\0&1&1&0&0\\0&1&0&1&0\end{smallmatrix}\right)$	1.4656	$\lambda^3-\lambda^2-1=0$	$\mathbb{Z}^1$	$\mathbb{Z}^3$	$\frac{1-z}{1-z-z^3}$	$p+q\cdot\lambda_1+r\cdot\lambda_1^2$	$p,q,r\in\mathbb{Z}$	Pisot	quasiperiodic
Periodic 1-2	$\begin{smallmatrix}0\mapsto 011\\1\mapsto 011\end{smallmatrix}$	$\left(\begin{smallmatrix}1&2\\1&2\end{smallmatrix}\right)$	$\begin{smallmatrix}a\mapsto acb\\b\mapsto acb\\c\mapsto acb\end{smallmatrix}$	$\left(\begin{smallmatrix}1&1&1\\1&1&1\\1&1&1\end{smallmatrix}\right)$	3	$\lambda^2-3\lambda=0$	$\mathbb{Z}^1$	$\mathbb{Z}$	$\frac{1-z}{1-3z}$	$\frac{k}{3}$	$k\in\mathbb{Z}$	Pisot	periodic
Periodic 1-3	$\begin{smallmatrix}0\mapsto 0111\\1\mapsto 0111\end{smallmatrix}$	$\left(\begin{smallmatrix}1&3\\1&3\end{smallmatrix}\right)$	$\begin{smallmatrix}a\mapsto accb\\b\mapsto accb\\c\mapsto accb\end{smallmatrix}$	$\left(\begin{smallmatrix}1&1&2\\1&1&2\\1&1&2\end{smallmatrix}\right)$	4	$\lambda^2-4\lambda=0$	$\mathbb{Z}^1$	$\mathbb{Z}$	$\frac{1-z}{1-4z}$	$\frac{k}{4}$	$k\in\mathbb{Z}$	Pisot	periodic
Periodic 1-4	$\begin{smallmatrix}0\mapsto 01111\\1\mapsto 01111\end{smallmatrix}$	$\left(\begin{smallmatrix}1&4\\1&4\end{smallmatrix}\right)$	$\begin{smallmatrix}a\mapsto acccb\\b\mapsto acccb\\c\mapsto acccb\end{smallmatrix}$	$\left(\begin{smallmatrix}1&1&3\\1&1&3\\1&1&3\end{smallmatrix}\right)$	5	$\lambda^2-5\lambda=0$	$\mathbb{Z}^1$	$\mathbb{Z}$	$\frac{1-z}{1-5z}$	$\frac{k}{5}$	$k\in\mathbb{Z}$	Pisot	periodic
Periodic 2-3	$\begin{smallmatrix}0\mapsto 00111\\1\mapsto 00111\end{smallmatrix}$	$\left(\begin{smallmatrix}2&3\\2&3\end{smallmatrix}\right)$	$\begin{smallmatrix}a\mapsto abddc\\b\mapsto abddc\\c\mapsto abddc\\d\mapsto abddc\end{smallmatrix}$	$\left(\begin{smallmatrix}1&1&1&2\\1&1&1&2\\1&1&1&2\\1&1&1&2\end{smallmatrix}\right)$	5	$\lambda^2-5\lambda=0$	$\mathbb{Z}^1$	$\mathbb{Z}$	$\frac{1-z}{1-5z}$	$\frac{k}{5}$	$k\in\mathbb{Z}$	Pisot	periodic
Periodic 2-5	$\begin{smallmatrix}0\mapsto 0011111\\1\mapsto 0011111\end{smallmatrix}$	$\left(\begin{smallmatrix}2&5\\2&5\end{smallmatrix}\right)$	$\begin{smallmatrix}a\mapsto abddddc\\b\mapsto abddddc\\c\mapsto abddddc\\d\mapsto abddddc\end{smallmatrix}$	$\left(\begin{smallmatrix}1&1&1&4\\1&1&1&4\\1&1&1&4\\1&1&1&4\end{smallmatrix}\right)$	7	$\lambda^2-7\lambda=0$	$\mathbb{Z}^1$	$\mathbb{Z}$	$\frac{1-z}{1-7z}$	$\frac{k}{7}$	$k\in\mathbb{Z}$	Pisot	periodic
Golden Mean	$\begin{smallmatrix}0\mapsto 10\\1\mapsto 0\end{smallmatrix}$	$\left(\begin{smallmatrix}1&1\\1&0\end{smallmatrix}\right)$	$\begin{smallmatrix}a\mapsto cb\\b\mapsto ca\\c\mapsto b\end{smallmatrix}$	$\left(\begin{smallmatrix}0&1&1\\1&0&1\\0&1&0\end{smallmatrix}\right)$	τ	$\lambda^2-\lambda-1=0$	$\mathbb{Z}^1$	$\mathbb{Z}^2$	$\frac{1-z}{1-z-z^2}$	$p+q\cdot\lambda_1$	$p,q\in\mathbb{Z}$	Pisot	quasiperiodic
Silver Mean	$\begin{smallmatrix}0\mapsto 100\\1\mapsto 0\end{smallmatrix}$	$\left(\begin{smallmatrix}2&1\\1&0\end{smallmatrix}\right)$	$\begin{smallmatrix}a\mapsto cab\\b\mapsto caa\\c\mapsto b\end{smallmatrix}$	$\left(\begin{smallmatrix}1&1&1\\2&0&1\\0&1&0\end{smallmatrix}\right)$	$\sqrt{2}+1$	$\lambda^2-2\lambda-1=0$	$\mathbb{Z}^1$	$\mathbb{Z}^2$	$\frac{1-z}{1-2z-z^2}$	$p+q\cdot\lambda_1$	$p,q\in\mathbb{Z}$	Pisot	quasiperiodic
Copper Mean	$\begin{smallmatrix}0\mapsto 1000\\1\mapsto 0\end{smallmatrix}$	$\left(\begin{smallmatrix}3&1\\1&0\end{smallmatrix}\right)$	$\begin{smallmatrix}a\mapsto caab\\b\mapsto caaa\\c\mapsto b\end{smallmatrix}$	$\left(\begin{smallmatrix}2&1&1\\3&0&1\\0&1&0\end{smallmatrix}\right)$	$\frac{\sqrt{13}}{2}+\frac{3}{2}$	$\lambda^2-3\lambda-1=0$	$\mathbb{Z}^1$	$\mathbb{Z}^2$	$\frac{1-z}{1-3z-z^2}$	$p+q\cdot\lambda_1$	$p,q\in\mathbb{Z}$	Pisot	quasiperiodic
Marginal	$\begin{smallmatrix}0\mapsto 001\\1\mapsto 011\end{smallmatrix}$	$\left(\begin{smallmatrix}2&1\\1&2\end{smallmatrix}\right)$	$\begin{smallmatrix}a\mapsto abc\\b\mapsto abc\\c\mapsto bdc\\d\mapsto bdc\end{smallmatrix}$	$\left(\begin{smallmatrix}1&1&1&0\\1&1&1&0\\0&1&1&1\\0&1&1&1\end{smallmatrix}\right)$	3	$\lambda^2-4\lambda+3=0$	$\mathbb{Z}^1$	$\mathbb{Z}\oplus\mathbb{Z}\left[\frac{1}{3}\right]$	$\frac{1-z}{(1-z)(1-3z)}$	$\frac{k}{2\cdot 3^N}$	$k,N\in\mathbb{Z}$	non-Pisot	limit-quasiperiodic
Binary non-Pisot	$\begin{smallmatrix}0\mapsto 01\\1\mapsto 000\end{smallmatrix}$	$\left(\begin{smallmatrix}1&1\\3&0\end{smallmatrix}\right)$	$\begin{smallmatrix}a\mapsto bc\\b\mapsto bc\\c\mapsto aaa\end{smallmatrix}$	$\left(\begin{smallmatrix}0&1&1\\0&1&1\\3&0&0\end{smallmatrix}\right)$	$\frac{\sqrt{13}}{2}+\frac{1}{2}$	$\lambda^2-\lambda-3=0$	$\mathbb{Z}^1$	$\mathbb{Z}^2\left[\frac{1}{3}\right]$	$\frac{1-z}{1-z-3z^2}$	$\frac{p+q\cdot\lambda_1}{3^N}$	$p,q,N\in\mathbb{Z}$	non-Pisot	limit-quasiperiodic
Ternary non-Pisot	$\begin{smallmatrix}0\mapsto 2\\1\mapsto 0\\2\mapsto 101\end{smallmatrix}$	$\left(\begin{smallmatrix}0&0&1\\1&0&0\\1&2&0\end{smallmatrix}\right)$	$\begin{smallmatrix}a\mapsto e\\b\mapsto f\\c\mapsto b\\d\mapsto a\\e\mapsto cad\\f\mapsto cac\end{smallmatrix}$	$\left(\begin{smallmatrix}0&0&0&0&1&0\\0&0&0&0&0&1\\0&1&0&0&0&0\\1&0&0&0&0&0\\1&0&1&1&0&0\\1&0&2&0&0&0\end{smallmatrix}\right)$	1.5214	$\lambda^3-\lambda-2=0$	$\mathbb{Z}^1$	$\mathbb{Z}^3\left[\frac{1}{2}\right]$	$\frac{1-z}{1-z^2-2z^3}$	$\frac{p+q\cdot\lambda_1+r\cdot\lambda_1^2}{2^N}$	$p,q,r,N\in\mathbb{Z}$	non-Pisot	limit-quasiperiodic

non-integer λ_* or C&P tilings with irrational slope, we must be more careful counting using the F_N and d_N numbers, respectively.

In tilings of higher dimensions, the interpretation of Čech cohomology is more convoluted. We summarize it succinctly below for dimensions $d \geq 1$.

- In dimension 0, the Čech cohomology counts connected components. Therefore, $\check{H}^0 \cong \mathbb{Z}$ for all tilings.
- In dimension 1, the Čech cohomology represents the tiling combinatorics. For example, $\check{H}^1_{\text{Penrose}} \cong \mathbb{Z}^5$ [45] alluding to its 5-fold rotational symmetry, or to total dimension $\dim\left(E_\parallel \oplus E_\perp\right)$ in the C&P case.
- In dimension d, the invariant transverse measure (or the Ruelle-Sullivan current) gives a real-valued functional on $\check{H}^d$ [58]. This pairing of the current with the cohomology is important in index theory.
- The role of the Čech cohomology is unclear for dimensions $1 < d' < d$.

Note that in $1d$, the Čech cohomology expresses both the combinatorics and the positive measure making the connection with the GLT natural.

3.1.5 Complexity and Cohomology

We define the *complexity* by the number of *nodes* in each complex [65],

$$c_n \doteq |\Gamma_n| \,. \tag{3.31}$$

Now, we inspect the projection maps $\pi_n : \Gamma_{n+1} \longrightarrow \Gamma_n$ between the complexes,

$$\Gamma_0 \xleftarrow{\pi_0} \Gamma_1 \xleftarrow{\pi_1} \Gamma_2 \xleftarrow{\pi_2} \Gamma_3 \xleftarrow{\pi_3} \dots \tag{3.32}$$

which act by omitting the last letter in Γ_{n+1}.

Fact. *There is a well-defined inverse limit [52],*

$$\Omega_T = \varprojlim \Gamma_n. \tag{3.33}$$

Consider the inverse maps π_n^{-1}, which give the options for the last adjacent letter to create Γ_{n+1} from Γ_n. In other words, π_n^{-1} corresponds to the *edges* in the Bratteli diagram; thus

$$\pi_n^{-1} = \gamma_n. \tag{3.34}$$

Hence, we define the complexity tree T_n by the sequence

$$T_n = \Gamma_0 \xrightarrow{\gamma_0} \Gamma_1 \xrightarrow{\gamma_1} \Gamma_2 \xrightarrow{\gamma_2} \dots \xrightarrow{\gamma_{n-1}} \Gamma_n. \tag{3.35}$$

This is seen in Figure 3.2. The tree T_n is also called a *dictionary* [50].

Consider the *splits* at each level Γ_n as shown in Figure 3.2. Here, y_n is the number of nodes in level n that have > 1 *outgoing* edges, and s_n is the total number of splits. Note that for binary substitutions, $y_n = s_n$.

Now, since β_n^1 counts the number of cocycles in Γ_n and the Bratteli graphs are connected ($\beta_n^0 = 1$ for all n), each split contributes an additional cocycle. Thus

$$\beta_n^1 = s_n + 1. \tag{3.36}$$

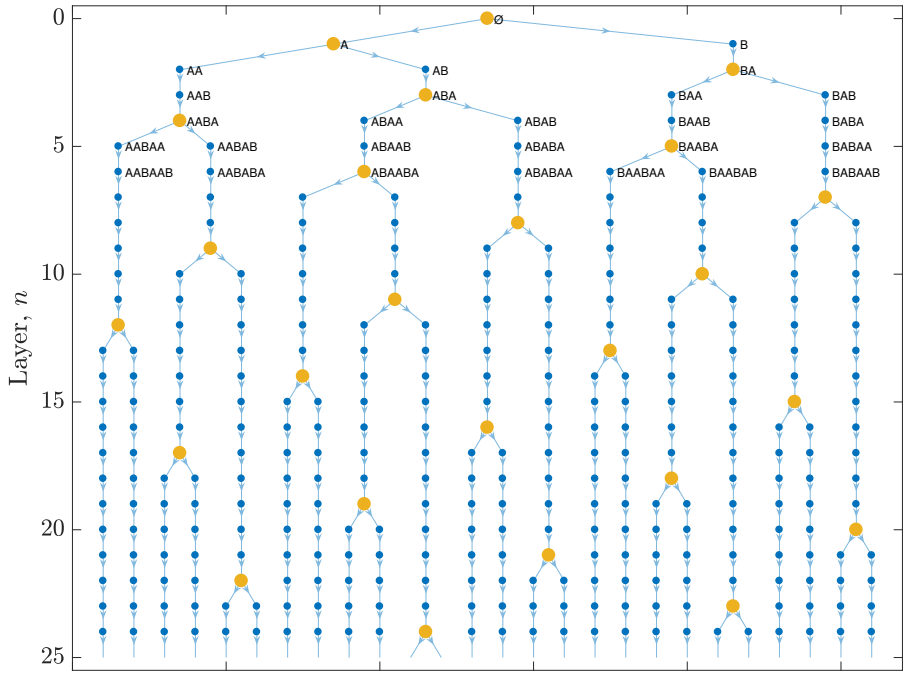

Figure 3.2: Complexity graph for the Fibonacci substitution. The arrows represent the mapping γ_n. In blue, the n-nodes (n-letter words) for each level (row) n, and in yellow – the n-nodes that split by γ_n into two $(n+1)$-nodes. The total sum of splits at each row n gives s_n. The first few nodes are labeled.

Next, we inspect the complexity $p(n) \doteq c_n$, the total number of letters at level n. At each level n, s_{n-1} letters are added to the letters of level $(n-1)$; thus

$$c_n = s_{n-1} + c_{n-1}, \qquad c_0 = 1. \tag{3.37}$$

Therefore,

$$c_n = 1 + \sum_{i=0}^{n-1} s_i. \tag{3.38}$$

Corollary. *For C&P (Sturmian) sequences, where $\beta_n^1 = 2$ (equally, $s_n = 1$) for all n, one has $c_n = n + 1$. For the connection with $\check{H}^1$, see Proposition 3.2.*

Corollary. *For primitive substitution tilings, the cohomology is bound, $\beta_n^1 \leq C + 1$; thus $c_n \leq Cn + 1 = O(n)$ [49, 65].*

Remark. For periodic tilings, $\beta_{n>N}^1 = 1$ (equally, $s_{n>N} = 0$) for some $N \in \mathbb{Z}$; thus, the complexity is constant, $c_{n>N} = C$.

Proposition. *The group $\check{H}^1(\Omega)$ has typically more information than $K_0(\mathcal{B})$, since one considers only the* frequency *of tiles in $K_0(\mathcal{B})$ [45], whereas $\check{H}^1(\Omega)$ must also include their* order *[52].*

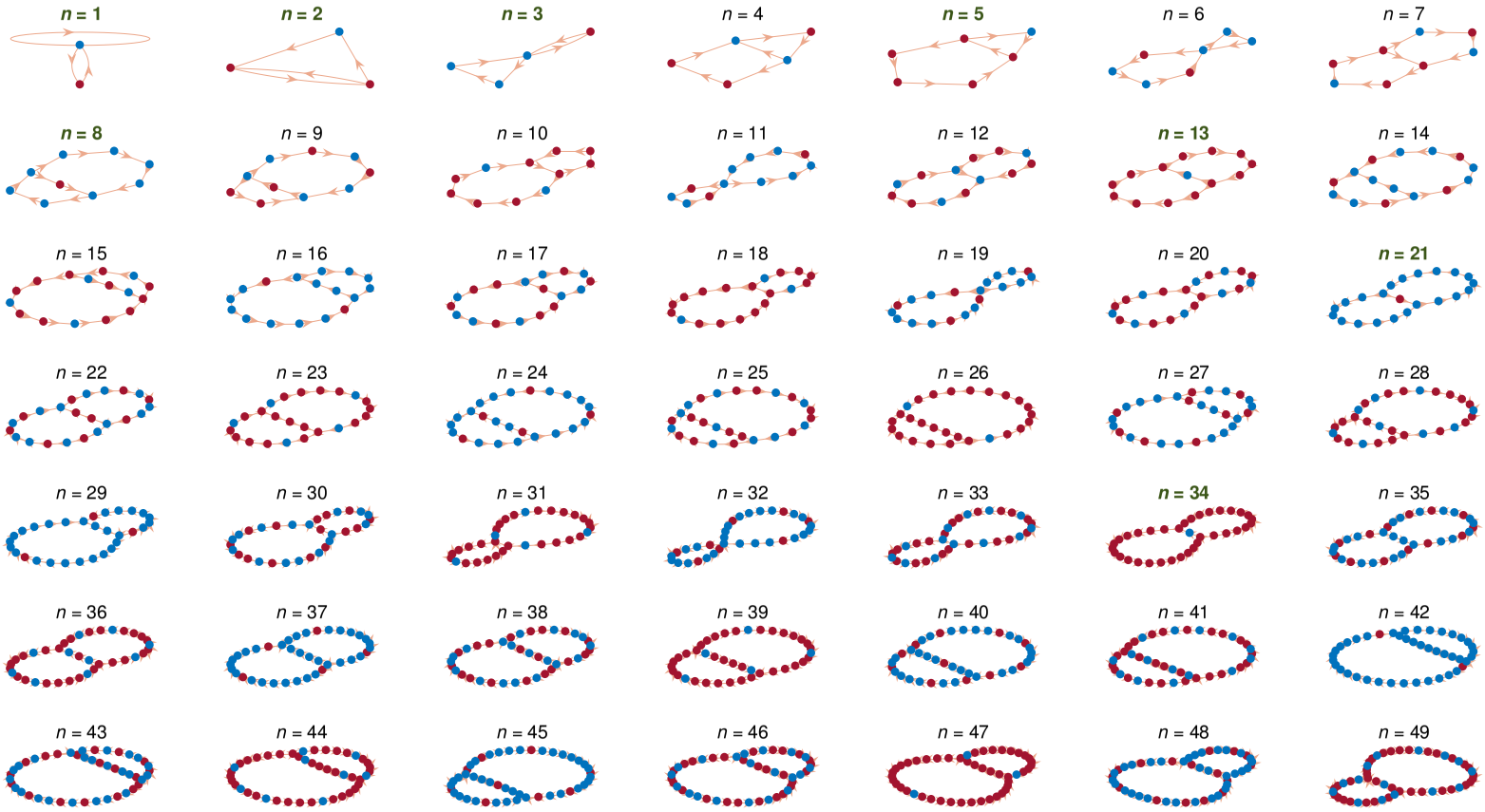

Figure 3.3: Bratteli graphs for the Fibonacci substitution for $n = 1 \ldots 49$. Green titles indicate $n = d_N$ of generalized d_N. Blue and red nodes indicate different families so that $L_B^I = \lfloor n \cdot s \rfloor$ for the blue nodes and $L_B^{II} = \lceil n \cdot s \rceil$ for the red ones (here, $s = \tau^{-2}$). Yellow arrows indicate the edges.

3.1.6 Lateral Bratteli Diagrams

Inspecting the tree in Figure 3.2, we find Bratteli diagrams G_n at each level n of the tree. An example for the Fibonacci sequence is given in Figure 3.3.

For C&P $2d \to 1d$ substitutions with slope s, we have the following observations.

1. There are always 2 cycles.
   - This is consistent with $\beta_n = 2$ and $s_n = 1$ for all n.
   - The cycles are always of the length of generalized d_N (recall (2.42)).
2. The nodes are divided into 2 families, dependent on L_B, the number of B-s in them (recall (2.70)). They are given by:
$$L_B^{I} = \lfloor n \cdot s \rfloor , \qquad L_B^{II} = \lceil n \cdot s \rceil . \tag{3.39}$$
   - The nodes in each family I or II are *cyclic permutations* of each other.
3. For each (generalized) $n = d_N$, the long cycle consists of a *single family* (see Figure 3.3).
   - Therefore, this family constitutes Σ_1 of size $d_N \times d_N$.
   - Since $c_n = n + 1$, there is only a *single node* of the other family (henceforth, the "*rogue sequence*").
   - For very small d_N-s, it might be the short cycle; it is inconsequential for the rest of the analysis.

The observations above can explain the diffraction spectrum and spectral properties of C&P sequences, as demonstrated in Section 4.1.1.

3.2 Dual Tilings

A natural question arises dealing with an aperiodic tilings: what is its dual tiling, and how to define it properly. In periodic tilings (lattices), the dual lattice is given by the Voronoï tessellation, implying some connection to the Fourier space. In aperiodic tilings, the same approach leads to some unexpected results.

3.2.1 Definitions

Let T be some tiling in $\mathbb{R}^n$ and V be its collection of vertices v_k located on the boundaries (another definition is on the "center of mass" of a tile). The dual lattice is given by the Voronoï tessellation,
$$T^* \doteq \bigcup_k t^* (v_k) , \tag{3.40}$$
where
$$t^* (v_k) = \{ \boldsymbol{x} \in \mathbb{R}^n \mid d(\boldsymbol{x}, v_k) \leq d(\boldsymbol{x}, v_l) \quad \forall l \neq k \} , \tag{3.41}$$
with $d(\boldsymbol{x}, \boldsymbol{y})$ some metric in $\mathbb{R}^n$. We typically take $d(\boldsymbol{x}, \boldsymbol{y}) = \|\boldsymbol{x} - \boldsymbol{y}\|$ unless stated otherwise. This is consistent with the usual dual lattice definitions [1] – taking the closest points to v_k. We can define the dual of a dual by
$$T^{**} \doteq (T^*)^* . \tag{3.42}$$
Note that for periodic lattices,
$$T^{**}_{\text{per}} = T_{\text{per}} . \tag{3.43}$$

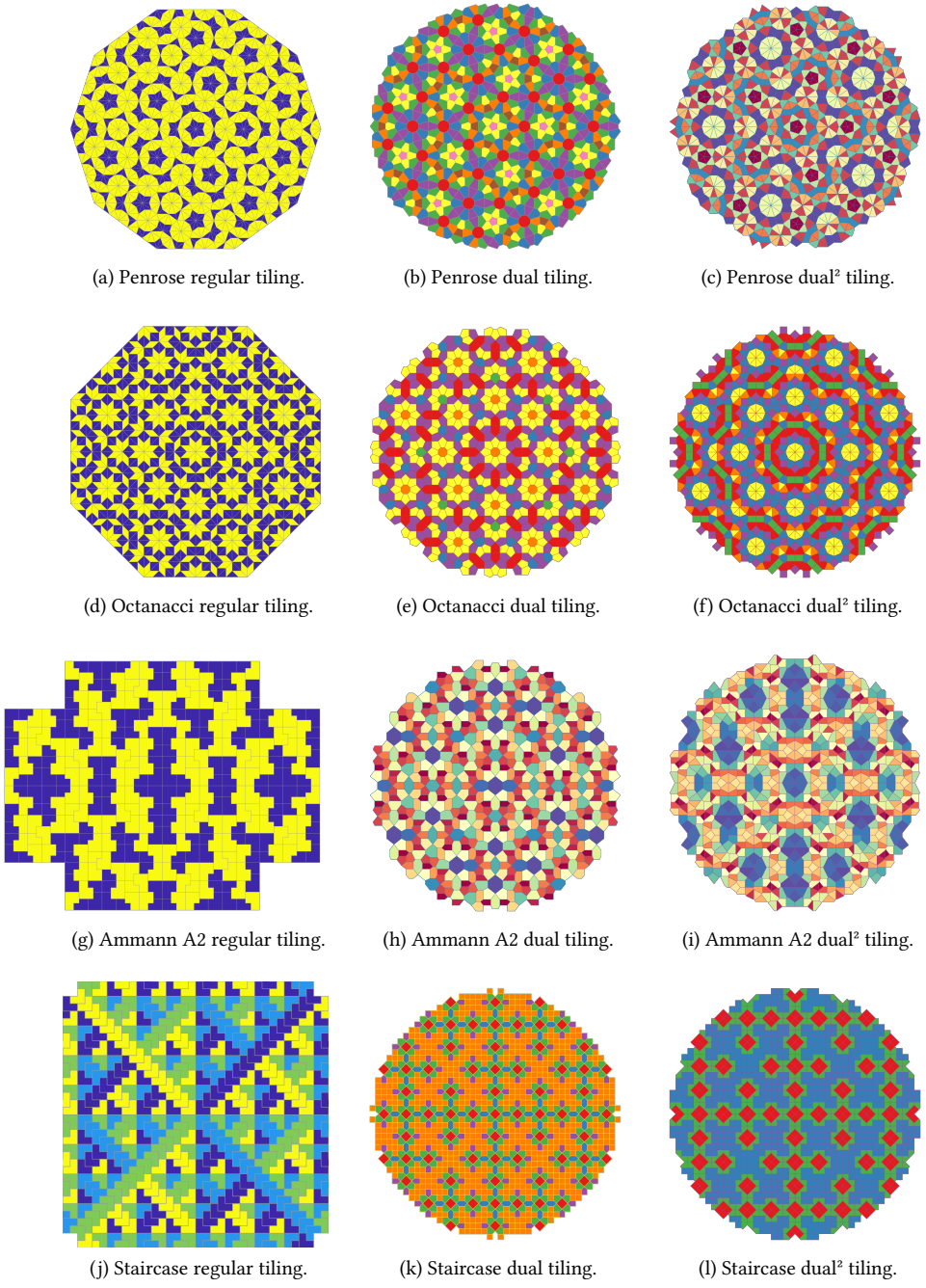

(a) Penrose regular tiling. (b) Penrose dual tiling. (c) Penrose dual² tiling.

(d) Octanacci regular tiling. (e) Octanacci dual tiling. (f) Octanacci dual² tiling.

(g) Ammann A2 regular tiling. (h) Ammann A2 dual tiling. (i) Ammann A2 dual² tiling.

(j) Staircase regular tiling. (k) Staircase dual tiling. (l) Staircase dual² tiling.

Figure 3.4: Comparison between regular, dual and double-dual $2d$ tilings. Different colors represent different tiles up to rotations and reflections. (a–c) Penrose regular, dual and dual² tilings for order $N = 5$; (d–f) Octanacci regular, dual and dual² tilings for order $N = 2$; (g–i) Ammann A2 regular, dual and dual² tilings for order $N = 5$; (j–l) Staircase regular, dual and dual² tilings for order $N = 4$.

3.2.2 One-dimensional Aperiodic Tilings

Let us consider a tiling T with tiles in $\Gamma_1 = \{A, B\}$ such that each tile has a length $l_{A/B}$ and a density $\rho_{A/B}$ (cf. Section 2.5, for instance). It is easy to see that for a vertex lying on the boundary between A and B, its dual tile t^*_{AB} has length $(l_A + l_B)/2$. Hence,

$$l\left(t^*_k\right) = \begin{cases} l_A & k = AA, \\ (l_A + l_B)/2 & k = AB, \\ (l_A + l_B)/2 & k = BA, \\ l_B & k = BB. \end{cases} \tag{3.44}$$

Notice that t^*_k has all its elements coming from Γ_2, with AB and BA indistinguishable using their length.

Corollary. *In 1d, the dual tiling T^* on Γ_1 can be deduced from the regular tiling T on Γ_2.*

Continuing further, we suppose one has a vertex between t^*_{AA} and t^*_{AB}, then its dual tile t^{**}_{AAB} has length $(l_{AA} + l_{AB})/2 = (3l_A + l_B)/4$. Thus,

$$l\left(t^{**}_k\right) = \begin{cases} l_A & k = AAA, \\ (3l_A + l_B)/4 & k = AAB, BAA, \\ (l_A + l_B)/2 & k = ABA, BAB \\ (l_A + 3l_B)/4 & k = ABB, BBA, \\ l_B & k = BBB. \end{cases} \tag{3.45}$$

We see a similar behavior as in the previous case.

Proposition. *In 1d, the dual tiling T^{*n} on Γ_1 can be deduced from the regular tiling T on Γ_{n+1}. Additionally, the dual tiling T^* on Γ_n can be deduced from the tiling T on Γ_{n+1}.*

Claim. The substitution $\sigma^*_1 : T^*(\Gamma_1) \longrightarrow T^*(\Gamma_1)$ is identified by $\sigma_2 : T(\Gamma_2) \longrightarrow T(\Gamma_2)$.

Note that, in general, $T^{**} \ncong T$, since T^{**} corresponds to the *collared tiling* (see [45, 52] and Section 3.1.4.1) and contains information about the neighbors. In periodic lattices, there exist m_0 such that $\Gamma^{\text{per}}_{m_0} \cong \Gamma^{\text{per}}_{m_0+1}$. Therefore, $T^{**}_{\text{per}} \cong T_{\text{per}}$ as expected (using, without loss of generality, $m_0 = 1$). In aperiodic tilings, such m_0 does not exist, and collaring plays an essential role.

Corollary 3.1. *The dual T^*_{per} is periodic itself; the dual T^*_{aper} is aperiodic. Additionally, $T^{**}_{\text{per}} \cong T_{\text{per}}$ whereas $T^{**}_{\text{aper}} \ncong T_{\text{aper}}$.*

3.2.3 Two-dimensional Aperiodic Tilings

Using the Voronoï tessellation definitions above, we arrive to the same conclusions (namely, Corollary 3.1). However, the details get messier, and we do not reiterate them, for simplicity. As before, the substitution rule σ^*_1 for the dual tiling is given by σ_2 with the proper identification.

The regular, dual and double-dual tilings are shown in Figure 3.4 for Penrose [15, 45], Octanacci [15], Ammann A2 [66] and Staircase [45, 52] tilings. For Penrose and Octanacci tilings, the substitution version was used. The double-dual tilings reminisce the regular ones with the following differences. First, as discussed above, the sizes do not necessarily match after double dual. Thus there are more tiles to consider. Second, the vertices do not respect the tile shape, and thus the tiles alter after double Voronoï.

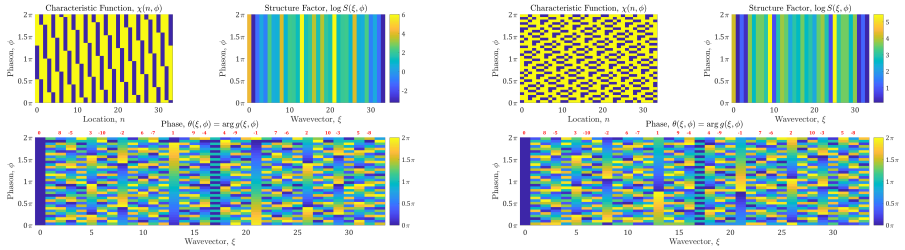

(a) χ, S and Θ for σ_5 with $F_N = 34$.

(b) χ, S and Θ for σ_3 with $F_N = 34$.

Figure 3.5: Structure factor S and structural phase Θ for the squared Fibonacci substitutions.

3.3 Topological Considerations

In the sections above, we have shown some topological features both in the structural and spectral spaces. In the following, we show comparison between both, and present universal topological parameters to consider.

3.3.1 Structural Features

As always, let us start with the structural features. We inspect quasiperiodic substitutions. These include the Metallic substitutions (Fibonacci=golden, silver, bronze) and their powers (Fibonacci^2, Fibonacci^3, and so on). One can naturally ask, whether all the quasiperiodic substitutions obtained that way are (isomorphic to) C&P. The answer is negative, as we shall shortly see below.

3.3.1.1 Non-C&P Substitutions

Let us inspect the following two substitutions (see [43, Eq. (4.2)] or [67, Sec. 5.4]),

$$\sigma_5 : \begin{array}{l} A \mapsto ABA \\ B \mapsto AB \end{array}, \qquad \sigma_3 : \begin{array}{l} A \mapsto AAB \\ B \mapsto BA \end{array}. \tag{3.46}$$

Both have the same occurrence matrix of the squared Fibonacci substitution

$$M_1^{\sigma_5} = M_1^{\sigma_3} = \left(\begin{smallmatrix} 2 & 1 \\ 1 & 1 \end{smallmatrix}\right), \tag{3.47}$$

with $\lambda_1 = \tau^2$, $\lambda_2 = \tau^{-2}$. We consider the normalized extension of the fluctuations u_k (recall (2.66)), namely

$$\Delta\theta = \sup_k u_k - \inf_k u_k. \tag{3.48}$$

In [43], the authors showed that for C&P sequences $\Delta\theta = 1$, whereas for all others $\Delta\theta > 1$. They have also showed that σ_5 is C&P, whereas $\Delta\theta\,(\sigma_3) = \tau > 1$.

Let us show it in a different way. Consider the sequence $s_0\,(n) = \sigma_i^N\,(B)$, build from it the matrix $\Sigma_1\,(n,\ell) = \mathcal{T}^{m(\ell,1)}\,[s_0\,(n)]$, and calculate the structure factor $S\,(\xi) = |\varsigma\,(\xi)|^2$ and the phase $\Theta\,(\xi,\ell) = \arg\omega^{m(\ell)\xi}$ (see Section 2.2.1). The structure factor $S\,(\xi)$ is dependent only on the initial sequence s_0 (see Figure 3.5).

The phase factor, however, is dependent only on the translation operators $\mathcal{T}^{m(\ell)}$. These, in turn, are dependent only on (F_{N-1}, F_N). Yet, the F_N numbers come from the substitution M, which is the same for σ_5 and σ_3. Thus, the windings are the same, as shown in Figure 3.5. They act as topological invariants for these substitutions.

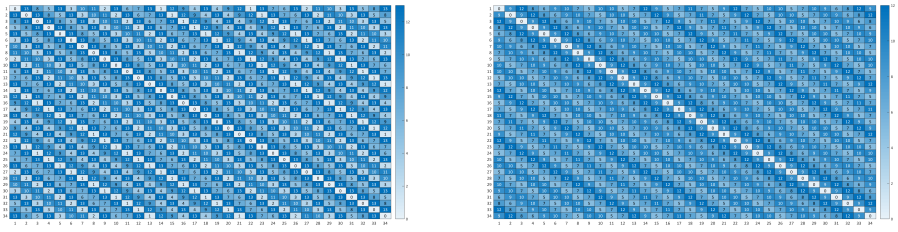

(a) Mismatching Pairs for σ_5 with $F_N = 34$.

(b) Mismatching Pairs for σ_3 with $F_N = 34$.

Figure 3.6: Mismatching pairs $P(i, j)$ for the squared Fibonacci substitutions.

3.3.1.2 Mismatching Pairs

The characteristic function $\chi(n, \phi)$ of Figure 3.5 is actually $\Sigma_1(n, \ell)$. We build this matrix initially such that in each row only a single pair changes

$$\ldots xxx\, AB\, xxx \ldots \longrightarrow \ldots xxx\, BA\, xxx \ldots \tag{3.49}$$

The Σ_1 matrix of σ_5 indeed acts that way. On the other hand, σ_3 behaves differently.

The main question now, is whether our order of Σ_1 is the best for σ_3, or there is another—better—order. Let us calculate how many pairs are changed from the row i to the row j. We inspect Σ_0 and assign $+1 \leftrightarrow A$ and $-1 \leftrightarrow B$. Compute the convolution:

$$C(i, j) = \Sigma_0(i, m) \cdot (\Sigma_0(j, m))^{\mathsf{T}}. \tag{3.50}$$

This gives us the distance from row i to the row j. For instance, on the main diagonal one gets the same row multiplied by itself; thus $C(i, i) = s_0 \cdot s_0^{\mathsf{T}} = F_N$, and it is the largest number.

Next, identify that if a pair changes, the value of C changes by 4. Explicitly,

$$\begin{pmatrix} 1 & -1 \end{pmatrix} \begin{pmatrix} 1 \\ -1 \end{pmatrix} = 2, \quad \begin{pmatrix} 1 & -1 \end{pmatrix} \begin{pmatrix} -1 \\ 1 \end{pmatrix} = -2. \tag{3.51}$$

Thus, the number of matching pairs is $C(i, j)/4$, and the number of *mismatching pairs* is given by

$$P(i, j) = \tfrac{1}{4}(F_N - C(i, j)). \tag{3.52}$$

Let us inspect $P(i, j)$ for σ_5 and σ_3 as in Figure 3.6. For σ_5, $P(i, j)$ shows that for each row there are only *two* other rows with distance 1 from it, as expected from a C&P sequence. Moreover, one can build the sequence of rows similarly to C&P as follows. (i) Take a row i and choose a difference-1 point j, where $P(i, j) = 1$; (ii) go to the row j, and choose the $k \neq i$ such that $P(j, k) = 1$; (iii) continue to build the sequence $i \to j \to k \to \cdots \to i$. Since there are only 2 j-s with $P(i, j) = 1\ \forall i$, this sequence is unique.

On the other hand, for σ_3, $P(i, j)$ shows that the minimal number of changes needed is 5. Moreover, it appears *six* times on the same row. Thus, it cannot be a C&P sequence.

Corollary. *Iff Σ_1 shows an "adiabatic" change depicted by 1-diagonals in the P-matrix, then a phason can be defined and the sequence corresponds to C&P.*

Proposition. *The P-matrix can distinguish C&P from non-C&P tilings* without prior knowledge *of the tiling itself, but only of its F_N-numbers. Therefore, one can make a physical experiment to characterize a tiling.*

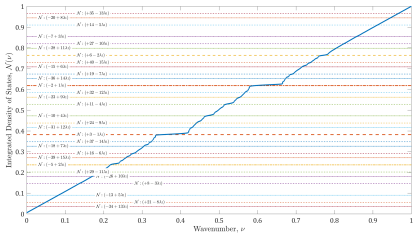

(a) IDOS for σ_5 with $F_N = 89$.

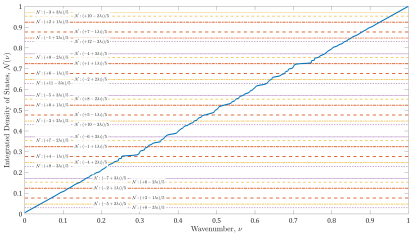

(b) IDOS for σ_3 with $F_N = 89$.

Figure 3.7: Integrated density of states for the squared Fibonacci substitutions using scattering matrix with $(n_A, n_B) = (1, 1.62)$ and $(l_A, l_B) = (1.62, 1)$. The wavenumber ν represents the energy axis.

3.3.2 Spectral Features

The next step is to investigate the spectral features of substitution sequences, namely, the eigenvalues of a Hamiltonian with an aperiodic potential. As before, our working horses will be σ_5 and σ_3. We shall show where the spectral features coincide with the structural, and where they significantly differ.

3.3.2.1 Introducing the Phason

We introduce the aperiodicity to the system. Consider the sequence $s_0(n)$ consisting of letters $\{A, B\}$. Construct the system by putting alternating dielectric slabs of refractive index $n_{A/B}$ and width $d_{A/B}$ in the order set by $s_0(n)$. We extract the topological behavior by comparing different sequences $s(n)$.

Take the substitutions σ_5 and σ_3 as in (3.46). Their traces of the gap-labeling groups are given by [27, 28]

$$\tau_*\left(K_0\left(\mathcal{B}_{\sigma_5}\right)\right) \cong \left(\mathbb{Z} + \tau^2\mathbb{Z}\right) \cap [0,1)\,, \qquad \tau_*\left(K_0\left(\mathcal{B}_{\sigma_3}\right)\right) \cong \frac{1}{5}\left(\mathbb{Z} + \tau^2\mathbb{Z}\right) \cap [0,1)\,, \tag{3.53}$$

so that the gaps lie on

$$\mathcal{N}_{\text{gap}}^{\sigma_5} = \left(p + \tau^2 q\right) \cap [0,1)\,, \qquad \mathcal{N}_{\text{gap}}^{\sigma_3} = \frac{p + \tau^2 q}{5} \cap [0,1)\,. \tag{3.54}$$

The results are clearly visible in Figure 3.7.

Consider now the sequences $s_\ell(n) \doteq \Sigma_1(n, \ell)$. The index ℓ infers the phason $\phi_\ell = 2\pi\ell/F_N$. Since both σ_5 and σ_3 have the same M_1 matrix (3.47), they have the same F_N numbers, so that Σ_1 is constructed by the same rule. This is a naïve approach, since σ_3 is not C&P—as seen in Figures 3.5 and (3.6)—yet it exhibits some interesting features.

Next, we build the ϕ-dependent scattering matrix $\mathcal{S}(k, \phi)$ (see Section 3.4.2 for the scattering matrix review). Extracting the phason information from $\mathcal{S}(k, \phi)$ requires some juggling. Since the total phase shift $\delta(k)$ is ϕ-independent, we need to inspect the chiral phase [68, 69],

$$\alpha(k, \phi) = \vec{\theta}(k, \phi) - \overleftarrow{\theta}(k, \phi)\,. \tag{3.55}$$

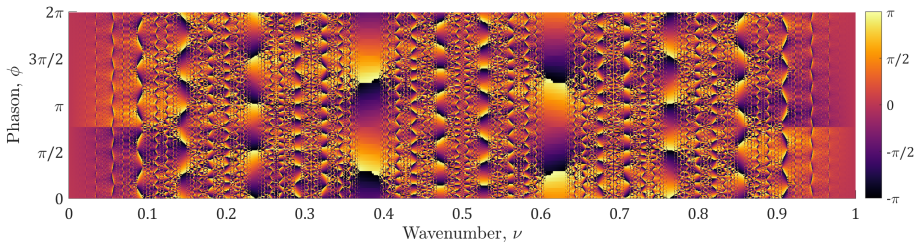

Figure 3.8: Chiral phase for the Fibonacci substitution with $d_N = 233$ using scattering matrix with $(n_A, n_B) = (1, 1.15)$ and $(l_A, l_B) = (1.15, 1)$. The wavenumber ν represents the energy axis.

Table 3.2: Number of edge-state windings $W_{p,q}$ in σ_3 for the gaps $\mathcal{N}^{\sigma_3}_{4,-1}$ and $\mathcal{N}^{\sigma_3}_{-10,5}$.

N	3	4	5	6
F_N	13	34	89	233
$W_{4,-1}$	1	-4	9	-25
$W_{-10,5}$	2	2	2	2

This phase winds exactly $2q$ times as seen in Figure 3.8,

$$W_{\alpha_g} = \frac{1}{2\pi}\int_0^{2\pi} \frac{\partial\alpha\left(k = k_{p,q}, \phi\right)}{\partial\phi}\,\mathrm{d}\phi = 2q, \tag{3.56}$$

where $k_{p,q}$ is the wavevector corresponding to the gap $\mathcal{N}_{p,q}$. Unfortunately, $\alpha\left(k, \phi\right)$ is hard to measure. One resorts to the following trick.

Take a sequence $s\left(n\right)$ and concatenate it to a flipped sequence $s\left(-n\right)$ thus creating $\overleftrightarrow{s} = \left[s\left(n\right) s\left(-n\right)\right]$. This generalized mirror procedure creates an edge-state inside the gaps so that

$$\overleftrightarrow{\varrho}(k, \phi) = \varrho\left(k\right) + \varrho_{\mathrm{es}}\left(k, \phi\right). \tag{3.57}$$

Here, $\varrho\left(k\right)$ is the density of states of a single sequence $s\left(n\right)$, and $\varrho_{\mathrm{es}}\left(k, \phi\right)$ are the additional edge-states inside the gaps implicitly given by

$$\varrho_{\mathrm{es}}\left(k, \phi\right) = \sum\nolimits_g \delta\left(k - k_g\left(\phi\right)\right), \tag{3.58}$$

with the sum on the gaps.

In quasiperiodic C&P sequences, the edge-state k_g of each gap with label (p, q) winds exactly $2q$ times inside the gap as the phason changes $\phi = 0 \ldots 2\pi$ [69],

$$W_{\mathrm{C\&P}}\left(k_g\left(p, q\right)\right) = 2q. \tag{3.59}$$

In other words, $\varrho_{\mathrm{es}}\left(k, \phi\right)$ is related to $\alpha\left(k, \phi\right)$ in C&P tilings. This is the case for σ_5 as seen in Figure 3.9a.

3.3.2.2 Non-C&P Tilings

In non-C&P tilings, however, this is not the case, as seen in Figure 3.9b. For instance, the edge-state of the $\mathcal{N}^{\sigma_3}_{4,-1} = \left(4 - 1 \cdot \tau^2\right)/5$ gap in σ_3 winds 9 times. Moreover, the winding number for each gap changes with N, as summarized in Table 3.2.

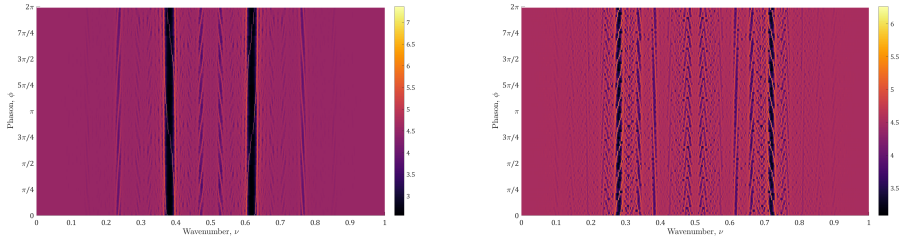

(a) Winding of gap states for σ_5 with $F_N = 89$.

(b) Winding of gap states for σ_3 with $F_N = 89$.

Figure 3.9: The density of states $\rho(\nu, \phi)$ in a logarithmic scale showing the winding of gap states for the squared Fibonacci substitutions using scattering matrix with $(n_A, n_B) = (1, 1.15)$ and $(l_A, l_B) = (1.15, 1)$.

Claim. The gap in σ_3 located at $\mathcal{N}^{\sigma_3}_{-10,5} = \left(-10 + 5 \cdot \tau^2\right)/5$ winds exactly 2 times, same as its corresponding gap in σ_5 located at $\mathcal{N}^{\sigma_5}_{-2,1} = -2 + 1 \cdot \tau^2$. Generally, $\mathcal{N}^{\sigma_3}_{5p,5q}$ and $\mathcal{N}^{\sigma_5}_{p,q}$ have the same winding $W = 2q$ of the edge state.

Corollary. *The winding of the gaps in both C&P and non-C&P sequences corresponds to their* structural *phase. However, it corresponds to the* gap label *only in C&P tilings.*

Corollary. *There are integral numbers in non-C&P sequences that can be extracted with the naïve approach. However, they cannot be interpreted as topological winding numbers.*

Conjecture. *The additional gaps in non-C&P sequences do not carry the same topological character as C&P sequences.*

3.3.3 Comparison of Spectral and Structural Properties

The spectral analysis between σ_5 and σ_3 shows a definite difference between both substitutions (see Figures 3.7 and 3.9). However, the structural phase $\Theta(\xi, \phi)$ is the same (Figure 3.5) despite Σ_1 being distinct. This is due to our definition of Σ_1, where the phase Θ comes from the translation operators $\mathcal{T}^{m(\ell)}$, as seen in (2.12). Since F_N numbers are the same, so are $\mathcal{T}^{m(\ell)}$. Thereby, we need another method.

The proper way to characterize the structure of a substitution is by its Čech cohomology $\check{H}^1(\Omega)$ [52]. In our case,

$$\check{H}^1\left(\Omega_{\sigma_5}\right) \cong \mathbb{Z}^2, \qquad \check{H}^1\left(\Omega_{\sigma_3}\right) \cong \mathbb{Z} \oplus \mathbb{Z}^2. \tag{3.60}$$

Thus, $\check{H}^1\left(\Omega_{\sigma_3}\right) \ncong \mathbb{Z}^2 = \mathbb{Z}^{\dim \sigma_3}$ immediately shows that σ_3 is not a C&P sequence (here, $\dim \sigma_3 = 2$ the number of letters in σ_3). Formally, we have found the following.

Proposition 3.2. *For a Sturmian (C&P or substitution) 1d tiling T, one has $\check{H}^1(\Omega_T) \cong \mathbb{Z}^a$, where periodic tilings have $a = 1$, and quasiperiodic abide $a = |\Gamma_1|$.*

Proof. We apply the procedure in Section 3.1.4.1. Since T is Sturmian, $p_1(z)$ is an irreducible polynomial over $\mathbb{Z}$ with degree $a = |\Gamma_1|$. Hence, $\check{H}^1(\Omega_T) \cong \mathbb{Z}^a$. □

Comparing $\check{H}^1(\Omega)$ and $K_0(\mathcal{B})$, we see that σ_5 is consistent with C&P tilings (see Tables 3.3 and 3.4). Thus it follows a Bloch theorem, and the winding numbers correspond to both structure and spectrum. The inconsistency in σ_3, namely that

Table 3.3: Some topological properties of selected substitution sequences.

Name		Rule	M_1	λ_1	$\check{H}^1(\Omega)$	$\tau_*(K_0(\mathcal{B}))$
Fibonacci	σ_{Fib}	$\begin{smallmatrix} A\mapsto AB \\ B\mapsto A \end{smallmatrix}$	$\left(\begin{smallmatrix}1&1\\1&0\end{smallmatrix}\right)$	τ	$\mathbb{Z}^2$	$\mathbb{Z}+\tau\mathbb{Z}$
Fibo^2	σ_5	$\begin{smallmatrix} A\mapsto ABA \\ B\mapsto AB \end{smallmatrix}$	$\left(\begin{smallmatrix}2&1\\1&1\end{smallmatrix}\right)$	τ^2	$\mathbb{Z}^2$	$\mathbb{Z}+\tau^2\mathbb{Z}$
Non-Fibo^2	σ_3	$\begin{smallmatrix} A\mapsto AAB \\ B\mapsto BA \end{smallmatrix}$	$\left(\begin{smallmatrix}2&1\\1&1\end{smallmatrix}\right)$	τ^2	$\mathbb{Z}\oplus\mathbb{Z}^2$	$\frac{1}{5}\left(\mathbb{Z}+\tau^2\mathbb{Z}\right)$
Periodic	σ_{Per}	$\begin{smallmatrix} A\mapsto AB \\ B\mapsto AB \end{smallmatrix}$	$\left(\begin{smallmatrix}1&1\\1&1\end{smallmatrix}\right)$	2	$\mathbb{Z}$	$\frac{1}{2}\mathbb{Z}$
Thue-Morse	σ_{TM}	$\begin{smallmatrix} A\mapsto AB \\ B\mapsto BA \end{smallmatrix}$	$\left(\begin{smallmatrix}1&1\\1&1\end{smallmatrix}\right)$	2	$\mathbb{Z}\oplus\mathbb{Z}\left[\frac{1}{2}\right]$	$\frac{1}{3}\mathbb{Z}\left[\frac{1}{2}\right]$
Period Doubling	σ_{PD}	$\begin{smallmatrix} A\mapsto AB \\ B\mapsto AA \end{smallmatrix}$	$\left(\begin{smallmatrix}1&1\\2&0\end{smallmatrix}\right)$	2	$\mathbb{Z}\oplus\mathbb{Z}\left[\frac{1}{2}\right]$	$\frac{1}{3}\mathbb{Z}\left[\frac{1}{2}\right]$
Silver	σ_{Sil}	$\begin{smallmatrix} A\mapsto AAB \\ B\mapsto A \end{smallmatrix}$	$\left(\begin{smallmatrix}2&1\\1&0\end{smallmatrix}\right)$	$\sqrt{2}+1$	$\mathbb{Z}^2$	$\frac{1}{2}\left(\mathbb{Z}+\lambda_1\mathbb{Z}\right)$
Marginal	σ_{Mar}	$\begin{smallmatrix} A\mapsto AAB \\ B\mapsto ABB \end{smallmatrix}$	$\left(\begin{smallmatrix}2&1\\1&2\end{smallmatrix}\right)$	3	$\mathbb{Z}\oplus\mathbb{Z}\left[\frac{1}{3}\right]$	$\frac{1}{2}\mathbb{Z}\left[\frac{1}{3}\right]$
Ternary	σ_{Ter}	$\begin{smallmatrix} A\mapsto AB \\ B\mapsto AC \\ C\mapsto ABC \end{smallmatrix}$	$\left(\begin{smallmatrix}1&1&0\\1&0&1\\1&1&1\end{smallmatrix}\right)$	2.247...	$\mathbb{Z}^3$	$\frac{1}{a}\left(\mathbb{Z}+\lambda_1\mathbb{Z}+\lambda_1^2\mathbb{Z}\right)$

Table 3.4: Some topological properties of Fibonacci substitution sequences. Here, $\Delta\Theta(S)$ is the atomic surface in accordance with [43]. The example rule corresponds to the bold sequence in each family.

Sequence Family	Example Rule	$\Delta\Theta(S)$	$\check{H}^1(\Omega)$	$\tau_*(K_0(\mathcal{B}))$
Fibonacci $M_1=\left(\begin{smallmatrix}1&1\\1&0\end{smallmatrix}\right),\ \lambda_1=\tau$				
σ_1, $\boldsymbol{\sigma_2}$	$\begin{smallmatrix} A\mapsto AB \\ B\mapsto A \end{smallmatrix}$	1	$\mathbb{Z}^2$	$\mathbb{Z}+\tau\mathbb{Z}$
Fibonacci^2 $M_1=\left(\begin{smallmatrix}2&1\\1&1\end{smallmatrix}\right),\ \lambda_1=\tau^2$				
$\sigma_1, \sigma_2, \sigma_5$, $\boldsymbol{\sigma_6}$	$\begin{smallmatrix} A\mapsto AAB \\ B\mapsto AB \end{smallmatrix}$	1	$\mathbb{Z}^2$	$\mathbb{Z}+\tau^2\mathbb{Z}$
σ_3, $\boldsymbol{\sigma_4}$	$\begin{smallmatrix} A\mapsto BAA \\ B\mapsto AB \end{smallmatrix}$	τ	$\mathbb{Z}\oplus\mathbb{Z}^2$	$\frac{1}{5}\left(\mathbb{Z}+\tau^2\mathbb{Z}\right)$
Fibonacci^3 $M_1=\left(\begin{smallmatrix}3&2\\2&1\end{smallmatrix}\right),\ \lambda_1=\tau^3$				
$\sigma_2, \sigma_3, \sigma_{13}, \sigma_{16}, \sigma_{17}, \sigma_{27}$, $\boldsymbol{\sigma_{29}}$	$\begin{smallmatrix} A\mapsto AABAB \\ B\mapsto AAB \end{smallmatrix}$	1	$\mathbb{Z}^2$	$\frac{1}{2}\left(\mathbb{Z}+\tau^3\mathbb{Z}\right)$
$\sigma_6, \sigma_{12}, \sigma_{19}$, $\boldsymbol{\sigma_{26}}$	$\begin{smallmatrix} A\mapsto ABABA \\ B\mapsto AAB \end{smallmatrix}$	$(\tau+1)/2$	$\mathbb{Z}^2$	$\frac{1}{2}\left(\mathbb{Z}+\tau^3\mathbb{Z}\right)$
$\boldsymbol{\sigma_{14}}$	$\begin{smallmatrix} A\mapsto BAAAB \\ B\mapsto ABA \end{smallmatrix}$	$3-\tau$	$\mathbb{Z}\oplus\mathbb{Z}^2$	$\frac{1}{4}\left(\mathbb{Z}+\tau^3\mathbb{Z}\right)$
$\sigma_1, \sigma_4, \sigma_5, \sigma_7, \sigma_{15}, \sigma_{18}$ $\sigma_{23}, \sigma_{24}, \sigma_{28}$, $\boldsymbol{\sigma_{30}}$	$\begin{smallmatrix} A\mapsto AAABB \\ B\mapsto AAB \end{smallmatrix}$	$3/2$	$\mathbb{Z}^2$	$\frac{1}{2}\left(\mathbb{Z}+\tau^3\mathbb{Z}\right)$
$\sigma_8, \sigma_9, \sigma_{11}, \sigma_{20}, \sigma_{22}$, $\boldsymbol{\sigma_{25}}$	$\begin{smallmatrix} A\mapsto ABBAA \\ B\mapsto AAB \end{smallmatrix}$	$\tau/2+1$	$\mathbb{Z}^2$	$\frac{1}{2}\left(\mathbb{Z}+\tau^3\mathbb{Z}\right)$
σ_{10}, $\boldsymbol{\sigma_{21}}$	$\begin{smallmatrix} A\mapsto BBAAA \\ B\mapsto AAB \end{smallmatrix}$	$(\tau+3)/2$	$\mathbb{Z}\oplus\mathbb{Z}^2$	$\frac{1}{4}\left(\mathbb{Z}+\tau^3\mathbb{Z}\right)$
Sequence Family	Example Rule	$\Delta\Theta(S)$	$\check{H}^1(\Omega)$	$\tau_*(K_0(\mathcal{B}))$

$\tau_*\left(K_0\left(\mathcal{B}_{\sigma_3}\right)\right) \ncong \tau_*\left(K_0\left(\mathcal{B}_{\sigma_5}\right)\right)$ as shown in (3.53), implies no Bloch theorem and irregular windings. In other words, since σ_5 is C&P, then $\check{H}^1\left(\Omega_{\sigma_3}\right) \cong K_0\left(\mathcal{B}_{\sigma_3}\right)$ so that we can identify $\tau_*^{\check{H}}\left(\check{H}^1\left(\Omega_{\sigma_3}\right)\right)$ with Bragg peaks and $\tau_*\left(K_0\left(\mathcal{B}_{\sigma_3}\right)\right)$ with spectral gaps, and infer Bloch theorem. Contrarily, comparing σ_3 with the Thue-Morse sequence suggests that $\tau_*^{\check{H}}\left(\check{H}^1\left(\Omega_{\sigma_3}\right)\right)$ cannot be identified with Bragg peaks and thus Bloch theorem does not hold. This can also be inferred from the P-matrix (3.52).

Next, we inspect the Fibonacci (regular, square and cubed) substitutions presented in Table 3.4. One can divide Fibonacci^2 into 2 families and Fibonacci^3 into 6 families based on the atomic surface $\Delta\Theta\left(S\right)$ [43]. These families are identified completely by inspecting the simplicial cohomologies $H^1\left(\Gamma_n\right)$ and their Betti numbers $\beta^1\left(\Gamma_n\right)$ (see Section 3.1.3), or by examining the complexity trees (see Section 3.1.5). These β_n^1 and T_n show a unique structure for each family, whereas the universal groups $\check{H}^1\left(\Omega\right)$ (or $K_0\left(\mathcal{B}\right)$) may not. This is summarized in Table 3.4.

Remark. In both Tables 3.3 and 3.4, we compare $\check{H}^1\left(\Omega\right)$ with $\tau_*\left(K_0\left(\mathcal{B}\right)\right)$. Although, in terms of groups, they are not on a par (since $\check{H}^1\left(\Omega\right) \cong K_0\left(\mathcal{B}\right)$ in $1d$ but not with its trace), we use them to compare structural and spectral properties of the tiling, respectively. We could also examine in contrast $\check{H}^1\left(\Omega\right)$ with $\tau_*^{\check{H}}\left(\check{H}^1\left(\Omega\right)\right)$, since $\tau_*^{\check{H}}\left(\check{H}^1\left(\Omega\right)\right) = \tau_*^K\left(K_0\left(\mathcal{B}\right)\right)$ (cf. Section 5.4 and Theorem 5.1).

3.4 Tight Binding and Scattering Matrix

In calculating the spectral features of the previous section, we used the scattering matrix approach. The scattering matrix itself was calculated using a transfer matrix on the *wave equation* (see [68, 69] for details). To use the scattering matrix for a general Hamiltonian, we must be more careful.

In this section, we shall review the essentials of the scattering matrix formalism. The avid reader is referred to [68, 70] for further details. Then, we shall show how to reproduce all the wave equation results using only a tight binding Hamiltonian.

3.4.1 Essentials of the Wave Equation Transfer Matrix

We now succinctly present the application procedure of transfer matrices in the wave equation. Consider a $1d$ system of size L of some dielectric material. There are waves incoming to the system from the left and right, and outgoing waves after transmission and reflection. The free part (without dielectrics) has a well-defined k vector, but the system itself need a more careful analysis. Neglecting internal losses in the system, the scattering matrix from the incoming to the outgoing waves is written as

$$\begin{pmatrix} \psi_L^o \\ \psi_R^o \end{pmatrix} = \begin{pmatrix} \vec{r} & t \\ t & \overleftarrow{r} \end{pmatrix} \begin{pmatrix} \psi_L^i \\ \psi_R^i \end{pmatrix} \doteq \mathcal{S}_W \begin{pmatrix} \psi_L^i \\ \psi_R^i \end{pmatrix}, \tag{3.61}$$

where $\vec{r}$ and $\overleftarrow{r}$ are the rightwards and leftwards reflection coefficients and t is the transmission coefficient (all complex), as presented in Section 3.4.2. The subscript W implies a wave equation, and will be omitted below unless specifically required. This scattering matrix can be calculated from the total transfer matrix. If we consider our system built of different dielectric media (by means of width and permittivity), the total transfer matrix from left to right is written as

$$\begin{pmatrix} \psi_R^i \\ \psi_R^o \end{pmatrix} = \mathcal{T} \begin{pmatrix} \psi_L^i \\ \psi_L^o \end{pmatrix} = T_M \cdots T_2 T_1 \begin{pmatrix} \psi_L^i \\ \psi_L^o \end{pmatrix}, \tag{3.62}$$

and all the T_m-s are either propagation inside a slab or transfer between slabs as follows [68, 71]. For propagation we use

$$T_A = \begin{pmatrix} \cos\delta_A & -\sin\delta_A \\ \sin\delta_A & \cos\delta_A \end{pmatrix}, \qquad T_B = \begin{pmatrix} \cos\delta_B & -\sin\delta_B \\ \sin\delta_B & \cos\delta_B \end{pmatrix}, \tag{3.63}$$

where the optical path is given by $\delta_A(k) = kn_A l_A$ with k the wavevector, n_A the refraction index of the slab of type A and l_A its width (similarly for δ_B). To simplify the calculations, we use the same optical path $\delta_A(k) = \delta_B(k) \doteq \delta(k)$, so that

$$n_A l_A = n_B l_B. \tag{3.64}$$

For the interface between slabs, we have

$$T_{A\to B} = \begin{pmatrix} 1 & 0 \\ 0 & n_B/n_A \end{pmatrix}, \qquad T_{B\to A} = \begin{pmatrix} 1 & 0 \\ 0 & n_A/n_B \end{pmatrix}. \tag{3.65}$$

Naïvely, we could just multiply all the transfer matrices as in (3.62). If all we seek is the integrated density of states (3.73), it would suffice. However, should we inspect the chiral phase (3.76) too, we would obtain numerical inaccuracies due to the sensitivity of the phase. To solve the issue, we define *effective* transfer matrices

$$\begin{aligned} \tilde{T}_A &\doteq T_A &&= \begin{pmatrix} \cos\delta & -\sin\delta \\ \sin\delta & \cos\delta \end{pmatrix}, \\ \tilde{T}_B &\doteq T_{B\to A} T_B T_{A\to B} &&= \begin{pmatrix} \cos\delta & -\frac{n_A}{n_B}\sin\delta \\ \frac{n_B}{n_A}\sin\delta & \cos\delta \end{pmatrix}. \end{aligned} \tag{3.66}$$

Thus, (3.62) transforms to

$$\mathcal{T} = \tilde{T}_{A/B}^{r_n} \cdots \tilde{T}_A^{r_3} \tilde{T}_B^{r_2} \tilde{T}_A^{r_1}, \tag{3.67}$$

where r_i is the number of repetitions of the i^{th} slab. Note that

$$\begin{aligned} \tilde{T}_A^r &= \begin{pmatrix} \cos r\delta & -\sin r\delta \\ \sin r\delta & \cos r\delta \end{pmatrix}, \\ \tilde{T}_B^r &= \begin{pmatrix} \cos r\delta & -\frac{n_A}{n_B}\sin r\delta \\ \frac{n_B}{n_A}\sin r\delta & \cos r\delta \end{pmatrix}. \end{aligned} \tag{3.68}$$

There is a well-defined procedure to translate $\mathcal{T}$ into $\mathcal{S}$ (see [68, 69]). Simply put, for $\mathcal{T}(k) = \begin{pmatrix} M_1(k) & M_3(k) \\ M_2(k) & M_4(k) \end{pmatrix}$, one has $\mathcal{S}(k) = \begin{pmatrix} \vec{r}(k) & t(k) \\ t(k) & \overleftarrow{r}(k) \end{pmatrix}$, where

$$\begin{aligned} \vec{r}(k) &= [(M_4 - M_1) + \mathrm{i}(M_2 + M_3)] \,/\, [(M_1 + M_4) + \mathrm{i}(M_3 - M_2)], \\ \overleftarrow{r}(k) &= [(M_1 - M_4) + \mathrm{i}(M_2 + M_3)] \,/\, [(M_1 + M_4) + \mathrm{i}(M_3 - M_2)], \\ t(k) &= 2 \,/\, [(M_1 + M_4) + \mathrm{i}(M_3 - M_2)]. \end{aligned} \tag{3.69}$$

3.4.2 Essentials of the Wave Equation Scattering Matrix

We shall use the scattering matrix formalism mainly due to its natural connection to experiments. We shortly summarize the scattering formalism below; the avid reader is referred to [68, 69].

Consider a $1d$ wave system of physical size L bounded by two semi-infinite free waveguides supporting incoming and outgoing waves. The free part has a well-defined

k vector, whereas the waveguide itself might not. To study it, we use the scattering of waves [69].

Take, for simplicity, the scattering of electromagnetic waves by dielectric media. We relate outgoing and incoming amplitudes of plane waves by an $\mathcal{S}$-matrix

$$\underbrace{\begin{array}{c|c} \vec{\imath} & \vec{o} \\ \hline \overleftarrow{o} & \overleftarrow{\imath} \end{array}}_{\mathcal{S}}$$

Here $\vec{\imath}$ and $\vec{o}$ are the rightward incoming and outgoing waves, and $\overleftarrow{\imath}$ and $\overleftarrow{o}$ are the leftward ones. Explicitly,

$$\begin{pmatrix} \vec{o} \\ \overleftarrow{o} \end{pmatrix} = \begin{pmatrix} \vec{r}\,(k) & t\,(k) \\ t\,(k) & \overleftarrow{r}\,(k) \end{pmatrix} \begin{pmatrix} \vec{\imath} \\ \overleftarrow{\imath} \end{pmatrix} \doteq \mathcal{S} \begin{pmatrix} \vec{\imath} \\ \overleftarrow{\imath} \end{pmatrix}. \tag{3.70}$$

Here t is the transmission coefficient with $\vec{r} = r\,\mathrm{e}^{\mathrm{i}\vec{\theta}}$ and $\overleftarrow{r} = r\,\mathrm{e}^{\mathrm{i}\overleftarrow{\theta}}$ the rightward and leftward reflection coefficients. Note the dependence on k. Since it is unitary, it can be diagonalized to

$$\mathcal{S}\,(k) \mapsto \begin{pmatrix} \mathrm{e}^{\mathrm{i}\varphi_1(k)} & 0 \\ 0 & \mathrm{e}^{\mathrm{i}\varphi_2(k)} \end{pmatrix}. \tag{3.71}$$

Now, defining the total phase shift as $\delta\,(k) = \frac{1}{2}\,(\varphi_1\,(k) + \varphi_2\,(k))$, we have

$$\det \mathcal{S} = \mathrm{e}^{2\mathrm{i}\delta(k)}\,. \tag{3.72}$$

The density of modes is found with the Krein-Schwinger formula [68–70]

$$\mathcal{N}\,(k) - \mathcal{N}_0\,(k) = \frac{\delta\,(k)}{\pi} = \frac{1}{2\pi}\,\mathrm{Im}\log\det \mathcal{S}_W\,(k)\,, \tag{3.73}$$

where $\mathcal{N}_0\,(k)$ is the integrated density of states of the free part. Differentiating, we obtain the density of states,

$$\varrho\,(k) - \varrho_0\,(k) = \frac{1}{\pi}\frac{\mathrm{d}}{\mathrm{d}k}\delta\,(k) = \frac{1}{2\pi}\,\mathrm{Im}\,\frac{\mathrm{d}}{\mathrm{d}k}\log\det \mathcal{S}\,(k)\,. \tag{3.74}$$

Noting that in this left-to-right basis, since $\mathcal{S}$ is unitary, we have two phases (eigenvalues). Thus, we can define an asymmetrical phase $\gamma\,(k,\phi) = \varphi_1\,(k,\phi) - \varphi_2\,(k,\phi)$ [68, 69]. Inside the gaps, when $r = 1$ (and $t = 0$), $\mathcal{S}\,(k)$ is diagonal. Hence, $\gamma\,(k,\phi)$ can be written in terms of $\mathcal{S}_W\,(k)$ similarly to before,

$$\gamma\,(k,\phi) = \mathrm{Im}\,\mathrm{Tr}\,[\sigma_z \log \mathcal{S}\,(k,\phi)]\,, \tag{3.75}$$

where $\sigma_z = \left(\begin{smallmatrix} 1 & 0 \\ 0 & -1 \end{smallmatrix}\right)$ is the Pauli matrix. Here, we used the identities $S^{\sigma_z} = \exp\,[\sigma_z \log S]$ and $\log\det A = \mathrm{Tr}\log A$. This asymmetrical phase $\gamma\,(k,\phi)$ has a topological interpretation, since it is dependent on the phason ϕ, whereas the total phase shift $\delta\,(k)$ is ϕ-independent (since it may depend on the order of the waveguide slabs but not their chiral permutations, which are set by the phason ϕ). The asymmetrical phase $\gamma\,(k,\phi)$ is related to the chiral phase (cf. Figure 3.8),

$$\alpha\,(k,\phi) = \arg\overleftarrow{r}\,(k,\phi) - \arg\vec{r}\,(k,\phi)\,, \tag{3.76}$$

by [69]

$$\cos\frac{\gamma}{2} = r\cos\frac{\alpha}{2}, \tag{3.77}$$

where $r = |\tilde{r}| = |\vec{r}|$ (and the implicit dependence on k and ϕ). Thus,

$$\gamma = 2\arccos\left(r\cos\alpha/2\right) \iff \alpha = 2\arccos\left(r^{-1}\cos\gamma/2\right). \tag{3.78}$$

Inside the gaps, when $r = 1$, we obtain $\gamma = \alpha$. Near $r \sim 0$ ("tunneling") the relation $\alpha = f(\gamma)$ is not well-defined.

3.4.3 Total Phase Shift

We now turn our attention to the tight binding formalism. The scattering matrix formalism we presented above must be independent of representation. Yet, in the Hamiltonian description, we do not have incoming and outgoing waves nor a k-vector. How to define the scattering matrix then?

Let us consider a tight binding Hamiltonian

$$\mathcal{H} \doteq \mathcal{H}_0 + \mathcal{V} = -\Delta + \mathcal{V}, \tag{3.79}$$

where Δ is the Laplacian, $\mathcal{V}$ is a potential defined in a quasiperiodic manner, and $\mathcal{H}_0$ is the free Hamiltonian (without a potential). Representing in the *site* basis $n = 1 \ldots N$, this Hamiltonian is an $N \times N$ matrix acting on ψ such that

$$\mathcal{H}\psi_n = -\left(\psi_{n+1} + \psi_{n-1}\right) + v_n\psi_n, \tag{3.80}$$

with periodic boundary conditions ($\psi_0 \doteq \psi_N$). Its eigenenergies are formally given by

$$\Lambda_{\mathcal{H}} \doteq \operatorname{spec}\mathcal{H} = \{E_i\}_{i=1}^{N}. \tag{3.81}$$

Let us define the resolvant operator

$$\mathcal{G}(z) \doteq \frac{1}{\mathcal{H} - z}, \tag{3.82}$$

and two auxiliary resolvant-like operators

$$\mathcal{G}_{\pm}(E) \doteq \frac{1}{\mathcal{H} - E \mp \mathrm{i}\epsilon}. \tag{3.83}$$

The scattering matrix is then defined as [68, 70]

$$\begin{aligned} \mathcal{S}(E) &\doteq \frac{\mathcal{G}_+(E)}{\mathcal{G}_+^0(E)} \Big/ \frac{\mathcal{G}_-(E)}{\mathcal{G}_-^0(E)} \\ &= \frac{\mathcal{H}_0 - E - \mathrm{i}\epsilon}{\mathcal{H} - E - \mathrm{i}\epsilon} \Big/ \frac{\mathcal{H}_0 - E + \mathrm{i}\epsilon}{\mathcal{H} - E + \mathrm{i}\epsilon}. \end{aligned} \tag{3.84}$$

The total phase shift is defined similarly to Section 3.4.2 above,

$$\delta(E) \doteq \frac{1}{N}\operatorname{Im}\log\det\mathcal{S}(E), \tag{3.85}$$

with the proper normalization $1/N$. Using the Krein-Schwinger formula, the integrated density of states reads

$$\eta(E) - \eta_0(E) \doteq \frac{\delta(E)}{\pi} = \frac{1}{N\pi}\operatorname{Im}\log\det\mathcal{S}(E). \tag{3.86}$$

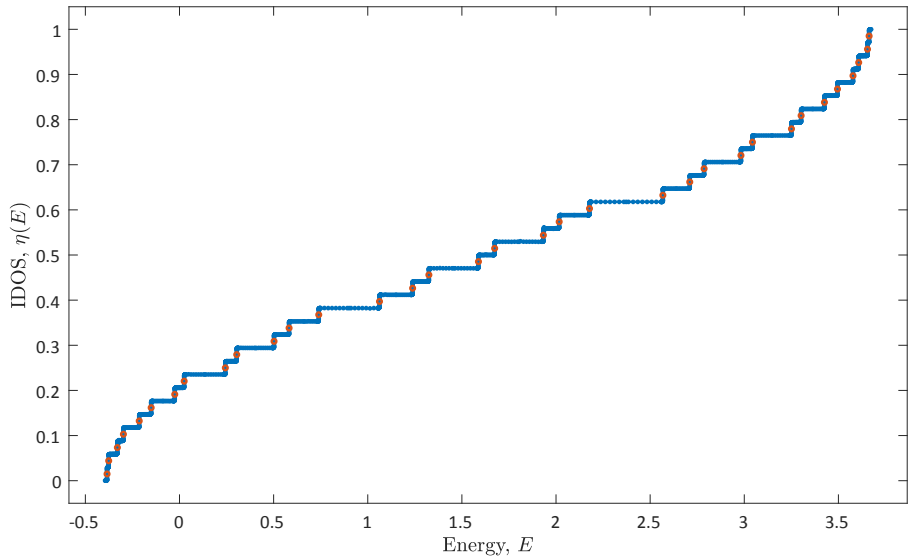

Figure 3.10: The integrated density of states $\eta(E)$ using scattering formalism with tight binding Hamiltonian in blue. The eigenvalues of H are shown as red dots. Here we used the Fibonacci sequence with $F_N = 34$, $\epsilon = 10^{-4}$ and $(v_A, v_B) = (\sqrt{2}, 2)$. Note that the width of each step is $\sim \epsilon$.

Let us analyze this definition. The free Hamiltonian $\mathcal{H}_0$ has a continuous spectrum, and thus does not introduce singularities into (3.84). All the singularities, therefore, come from the spectrum of $\mathcal{H}$. Thus,

$$\begin{cases} \mathcal{S}(E) \xrightarrow{\epsilon \to 0} -\mathbb{1} & \text{if } E \in \Lambda_{\mathcal{H}}, \\ \mathcal{S}(E) \xrightarrow{\epsilon \to 0} \mathbb{1} & \text{if } E \notin \Lambda_{\mathcal{H}}. \end{cases} \tag{3.87}$$

Hence, up to ϵ, the spectrum of $\mathcal{S}$ is given by

$$\Lambda_{\mathcal{S}} \doteq \operatorname{spec} \mathcal{S} = \begin{cases} (-1, 1, \ldots, 1) & \text{if } E \in \Lambda_{\mathcal{H}}, \\ (+1, 1, \ldots, 1) & \text{if } E \notin \Lambda_{\mathcal{H}}. \end{cases} \tag{3.88}$$

The total phase shift is therefore,

$$\delta(E) = \begin{cases} \pi/N & \text{if } E \in \Lambda_{\mathcal{H}}, \\ 0 & \text{if } E \notin \Lambda_{\mathcal{H}}. \end{cases} \tag{3.89}$$

Corollary. *The integrated density of states $\eta(E)$ makes a discrete jump of N^{-1} only at those values where $E \in \Lambda_{\mathcal{H}}$. For all other energies, $\eta(E)$ does not change, and we have a plateau (see Figure 3.10).*

Remark. The density of states $\rho(E)$ consists only of Lorentzian peaks at $E \in \Lambda_{\mathcal{H}}$ of width ϵ (at half-maximum).

3.4.4 Asymmetrical Phase

Let us now draw our attention to the asymmetrical phase. Since it is dependent on the phason ϕ, we rewrite our Hamiltonian as

$$\mathcal{H}(\phi) \doteq \mathcal{H}_0 + \mathcal{V}(\phi). \tag{3.90}$$

The scattering matrix is now also ϕ-dependent $\mathcal{S} = \mathcal{S}(E, \phi)$. Note that since the Hamiltonian admits periodic boundary conditions, all $\mathcal{V}(\phi)$ and thus $\mathcal{H}(\phi)$ are cyclic permutations of each other. Therefore, its spectrum is ϕ-independent.

Similarly to the discussion in Section 3.4.2, let us define the asymmetrical phase as

$$\gamma(E, \phi) \doteq \operatorname{Im} \operatorname{Tr} [\mathcal{Z} \log \mathcal{S}(E, \phi)], \tag{3.91}$$

where now

$$\mathcal{Z} = \operatorname{diag}(+1, -1, +1, \ldots, \pm 1), \tag{3.92}$$

is an alternating matrix analogous to σ_z. Let us connect it to the chiral phase $\alpha(E, \phi)$. Defining the normalized Green function as

$$\mathcal{W}_{\pm} = \frac{\mathcal{G}_{\pm}(E)}{\mathcal{G}^0_{\pm}(E)}, \tag{3.93}$$

the transmission probability $T(E) = |t(E)|^2$ is given by [68]

$$T(E) = \det W_+(E) \det W_-(E) = |\det W_+(E)|^2. \tag{3.94}$$

The reflection probability is defined by $R(E) = |\vec{r}(E)|^2 = r^2(E)$. In a lossless system, $R(E) = 1 - T(E)$; thus, the reflection coefficient $r(E)$ is given by

$$r(E) = \sqrt{1 - |\det W_+(E)|^2}. \tag{3.95}$$

There is one technical—but important—detail left to consider. In order to see the dependence on ϕ, we need the spectrum of $\mathcal{S}$ be also dependent on ϕ, namely, $\Lambda_{\mathcal{S}}$ must be ordered. Yet, if we diagonalize $\mathcal{S}$ numerically, the special eigenvalue of -1 always comes first. To solve this issue we note that $\mathcal{H}(\phi)$ are similar, and thus $\mathcal{S}(E, \phi)$ are also similar. We therefore choose some ϕ_0 and diagonalize $\mathcal{S}$ within it as

$$\mathcal{S}(E, \phi_0) = U^{\dagger}_{\phi_0} \Lambda_{\mathcal{S}} V_{\phi_0}, \tag{3.96}$$

where U_{ϕ_0} and V_{ϕ_0} are the right- and left-eigenvectors, respectively, properly normalized. Thus, we rewrite $\gamma(E, \phi)$ with respect to ϕ_0 as

$$\gamma(E, \phi) = \operatorname{Im} \operatorname{Tr} \left[\mathcal{Z} \left(V^{\dagger}_{\phi_0} \log \mathcal{S}(E, \phi) U_{\phi_0} \right) \right]. \tag{3.97}$$

Remark. The definition above of $\gamma(E, \phi)$ indeed works, but there are some numerical instabilities. These are mainly due to a bad condition number to inversion of $\mathcal{S}(E, \phi)$, which is also non-Hermitian.

3.4.5 Comparison between Tight Binding and Transfer Matrix

We have seen some results with the scattering formalism using two different approaches. The first, is the transfer matrix method, which we used to calculate the $\mathcal{S}$-matrix of the wave equation in Section 3.3.2; the second is tight binding of Section 3.4, with which we have the solved Schrödinger equation. The wave and Schrödinger equations are similar but not identical. What is the distinction then?

Looking on the IDOS, we do not see much difference between both cases. Remarkably, the plateaus obey the same $\eta_{p,q} = p + qs$ equation, although Bellissard's gap-labeling theorem [27] has been proven for tight binding Hamiltonians only. This emphasizes the topological nature of the quasiperiodic sequences.

Inspecting a bit closer, there is a slight numerical advantage in favor of the tight binding scheme. Since we know the eigenenergies of the Hamiltonian (can be calculated independently) and since the DOS peak width is of the order of ϵ, we know exactly how to mesh the energy axis. Thus we can freely choose between runtime and resolution of the IDOS calculation. Conversely, in the transfer matrix case, we do not know *a priori* the density of modes (DOM) peaks vs. k, and they must be found numerically. Consequently, we must employ a search-and-refine algorithm of k with respect to the emergent peaks, which is both unstable and time consuming. This limits the resolution we obtain with this method.

Let us now move our attention to the topological (chiral/asymmetrical) phases. Here, we see a large distinction between both cases. In the tight binding formalism, *any* topological information resides ϵ-near the eigenenergies; all parameters inside the gaps are trivial. Thus, it is quite difficult to see both numerically and experimentally the topological phase. On the other hand, in the transfer matrix formalism, the chiral phase itself changes *inside the gap* as a function of the phason ϕ (cf. Figure 3.8). This is a consequence of the transfer matrices. Thus we can inspect the chiral phase quite easily both numerically and experimentally using generalized edge states.

Chapter 4

Diffraction of Tilings

Diffraction of aperiodic tilings is quite complicated compared to spectral properties. Whereas the latter can be described by a simple formula for the gaps (3.4), diffraction peaks cannot be determined in the same way. In this chapter, we review the known theory behind diffraction of aperiodic tilings with an emphasis on the Thue-Morse tiling, we present how to identify diffraction peaks, and we show how to calculate them in several cases.

4.1 Introduction

Let us begin with a general review (see [23, 72–76]). Let $\{v_n\}$ be some aperiodic sequence with $v_n \in \{v_A, v_B\}$ (be it substitution or C&P). Its Fourier transform to order N is given by

$$\bar{G}_N(k) = \sum_{n=1}^{L_N} s_n \, \mathrm{e}^{2\pi i k n}, \tag{4.1}$$

where s_n are the scattering amplitudes, and L_N is the number of tiles at order N of the substitution. The diffracted intensity is

$$S_N(k) = \frac{1}{L_N} \left| \bar{G}_N(k) \right|^2. \tag{4.2}$$

Naturally, we go to the limit $N \to \infty$. The normalization varies between authors. Cheng, Savit, and Merlin [72], Kolář, Iochum, and Raymond [76], Peyrière, Cockayne, and Axel [77] do not use the L_N^{-1} factor, whereas Luck [23], Gähler and Klitzing [78] have it. A simple analysis (see Section 4.1.1) suggests the latter.

The intensity can be considered as a positive (Lebesgue-Stieltjes) measure,

$$\mathrm{d}\mu(k) = S(k) \, \mathrm{d}k = \lim_{N\to\infty} S_N(k) \, \mathrm{d}k. \tag{4.3}$$

The measure $\mu(k) = \int_0^k \mathrm{d}\mu(\kappa)$ can be considered as an integrated intensity (or, cumulative distribution function). It can also be represented as the Fourier-Transform of the autocorrelation,

$$\lim_{N\to\infty} \frac{1}{N} \sum_{n=0}^{N-1} s_n s_{n+a} \doteq \langle s_n s_{n+a} \rangle = \int \mathrm{d}\mu(k) \, \mathrm{e}^{2\pi i k a}. \tag{4.4}$$

Each positive measure $\mu(k)$ can be divided into 3 parts.

1. The discrete (atomic, pure-point) part μ_{PP}. Here, all discontinuities of $\mu(k)$ are delta functions $C(k_{\text{B}})\ \delta(k-k_{\text{B}})$ for some C, and the support $\{k_{\text{B}}\}$ is countable. These are the Bragg peaks. Equivalently,

$$G_N(k_{\text{B}}) \sim C(k_{\text{B}})\, L_N. \tag{4.5}$$

2. The absolutely continuous part μ_{AC}. Loosely speaking, the derivative exists at each point,

$$S(k) = \frac{\mathrm{d}\mu_{\text{AC}}}{\mathrm{d}k}. \tag{4.6}$$

3. The singularly continuous part μ_{AC}. This is "what is left" after the previous two were taken into account. It is continuous but nowhere differentiable; its support is a Cantor set. Moreover, its peaks behave as a power law [23, 79, 80],

$$\mu(k) - \mu(k_{\text{C}}) \sim \pm A_{\pm} |k-k_0|^{\alpha}, \quad k \to \pm k_0, \quad 0 < \alpha \leq 2, \tag{4.7}$$

where $\pm$ indicates convergence from above/below. The value $\alpha = 0$ would indicate the first case.

4.1.1 Bragg Peak Amplitude Scaling

Let us make a few remarks regarding the scaling of different peaks.

4.1.1.1 Scaling Approach

Let us inspect a periodic tiling with $l_A = a$ with L_N tiles. The location of atoms is given by $x_n = a(n - L_N/2)$ with constant scattering amplitude $s_n = 1$ and atomic density (4.18). Taking $n' = n - L_N/2$, its diffraction amplitude (4.19) reads

$$G_N(k) = \sum_{n'=-L_N/2}^{L_N/2} \mathrm{e}^{2\pi \mathrm{i} k a n'}. \tag{4.8}$$

Taking the limit $n' \to \infty$ and using Poisson summation formula, one has

$$G(k) = \sum_{n' \in \mathbb{Z}} \mathrm{e}^{2\pi \mathrm{i} k a n'} = \sum_{m \in \mathbb{Z}} \delta(m - ka) = \sum_{m \in \mathbb{Z}} \frac{1}{a} \delta\left(k - \frac{m}{a}\right). \tag{4.9}$$

Hence, $k_m = m/a$. Putting it back into (4.8), one has

$$G_N(k_m) = \mathrm{e}^{2\pi \mathrm{i} N a/2} \sum_{n=0}^{L_N} \mathrm{e}^{2\pi \mathrm{i} m n} = \mathrm{e}^{2\pi \mathrm{i} N a/2} \sum_{n=0}^{L_N} 1 \sim L_N. \tag{4.10}$$

Thus, generally, for Bragg peaks, $G_N(k_m) \sim C(k_m)\, L_N$.

4.1.1.2 Direct Approach

Let us explicitly calculate (4.8) yielding

$$G_N(k) = \mathrm{e}^{\mathrm{i}\phi} \frac{\sin \pi L_N k a}{\sin \pi k a} = \mathrm{e}^{\mathrm{i}\phi} L_N \frac{\operatorname{sinc} \pi L_N k a}{\operatorname{sinc} \pi k a}, \tag{4.11}$$

with some phase ϕ. At each $ka \in \mathbb{Z}$, the ratio of sines $\to L_N$ (sincs $\to 1$), and we retrieve the previous result $G_N(k_m) \sim L_N$. Moreover, the structure factor (4.2) yields

$$S_N(k) = \frac{1}{L_N}\left|\frac{\sin \pi L_N k a}{\sin \pi k a}\right|^2 = L_N\left|\frac{\operatorname{sinc} \pi L_N k a}{\operatorname{sinc} \pi k a}\right|^2. \tag{4.12}$$

The first zeroes around each peak k_m are given by $k_m^0 = k_m \pm 1/L_N a$. Hence, the width of a peak scales as $w_N \sim L_N^{-1}$. Together with the height scaling as $S_N(k_m) \sim L_N$, this gives rise to δ-peaks.

Let us apply a similar logic to singular continuous peaks at k_0. For Bragg peaks, we have concluded that $S_N(k_B) \sim L_N^1$ and $w_N(k_B) \sim L_N^{-1}$. For singular continuous peaks, $S_N(k_0) \sim L_N^\gamma$ with $0 < \gamma < 1$ as given by (4.15). Therefore, demanding a 0-width peak (singular, like δ) with a 0-area (continuous, unlike δ), we conclude that $w_N(k_0) \sim L_N^{-\beta}$ with $\gamma < \beta \leq 1$.

4.2 Diffraction of the Thue-Morse Tiling

In this section, we dwell into the intricacies of the Thue-Morse tiling diffraction.

4.2.1 Analytical Summary

Here, we show the main analytical results from the literature.

4.2.1.1 Scaling of Peaks

In the following calculation, we take $s_A = 1, s_B = -1$ to get rid of the pure-point part [73, 74] (more on that later). According to Luck [23] based on Cheng, Savit, and Merlin [72], taking a primitive wavevector of the form $k_0 = \ell/(2n+1)$ (note the odd denominator) yields

$$\mu(k) - \mu(k_0) \sim \pm|k - k_0|^\alpha, \quad 0 < \alpha < 1. \tag{4.13}$$

A general wavevector with a similar singularity is given by

$$k_1 = 2^{-n}(k_0 + M) = 2^{-n}\frac{m}{2\ell+1}. \tag{4.14}$$

The strongest singularity is at $k_0 = \frac{1}{3}, \frac{2}{3}$ with $\alpha = 2 - \log 3/\log 2$. These singularities were measured and identified in [75]. The intensity scaling goes as

$$S_N(k_0) \sim L_N^{\gamma_N} = 2^{N\gamma_N}, \quad \lim_{N\to\infty}\gamma_N = \gamma = 1 - \alpha, \tag{4.15}$$

and L_N is the number of tiles. Numerically, for $k_0 = \frac{1}{3}$ I get $\gamma = \log_2 3 - 1$ implying $\alpha = 2 - \log_2 3$ as expected.

Another (weaker) type of singularities exists at dyadic $k_w = M2^{-n}$ for which

$$\mu(\kappa) \sim \exp\left(-\frac{\log^2 \kappa}{\log 2}\right), \quad \kappa = |k - k_w|. \tag{4.16}$$

Note that the intensity $S(k) = \frac{\mathrm{d}\mu}{\mathrm{d}k}$ is repeating each integer value [73, 74],

$$S(k) = \delta_{\mathbb{Z}} + S_{\mathrm{TM}}(k), \tag{4.17}$$

where $S_{\mathrm{TM}}(k)$ is restricted to $[0, 1)$. The spectrum is singularly continuous (apart of trivial points). Moreover, the measure $\mu_{\mathrm{TM}}(k)$ is singular continuous and strictly increasing [73, 74].

4.2.1.2 Diffraction Spectrum

Now we follow Kolář, Iochum, and Raymond [76]. A parallel way is to define the atomic density,

$$\rho_N(x) = \sum_{n=1}^{L_N} s_n \delta(x - x_n) \tag{4.18}$$

with s_n a scattering amplitude term, $x_n = \sum_{i=1}^{n} l_i$ and $l_i \in \{l_A, l_B\}$ are tile lengths. The diffraction amplitude is given by

$$G_N(k) = \sum_{n=1}^{L_N} s_n \, \mathrm{e}^{2\pi \mathrm{i} k x_n} . \tag{4.19}$$

All other definitions are identical to the former ones. The critical exponent is now given by

$$\bar{\alpha} = 2 \frac{\log \lambda_{\max}}{\log \lambda_*}, \quad 0 \le \alpha \le 2, \tag{4.20}$$

where λ_* is the largest eigenvalue of the occurrence matrix and $\lambda_{\max}$ is the largest eigenvalue of the Fourier matrix $T(k)$ (see [76]). This time, $\bar{\alpha} = 2$ is equivalent to Bragg peaks.

- For the periodic tiling, Bragg peaks exist at each $k_{\mathrm{per}} = m/(l_A + l_B)$.
- For the Thue-Morse tiling, if $l_A \neq l_B$, Bragg peaks exist at the same k_{per} but with different intensities; if $l_A = l_B$, only "trivial" Bragg peaks survive; all other peaks of the form $k_{\mathrm{TM}} = m2^{-n}(l_A + l_B)$ belong to the singular continuous part of the spectrum. Trivial peaks are those that exist in every tiling (even a random tiling), e.g., at $k_{\mathrm{triv}} = 0$.

4.2.2 Simulations

In Figure 4.1, we show the diffraction amplitude $|G_N(k)|/L_N$. The amplitude of the Fibonacci peaks does not decay with N in correspondence with the definition of Bragg peaks (4.5). The amplitude of the Thue-Morse peaks visibly decays. It is analyzed in Figure 4.2.

In Figure 4.2, we show the peak intensity $S_N(k_0)$ of chosen peaks for different families $\frac{1}{r} \in \left\{\frac{1}{3}, \frac{1}{5}, \frac{1}{7}, \frac{1}{9}\right\}$ for $k_0 = m\,2^{-n}/r$ with $r > 1$ odd and $\gcd(m, r) = 1$. Each family has its own exponent γ_r. Families $r \ge 5$ oscillate, but have a definite trend. For families $7 \le r < 17$, the exponent $\gamma < 0$, which implies that there are no peaks for $N \to \infty$. The modeled exponents were calculated as follows. • Family $\frac{1}{3}$ is well known in the literature [23, 81]; • family $\frac{1}{5}$ was found by E. Akkermans (private communication) and by Wolny et al. [82, 83]; • family $\frac{1}{7}$ was calculated by [82, 83]; • family $\frac{1}{9}$ was matched to a best guess. There are more families with positive exponents (such as $r = 17$ and $r = 31$, where *some* of the fractions $m\,2^{-n}/r$ exhibit positive exponents), but the behavior is more erratic. The results are summarized in Table 4.1.

The general formula of the exponents γ for any $k = p/q$ (with $\gcd(p, q) = 1$ and odd $q \ge 3$) is given by Baake, Grimm, and Nilsson [84],

$$\gamma_{p/q} = \frac{1}{|S_q|} \sum_{n \in S_q} \log_2 \left(1 - \cos\left(2\pi \frac{pn}{q}\right)\right), \tag{4.21}$$

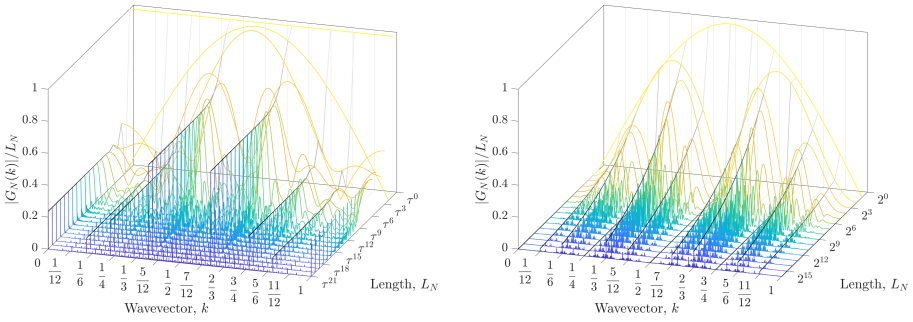

(a) Fibonacci. (b) Thue-Morse.

Figure 4.1: Diffraction amplitude scaling $|G_N(k)|/L_N$. Color represents the increasing order of N. Black lines: the top of chosen peaks. Here, $l_A = l_B = 1$ and $s_A = -s_B = 1$.

with

$$\begin{aligned} S_q &= \{2^n \bmod q \mid n \geq 0\} &&\subseteq U_q, \\ U_q &= \{1 \leq p < q \mid \gcd(p,q) = 1\} \doteq \left(\mathbb{Z}/\mathbb{Z}_q\right)^\times. \end{aligned} \tag{4.22}$$

Here, $\left(\mathbb{Z}/\mathbb{Z}_q\right)^\times$ is the multiplicative group of integers modulo q excluding 0.

The power-law dependence of singular continuous peaks (4.7) was first found numerically in Aubry, Godrèche, and Luck [79] for a "circle map" model. Later, in Aubry, Godrèche, and Luck [80], this model was proven to have a singular continuous diffraction spectrum with the exponent found numerically. It was conjectured that for the Thue-Morse sequence the dependence is the same.

4.2.3 General Analysis

In the next section, we analyze the Thue-Morse diffraction from several additional angles.

4.2.3.1 Peak Study

Let us start inspecting diffraction spectra that have a single peak only. The measure $\mu(k)$ at a pure-point (Bragg) peak k_B can be written as

$$\mu(k) - \mu(k_\mathrm{B}) = C_\pm(k_B), \tag{4.23}$$

namely, it is a step function with intensity $C_+ - C_- = C(k_\mathrm{B})$ from (4.5). Its value at k_B is immaterial since it is of 0-measure. Hence, it is a δ-peak.

Let us now focus on singular continuous peaks k_0. Take an ϵ neighborhood of k_0, specifically, $k_\pm = k_0 \pm \epsilon$. Applying (4.7), the power contained in (k_-, k_+) is given by

$$I_\epsilon = \mu(k_+) - \mu(k_-) = (A_+ + A_-)\,\epsilon^\alpha, \tag{4.24}$$

and $I_\epsilon \xrightarrow{\epsilon \to 0} 0$, unlike the pure-point case. Moreover, its total intensity $I_\mathrm{tot} \sim \mu(\infty) - \mu(-\infty)$ is unbound. Inspecting the diffraction spectrum $S(k)$ using (4.3) and (4.7), (simply, $\mathrm{d}\mu(k) = S(k)\,\mathrm{d}k$), we find that

$$S(k) = A_\pm \alpha\,|k - k_0|^{\alpha-1} = A_\pm \alpha\,|k - k_0|^{-\gamma}. \tag{4.25}$$

Table 4.1: Peak intensity exponents for different families.

Family $1/r$	γ_{fit}	γ_{model}	Type	Positive?	Osc. per.
$1/2$	$\log_2 4.0000 - 1$	$\log_2 4 - 1$	pure-point	✓	1
$1/3$	$\log_2 3.0000 - 1$	$\log_2 3 - 1$	sing. cont.	✓	1
$1/5$	$\log_2 2.2361 - 1$	$\frac{1}{2}\log_2 5 - 1$	sing. cont.	✓	2
$1/7$	$\log_2 1.9226 - 1$	$\frac{1}{3}\log_2 7 - 1$	sing. cont.	✗	3
$1/9$	$\log_2 1.4528 - 1$	$\frac{1}{6}\log_2 9 - 1$	sing. cont.	✗	3
$\frac{1}{11}, \frac{1}{13}, \frac{1}{15}, \frac{1}{19}, \ldots, \frac{1}{29}$	*varies*	*varies*	sing. cont.	✗	*varies*
$1/17$, $1/31$	*varies*	*varies*	sing. cont.	✓/✗	*varies*

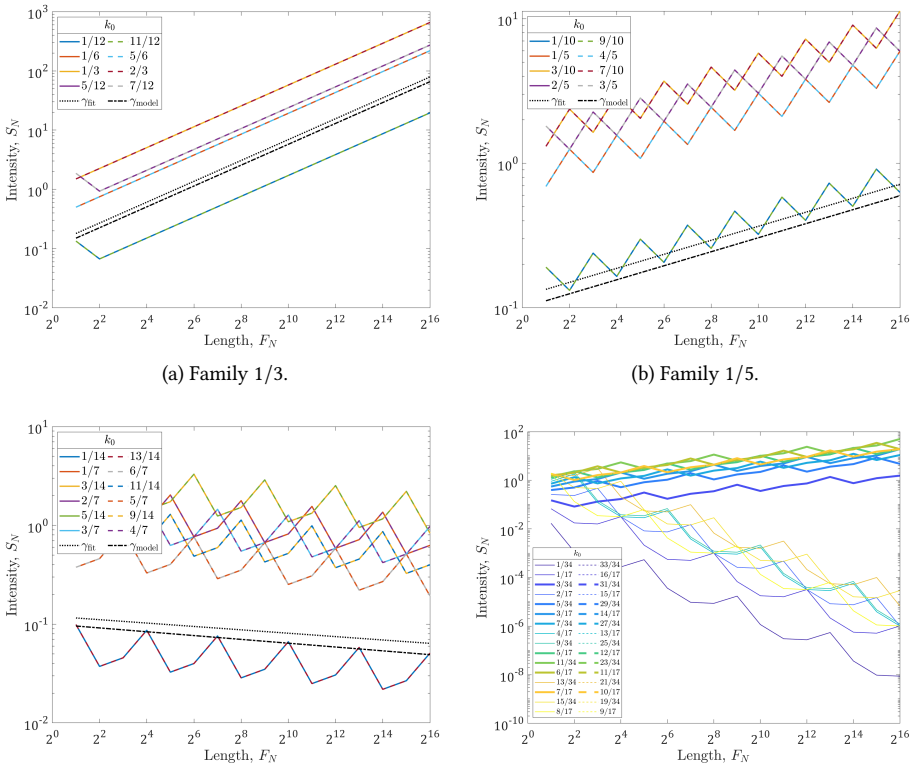

(a) Family $1/3$.

(b) Family $1/5$.

(c) Family $1/7$.

(d) Family $1/17$.

Figure 4.2: Peak intensity $S_N(k_0)$ for different families. Dashed lines indicate lines atop of each other (symmetry around $k = \frac{1}{2}$). Thick and thin lines come to discern positive and negative exponents. Here, $l_A = l_B = 1$ and $s_A = -s_B = 1$. The black dotted and dash-dotted lines represent a fitted γ and modeled one, as in Table 4.1.

Unlike a δ-function, its width is unbound. For $\alpha \geq 1$ (equivalently, $\gamma \leq 0$), there is no singularity in k_0 and thus the spectrum is absolutely continuous.

To avoid infinite power in a single peak, we promote μ into a logistic-like distribution function $\tilde{\mu}$, which behaves as a power-law in the peak's vicinity. A possible solution is

$$\tilde{\mu}(k) - \tilde{\mu}(k_0) = \pm A_\pm \left(1 - \left(1 + |k - k_0|^\alpha\right)^{-1}\right). \tag{4.26}$$

Note that $\tilde{\mu} \to \mu$ of (4.7) when $|k - k_0| \ll 1$. The diffraction spectrum thus reads

$$\tilde{S}(k) = A_\pm \frac{\alpha |k - k_0|^{-\gamma}}{\left(1 + |k - k_0|^\alpha\right)^2}. \tag{4.27}$$

This peak's intensity is $A = A_+ + A_-$; its width is unfortunately unbound (similarly to a Lorentzian).

To remedy the width problem, we choose an erf-like distribution function,

$$\bar{\mu}(k) - \bar{\mu}(k_0) = \pm A_\pm \frac{\sqrt{\pi}}{2} \operatorname{erf}\left(|k - k_0|^\alpha\right), \tag{4.28}$$

so that $\tilde{\mu} \xrightarrow{|k-k_0| \ll 1} \mu$. The diffraction spectrum is thus

$$\bar{S}(k) = A_\pm \alpha \exp\left(-|k - k_0|^{2\alpha}\right) |k - k_0|^{-\gamma}. \tag{4.29}$$

This peak's intensity is $A = (A_+ + A_-)\sqrt{\pi}/2$. The width is given by

$$W_\pm^2 = \frac{\int (k - k_0)^2 \bar{S}(k)\, \mathrm{d}k}{\int \bar{S}(k)\, \mathrm{d}k} = \frac{A_\pm \frac{1}{2} \Gamma\left[\frac{1}{2} + \frac{1}{\alpha}\right]}{A_\pm \frac{\sqrt{\pi}}{2}} = \frac{1}{\sqrt{\pi}} \Gamma\left[\frac{1}{2} + \frac{1}{\alpha}\right], \tag{4.30}$$

so that $W^2 = W_+^2 + W_-^2 = \frac{2}{\sqrt{\pi}} \Gamma\left[\frac{1}{2} + \frac{1}{\alpha}\right]$. However, $W\left(\alpha = 2 - \log_2 3\right) = 1.442$, which is still too high.

In summary, the power law (4.7) infers infinite spectral power. Any logistic function amends the issue, but only some functions lead to a finite peak width. In any case, it is not unique.

4.2.3.2 The Missing Dyadic Component of Thue-Morse

For a substitution tiling with leading eigenvalue λ_*, one expects that the Bragg spectrum is supported on the dyadic values $\mathbb{Z}\left[\lambda_*^{-1}\right]$. It happens for quasiperiodic tilings, for which $\mathbb{Z}\left[\lambda_*^{-1}\right] \cong \mathbb{Z} + \lambda_*^{-1}\mathbb{Z}$; for Period Doubling tiling with $\mathbb{Z}\left[\frac{1}{2}\right]$; and other tilings. In Thue-Morse, however, this is not the case, and the Bragg spectrum is supported on $\mathbb{Z}$ only. We shall explain the reason below.

Let us start with a periodic tiling as in the previous section. Any dyadic component infers wavevectors of the form $k_p = 1/pa$. However,

$$\begin{aligned}
G(k_2) &= \sum_n \mathrm{e}^{2\pi i n/2} = \sum_{n=2r} \mathrm{e}^{2\pi i r} + \sum_{n=2r+1} \mathrm{e}^{2\pi \mathrm{i}\left(r+\frac{1}{2}\right)} = \sum_{n=2r} (1) + \sum_{n=2r+1} (-1) &&= 0, \\
G(k_3) &= \sum_n \mathrm{e}^{2\pi i n/3} = \sum_{n=3r} \mathrm{e}^{2\pi \mathrm{i} 0 + 2\pi i r} + \sum_{n=3r+1} \mathrm{e}^{2\pi \mathrm{i} \frac{1}{3} + 2\pi i r} + \sum_{n=3r+2} \mathrm{e}^{2\pi \mathrm{i} \frac{2}{3} + 2\pi i r} &&= 0, \\
&\vdots
\end{aligned} \tag{4.31}$$

In other words, if a periodic component exists, the wavevectors $k_p = 1/pa$ nullify due to *destructive interference*.

Let us return to Thue-Morse. Note that the tiles A and B come always in pairs: if the tile in the $(2r-1)^{\text{th}}$ position is A, then the tile in $2r^{\text{th}}$ is B, and vice versa. Therefore, $x_{n=2r} = r\,(l_A + l_B)$. In other words, the Thue-Morse tiling admits an underlying periodic tiling with tile length $l_0 \doteq l_A + l_B$. Hence, all the dyadic wavevectors $k = \frac{m}{2^n} \in \mathbb{Z}\left[\frac{1}{2}\right]$ for $n > 1$ must nullify.

4.2.3.3 Thue-Morse with General Parameters

Let us take a general lattice with atomic density (4.18) with general s_n and l_n. Note that by adding an atomic density with a constant $s_i = 1$, we can always rescale s_n to ± 1. Therefore, a general diffraction pattern has an $s_n = \pm 1$ component and an underlying $s_n = 1$ component.

Inspecting the $s_n = \pm 1$ component, we have from (4.19),

$$G_N(k) = \sum_{n=1}^{L_N} s_n\, \mathrm{e}^{2\pi \mathrm{i} k x_n} = \sum_{n=1}^{L_N} \mathrm{e}^{2\pi \mathrm{i}(k x_n + \phi_n)}, \quad s_n = \mathrm{e}^{2\pi \mathrm{i}\phi_n}\,. \tag{4.32}$$

From a previous discussion, $x_{2r} = r\,(l_A + l_B) = r l_0$. Hence

$$G_N(k) = \sum_{n=2r}^{L_N/2} \mathrm{e}^{2\pi \mathrm{i}(k r l_0 + \phi_{2r})} + \sum_{n=2r-1}^{L_N/2} \mathrm{e}^{2\pi \mathrm{i}(k(r-1)l_0 + k l_{2r-1} + \phi_{2r-1})}\,. \tag{4.33}$$

The first sum is exactly the Thue-Morse sequence for the even positions with constant length $l_{A/B} = r l_0$ and with scattering amplitudes $s_{2r} = \mathrm{e}^{2\pi \mathrm{i}\phi_{2r}} = \pm 1$. The second sum is the Thue-Morse sequence for the odd positions with a phase respecting the sequence s_{2r-1}, and positions $\bar{x}_r = (r-1)\,l_0 + l_{2r-1}$ implying tile widths $l_0, l_0 \pm \delta l$, where $\delta l = l_A - l_B$. This corresponds to the tile length of *doublets* on Thue-Morse sequence, which have the same characteristic as the original sequence. Thus, the amplitude is (recursively) the sum of

$$G_N(k; l_A, l_B) = G_{N-1}(k; l_0, l_0) + G^{(2)}_{N-1}(k; l_0, l_0 + \delta l, l_0, l_0 - \delta l)\,. \tag{4.34}$$

4.2.4 Data Analysis

In this section, we perform analysis on experimental data.

4.2.4.1 Check Families

The family of $\frac{1}{5}$ seems to be well shown in the experiments of Axel and Terauchi [75]. Figure 4.3 shows this for $N = 1024$ ($N = 128$ exhibits similar results). Several chosen peaks were matched to the closest rational data of families $\frac{1}{3}$ and $\frac{1}{5}$. The results, which

Table 4.2: Peak comparison of Axel and Terauchi [75] for families $\frac{1}{3}$ and $\frac{1}{5}$ for $N = 1024$ data.

Family 1/3	$\frac{19}{192}$	$\frac{29}{192}$	$\frac{17}{96}$	$\frac{19}{96}$	$\frac{11}{48}$	$\frac{53}{192}$	$\frac{29}{96}$	$\frac{31}{96}$	$\frac{17}{48}$	$\frac{41}{96}$	$\frac{43}{96}$	–	$\frac{53}{96}$	$\frac{55}{96}$	$\frac{29}{48}$	$\frac{65}{96}$	$\frac{67}{96}$	$\frac{71}{96}$	$\frac{79}{96}$
Family 1/5	$\frac{1}{10}$	$\frac{3}{20}$	$\frac{7}{40}$	$\frac{1}{5}$	$\frac{9}{40}$	$\frac{11}{40}$	$\frac{3}{10}$	$\frac{13}{40}$	$\frac{7}{20}$	$\frac{17}{40}$	$\frac{9}{20}$	$\frac{19}{40}$	$\frac{11}{20}$	$\frac{23}{40}$	$\frac{3}{5}$	$\frac{27}{40}$	$\frac{7}{10}$	$\frac{29}{40}$	$\frac{4}{5}$
Diff. × 200	0.21	0.21	0.42	0.42	0.83	0.21	0.42	0.42	0.83	0.42	0.42	–	0.42	0.42	0.83	0.42	0.42	2.92	4.58

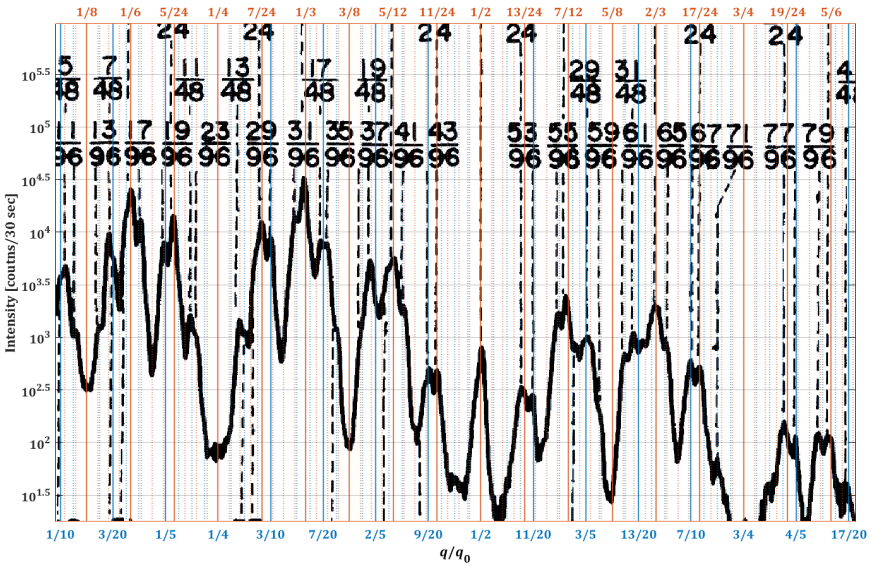

Figure 4.3: Thue-Morse diffraction data of Axel and Terauchi [75]. Grids are superimposed on the original data to better decipher the peaks. Blue grid: family of $\frac{1}{5}$ (divisions: coarse = $\frac{1}{20}$, fine = $\frac{1}{80}$); red grid: family of $\frac{1}{5}$ (divisions: coarse = $\frac{1}{24}$, fine = $\frac{1}{92}$). The x-axis was calibrated using the 0 and $\frac{1}{2}$ peaks.

are presented in Table 4.2, show that most of them differ by less than the $1/200$ error reported in [75]. Therefore, using these experiments to undisputedly prove any family is futile; the results are at most inconclusive.

4.2.5 The Rudin-Shapiro Tiling

The Rudin-Shapiro sequence is famous, since its diffraction spectrum in absolutely continuous [85]. Its Hamiltonian spectrum, however, admits the GLT of Bellissard [27]. It is a good candidate to disprove the Bloch theorem for aperiodic tilings, as it is more distinctive than the Thue-Morse tiling.

4.2.5.1 Definitions

We use the following operative definition.

- Start with B or C (this is relevant in finite tilings).
- Apply the following substitution N times:

$$\begin{aligned} A &\mapsto AC, \quad & C &\mapsto AB, \\ B &\mapsto DC, \quad & D &\mapsto DB. \end{aligned} \tag{4.35}$$

- Decorate the final tiling of order N by

$$\begin{aligned} A &\mapsto 00, \quad & C &\mapsto 01, \\ B &\mapsto 10, \quad & D &\mapsto 11. \end{aligned} \tag{4.36}$$

The resulting tiling in $\tilde{\Gamma} = \{0, 1\}$ alphabet is the Rudin-Shapiro tiling.

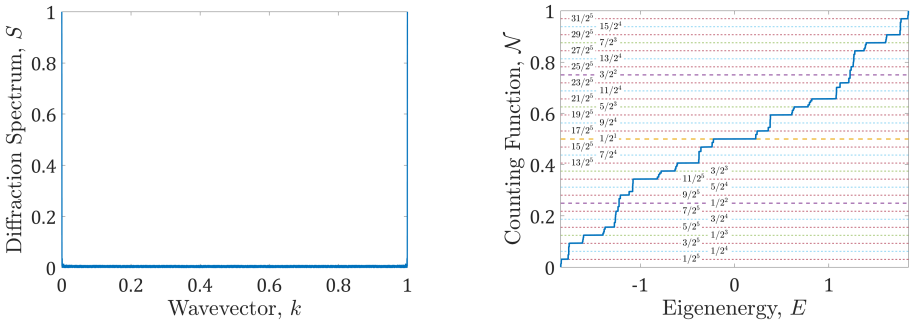

(a) Diffraction. (b) IDOS.

Figure 4.4: The Rudin-Shapiro tiling diffraction and IDOS.

4.2.5.2 Simulation

The potential values used are $v_0 = -v_1 = 1$ for the tight binding simulations; the structure factor calculations employed scattering amplitudes of $s_0 = -s_1 = 1$ with equal tile widths $d_0 = d_1 = 1$. The results are shown in Figure 4.4. Gaps are visible in the counting function, but the structure factor shows no peaks.

The "flat" structure factor in Figure 4.4 is a result of $d_0 = d_1$. Varying the tile widths produced additional features, which are not found to be diffraction peaks of any kind. Although the absolutely continuous structure factor was derived assuming $d_0 = d_1 = 1$ in [85], the general—unequal—case seems to be absolutely continuous as well.

If we wish to not decorate, we apply $v_A = v_C = 1 = -v_B = -v_D$. Note that switching $v_C \leftrightarrow v_D$ will result in a periodic-like spectrum [85].

4.3 Autocorrelation and Diffraction

Recall that the diffraction measure is also given by

$$\int_{-\infty}^{\infty} \mathrm{d}\mu\,(k)\,\mathrm{e}^{2\pi \mathrm{i} k m} = \int_{-\infty}^{\infty} \mathrm{d}k\,S\,(k)\,\mathrm{e}^{2\pi \mathrm{i} k m} = C\,(m)\,, \tag{4.37}$$

with the inverse transform,

$$S\,(k) = \sum_{m\in\mathbb{Z}} C\,(m)\,\mathrm{e}^{-2\pi \mathrm{i} k m} = C\,(0) + 2\sum_{m\geq 1} C\,(m)\cos\,(2\pi k m)\,. \tag{4.38}$$

So the question of calculating diffraction boils down to computing the autocorrelation function $C\,(m)$. We shall do it in the section below.

4.3.1 The Model – Edge of Supertiles

Consider the autocorrelation function

$$C\,(m) = \langle l_n l_{n+m}\rangle\,, \tag{4.39}$$

where l_n are letters (supertiles of size 1) at location n. We demand either of

$$l_n l_{n+m} = \delta_{l_n, l_{n+m}} \qquad = \begin{cases} 1 & \text{if } l_n = l_{n+m}, \\ 0 & \text{otherwise;} \end{cases} \tag{4.40a}$$

$$l_n l_{n+m} = 2\,\delta_{l_n,l_{n+m}} - 1 = \begin{cases} 1 & \text{if } l_n = l_{n+m}, \\ -1 & \text{otherwise.} \end{cases} \tag{4.40b}$$

Therefore, looking on supertiles of size $p = m+1$, we require that the first and the last letters are the same. In other words, we seek supertiles of type $AxxxxxxA$ and $BxxxxxxB$. Taking a probabilistic approach as in [82, 83], the probabilities of these supertiles are given by the proper elements in the leading eigenvector v^*_{m+1} (recall, $v^*_{m+1}A_{m+1} = v^*_{m+1}\lambda^*$ and $\sum_k \left(v^*_{m+1}\right)_k = 1$ in Section 3.1.2.3). Explicitly, using correlation rule (4.40a), we obtain

$$C(m) = \sum_{l_1 = l_{m+1}} \left(v^*_{m+1}\right)_{\overline{l_1 \ldots l_{m+1}}}, \quad \overline{l_1 \ldots l_{m+1}} \in \Gamma_{m+1}. \tag{4.41}$$

Since $l_1 = l_{m+1}$, then $C(m) = C(-m)$ as expected. Also, by this definition, $C(0) = 1$. Note that unlike in the calculation of the GLT, we do not take *all* supertiles $l^{(m+1)} \in \Gamma_{m+1}$, but rather a subset of them.

It is useful to define an autocorrelation without its average,

$$\tilde{C}(m) = C(m) - \bar{C}, \quad \bar{C} = \lim_{M\to\infty} \frac{1}{2M+1} \sum_{m=-M}^{M} C(m), \tag{4.42}$$

so that the peaks at $k \in \mathbb{Z}$ are excluded from its structure factor.

Next, we need to calculate $C(m)$ according to the rule (4.41). It is quite simple to compute it to any order using the standard tools, but we are not aware of a general formula except for simple cases.

4.3.1.1 Examples

Let us inspect a few known examples.

Periodic.

- Here, $v^*_p = \left(\frac{1}{2}, \frac{1}{2}\right)$ to any order p. Additionally, for even p, $l^{(p)} = AB \ldots AB$; and for odd p, $l^{(p)} = AB \ldots ABA$ (similarly for B). Thus, using correlation rule (4.40a), we obtain $C_{\text{per}}(m) = 0$ for an odd m, and $C_{\text{per}}(m) = \frac{1}{2} + \frac{1}{2} = 1$ for an even m. Hence, applying (4.38), we have

$$S_{\text{per}}(k) = \sum_{m' \in \mathbb{Z}} 1 \cdot \mathrm{e}^{-2\pi \mathrm{i} k\, 2m'} = \sum_{n \in \mathbb{Z}} \frac{1}{2} \delta(k - k_n), \tag{4.43}$$

  with $k_n = \frac{1}{2}n$ using Poisson summation formula in the last step.

- There is a strong Gibbs phenomenon.

Thue-Morse.

- Calculating $C_{\text{TM}}(m)$ using correlation rule (4.40a), we have

$$C_{\text{TM}}(m) = 1, \tfrac{1}{3}, \tfrac{1}{3}, \tfrac{2}{3}, \tfrac{1}{3}, \tfrac{1}{2}, \tfrac{2}{3}, \tfrac{1}{2}, \tfrac{1}{3}, \tfrac{7}{12}, \tfrac{1}{2}, \tfrac{5}{12}, \tfrac{2}{3}, \tfrac{5}{12}, \tfrac{1}{2}, \tfrac{7}{12}, \tfrac{1}{3}, \tfrac{13}{24}, \\ \tfrac{7}{12}, \tfrac{11}{24}, \tfrac{1}{2}, \tfrac{13}{24}, \tfrac{5}{12}, \tfrac{11}{24}, \tfrac{2}{3}, \tfrac{11}{24}, \tfrac{5}{12}, \tfrac{13}{24}, \tfrac{1}{2}, \tfrac{11}{24}, \tfrac{7}{12}, \tfrac{13}{24}, \tfrac{1}{3}, \ldots \tag{4.44}$$

Table 4.3: Summary of properties of chosen substitutions.

Name	Rule	$\tau^*(K_0)$	$\check{H}^1(\Omega,\mathbb{Z})$	Diffraction
Periodic	$\begin{cases} A\mapsto AB \\ B\mapsto AB \end{cases}$	$\mathbb{Z}$	$\mathbb{Z}$	Bragg: $k=p$
Fibonacci	$\begin{cases} A\mapsto AB \\ B\mapsto A \end{cases}$	$\mathbb{Z}^2$	$\mathbb{Z}^2$	Bragg: $k=p+q/\tau$
Thue-Morse	$\begin{cases} A\mapsto AB \\ B\mapsto BA \end{cases}$	$\frac{1}{3}\mathbb{Z}\left[\frac{1}{2}\right]$	$\mathbb{Z}\left[\frac{1}{2}\right]\oplus\mathbb{Z}$	SC: $k=\frac{p}{q}\frac{1}{2^n}$ odd q
Period Doubling	$\begin{cases} A\mapsto AB \\ B\mapsto AA \end{cases}$	$\frac{1}{3}\mathbb{Z}\left[\frac{1}{2}\right]$	$\mathbb{Z}\left[\frac{1}{2}\right]\oplus\mathbb{Z}$	Bragg: $k=\frac{m}{2^n}$
Rudin-Shapiro	$\begin{cases} A\mapsto AC \\ B\mapsto DC \\ C\mapsto AB \\ D\mapsto DB \end{cases}$	$\mathbb{Z}\left[\frac{1}{2}\right]$	$\mathbb{Z}\left[\frac{1}{2}\right]\oplus\mathbb{Z}\oplus\mathbb{Z}^2\left[\frac{1}{2}\right]$	AC: no peaks

- We find the following recursive rules for normalization (4.40a)

$$\begin{aligned} C_{\mathrm{TM}}(1)&=\tfrac{1}{3}, \qquad C_{\mathrm{TM}}(2m)=C_{\mathrm{TM}}(m), \\ C_{\mathrm{TM}}(2)&=\tfrac{1}{3}, \quad C_{\mathrm{TM}}(2m+1)=1-\tfrac{1}{2}\left(C_{\mathrm{TM}}(m)+C_{\mathrm{TM}}(m+1)\right). \end{aligned} \tag{4.45a}$$

  Removing Bragg peaks in normalization (4.40b) (cf. [73, Sec. 10.1] and [86]) yields,

$$\begin{aligned} \tilde{C}_{\mathrm{TM}}(1)&=-\tfrac{1}{3}, \qquad \tilde{C}_{\mathrm{TM}}(2m)=\tilde{C}_{\mathrm{TM}}(m), \\ \tilde{C}_{\mathrm{TM}}(2)&=-\tfrac{1}{3}, \quad \tilde{C}_{\mathrm{TM}}(2m+1)=-\tfrac{1}{2}\left(\tilde{C}_{\mathrm{TM}}(m)+\tilde{C}_{\mathrm{TM}}(m+1)\right). \end{aligned} \tag{4.45b}$$

- The structure factor $\tilde{S}(k)$ (with rule (4.40b)) replicates previous results, but with slower convergence (see Figure 4.5).

- The Gibbs phenomenon is less prominent than in the periodic case, since the peaks are singular continuous rather than Bragg ones.

Period Doubling.

- Calculating $C_{\mathrm{PD}}(m)$ using rule (4.40a), we have $C_{\mathrm{PD}}(0)=1$ and

$$C_{\mathrm{PD}}\left(m_{p,q}\right)=1-\tfrac{2}{3}2^{-p}, \quad m_{p,q}=2^p+2^{p+1}q, \quad p\geq 0, q\in\mathbb{Z}. \tag{4.46}$$

  Similar expression exists for the regular Paper Folding tiling [73, 85].

- $S_{\mathrm{PD}}(k)$ exhibits Bragg peaks at $k=2^{-p}$ as expected. Explicit, but tedious, calculation yields (cf. [23, Sec. IV B] and [73, Sec. 9.4.4]),

$$S_{\mathrm{PD}}(k)=\sum_{n\in\mathbb{Z}}\frac{13}{9}\delta(k-n)+\sum_{n\in\mathbb{Z}}\sum_{p\geq 0}\frac{10}{9}\frac{1}{4^p}\delta\left(k-\frac{2n+1}{2^{p+1}}\right). \tag{4.47}$$

The summary of the diffraction spectra and Hamiltonian spectra of some chosen substitutions is given in Table 4.3.

4.3.2 Correspondence between $S(k) = |G(k)|^2$ and $S(k) = \hat{\mathcal{F}}_m[C(m)]$

Let us show the correspondence between both definitions (4.2) and (4.38). We start with $C(m) = \langle s_n s_{n+m} \rangle$ and take rule (4.40b), i.e., assign $s_n = \pm 1$ for tiles A and B, respectively. Taking the Fourier transform of the autocorrelation yields the diffraction [87, 88], namely, $S(k) = \hat{\mathcal{F}}_m[C(m)]$. Thus, we have

$$\begin{aligned} S(k) &= \sum_m \mathrm{e}^{-2\pi \mathrm{i} k m} \sum_n s_n s_{n+m} \\ &= \sum_n s_n \, \mathrm{e}^{2\pi \mathrm{i} k n} \sum_m \mathrm{e}^{-2\pi \mathrm{i} k (m+n)} \, s_{n+m} \\ &= \sum_n s_n \, \mathrm{e}^{2\pi \mathrm{i} k n} \sum_m s_m \, \mathrm{e}^{-2\pi \mathrm{i} k m} = \bar{G}(-k) \, \bar{G}(k), \end{aligned} \tag{4.48}$$

where $\bar{G}(k) = \hat{\mathcal{F}}[\bar{\rho}(x)]$ with $\bar{\rho}(x) = \sum_m s_m \delta(x - x_m)$, $x_m = ma$ and $a = 1$. Since $\bar{\rho}(x)$ is real, then $\bar{G}(-k) = \bar{G}^*(k)$; thus $\bar{S}(k) = \left|\bar{G}(k)\right|^2$ as required. The results of comparison for the Thue-Morse tiling are given in Figure 4.5.

In order to have the proper normalization for an infinite tiling, set

$$\begin{cases} C(m) = \lim\limits_{N \to \infty} \dfrac{1}{N} \displaystyle\sum_{n=0}^{N-1} s_n s_{n+m}, \\ S(k) = \lim\limits_{N \to \infty} \dfrac{1}{N} \left| G_N(k) \right|^2. \end{cases} \tag{4.49}$$

This will not affect the calculation above.

To match with the structure factor using $\rho(x)$ of (4.18) for a tiling-dependent position x_n, we update the definition of the autocorrelation to a continuous one by

$$C(x) = \int \mathrm{d}y \, \rho^*(y) \, \rho(x + y), \tag{4.50}$$

for a general $\rho(x)$ (not necessarily real). Then

$$\begin{aligned} S(k) &= \int \mathrm{d}x \, \mathrm{e}^{-2\pi \mathrm{i} k x} \int \mathrm{d}y \, \rho^*(y) \, \rho(x + y) \\ &= \int \mathrm{d}y \, \rho^*(y) \, \mathrm{e}^{2\pi \mathrm{i} k y} \int \mathrm{d}x \, \mathrm{e}^{-2\pi \mathrm{i} k (x+y)} \, \rho(x + y) \\ &= \int \mathrm{d}y \, \rho^*(y) \, \mathrm{e}^{2\pi \mathrm{i} k y} \int \mathrm{d}x \, \rho(x) \, \mathrm{e}^{-2\pi \mathrm{i} k x} = G^*(k) \, G(k), \end{aligned} \tag{4.51}$$

as required. The proper normalization is now: $\lim_{N \to \infty} \frac{1}{x_N} \int_0^{x_N} \mathrm{d}x$.

4.4 Diffraction $S(k)$ via Cohomology $\check{H}^1(\mathbb{Z})$

In this section, we show how to calculate the diffraction—and windings using a phason—of various tilings from the Čech cohomology (and its Bratteli diagrams).

4.4.1 Diffraction of Period Doubling Tiling

The Period Doubling tiling Čech cohomology is $\check{H}^1_{\mathrm{PD}} \cong \mathbb{Z} \oplus \mathbb{Z}\left[\frac{1}{2}\right]$ [53, 89].

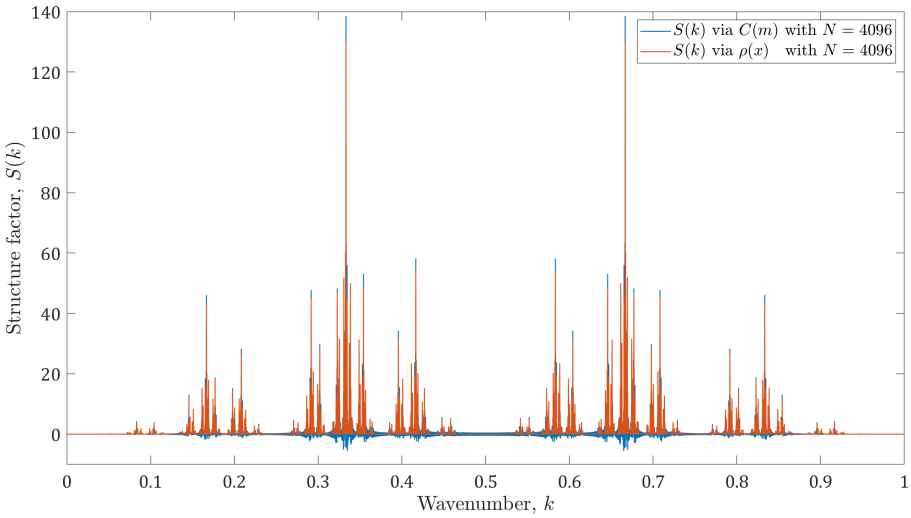

Figure 4.5: Comparison of both diffraction procedures for the Thue-Morse sequence.

4.4.1.1 Observations

The Bratteli diagrams of the Period Doubling tiling exhibit a definite structure at each order $n = F_N = 2^N$ as shown in Figure 4.6. This is to be expected as $\lambda^*_{\mathrm{PD}} = 2$. Excluding $F_N = 1$, the following holds for each order $F_N = 2^N$.

- There are *exactly* 2 cycles (connected in 2 adjacent nodes) of cyclically-permuted 2^N-supertiles each.
- The long cycle is of length F_N; the short one is of length $F_N/2$.
- The cyclic permutation is exactly by 1 tile (the leftmost goes rightwards).
- Each 2^N-supertile in the short 2^N-cycle is *twice* a 2^{N-1}-supertile of the long 2^{N-1}-cycle with the same ordering.
- All supertiles have the same probability of $p_n = v^*_{n,j} = 1/3\, 2^{N-1}$.
- The number of B-s for the 2^N-supertiles is $n^{\mathrm{L}}_B = [F_N/3]$ in the long cycle, and $n^{\mathrm{S}}_B = 2\,[F_N/6]$ in the short one, where $[x]$ is the nearest integer to x.

For example, in order $N = 3$ (length $F_N = 8$), the long and short cycles read (with $A \leftrightarrow 0$ and $B \leftrightarrow 1$),

$$C_3^{\mathrm{long}} = \begin{matrix} 01000101 \\ 10001010 \\ 00010101 \\ 00101010 \\ 01010100 \\ 10101000 \\ 01010001 \\ 10100010 \end{matrix}, \qquad C_3^{\mathrm{short}} = \begin{matrix} 0100\ 0100 \\ 1000\ 1000 \\ 0001\ 0001 \\ 0010\ 0010 \end{matrix}; \tag{4.52a}$$

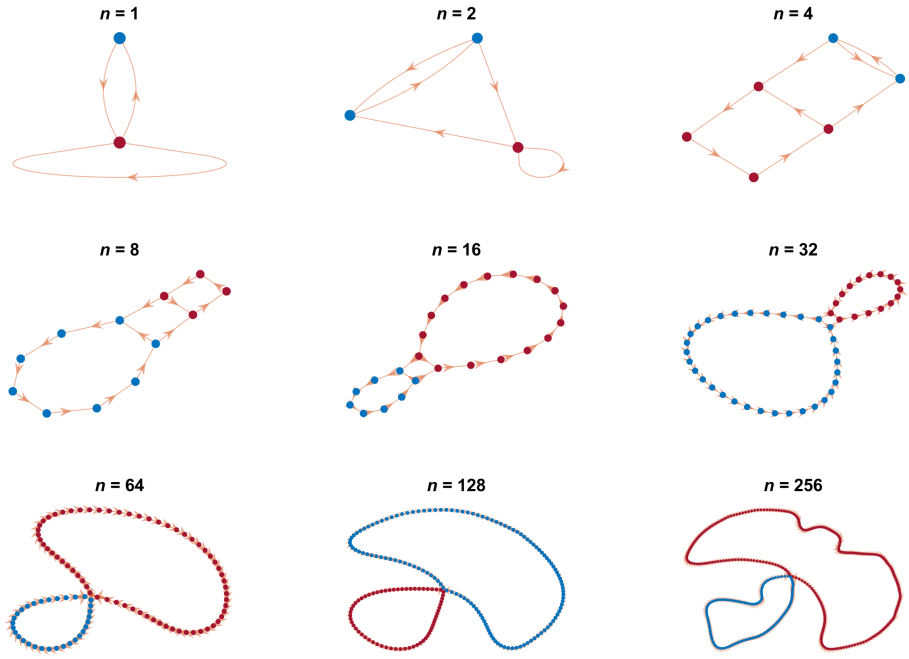

Figure 4.6: Bratteli diagrams of the Period Doubling tiling for orders $n = 2^N$.

and in order $n = 4$,

$$C_2^{\text{long}} = \begin{matrix} 0100 \\ 1000 \\ 0001 \\ 0010 \end{matrix}, \qquad C_2^{\text{short}} = \begin{matrix} 01\ 01 \\ 10\ 10 \end{matrix}. \tag{4.52b}$$

Remark. For $n = 1$, the long cycle is of length 1 ($A \to A$); the short one is of length 0. The probabilities of the tiles are $p_0^A = \frac{2}{3}$ and $p_0^B = \frac{1}{3}$.

4.4.1.2 Phason and Diffraction

The observations above allow us to define a phason $\phi^{(N)}$ for each *long* cycle of order 2^N (the phason for the short cycle is already given by $\phi^{(N-1)}$). In other words, the matrix $C_N^{\text{long}}(n, \phi)$ acts as the $\Sigma_N^1(n, \phi)$ matrix in the Fibonacci case. Let us define it more carefully.

Let $n = 0 \ldots 2^N - 1$ be the location of a 2^N-supertile in the horizontal direction in C_N and let $\phi = \phi^{(N)} = 2\pi\left(0 \ldots 2^N - 1\right)/2^N$ be the vertical one. The phason is well-defined, since there are exactly 2^N supertiles (of order N) in the long cycle. We define the Fourier transform over n,

$$G_N(\xi, \phi) \doteq \hat{\mathcal{F}}_n C_N(n, \phi), \tag{4.53}$$

with

$$S_N(\xi, \phi) \doteq |G_N(\xi, \phi)|^2 / F_N, \tag{4.54a}$$

$$\Theta_N(\xi, \phi) \doteq \arg G_N(\xi, \phi). \tag{4.54b}$$

We also define the Fourier transform in both directions m and ϕ,

$$\Upsilon_N(\xi,\eta) \doteq \hat{\mathcal{F}}_\phi \hat{\mathcal{F}}_n C(n,\phi). \tag{4.55}$$

This allows a scattering experiment as in Dareau et al. [38].

Remark. Recall that $\xi,\eta \in 0\ldots F_N-1$. It is also convenient to use $k=\xi/F_N$ and $q=\eta/F_N$ so that $k,q\in[0,1)$.

Let us calculate it explicitly. Take t_N be a representative 2^N-supertile, let $\mathcal{T}$ be a cyclic permutation over n by a single tile ($\mathcal{T}t_N(n)=t_N(n+1)$), and set $\phi_m=2\pi m/F_N$. Note that C_N can be written as

$$C_N(n,m)=\mathcal{T}^m t_N(n). \tag{4.56}$$

Taking $\omega=\omega_N=\exp(2\pi\mathrm{i}/F_N)$, its Fourier transform reads

$$G_N(\xi,m)=\sum_{n=0}^{F_N-1}\omega^{-n\xi}\mathcal{T}^m t_N(n)=\omega^{m\xi}\sum_{n=0}^{F_N-1}\omega^{-n\xi}t_0(n)=\omega^{m\xi}\tau_N(\xi), \tag{4.57}$$

with τ_N the Fourier transform of t_N. Thus, setting $\theta_N(\xi)=\arg t_N(\xi)$, we obtain

$$S_N(\xi)=|\tau_N(\xi)|^2/F_N, \tag{4.58a}$$

$$\Theta_N(\xi,\phi)=2\pi\xi m/F_N+\theta_N=\phi_m\xi+\theta_N. \tag{4.58b}$$

Additionally,

$$\Upsilon_N(\xi,\eta)=\sum_{m=0}^{F_N-1}\omega^{-m\eta}\omega^{m\xi}\tau_N(\xi)=\tau_N(\xi)F_N\delta_{\xi,\eta}. \tag{4.59}$$

Hence, in a $2d$ diffraction experiment [38], we expect a straight diagonal line.

Remark. One may ask how is that in Fibonacci we have a phason with a definite slope ($\Sigma_1=\mathcal{T}^{s(m)}t_N$), whereas in PD it only moves by 1. The reason is that is Fibonacci permuting cyclically by $c_N^{-1}=F_{N-1}^{-1}$ (modulo $d_N=F_N$) gives $\mathcal{T}^{c_N^{-1}}t_N\simeq t_N$—up to a single adjacent pair of tilings. This leads to a natural definition of $s(m)=m\,c_N^{-1}$ (mod d_N). The Period Doubling tiling, however, is not C&P, and thus there is no "magic" translation. Nonetheless, we can define a simple phason—of walking along the long cycle on the Bratteli graph.

4.4.1.3 Calculating Structure Factor from Bratteli Diagrams

We choose a random 2^N-supertile. It may be either a cyclic permutation of $t^{(1)}=t_N$ or of the double $t^{(2)}=t_{N-1}t_{N-1}$. We denote $A_N=|G_N|$, and denote the contribution of $t^{(1)}$ to it by $A_N^{(1)}$. The contribution of $t^{(2)}$ is *twice* that of $t_{N-1}^{(1)}$ but on *even* ξ *only*:

$$A_N^{(2)}(2\xi)=\begin{cases}2A_{N-1}^{(1)}(\xi) & \text{even } \xi,\\ 0 & \text{odd } \xi.\end{cases}$$

Counting in the probabilities (over all cyclic permutations), $p\left(t^{(1)}\right)=\frac{2}{3}$ and $p\left(t^{(2)}\right)=\frac{1}{3}$. Together,

$$A_N(\xi)=\frac{2}{3}A_N^{(1)}(\xi)+\frac{1}{3}A_N^{(2)}(\xi)=\frac{2}{3}\begin{cases}A_N^{(1)}(\xi)+A_{N-1}^{(1)}(\xi/2) & \text{even } \xi,\\ A_N^{(1)}(\xi) & \text{odd } \xi.\end{cases} \tag{4.60}$$

We assume next:

1. Self similarity. For large N, tilings of consecutive orders seem similar: $A_N^{(1)}(2\xi) \simeq 2A_{N-1}^{(1)}(\xi)$.
2. Equal contribution. Each new contribution of A_N is the same. Explicitly, $A_N^{(1)}(\text{odd } \xi) = A_0$ for all N.

With these assumptions, we obtain for each $\xi_{p,q} = p\,2^q$.

$$A_N\left(\xi_{p,l}\right) = \frac{2}{3}\left(2^{q+1}-1\right)A_0 \xrightarrow{q\gg 1} \frac{4}{3}2^q A_0. \tag{4.61}$$

As $S_N = |A_N|^2 / F_N$, we obtain for each $k_{p,l} = p/2^l = p\,2^{q-N}$,

$$S\left(k_{p,l}\right) = \frac{16}{9}A_0^2\,2^{2(N-l)}2^{-N} \sim 4^{-l}F_N. \tag{4.62}$$

Since $S\left(k_{p,l}\right) \sim F_N$, these are Bragg peaks [23]. The scaling by 4^{-l} retrieves the Period Doubling tiling results (cf. (4.47), [23, Sec. IV B] and [73, Sec. 9.4.4]).

4.4.1.4 Windings

The (discrete) winding number of Θ_N at some ξ is

$$W(\xi) \doteq \frac{1}{F_N}\sum_{m=0}^{F_N-1}\frac{\partial\Theta_N(\xi,m)}{\partial\phi_m} = \xi. \tag{4.63}$$

Hence, for any Bragg peak at $k_{p,l} = p\,2^{-l}$ with an odd p, the winding reads

$$W\left(k_{p,l}\right) = p\,2^{N-l}. \tag{4.64}$$

Since $W\left(k_{p,l}\right) \xrightarrow{N\to\infty} \infty$, it is not well defined. However, we can inspect the finite *relative winding*,

$$\Xi\left(k_{p,l},k_{p',l'}\right) \doteq \frac{W\left(k_{p,l}\right)}{W\left(k_{p',l'}\right)} = \frac{p}{p'}\,2^{l'-l} < \infty. \tag{4.65}$$

4.4.2 Diffraction of Periodic Tilings

In the following section, we show how to calculate the diffraction of a purely periodic tiling. Its Čech cohomology is $\check{H}^1_{\text{Per}} \cong \mathbb{Z}$.

4.4.2.1 Diffraction via Autocorrelation

Suppose there is a tiling with a period R, and suppose, for simplicity, that all the tiles are different. Therefore,

$$C(m) = c_l\,\delta_{m,Rj+l}, \quad 0 \le l < R,\ j \in \mathbb{Z},\ c_0 = 1. \tag{4.66}$$

Hence, the diffraction $S(k) = \sum_m C(m)\,\mathrm{e}^{2\pi\mathrm{i}mk}$ reads,

$$\begin{aligned} S(k) &= \sum_{l=0}^{R-1} c_l \sum_{j\in\mathbb{Z}} \mathrm{e}^{2\pi\mathrm{i}(Rj+l)k} = \sum_{l=0}^{R-1} c_l\,\mathrm{e}^{2\pi\mathrm{i}lk}\sum_{j\in\mathbb{Z}}\mathrm{e}^{2\pi\mathrm{i}Rjk} \\ &= \tilde{c}_R(k)\sum_{p\in\mathbb{Z}}\delta(p-Rk) = \frac{\tilde{c}_R(k)}{R}\sum_{p\in\mathbb{Z}}\delta(k-p/R)\,. \end{aligned} \tag{4.67}$$

4.4.2.2 Diffraction via Bratteli

Let us look on Bratteli diagrams of order $F_N = R^N$. Note that each F_N diagram has a single loop of size R with all supertiles cyclically permuted. Additionally, each F_N-supertile has R copies of F_{N-1} supertile, or equivalently, F_{N-1} copies of R-supertile. We take a representative t_N and denote by $G_N(k)$ the contribution of t_N to the diffraction. Therefore,

$$G_N(k) = \hat{\mathcal{F}}\left[t_R(n) * \sum_{l=0}^{F_{N-1}-1} \delta(n - Rl)\right] = G_R(k) \cdot \sum_{l=0}^{F_{N-1}-1} \mathrm{e}^{2\pi \mathrm{i} Rlk}. \tag{4.68}$$

Taking $N \to \infty$, we have (up to a phase),

$$G(k) = G_R(k) \sum_{p \in \mathbb{Z}} \delta(p - Rk). \tag{4.69}$$

Thus,

$$S(k) = S_R(k) \sum_{p \in \mathbb{Z}} R^{-1} \delta(k - p/R). \tag{4.70}$$

4.4.3 Diffraction of C&P Tilings

After we have shown the diffraction for Period Doubling tilings, we shall calculate it for the C&P ones. Their Čech cohomology is $\check{H}^1_{\mathrm{C\&P}} \cong \mathbb{Z}^2$.

4.4.3.1 Observations

There are several immediate findings we make on C&P Bratteli diagrams.

- There are exactly 2 cycles, Short and Long, for each approximation N.
- The long d_N-cycle consists of d_N cyclically permuted d_N-supertiles. The short cycle is of length d_{N-1} and contains a "rogue" supertile. This is true for any semi-convergent continued fraction[1] $s_N^{(m)}$ with the corresponding lengths $D_{\mathrm{L}} = d_N^{(m)}$ and $D_{\mathrm{S}} = d_{N-1}$.
- The number of B-s in each F_N-supertile corresponds to the slope s such that if $s_N = n_B/F_N$ then $|s - s_N| < 1/F_N$.
- The topology of the cycles may vary.

Next, we make a several assumptions.

1. The two cycles have total probability P_{S} and P_{L}, respectively, for a random node (d_N-supertile) to be inside them, with
$$P_{\mathrm{S}} + P_{\mathrm{L}} = 1. \tag{4.71}$$
2. These probabilities satisfy in the $N \to \infty$ limit
$$P_{\mathrm{S}}/P_{\mathrm{L}} = s. \tag{4.72}$$
Hence
$$P_{\mathrm{L}} = s/(s+1), \qquad P_{\mathrm{S}} = 1/(s+1). \tag{4.73}$$

[1] Let $s = [0; a_1, a_2, \ldots]$ and $s_N = [0; a_1, a_2, \ldots, a_N] = c_N/d_N$ be continued fractions with $\begin{cases} c_N = a_N c_{N-1} + c_{N-2} \\ d_N = a_N d_{N-1} + d_{N-2} \end{cases}$ using $\left(\begin{smallmatrix} c_{-2} & c_{-1} \\ d_{-2} & d_{-1} \end{smallmatrix}\right) = \left(\begin{smallmatrix} 0 & 1 \\ 1 & 0 \end{smallmatrix}\right)$. Then the semi-convergent continued fraction is given by $s_N^{(m)} = [0; a_1, a_2, \ldots, a_{N-1}, m] = c_N^{(m)}/d_N^{(m)}$ with $1 \le m \le a_N$ so that $\begin{cases} c_N^{(m)} = m\, c_{N-1} + c_{N-2} \\ d_N^{(m)} = m\, d_{N-1} + d_{N-2} \end{cases}$.

3. The probabilities of the nodes (supertiles) are *equally divided* in each cycle of length $D_{\mathrm{S}} = d_{N-1}$ and $D_{\mathrm{L}} = d_N$.

4. Nodes contained in both cycles accumulate both probabilities. Explicitly,

$$P_k = \begin{cases} P_{\mathrm{S}}/D_{\mathrm{S}} + P_{\mathrm{L}}/D_{\mathrm{L}} & k \in C_{\mathrm{S}}, C_{\mathrm{L}}, \\ P_{\mathrm{S}}/D_{\mathrm{S}} & k \notin C_{\mathrm{L}}, \\ P_{\mathrm{L}}/D_{\mathrm{L}} & k \notin C_{\mathrm{S}}. \end{cases} \tag{4.74}$$

4.4.3.2 Diffraction for Periodic C&P Tilings

Let us take a periodic tiling from a C&P procedure with slope $s_N = c_N/d_N$. We know that from $n \geq d_N - 1$, there is a single cycle of length d_N. We take such a d_N-supertile representative $t_N\,(m)$. Then, the autocorrelation reads

$$C_N\,(m) \doteq t_N \star t_N, \tag{4.75}$$

and the structure factor

$$S_N\,(\xi) = \hat{\mathcal{F}}\,[t_N \star t_N] = G_N\,(\xi)\,G_N^*\,(\xi)\,. \tag{4.76}$$

Since it is periodic, it has Bragg peaks each $\xi_l = l + d_N p$,

$$S_N\,(\xi) = \sum_{p\in\mathbb{Z}} \sum_{l=0}^{d_N-1} a_l \delta_{\xi, l+d_N p}. \tag{4.77}$$

Now, similarly to the Period Doubling case, we need information about the inner structure of the supertiles. This is the *winding*. In C&P, cyclically permuting t_N by $c_N^{-1} \pmod{d_N}$ results in the same supertile up to a single pair switch. Therefore, we inspect

$$\tilde{C}_N\,(m) = \left(\mathcal{T}^{c_N^{-1}} t_N\right) \star t_N = C_N\,(m) + O\,(1/d_N)\,. \tag{4.78}$$

Its Fourier transform reads,

$$\tilde{S}_N\,(\xi) \simeq \mathrm{e}^{2\pi \mathrm{i} c_N^{-1}\xi}\, G_N\,(\xi)\, G_N^*\,(\xi) = \mathrm{e}^{2\pi \mathrm{i} c_N^{-1}\xi}\, S_N\,(\xi)\,. \tag{4.79}$$

Since S_N and $\tilde{S}_N$ must match, we have a consistency relation,

$$\mathrm{e}^{2\pi \mathrm{i} c_N^{-1}\xi} = 1 \implies \xi_q = c_N q. \tag{4.80}$$

Hence, the Bragg peaks must obey this relation by

$$S_N\,(\xi) = \sum_{p\in\mathbb{Z}} \sum_{q=0}^{d_N-1} a_q \delta_{\xi, c_N q + d_N p}. \tag{4.81}$$

Note that a is dependent on q rather than on l due to $\tilde{S}_N = S_N$. Additionally, $a_q = a_{-q}$ from symmetry considerations.

Remark. Writing the remainder as $R_N\,(m) = \tilde{C}_N\,(m) - C_N\,(m)$, we calculate

$$R_N\,(m) = b \sum_{l\in\mathbb{Z}} \delta_{m, d_N l + c_N^{-1}}, \tag{4.82}$$

so that its Fourier transform reads

$$\Delta_N\,(\xi) = \hat{\mathcal{F}} R_N = b\,\mathrm{e}^{2\pi \mathrm{i} c_N^{-1}\xi} \sum_{l\in\mathbb{Z}} \mathrm{e}^{2\pi \mathrm{i} d_N l \xi} = b\,\mathrm{e}^{2\pi \mathrm{i} c_N^{-1}\xi} \sum_{p\in\mathbb{Z}} \delta_{p, d_N \xi}. \tag{4.83}$$

Therefore,

$$\tilde{S}_N\,(\xi) = \mathrm{e}^{2\pi \mathrm{i} c_N^{-1}\xi} \Big(S_N\,(\xi) + b \sum_{p\in\mathbb{Z}} \delta_{p, d_N \xi} \Big), \tag{4.84}$$

and the difference only amounts to the trivial Bragg peaks ($k_p = \xi_p/d_N \in \mathbb{Z}$).

4.4.3.3 Diffraction for Quasiperiodic C&P Tilings

We take (4.81) and change the variables to $k = \xi/d_N$ obtaining[2]

$$S_N(k) = \sum_{p\in\mathbb{Z}} \sum_{q=0}^{d_N-1} \bar{a}_q \delta(k - (p + s_N q)). \tag{4.85}$$

In each N-approximation of an irrational slope s, we have two cycles implying the approximation is incomplete.

- The long cycle is exactly the periodic approximation of the current order. Permuting cyclically by c_N^{-1} results in a single pair flip.
- The short cycle is a periodic approximation for the previous order. Permuting cyclically by c_{N-1}^{-1} results in at most 2 pair flips: one in the first d_{N-1} tiles, and the other in the rest, if it exists.

Thus, there are two copies of $S_N(k)$ throughout the Bratteli graphs. Hence, we can safely take the limit $N \to \infty$,

$$S(k) = \sum_{p\in\mathbb{Z}} \sum_{q\in\mathbb{Z}} \hat{a}_q \delta(k - (p + sq)). \tag{4.86}$$

4.4.4 Diffraction of the Thue-Morse Tiling

The Thue-Morse tiling does not show Bragg diffraction. Let us examine the Bratteli diagrams and show possible explanations to this.

4.4.4.1 Observations

The Thue-Morse Bratteli diagrams show some structure for two families.

Family 1: length $n = 2^N$ (order N).

- There are two cycles: a small of length n and a large of length $2n$.
- The smaller is inside the larger with two shared nodes.
- The smaller cycle is circularly permuted; the long is not.
- The probability is $2/3n$ for the shared nodes and $1/3n$ for all the others.
- The shared nodes constitute the Thue-Morse sequence built from substitutions.

Family 2: length $n = 2^N + 2^{N-1}$ (order $\frac{3}{2}N$).

- There are five cycles.
- Their topology reminds a driving wheel.
- Only two of these cycles are circularly permuted. They are of size n.
- Each node's probability is either $1/2n$ (if shared between cycles) or $1/4n$ (else).

Other orders do not show any particular structure.

Since there are no cyclic permutations of (almost) all nodes to each order N, we do not expect a Bragg diffraction as we derived in the previous sections. However, seeing that at least *some* cycles are cyclically permuted, we might expect peaks of another characteristic. These happen to be singular-continuous peaks.

[2] The Dirac rather than Kronecker delta notation is used for visual aid only.

4.4.5 Diffraction of Other Tilings

Here we show examples of some tilings and their diffraction.

4.4.5.1 Rudin-Shapiro

The Rudin-Shapiro tiling (see Table 4.3) has an AC diffraction component only [85]. It has some structure for $n = 2^N$. There are 2 main cycles, but they have no particular order nor rule. The main cycles are interconnected by 4 smaller cycles ("ears"), which are cyclically permuted. They consist of ears of order $N - 1$, but permuted between the 4 families.

4.4.5.2 Paper Folding

The Paper Folding tiling diffraction is $\mathbb{D} = \mathbb{D}_2 \doteq \mathbb{Z}\left[\frac{1}{2}\right]$ [85]. Its rule is $A \mapsto AC$, $B \mapsto AD$, $C \mapsto BC$, $D \mapsto BD$; its Čech cohomology is $\check{H}^1 \cong \mathbb{Z} \oplus \mathbb{Z}\left[\frac{1}{2}\right]$. Like the Period Doubling tiling, it has special structure each $n = 2^N$. There are two twice-doubly-interconnected main cycles encompassing *all nodes*. Each main cycle consists of (same) 4 families dividing it in 4 equal parts. Moreover, each main cycle of order N consists of the previous cycles of order $N - 1$.

4.4.5.3 Non-Fibonacci²

The rule is $A \mapsto AAB$, $B \mapsto BA$; its Čech cohomology is $\check{H}^1 \cong \mathbb{Z} \oplus \mathbb{Z}^2$. Its diffraction is unknown; extrapolating from the Fibonacci and Thue-Morse sequences, it most probably has a Bragg component at $k_B = p + q/\tau$ and a SC component on top of that. The Bratteli graphs show a similar characteristic to Thue-Morse each Fibonacci number F_N—that is a single cyclically-permuted cycle among many others, which do not have any particular structure.

4.4.5.4 Period Tripling

This tiling given by $A \mapsto AAB$, $B \mapsto AAA$ producing the Čech cohomology of $\check{H}^1 \cong \mathbb{Z} \oplus \mathbb{Z}\left[\frac{1}{3}\right]$. It is similar to Periodic Doubling with the following differences. The diffraction consists only of Bragg peaks on the triadic $\mathbb{D}_3 \doteq \mathbb{Z}\left[\frac{1}{3}\right]$. The Bratteli diagrams produce on each $n = 3^N$ the same properties as in the Period Doubling case (cf. Sec. 4.4.1.1 with the obvious changes).

The Period Tripling tiling can be generalized to any $r > 1$ ("Period r-ing") so that $A \mapsto A^{r-1}B$, $B \mapsto A^r$ with $\check{H}^1 \cong \mathbb{Z} \oplus \mathbb{Z}\left[\frac{1}{r}\right]$ and a Bragg diffraction component on $\mathbb{D}_r \doteq \mathbb{Z}\left[\frac{1}{r}\right]$. Note that the gap-labeling group has $\mathcal{N} \in \frac{1}{r+1}\mathbb{D}_r \cap [0, 1)$.

It can further be generalized to any rational $t/r \in \mathbb{Q}$ with $1 \leq t < r$ (not necessarily coprime) by $A \mapsto A^{r-t}B^t$, $B \mapsto A^r$. This results in $\check{H}^1 \cong \mathbb{Z}\left[\frac{1}{t}\right] \oplus \mathbb{Z}\left[\frac{1}{r}\right]$ having a gap labeling group $\mathcal{N} \in \frac{1}{r+t}\mathbb{D}_r \cap [0, 1)$. Its diffraction has a Bragg component on $\mathbb{D}_r$ and possibly other components.

Chapter 5

Bloch Theorem

In the previous, sections we have shown that the structure of a quasiperiodic systems contains topological character encoded in its winding. It corresponds exactly to the gap labeling of [27, 90], containing the same information. Therefore, there is some link between the structural and spectral topologies. The most obvious tool to inspect it is the Bloch theorem. In this section, we shall analyze the Bloch theorem for aperiodic tilings.

5.1 Bloch Theorem in Periodic Systems

In periodic systems, the Bloch theorem states that any eigenfunction of a periodic Hamiltonian with period $\boldsymbol{a}$ can be written in the following way [1],

$$\psi_{\boldsymbol{k}}(\boldsymbol{x}) = \mathrm{e}^{\mathrm{i}\boldsymbol{k}\cdot\boldsymbol{x}}\, u_{\boldsymbol{k}}(\boldsymbol{x}), \qquad u_{\boldsymbol{k}}(\boldsymbol{x}+\boldsymbol{a}) = u_{\boldsymbol{k}}(\boldsymbol{x}). \tag{5.1}$$

Here, $u_{\boldsymbol{k}}(\boldsymbol{x})$ is the Bloch function with period $\boldsymbol{a}$. The elementary proof of this theorem exploits the commutativity between the Hamiltonian $\mathcal{H}_{\mathrm{per}}$ and the translation operator $\mathcal{T}^{\boldsymbol{a}}$, namely $\left[\mathcal{H}_{\mathrm{per}}, \mathcal{T}^{\boldsymbol{a}}\right] = 0$. Moreover, the atomic density $\rho_{\mathrm{per}}(\boldsymbol{x})$ is also an eigenstate of the translation operator,

$$\mathcal{T}^{\boldsymbol{a}}\rho_{\mathrm{per}}(\boldsymbol{x}) = \rho_{\mathrm{per}}(\boldsymbol{x}). \tag{5.2}$$

In quasiperiodic systems, however, the translation operator neither commutes with the Hamiltonian nor has the density as its eigenvector. Thus, writing the Bloch theorem naïvely would not work. A different approach is therefore required.

5.2 Bloch Theorem in Cut and Project Tilings

There are many ways to construct quasiperiodic tilings. In this section, we confine ourselves to the Cut and Project (C&P) structures.

5.2.1 Cut and Project – Reminder

The canonical C&P procedure from n to m dimensions is defined as follows [42] (see Section 2.1.1 and Figure 2.1 for a $2d \longrightarrow 1d$ example).

Cut.

1. Start with an n-dimensional space $R = \mathbb{R}^n$.
2. Insert "atoms" on the integer lattice $Z = \mathbb{Z}^n$.
3. Divide R into a *physical space* $E_\parallel$ and an *internal space* $E_\perp$ such that $E_\parallel \oplus E_\perp = R$ and $E_\parallel \cap E_\perp = \{\boldsymbol{c}\}$ with $\boldsymbol{c} \in R$ defined below.
4. To resolve ambiguity for $E_\parallel$, choose an initial location $\boldsymbol{c} \in R$ such that $E_\parallel$ passes through $\boldsymbol{c}$. There is no such requirement for $E_\perp$.

Project.

1. Inspect the hypercube $\mathbb{I}_n = [-0.5, 0.5)^n$.
2. The *window* is its projection on the internal space $W = \pi_\perp(\mathbb{I}_n)$.
3. The *strip* is the product with the physical space $S = W \otimes E_\parallel$.
4. Choose only the points inside the strip $S \cap Z$, and project them onto the physical space, $Y = \pi_\parallel(S \cap Z)$.
5. The *atomic density* is given by $\rho(\boldsymbol{x}) \doteq \rho_{\boldsymbol{c}}(\boldsymbol{x}) = \sum_{\boldsymbol{y} \in Y} \delta(\boldsymbol{x} - \boldsymbol{y})$ with $\boldsymbol{x} \in E_\parallel$. Note the implicit dependence of Y on $\boldsymbol{c}$.

5.2.2 Bloch at Last

We observe that a translation of $\boldsymbol{c}$ in the physical space $E_\parallel$ *does not* change Y nor $\rho_{\boldsymbol{c}}(\boldsymbol{x})$ for all $\boldsymbol{c} \in R$. The density is thus changed only by internal space translations $\mathcal{T}_\perp^{\boldsymbol{b}}$, $\boldsymbol{b} \in E_\perp$, which we have previously identified with the phason. Generally, we can write such translations as

$$\mathcal{S}^{\boldsymbol{b}} \rho_{\boldsymbol{c}}(\boldsymbol{x}) \doteq \rho_{\boldsymbol{c}+\boldsymbol{b}}(\boldsymbol{x}), \qquad \boldsymbol{b} \in E_\perp. \tag{5.3}$$

Note that $\mathcal{S}^{\boldsymbol{b}}$ is not a translation, but rather a *permutation* of the atomic density. Moving the entire length of the hypercube $\mathbb{I}_n$ leaves Y unchanged. Thus, there are fixed points $\boldsymbol{a}$ such that $\forall \boldsymbol{c} \in R$,

$$\mathcal{S}^{\boldsymbol{a}} \rho_{\boldsymbol{c}}(\boldsymbol{x}) = \rho_{\boldsymbol{c}}(\boldsymbol{x}), \qquad \boldsymbol{a} \in E_\perp. \tag{5.4}$$

This reminds the condition (5.2). Explicitly, the operator $\mathcal{S}^{\boldsymbol{b}}$ is given by

$$\mathcal{S}^{\boldsymbol{b}} = \pi_\parallel \circ \mathcal{T}_\perp^{\boldsymbol{b}} \circ \pi_\parallel^{-1}. \tag{5.5}$$

More carefully (since $\pi_\parallel^{-1}$ might not exist), $\mathcal{S}^{\boldsymbol{b}}$ is defined by

$$\mathcal{S}^{\boldsymbol{b}} \circ \pi_\parallel = \pi_\parallel \circ \mathcal{T}_\perp^{\boldsymbol{b}}. \tag{5.6}$$

There are several conditions to be met.

1. We need to specify how $\pi_\parallel$ acts on functions $f(\boldsymbol{r})$, $\boldsymbol{r} \in R$. To resolve ambiguity, we abandon the strip S and project directly on $E_\parallel$ by

$$\pi_\parallel [f(\boldsymbol{r})] = f(\boldsymbol{r} \cap E_\parallel) \doteq f(\boldsymbol{x}), \qquad \boldsymbol{x} \in E_\parallel. \tag{5.7}$$

2. For consistency, the atomic density $\rho_Z(\boldsymbol{r})$ must be redefined to

$$\varrho_W(\boldsymbol{r}) = \rho_Z(\boldsymbol{r}) * W, \tag{5.8}$$

namely, convoluted with the window. Hence, $\rho_Y(\boldsymbol{x}) = \pi_{\parallel}[\varrho_W(\boldsymbol{r})]$.

3. By requiring $f(\boldsymbol{r})$ to be continuous, $\pi_{\parallel}^{-1}$ is well-defined for quasiperiodic sequences by means of cyclic permutations, as described previously. Periodic sequences may leave some ambiguity so that the operators $\mathcal{S}^{\boldsymbol{b}}$ can only be defined by (5.6). This is shown in the following section.

These conditions imply that $\mathcal{S}^{\boldsymbol{b}}$ is well-defined. Hence, we can write the Bloch theorem for quasiperiodic C&P sequences as

$$\begin{aligned} \psi_{\boldsymbol{k}}(\boldsymbol{x}) &= \mathrm{e}^{\mathrm{i}\boldsymbol{k}\cdot\boldsymbol{x}}\, u_{\boldsymbol{k}}(\boldsymbol{x}), \\ \mathcal{S}^{\boldsymbol{a}} u_{\boldsymbol{k}}(\boldsymbol{x}) &= u_{\boldsymbol{k}}(\boldsymbol{x}). \end{aligned} \tag{5.9}$$

Notice that $u_{\boldsymbol{k}}(\boldsymbol{x})$ is *pattern equivariant* (PE), which incorporates the symmetries of the quasiperiodic tiling (see [52, 54] for more details). In customary terms, $u_{\boldsymbol{k}}(\boldsymbol{x})$ is symmetric to *infinite permutations*.

5.2.3 Quasiperiodic (C&P) Hamiltonian

Let us inspect a Hamiltonian in $R = \mathbb{R}^n$, which has a hyper-cubic periodicity of $Z = \mathbb{Z}^n$, namely

$$\mathcal{H}(\boldsymbol{r} + \boldsymbol{m}) = \mathcal{H}(\boldsymbol{r}), \ \boldsymbol{m} \in Z. \tag{5.10}$$

The spectral decomposition of this Hamiltonian is

$$\mathcal{H}(\boldsymbol{r})\, \Psi_{n,\boldsymbol{\kappa}}(\boldsymbol{r}) = E_{n,\boldsymbol{\kappa}} \Psi_{n,\boldsymbol{\kappa}}(\boldsymbol{r}), \tag{5.11}$$

where n is the band index, and $\boldsymbol{\kappa}$ the crystal momentum. Consequently, we can write its Bloch theorem as

$$\begin{aligned} \Psi_{n,\boldsymbol{\kappa}}(\boldsymbol{r}) &= \mathrm{e}^{\mathrm{i}\boldsymbol{\kappa}\cdot\boldsymbol{r}}\, v_{n,\boldsymbol{\kappa}}(\boldsymbol{r}); \\ v_{n,\boldsymbol{\kappa}}(\boldsymbol{r} + \boldsymbol{m}) &= v_{n,\boldsymbol{\kappa}}(\boldsymbol{r}), \quad \boldsymbol{m} \in Z. \end{aligned} \tag{5.12}$$

Applying $\pi_{\parallel}$ on $\Psi_{\boldsymbol{\kappa}}(\boldsymbol{r})$ by

$$\psi_{n,\boldsymbol{k}}(\boldsymbol{x}) = \pi_{\parallel}\left[\Psi_{n,\boldsymbol{\kappa}}(\boldsymbol{r})\right] \tag{5.13}$$

and comparing to (5.9), we obtain the following relations,

$$u_{n,\boldsymbol{k}}(\boldsymbol{x}) = \pi_{\parallel}\left[v_{n,\boldsymbol{\kappa}}(\boldsymbol{r})\right] \tag{5.14a}$$

$$\mathrm{e}^{\mathrm{i}\boldsymbol{k}\cdot\boldsymbol{x}} = \pi_{\parallel}\left[\mathrm{e}^{\mathrm{i}\boldsymbol{\kappa}\cdot\boldsymbol{r}}\right], \tag{5.14b}$$

where $\boldsymbol{k} = \pi_{\parallel}[\boldsymbol{\kappa}]$ with $\boldsymbol{\kappa} = \boldsymbol{k} \oplus \boldsymbol{k}_{\perp}$.

Corollary. *The conditions in (5.9) hold with* $\boldsymbol{a} = \pi_{\perp}[\boldsymbol{m}]$.

By applying $\pi_{\parallel}$ on $\mathcal{H}(\boldsymbol{r})$, we obtain the *quasiperiodic* Hamiltonian

$$\mathcal{H}(\boldsymbol{x}) = \pi_{\parallel}\, \mathcal{H}(\boldsymbol{r})\, \pi_{\parallel}^{\dagger}, \tag{5.15}$$

with $\pi_{\parallel}^{\dagger} = \pi_{\parallel}^{-1}$, so that

$$\mathcal{S}^{\boldsymbol{a}}\, \mathcal{H}(\boldsymbol{x})\, \mathcal{S}^{-\boldsymbol{a}} = \mathcal{H}(\boldsymbol{x}). \tag{5.16}$$

Thus, we write the eigenvalue equation as

$$\mathcal{H}(\boldsymbol{x})\,\psi_{n,\boldsymbol{k}}(\boldsymbol{x}) = E_{n,\boldsymbol{k}}\psi_{n,\boldsymbol{k}}(\boldsymbol{x}), \tag{5.17}$$

where the eigenenergy preserves,

$$E_{n,\boldsymbol{k}} = E_{n,\boldsymbol{\kappa}}. \tag{5.18}$$

The Bloch condition is, therefore, the same as in (5.9)

$$\begin{aligned} \psi_{n,\boldsymbol{k}}(\boldsymbol{x}) &= \mathrm{e}^{\mathrm{i}\boldsymbol{k}\cdot\boldsymbol{x}}\, u_{n,\boldsymbol{k}}(\boldsymbol{x}), \\ \mathcal{S}^{\boldsymbol{a}} u_{n,\boldsymbol{k}}(\boldsymbol{x}) &= u_{n,\boldsymbol{k}}(\boldsymbol{x}). \end{aligned} \tag{5.19}$$

Remark. In a Hamiltonian $\mathcal{H} = -\nabla^2 + V$, the operators $\mathcal{T}^{\boldsymbol{m}}$ in (5.10) and $S^{\boldsymbol{a}}$ in (5.16) act on the *potential* V; equivalently, the Laplacian ∇^2 is indifferent to these operators.

5.2.4 Periodicity and Pattern Equivariance

Let us continue towards pattern equivariance. Since $v(\boldsymbol{r})$ is periodic, it can be written as (omitting the indices n and $\boldsymbol{\kappa}$ for simplicity),

$$v(\boldsymbol{r}) = f(\boldsymbol{r}) * \sum_{\boldsymbol{z}\in Z} \delta(\boldsymbol{r}-\boldsymbol{z}) \doteq f(\boldsymbol{r}) * \rho_Z(\boldsymbol{r}), \tag{5.20}$$

for a (square-integrable) smooth $f(\boldsymbol{r})$ on $\mathbb{I}_n$ with periodic boundary conditions. Now, using $\boldsymbol{r} = \boldsymbol{x} \oplus \boldsymbol{x}_\perp$, both $f(\boldsymbol{r})$ and $\rho_Z(\boldsymbol{r})$ can be (Schmidt) decomposed to

$$f(\boldsymbol{r}) = \textstyle\sum_i f_\parallel^i(\boldsymbol{x}) \cdot f_\perp^i(\boldsymbol{x}_\perp), \qquad \rho_Z(\boldsymbol{r}) = \rho_\parallel(\boldsymbol{x}) \cdot \rho_\perp(\boldsymbol{x}_\perp), \tag{5.21}$$

so that $v(\boldsymbol{r})$ reads

$$\begin{aligned} v(\boldsymbol{r}) &= \textstyle\sum_i \left(f_\parallel^i(\boldsymbol{x}) \cdot f_\perp^i(\boldsymbol{x}_\perp)\right) * \left(\rho_\parallel(\boldsymbol{x}) \cdot \rho_\perp(\boldsymbol{x}_\perp)\right) \\ &= \textstyle\sum_i \left(f_\parallel^i(\boldsymbol{x}) * \rho_\parallel(\boldsymbol{x})\right) \cdot \left(f_\perp^i(\boldsymbol{x}_\perp) * \rho_\perp(\boldsymbol{x}_\perp)\right) \\ &= \textstyle\sum_i f_\parallel^i(\boldsymbol{x}) * \left[\rho_\parallel(\boldsymbol{x}) \cdot \left(f_\perp^i(\boldsymbol{x}_\perp) * \rho_\perp(\boldsymbol{x}_\perp)\right)\right] \\ &\doteq \textstyle\sum_i f_\parallel^i(\boldsymbol{x}) * \varrho_\perp^i(\boldsymbol{r}), \end{aligned} \tag{5.22}$$

where $\varrho_\perp^i(\boldsymbol{r})$ is defined similarly to (5.8). Projecting $v(\boldsymbol{r})$ on $E_\parallel$ one obtains

$$u(\boldsymbol{x}) = \textstyle\sum_i f_\parallel^i(\boldsymbol{x}) * \sum_j w_{ij}\delta(\boldsymbol{x}-\boldsymbol{x}_j). \tag{5.23}$$

Proposition. *If $E_\parallel$ is incommensurate (quasiperiodic), then $f_\perp^i(\boldsymbol{x}_\perp)$ can be inferred uniquely from w_{ij}, since w_{ij} are dense on W. Thus, $\pi_\parallel^{-1}$ is well-defined in this case.*

Corollary. *By the means of (5.5), $\mathcal{S}^{\boldsymbol{a}}$ is well-defined.*

The sum on j gives a weighted atomic density. To accommodate the weight, choose smooth $w^i(\boldsymbol{x})$ such that $w^i(\boldsymbol{x}_j) = w_{ij}$, and define

$$g^i(\boldsymbol{x}) = f_\parallel^i(\boldsymbol{x})\, w^i(\boldsymbol{x}), \tag{5.24}$$

so that for each i,

$$\textstyle\sum_j g^i(\boldsymbol{x}) * \delta(\boldsymbol{x}-\boldsymbol{x}_j) = \sum_j f_\parallel^i(\boldsymbol{x}_j)\, w^i(\boldsymbol{x}_j)$$

$$= \sum_j f_{\parallel}^i (\boldsymbol{x}_j) w_{ij} \tag{5.25}$$
$$= \sum_j f_{\parallel}^i (\boldsymbol{x}) * w_{ij} \delta (\boldsymbol{x} - \boldsymbol{x}_j) .$$

Thus,

$$u (\boldsymbol{x}) = \sum_i g^i (\boldsymbol{x}) * \sum_j \delta (\boldsymbol{x} - \boldsymbol{x}_j)$$
$$\doteq g (\boldsymbol{x}) * \rho (\boldsymbol{x}) . \tag{5.26}$$

Since $f_{\parallel}^i (\boldsymbol{x})$ are smooth (up to boundaries) and compact-supported, so are $g^i (\boldsymbol{x})$. Moreover, a smooth $f (\boldsymbol{r})$ implies a smooth $g (\boldsymbol{x})$.

Corollary. *$u (\boldsymbol{x})$ coincides with the definition of (strongly) PE functions in [54].*

Corollary. *The eigenfunctions (5.9) of quasiperiodic Hamiltonians have PE symmetry.*

5.2.5 Windings Revisited – Fourier Transform of Σ_2

Thus far, when we considered the C&P procedure, we took its rational approximation Σ_1. This gave us relations between different sequences by a discrete phason. We built the phase Θ_N and constructed the winding numbers in a simple algebraic way.

Nevertheless, there are some problems with this approach. The phason is discrete, which is a bit peculiar for a gauge field. Moreover, since it is discrete and can only have d_N value, we cannot distinguish Σ_1 from a periodic structure. Comparing with section 3.1.5, we see that we miss a sequence, as there are $d_N + 1$ sequences of size d_N. We can also see it if we try to reconstruct Σ_1 with $\mathcal{S}^{\boldsymbol{b}}$ described above. When s is irrational, we can never return to the same place, only approximately by $1/d_N$.

To remedy the issue, let us indeed apply the $\mathcal{S}^{\boldsymbol{b}}$ as prescribed. A simpler way is to use the celebrated characteristic function,

$$\Sigma_2 (n, \phi) = \operatorname{sign} [\cos (2\pi n s + \phi) - \cos (\pi s)] . \tag{5.27}$$

Here, $n \in \{0, \dots, d_N - 1\}$ is taken discretely as before, but $\phi \in [0, 2\pi)$ is a *continuous* parameter thus resulting in a different characteristic function. Now, we obtain $d_N + 1$ different sequences, where the frequency of the rogue sequence is $\Delta\phi_{\text{rogue}} < 2\pi/d_N$ (see Section 4.4.3). The results are seen in Figure 5.1.

Next, we can apply the same procedure as in Section 2.2. Take the discrete Fourier transform of Σ_2 with respect to n to have

$$\tilde{G} (\xi, \phi) \doteq \sum_{n=0}^{d_N - 1} \omega^{-\xi n} \Sigma_2 (n, \phi) , \quad \omega = \mathrm{e}^{2\pi \mathrm{i}/d_N} . \tag{5.28}$$

Although we do not any longer have a nice algebraic expression, we can still take the absolute value to have the structure factor

$$\tilde{S} (\xi, \phi) \doteq \left| \tilde{G} (\xi, \phi) \right|^2 , \tag{5.29}$$

which is now *dependent* on ϕ due to the rogue sequence. Similarly, define the phase

$$\tilde{\Theta} (\xi, \phi) \doteq \arg \tilde{G} (\xi, \phi) . \tag{5.30}$$

Both are very similar to the previous $S (\xi)$ and $\Theta (\xi, \phi)$ up to the rogue sequence, as seen in Figure 5.2.

This rogue sequence makes a lot of mess but is extremely important. It is what distinguishes between a periodic and a quasiperiodic sequence, as the former must have all sequences similar. We use Σ_1 only because of its simpler algebraic form, and justify it by the small difference from Σ_2 – smaller than $1/d_N$.

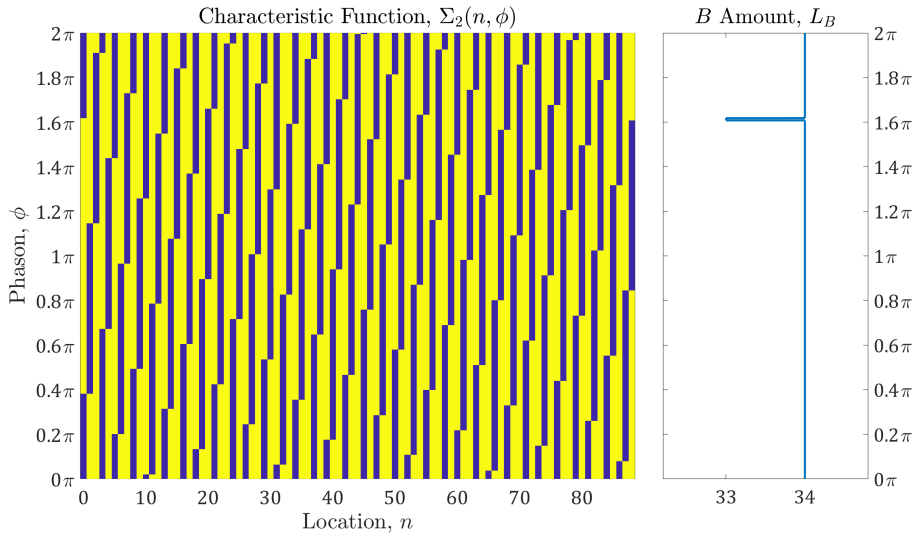

Figure 5.1: The continuous characteristic function Σ_2 for the Fibonacci sequence. Here, $d_N = 89$ points were taken. The amount of B-s in a sequence is indicated in the right graph. Note the location of the rogue sequence.

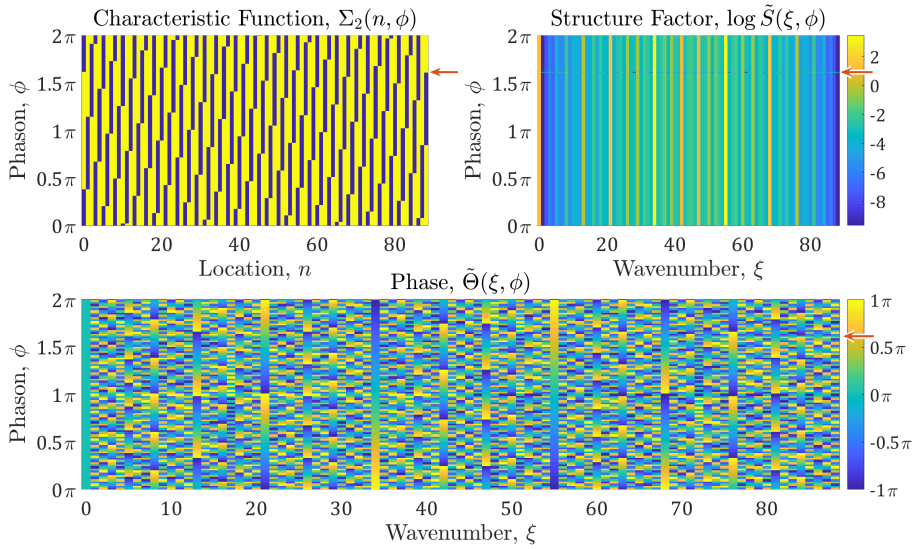

Figure 5.2: The The Fourier transform of Σ_2 for the Fibonacci sequence. Here, $d_N = 89$ points were taken. The rogue sequence is indicated by the red arrow.

5.2.6 Manifestation of Topology

In previous sections, we saw that the topology is revealed through the Fourier transform. Let us take the quasiperiodic $u(\boldsymbol{x})$ from (5.9) with $\mathcal{S}^{\boldsymbol{a}}u(\boldsymbol{x}) = u(\boldsymbol{x})$. Let its Fourier transform be

$$\hat{\mathcal{F}}_{\boldsymbol{x}}[u(\boldsymbol{x})] \doteq \hat{u}_{\boldsymbol{0}}(\boldsymbol{\xi}), \qquad \hat{\mathcal{F}}_{\boldsymbol{x}}\left[\mathcal{S}^{\boldsymbol{b}}u(\boldsymbol{x})\right] \doteq \hat{u}_{\boldsymbol{b}}(\boldsymbol{\xi}). \tag{5.31}$$

By definition of the fixed point $\boldsymbol{a}$, $\hat{u}_{\boldsymbol{0}}(\boldsymbol{\xi}) = \hat{u}_{\boldsymbol{a}}(\boldsymbol{\xi})$. Note that $\boldsymbol{\xi}$ is unitless. The interesting phenomena are when $\boldsymbol{b} \neq \boldsymbol{a}$ (without loss of generality, $\boldsymbol{b} \parallel \boldsymbol{a}$).

Let us inspect, for simplicity, a finite $1d$ system of size d_N. Similarly to the ideas of the previous section,

$$\hat{u}_b(\xi) = \mathrm{e}^{\mathrm{i}\Theta_N(\xi,b)}\,\hat{u}_0(\xi), \tag{5.32}$$

such that

$$\Theta_N(\xi,b) = 2\pi\,\frac{b}{a}\,\frac{\xi}{c_N} \pmod{2\pi}. \tag{5.33}$$

Here, $\phi_b \doteq 2\pi b/a$ takes the role of the phason. Next, let $\nu = \xi/d_N$, and take the limit to obtain

$$\Theta(\nu,b) \doteq \lim_{N\to\infty}\Theta_N(\xi,b) = \phi_b\, s^{-1}\,\nu \pmod{2\pi}, \tag{5.34}$$

so that

$$\hat{u}_b(\nu) = \exp\left(\mathrm{i}\,\phi_b\, s^{-1}\,\nu\right)\hat{u}_0(\nu). \tag{5.35}$$

The previous section's idea of phase winding recurs here. For each $\nu_q = sq$, the phase winds exactly q times as we change ϕ_b from 0 to 2π. More generally, inspect $\nu_{pq} = p + sq$ for wavevectors outside the first quasi-Brillouin zone ($p = 0$). Thus, $\hat{u}_b(\nu)$ is characterized by the two numbers (p,q) given by the Čech cohomology group $\check{H}^1$ on the tiling hull Ω_T [52, 91],

$$\check{H}^1(\Omega_T) \cong \mathbb{Z}^2. \tag{5.36}$$

In order to get extra topological information on the tiling, we inspect the K_0 group. Recall that $\check{H}^1(\Omega_T) \cong K_0(\mathcal{B}_T)$ in the $1d$ case [45, 52, 91, 92] with

$$\tau_*(K_0(\mathcal{B}_T)) \cong (\mathbb{Z} + s\mathbb{Z}) \cap [0,1), \tag{5.37}$$

on $1d$ C&P tilings [52, 91]. Additionally, K-theory gives the gap-labeling theorem [90]. Moreover, since $u(\boldsymbol{x})$ is (strongly) PE, one can build the (strong) PE de Rham cohomology groups on tilings, $H^1_P(T)$ [52, 54]. Furthermore, there exists an equivalence between the de Rham and Čech cohomology groups [52, 54],

$$H^*_P(T) \cong \check{H}^*(\Omega_T, \mathbb{R}). \tag{5.38}$$

Thus, the PE de Rham cohomology classes $\Lambda \in H^1_P(T)$ can be labeled with (p,q) so that $\Lambda = \Lambda_{p,q}$.

Corollary. *The cohomology class of a PE function $u(x) \in \Lambda_{p,q}$ can be inferred from the Fourier transform $\hat{u}(\nu)$.*

Remark. These ideas can be readily generalized to higher dimensions.

5.3 Numerical Validation of the Bloch Theorem

In this section, we show numerical calculations of the above. For simplicity, we project from $2d$ to $1d$, namely, $R = \mathbb{R}^2$ and $Z = \mathbb{Z}^2$.

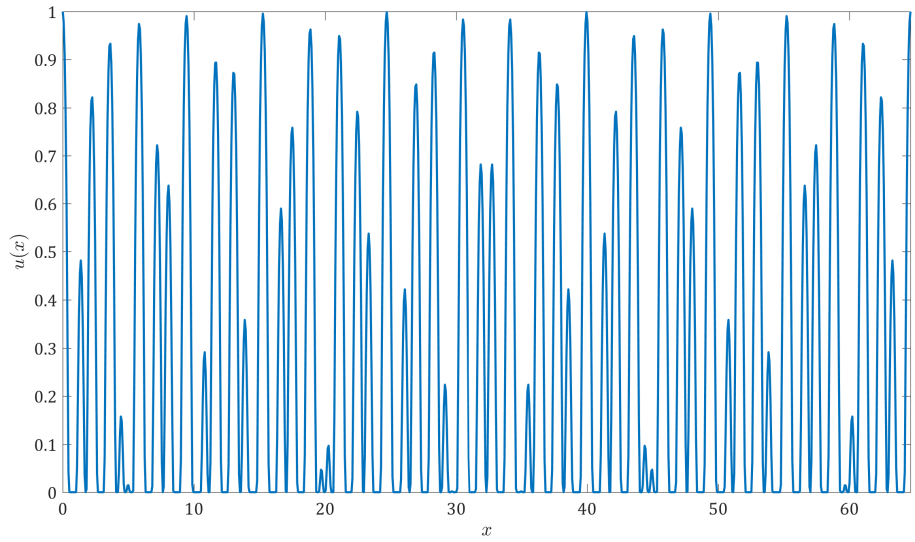

Figure 5.3: The projection $u(x)$ of the top-hat function on $E_{\parallel}$ using the Fibonacci sequence with $\boldsymbol{c} = (0,0)$ corresponding to $d_N = 89$.

5.3.1 The Projected Functions

We consider the top-hat function

$$f_{\mathrm{TH}}(\boldsymbol{r}) = \begin{cases} \exp\left(1 - \frac{1}{1-\alpha^2 r^2}\right) & r = |\boldsymbol{r}| < 1 \\ 0 & \text{otherwise,} \end{cases} \tag{5.39}$$

for $\alpha = 2$, which is smooth and compact-supported on $\mathbb{I}_2$. It realizes the amplitude of the periodic $v(\boldsymbol{r}) = f_{\mathrm{TH}}(\boldsymbol{r}) * \rho_Z(\boldsymbol{r})$. Next, we consider the Fibonacci sequence with a slope of $s = \tau^{-1} = (\sqrt{5}-1)/2$ and initial location of $\boldsymbol{c} = (0,0)$; this defines the physical and internal spaces, and the projection $\pi_{\parallel}$.

The projected function $u(x)$ is shown in Figure 5.3. The dependence of $u_b(x)$ on ϕ_b together with the amplitude and phase of the Fourier transformed $\hat{u}_b(\nu)$ are shown in Figure 5.4. One can readily see that the amplitude $|\hat{u}_b(\nu)|$ is only negligibly dependent on ϕ_b due to finite d_N. However, the phase $\arg \hat{u}_b(\nu)$ shows a winding behavior similar to $\Theta_N(\nu, \phi_\ell)$ in Section 2. Up to numerical errors, they are the same. The difference originates in $\mathcal{S}^{\boldsymbol{a}} u(x)$ that does not revert to $u(x)$ for any finite N (up to s_N).

Corollary. *The discrepancy of* $\arg \hat{u}_b(\nu)$ *from* $\Theta_N(\nu, \phi_\ell)$ *is the deviation from a perfect cyclic permutation. It is a finite-size effect that disappears with* $N \to \infty$.

Remark. One can choose any irrational slope $s \in [0,1]$ instead of Fibonacci; the results are the same.

An interesting phenomenon is observed in simulations. The Gaussian function $f_{\mathrm{Gss}}(\boldsymbol{r}) = \exp\left(-\alpha^2 r^2/2\right)$ with $\alpha = 3$ is not compact-supported. Nonetheless, it does not change significantly the results. Moreover, one can take a Lorentzian function $f_{\mathrm{Lor}}(\boldsymbol{r}) = 1/\left(1+\alpha^2 r^2\right)$ with $\alpha = 5$, or any similar function with long tails (such as the Student t or Poisson distributions), without much numerical penalty. Surprisingly,

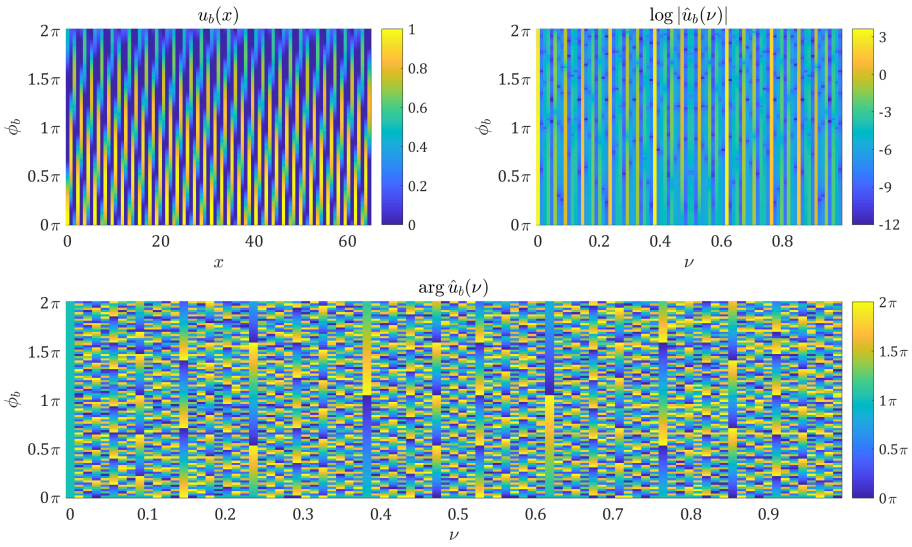

Figure 5.4: The projection $u_b(x)$ of the top-hat function on $E_\parallel$ using the Fibonacci sequence corresponding to $d_N = 89$, and its Fourier transform $\hat{u}_b(\nu)$ on the first quasi-Brillouin zone ($\nu \in [0,1]$) for $\phi_b = 0 \ldots 2\pi$.

even a checker-board function $f_{\mathrm{CB}}(\boldsymbol{r}) = \lfloor 2r_1 \rfloor + \lfloor 2r_2 \rfloor \pmod 2$ with $\boldsymbol{r} = (r_1, r_2)$ shows some results, despite being not smooth. Numerical analysis shows preference for circular-symmetric functions (of $|\boldsymbol{r}| = r$).

Since any function $f(\boldsymbol{r})$ is numerically equivalent to a smooth and compact supported one, the analysis above holds. More carefully, one needs to impose that (a) the envelope of $f(\boldsymbol{r})$ is not too abrupt, and (b) the cut $\pi_\parallel$ does not fall on any problematic (discontinuity) points.

Corollary. *A* weakly *PE function $f(\boldsymbol{r})$ [52] is numerically indistinguishable from a strongly PE one. Therefore, the requirement of compact-support is inessential.*

Proposition. *Any Bloch eigenfunction $\psi(\boldsymbol{x}) = \mathrm{e}^{\mathrm{i}\boldsymbol{k}\cdot\boldsymbol{x}}\, u(\boldsymbol{x})$ of a quasiperiodic Hamiltonian has a (strong or weak) PE $u(\boldsymbol{x})$.*

Remark. The weakly PE de Rham cohomology $H^*_{P,w}(T)$ is not equivalent to the Čech cohomology $\check{H}^*(\Omega_T)$ [52] but rather to a tangential cohomology [93].

5.3.2 Bloch Phase from 2 to 1 Dimensions

Let us reinspect the $2d$ periodic Hamiltonian

$$\mathcal{H}(\boldsymbol{r})\,\Psi_{n,\boldsymbol{\kappa}}(\boldsymbol{r}) = \left(-\boldsymbol{\nabla}^2 + \mathcal{V}(\boldsymbol{r})\right)\Psi_{n,\boldsymbol{\kappa}}(\boldsymbol{r}) = E_{n,\boldsymbol{\kappa}}\Psi_{n,\boldsymbol{\kappa}}(\boldsymbol{r}), \tag{5.40}$$

for $\boldsymbol{r} = (x, y)$ and $\boldsymbol{\nabla}^2 = \partial^2/\partial x^2 + \partial^2/\partial y^2$. In terms of the $\mathbb{Z}^2$-periodic function $v_{n,\boldsymbol{\kappa}}(\boldsymbol{r}) = \mathrm{e}^{-\mathrm{i}\boldsymbol{\kappa}\cdot\boldsymbol{r}}\,\Psi_{n,\boldsymbol{\kappa}}(\boldsymbol{r})$, it is written with periodic boundary conditions as

$$\left(-\boldsymbol{\nabla}^2 - 2\mathrm{i}\boldsymbol{\kappa}\cdot\boldsymbol{\nabla} + \kappa^2 + \mathcal{V}(\boldsymbol{r})\right) v_{n,\boldsymbol{\kappa}}(\boldsymbol{r}) = E_{n,\boldsymbol{\kappa}} v_{n,\boldsymbol{\kappa}}(\boldsymbol{r}) \tag{5.41}$$

Generally, it is a hard problem to solve. However, should we choose a separable potential,

$$\mathcal{V}(\boldsymbol{r}) = \mathcal{V}_x(x) + \mathcal{V}_y(y), \tag{5.42}$$

the Hamiltonian becomes separable as well,

$$\mathcal{H}(\boldsymbol{r}) = \mathcal{H}(x) + \mathcal{H}(y) = \left(-\frac{\partial^2}{\partial x^2} + \mathcal{V}_x(x)\right) + \left(-\frac{\partial^2}{\partial y^2} + \mathcal{V}_y(y)\right). \tag{5.43}$$

Thus, we are left to solve two $1d$ Hamiltonians with periodic boundary conditions,

$$\left(-\frac{\partial^2}{\partial q^2} - 2\mathrm{i}\kappa_q\frac{\partial}{\partial q} + \kappa_q^2 + \mathcal{V}_q(x)\right) v_{n_q,\kappa_q}(q) = E_{n_q\kappa_q} v_{n_q,\kappa_q}(q), \tag{5.44}$$

with $q = \{x, y\}$ so that

$$\begin{cases} v_{n,\boldsymbol{\kappa}}(\boldsymbol{r}) = v_{n_x,\kappa_x}(x)\, v_{n_y,\kappa_y}(y), & n = n_x + n_y, \\ E_{n,\boldsymbol{\kappa}} = E_{n_x,\kappa_x} + E_{n_y,\kappa_y}, & \boldsymbol{\kappa} = (\kappa_x, \kappa_y). \end{cases} \tag{5.45}$$

Simplifying even further, we choose $\mathcal{V}_x = \mathcal{V}_y \doteq \mathcal{V}_0$. Thus, we need to solve only a *single* $1d$ Hamiltonian, but we have an energy degeneracy of $g_n = n + 1$.

We can now project the $2d$ periodic eigenfunctions to the quasiperiodic axis $\hat{z}$ (using $\pi_{\|}$ of the previous sections) to obtain $u_{n,k}$. Since we work in a finite approximation of order N, the length of this axis, L_z is also finite. A short calculation yields,

$$L_z = \sqrt{\left(L_A^N\right)^2 + \left(L_B^N\right)^2} = \sqrt{(d_N - c_N)^2 + c_N^2} \simeq d_N\sqrt{(1-s)^2 + s^2}. \tag{5.46}$$

5.4 Bloch Theorem for General Tilings

The diffraction pattern Bragg peaks locations were thought to be inferred from the Čech cohomology $\check{H}^1(\Omega_T)$ by the Ruelle-Sullivan map $C_\mu : \check{H}^1(\Omega_T) \to \mathbb{R}$ [89, 94]. However, as careful definition of a trace $\tau_*^{\check{H}} : \check{H}^1 \to \mathbb{R}$ is enough [58]. The gap-labeling theorem provides a similar mapping for spectral gaps $\tau_*^K : K_0(\mathcal{B}_T) \to \mathbb{R}$ [90, 92].

In general and in all dimensions (given an invariant transverse measure), there is a natural map $K_0(\mathcal{B}_T) \to \check{H}^d(\Omega_T, \mathbb{R})$. If $d \leq 3$, then this map factors through to give a map $K_0(\mathcal{B}_T) \to \check{H}^d(\Omega_T, \mathbb{Z})$ and this map is onto. If $d = 1$, then the map $K_0(\mathcal{B}_T) \to \check{H}^1(\Omega_T, \mathbb{Z})$ is an isomorphism [58]. Together, one has the following commutative diagram,

$$\begin{array}{ccc} \check{H}^1(\Omega_T) & \xleftarrow{\cong} & K_0(\mathcal{B}_T) \\ \Big\downarrow{\scriptstyle \tau_*^{\check{H}}} & & \Big\downarrow{\scriptstyle \tau_*^K} \\ \mathbb{R} & \xleftrightarrow{\quad\mathrm{id}\quad} & \mathbb{R} \end{array} \tag{5.47}$$

The equivalence of the last row—between the images of $\tau_*^{\check{H}}$ and τ_*^K—is the Bloch theorem from the mathematical point of view [58]. It is valid in C&P tilings, but in others the correspondence between $\tau_*^{\check{H}}(\check{H}^1)$ and diffraction peaks is not clear. In the following, we show this claim.

Theorem 5.1 (Generalized Bloch Theorem). *For finite local complexity tilings [52] with finitely many tile orientations, the diagram (5.47) commutes [58].*

5.4.1 The Role of the Čech Cohomology $\check{H}^1$

Let us inspect the C&P sequences in $1d$. Recall the Bragg peaks location given by

$$k_{p,q} = k_0 \left(p + qs^{-1}\right), \quad k_0 = 2\pi/l, \tag{5.48}$$

with d a normalization constant. For Pisot substitution sequences $l = \bar{l}/(\lambda_1 - \lambda_2)$, where $\bar{l} = l_a\rho_a + l_b\rho_b$ is the mean length of the sequence and $s = f(\lambda_1)$.

Let us inspect this condition from another perspective,

$$k_{p,q} = (p, q) \cdot (k_0, k_0/s) \doteq \mathbf{\Lambda} \cdot \boldsymbol{G}. \tag{5.49}$$

Here we identify $\mathbf{\Lambda} = (p, q)$ with the Miller indices [1], and $\boldsymbol{G} = (k_0, k_0/s)$ with the reciprocal-lattice vectors. Observe that since

$$\mathbf{\Lambda} \in \mathbb{Z}^2 \cong \check{H}^1(\Omega), \tag{5.50}$$

we have the following.

Corollary. *The Čech cohomology $\check{H}^1(\Omega)$ gives the Miller indices of the Bragg peaks $\mathbf{\Lambda}$, and the trace $\tau_*^{\check{H}}$ projects them on the reciprocal-lattice vectors $\boldsymbol{G}$.*

We can therefore rephrase (5.47) for quasiperiodic tilings to

$$\begin{array}{ccc} \mathbb{Z}^2 \cong \check{H}^1(\Omega_{\text{C\&P}}) & \xleftarrow{\cong} & K_0(\mathcal{B}_{\text{C\&P}}) \\ \Big\downarrow{\scriptstyle \tau_*^{\check{H}}} & & \Big\downarrow{\scriptstyle \tau_*^{K}} \\ \mathbb{Z} + \mathbb{Z}\rho_B & \xleftarrow{\text{id}} & \mathbb{Z} + \mathbb{Z}\rho_B \pmod 1 \end{array} \tag{5.51}$$

where $\rho_B = s$ for C&P tilings and $\rho_B = v_B^*$ for substitutions.

Remark. Above $1d$ the situation is more involved. For instance, the Penrose tiling, which is $5d \to 2d$, has $\check{H}^2(\Omega) = \mathbb{Z}^8$, $\check{H}^1(\Omega) = \mathbb{Z}^5$ and $\check{H}^0(\Omega) = \mathbb{Z}$. However, for $2d$ tilings, $K_0(\mathcal{B}) \cong \check{H}^2(\Omega) \oplus \check{H}^0(\Omega)$ and $K_1(\mathcal{B}) \cong \check{H}^1(\Omega)$ (see [45]). Thus, the commutative diagram (5.47) has to be updated correspondingly.

The commutative diagram above is not yet the end of the story. We saw that we can associate a structural phase $\Theta(\xi, \phi)$ to the partial cohomologies $H^1(\Gamma_N)$. Each structural phase gave, in turn, an integer winding number with respect to the phason $\mathcal{W}_\phi[\Theta(\xi, \phi)]$. Similarly, we used the chiral phase $\alpha(k, \phi)$ to construct winding numbers to the gaps $\mathcal{W}_\phi[\alpha(k, \phi)]$. This additional topological information is presented only in quasiperiodic structures, since we the limit is well-defined. The new—generalized—diagram reads

$$\begin{array}{ccccc} \mathbb{Z} \cong \mathcal{W}_\phi[\Theta(\xi,\phi)] & & \xleftarrow{\overset{!}{\cong}} & & \mathcal{W}_\phi[\alpha(k,\phi)] \cong \mathbb{Z} \\ \uparrow & & & & \uparrow \\ \mathbb{Z}^2 \cong \check{H}^1(\Omega_{\text{C\&P}}, \mathbb{Z}) & & \xleftarrow{\psi} & & K_0(\mathcal{B}_{\text{C\&P}}) \cong \mathbb{Z} \oplus \mathbb{Z} \\ \Big\downarrow{\scriptstyle \tau_*^{\check{H}}} & & & & \Big\downarrow{\scriptstyle \tau_*^{K}} \\ \mathbb{Z} \oplus s\mathbb{Z} & & \xleftarrow{=} & & \mathbb{Z} \oplus s\mathbb{Z} \end{array} \tag{5.52}$$

This is the "generalized Bloch theorem" for C&P tilings. Note that since the diagram is commutative, we can infer GLT from $\check{H}^1(\Omega)$.

Corollary. *All topological numbers can be inferred from the Čech cohomology $\check{H}^1(\Omega)$. It is therefore the preferred topological invariant for aperiodic tilings.*

5.4.2 Non-C&P Sequences

We begin our analysis with the following observation. Since the vectors $\boldsymbol{G}$ span the Bragg peaks space, then $\pi^{-1}(G)$ spans the corresponding Bragg hyperspace for the original $R = \mathbb{R}^n$. But there are exactly n spanning vectors, which must much those of G. Formally, we have the following.

Proposition. *In 1d C&P sequences [65],*

$$\dim G = \operatorname{rank} \check{H}^1(\Omega) = \operatorname{rank} R = n. \tag{5.53}$$

The above proposition has an immediate consequence in identifying non-C&P sequences. If $\check{H}^1(\Omega) \ncong \mathbb{Z}^n$, such as σ_3 (see Table 3.3), then it needs an infinite number of eigenvectors to span itself. Thus, its rank is also infinite, and it cannot be C&P. The converse is not necessarily true (cf. Marginal sequence in Table 3.3 or σ_{30} in Table 3.4).

Next, we find the enumeration of $\check{H}^1(\Omega)$ in non-C&P sequences. Take, for example, the Thue-Morse sequence with $\check{H}^1(\Omega) = \mathbb{Z} \oplus \mathbb{Z}\left[\frac{1}{2}\right]$ such that $\left(n, m/2^N\right) = \Lambda_N \in \check{H}^1(\Omega)$. Then, the cochain represented by Λ_N evaluates to m every 2^N tiles at the N^{th} supertile of size $F_N = 2^N$ [52, Sec. 5.4]; the additional $\mathbb{Z}$ term describes the combinatorics between the supertiles [52, Sec. 6.4].

Now, consider the atomic diffraction spectrum as in (2.23). The Bragg peak locations of the Thue-Morse sequence are given by [23, 84] (see Section 4.2)

$$k^{\text{TM}}_{n,m,N} = 2\pi \frac{m}{n} 2^{-N}, \qquad n, m, N \in \mathbb{Z} \text{ for some odd } n. \tag{5.54}$$

Here, we identify the $\mathbb{Z}\left[\frac{1}{2}\right]$ part as the group describing an infinite number of peaks (cf. periodic sequences); the $\mathbb{Z}$ part is an additional degree of freedom given to the families $\tilde{\Lambda} \in \mathbb{Z}\left[\frac{1}{2}\right]$. Note the the K_0 group does not have this degree of freedom, as $\tau_*\left(K_0\left(\mathcal{B}_{\text{TM}}\right)\right) \cong \frac{1}{3}\mathbb{Z}\left[\frac{1}{2}\right]$ (see Table 3.3).

Next, inspect the *difference* in the diffraction spectrum between C&P and non-C&P sequences having the same occurrence matrix M_1, such as σ_6 and σ_4 of the Fibonacci² clan presented in Table 3.4. Here, the Čech cohomology groups are

$$\check{H}^1\left(\Omega_{\sigma_6}\right) \cong \mathbb{Z}^2, \qquad \check{H}^1\left(\Omega_{\sigma_4}\right) \cong \mathbb{Z} \oplus \mathbb{Z}^2. \tag{5.55}$$

Both sequences exhibit Bragg peaks, but σ_4 has much richer structure than σ_6, and contains singularly-continuous peaks. The latter, having $\check{H}^1_{\sigma_6} \cong \mathbb{Z}^2 \ni (p, q)$, needs only the 2 numbers (p, q) to enumerate the Bragg peaks,

$$\tau^{\check{H}}_*\left(\check{H}^1\left(\Omega_{\sigma_6}\right)\right) \doteq k^{\sigma_6}_{p,q} = k_0\left(p + q\tau^2\right), \tag{5.56}$$

with k_0 a normalization wavevector. The non-C&P σ_4 with $\check{H}^1 \cong \mathbb{Z} \oplus \mathbb{Z}^2 \ni (n; p, q)$ needs at least 3 integral numbers for enumeration. In this case, the Bragg peak location are known only for the $n = 0$ case,

$$\tau^{\check{H}}_*\left(\check{H}^1\left(\Omega_{\sigma_4}\right) \mid n = 0\right) \doteq k^{\sigma_4}_{0,p,q} = k_0\left(p + q\tau^2\right). \tag{5.57}$$

These results are presented in Figure 5.5.

The association of the $\check{H}^1(\Omega)$ elements with the tiling enumeration leads to their identification with *Miller indices* as in the C&P case. Note that there is an *infinite number* of reciprocal lattice vectors, and thus Bragg peaks are not assured to exist. Similar considerations exist for the gap-labeling group $\tau^K_*\left(K_0\left(\mathcal{B}\right)\right)$.

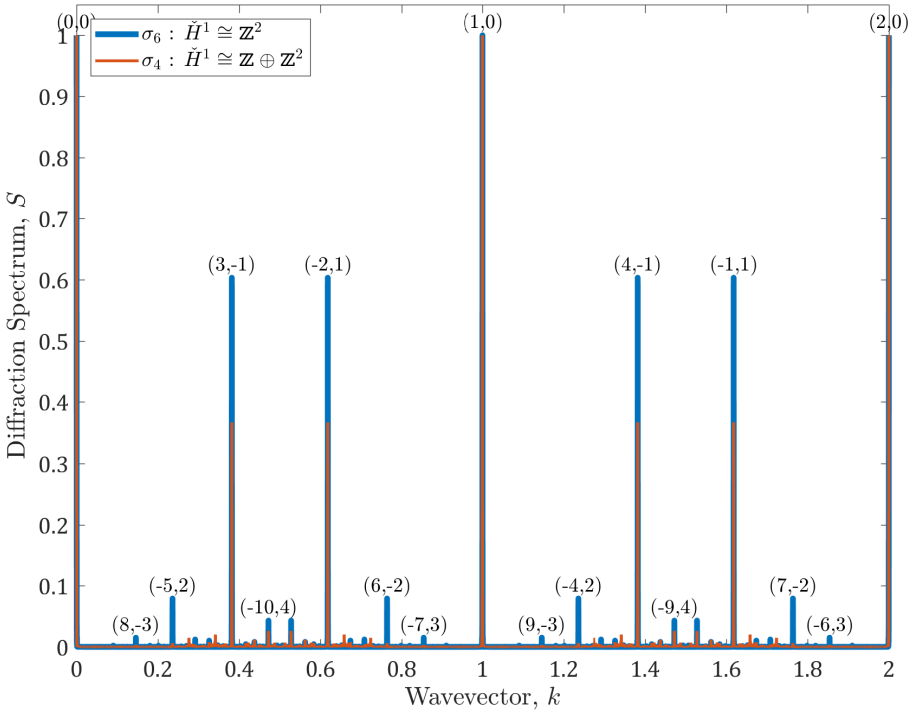

Figure 5.5: Diffraction spectrum of the Fibonacci² substitutions σ_6 (blue) and σ_4 (red). The enumeration of selected peaks in σ_6 is shown.

Claim. The K_0 group is not a good candidate to identify quasiperiodic sequences. Take, for instance, σ_{29} and σ_{26} from Table 3.4. They both have

$$\tau_*^K\left(K_0\left(\mathcal{B}_{\sigma_{29}}\right)\right) = \tau_*^K\left(K_0\left(\mathcal{B}_{\sigma_{26}}\right)\right) \cong \frac{1}{2}\left(\mathbb{Z} + \tau^3\mathbb{Z}\right), \tag{5.58}$$

but σ_{26} is C&P while σ_{26} is not, as seen from their $\check{H}^1$.

Remark. The different families in Table 3.4 mean that the enumeration is identical for sequences in the *same family*. However, in different families, such as σ_{26} and σ_{30}, the enumeration would be different even though $\check{H}^1(\Omega)$ is the same. This is similar to the case of two different sequences, such as Fibonacci and Silver with $H^1(\Omega) \cong \mathbb{Z}^2$.

5.4.3 Topological Bloch Theorem for Tilings

Let us clarify the content of Theorem 5.1 and its conditions of applicability. Recall the Thue-Morse aperiodic tiling (Section 4.2). It is not a C&P quasicrystal, yet it is a Pisot substitution. The possible values of $\mathcal{N}_{\text{gap}}$ are obtained from the gap labeling group $\tau_*^K\left(K_0\left(\mathcal{B}_{\text{TM}}\right)\right)$. This is to be compared to the diffraction spectrum composed of Bragg peaks (PP) and of a SC broad range contribution which does not appear in the cohomology $\tau_*^{\check{H}}\left(\check{H}^1\left(\Omega_{\text{TM}}\right)\right) = \frac{1}{3}\mathbb{Z}\left[\frac{1}{2}\right]$. This lack of equivalence between diffraction and (Laplacian) spectral data is not a limitation of Theorem 5.1, since the Thue-Morse tiling abides its conditions of applicability. It is the expression of a discrepancy between

Table 5.1: Summary of structural and spectral features applied to main representatives of $1d$ tilings. For each of them, we have indicated the Čech cohomology $\check{H}^1(\Omega_T)$, the nature of the diffraction spectrum, pure-point (PP), absolutely continuous (AC) and singular continuous (SC). Theorem 5.1 applies to all cases so that the cohomology trace $\tau_*^{\check{H}}\big(\check{H}^1(\Omega_T)\big)$ is calculated using the trace of the $K_0(\mathcal{B})$ group. The spectral gaps are taken modulo 1. Here, τ is the golden ratio with $\rho_b = 1-\tau^{-1}$, and $n, p, q, m, N \in \mathbb{Z}$.

Family	$\check{H}^1(\Omega_T)$	Diffraction peaks		$\tau_*^{\check{H}}\big(\check{H}^1(\Omega_T)\big)$	Spectral Gaps
Periodic	$\mathbb{Z}$	$k_n = n$	PP	$\mathbb{Z}$	$\mathcal{N} = \text{const}$
Fibonacci	$\mathbb{Z}^2$	$k_{p,q} = p + q/\tau$	PP	$\mathbb{Z} + \tau^{-1}\mathbb{Z}$	$\mathcal{N}_q = q/\tau$
Thue-Morse	$\mathbb{Z} \oplus \mathbb{Z}\left[\frac{1}{2}\right]$	$k_{n,m,N} = \frac{1}{2n+1}\,\frac{m}{2^N}$	SC+PP	$\frac{1}{3}\,\mathbb{Z}\left[\frac{1}{2}\right]$	$\mathcal{N}_{m,N} = \frac{1}{3}\,\frac{m}{2^N}$
Period Doubling	$\mathbb{Z} \oplus \mathbb{Z}\left[\frac{1}{2}\right]$	$k_{m,N} = \frac{m}{2^N}$	PP	$\frac{1}{3}\,\mathbb{Z}\left[\frac{1}{2}\right]$	$\mathcal{N}_{m,N} = \frac{1}{3}\,\frac{m}{2^N}$
Rudin-Shapiro	$\mathbb{Z} \oplus \mathbb{Z}\left[\frac{1}{2}\right] \oplus \mathbb{Z}^2\left[\frac{1}{2}\right]$	N/A	AC	$\mathbb{Z}\left[\frac{1}{2}\right]$	$\mathcal{N}_{m,N} = \frac{m}{2^N}$

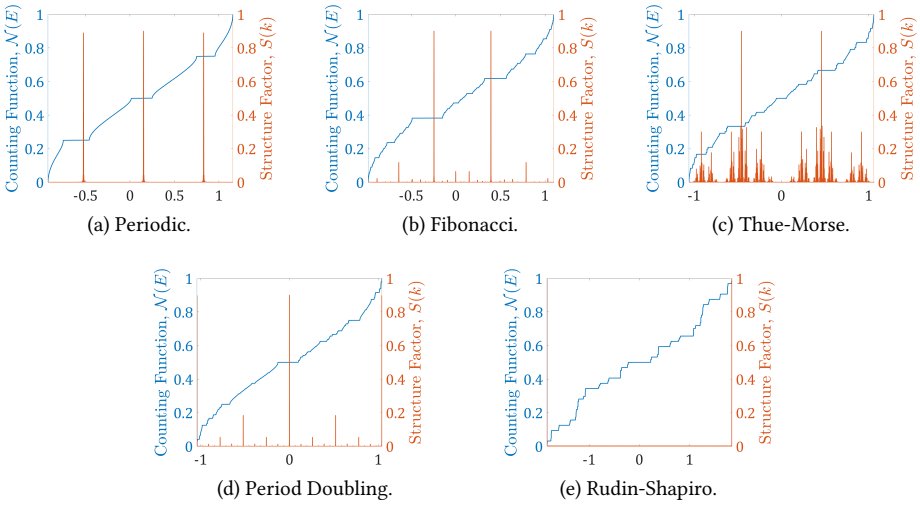

(a) Periodic. (b) Fibonacci. (c) Thue-Morse.

(d) Period Doubling. (e) Rudin-Shapiro.

Figure 5.6: Comparison between diffraction and spectral data for the five representative families of one-dimensional tilings considered previously and to which Theorem 5.1 applies. For the periodic (a), quasiperiodic (b) and aperiodic (limit-quasiperiodic) (d) tilings, there is a direct correspondence between the two sets of data. This can be viewed as an extension of the Bloch theorem. Note that for these three cases, the diffraction spectrum is PP, a result to be contrasted with the non-quasiperiodic Pisot Thue-Morse (c) and the aperiodic Rudin-Shapiro (e) tilings for which the diffraction spectrum is respectively SC and AC, while the spectral counting function accounts for infinitely countable gaps well described by the GLT.

$\tau_*^{\check{H}}\left(\check{H}^1\left(\Omega,\mathbb{Z}\right)\right)$ and the structure factor $S\left(k\right)$ which contains additional information not accessible from the cohomology description.

Furthermore, the aforementioned lack of equivalence is unrelated to the lack of periodicity or quasiperiodicity (e.g. Period Doubling tiling) but rather a consequence of the nature of the diffraction spectrum, a quantity which, unlike spectral data, is sensitive to both local symmetries of the tiles, a condition of applicability of Theorem 5.1, and to long-range correlations driven, e.g., by the order of the letters (immaterial for periodic or C&P quasicrystals). For instance, the Rudin-Shapiro tiling has an absolutely continuous and structureless diffraction spectrum, but a fractal spectral gap distribution well accounted by $\tau_*^{\check{H}}\left(\check{H}^1\left(\Omega_{\mathrm{RS}}\right)\right)=\mathbb{Z}\left[\frac{1}{2}\right]$. These features are summarized in Table 5.1 and compared in Figure 5.6.

We must further emphasize that the identification of $\tau_*^{\check{H}}\left(\check{H}^1\right)$ with the diffraction $S\left(k\right)$ is valid in periodic and C&P tilings only. In other tilings, it happens only if the diffraction admits only a Bragg spectrum such as in the Period Doubling tiling (see Figure 5.6d). For mixed spectrum, or a non-Bragg one, this correspondence cannot be made.

Proposition. $\tau_*^{\check{H}}\left(\check{H}^1\right)\simeq S\left(k\right)$ *if and only if the diffraction is purely Bragg.*

Complement 5.A Derivations for C&P Tilings

Let us address some recurring points of Section 5.2.

5.A.1 Gaps in Quasiperiodic Approximants

Let us show the existence of d_N gaps for the N^{th} approximant of a quasiperiodic system. To prove that we shall first show the pattern of Bragg peaks of the aforementioned approximant and then use the Bloch theorem to connect Bragg peaks to gaps.

We shall follow the argumentation of [15]. Consider points x_n on the $1d$ line following the rule (as in (2.67) or in Section 4.1.1),

$$x_n=an+g\left(n\right),\quad n\in\mathbb{Z},\quad g\left(x+s^{-1}\right)=g\left(x\right). \tag{5.59}$$

Note that s may be rational or irrational. We shall also assume that a and s are chosen such that x_n forms a Delone set [15] (simply put, a crystal or quasicrystal). The atomic density is thus

$$\rho\left(x\right)=\sum_{n\in\mathbb{Z}}\delta\left(x-x_n\right). \tag{5.60}$$

For a diffraction spectrum, we need to calculate the Fourier transform. Taking it for $\rho\left(x\right)$, one has

$$\hat{\rho}\left(\nu\right)=\sum_{n\in\mathbb{Z}}\mathrm{e}^{-2\pi\mathrm{i}x_n\nu}=\sum_{n\in\mathbb{Z}}\mathrm{e}^{-2\pi\mathrm{i}\left(an+g(n)\right)\nu}. \tag{5.61}$$

Since $g\left(x\right)$ is periodic in s^{-1}, we may divide $\mathrm{e}^{-2\pi\mathrm{i}g(x)}$ into its Fourier components,

$$\mathrm{e}^{-2\pi\mathrm{i}g(x)}=\sum_m e_m\left(\nu\right)\mathrm{e}^{2\pi\mathrm{i}mxs}. \tag{5.62}$$

Thus,

$$\hat{\rho}\left(\nu\right)=\sum_m e_m\left(\nu\right)\sum_{n\in\mathbb{Z}}\mathrm{e}^{-2\pi\mathrm{i}n\left(a\nu-ms\right)}. \tag{5.63}$$

Using Poisson summation formula for the second sum, one has

$$\begin{aligned}\hat{\rho}(\nu) &= \sum_m e_m(\nu) \sum_{\ell\in\mathbb{Z}} \delta(\ell - a\nu + ms) \\ &= \sum_m \frac{e_m(\nu)}{a} \sum_{\ell\in\mathbb{Z}} \delta\left(\nu - \frac{1}{a}(\ell + ms)\right).\end{aligned} \tag{5.64}$$

If s is irrational, then $m \in \mathbb{Z}$ as in [15]. However, if $s = c/d \in \mathbb{Q}$ a reduced fraction, then $m \in \{1, \ldots, d\}$. Hence, in the rational case, there are d Bragg peaks located at $\nu_{\ell,m} = (\ell + ms_N)/a$ in the Brillouin zone $[-1/2a, 1/2a]$ with weights given by $e_m(\nu_{\ell,m})$. This also holds for any approximant $s_N = c_N/d_N$ by construction. Moreover, since $a\nu_{\ell,m} = \ell + ms_N$, these Bragg peaks are equally distributed over the Brillouin zone.

Next, use Bloch theorem to calculate the gaps for the rational case of $s_N = c_N/d_N$. Since the Bragg peaks equally distributed, so are the gaps over the normalized integrated density of states. Thus, there are d_N distinct gaps located at $\mathcal{N}_{\ell,m} = \ell + ms_N \pmod 1$. This is the gap labeling theorem for rational approximants.

5.A.2 The Structure Factors of Σ_1 and Σ_2

We have stated before (in Section 2.2) that the absolute value of the Fourier transform (with respect to n) of $\Sigma_{1,2}(n, \ell)$ is the structure factor. Let us show it here.

In the case of Σ_1 and Σ_2, we need to inspect $h(x)$, where

$$h(x) = g(x) - g\left(x - s^{-1}\right). \tag{5.65}$$

Note that $h(x)$ is also periodic in s^{-1} and gets only 2 values. The density thus reads

$$\varrho(x) = \sum_{n\in\mathbb{Z}} h(x)\,\delta(x - n), \tag{5.66}$$

up to, maybe, an envelope $\varrho(x) \longleftrightarrow \Pi(x) * \varrho(x)$. As before, we divide it into its Fourier components,

$$h(x) = \sum_m h_m(\nu)\, \mathrm{e}^{2\pi i m x s}, \tag{5.67}$$

so that

$$\hat{\varrho}(\nu) = \sum_m h_m(\nu) \sum_{n\in\mathbb{Z}} \mathrm{e}^{-2\pi i n(\nu - ms)}. \tag{5.68}$$

Using Poisson summation formula for the second sum, one has

$$\begin{aligned}\hat{\varrho}(\nu) &= \sum_m h_m(\nu) \sum_{\ell\in\mathbb{Z}} \delta(\ell - \nu + ms) \\ &= \sum_m h_m(\nu) \sum_{\ell\in\mathbb{Z}} \delta(\nu - (\ell + ms)).\end{aligned} \tag{5.69}$$

Therefore, we have as in the previous case Bragg peaks at $\nu_{\ell,m} = \ell + ms$ with amplitude dependent only on m. The only difference between Σ_1 and Σ_2 is that we take the approximant s_N for the former and the irrational s for the latter.

Corollary. *The Fourier transform (with respect to n) of $\Sigma_{1,2}$ a "structure factor."*

COMPLEMENT 5.B Wannier Diagrams

Using the continued fraction expatiation of $s \in [0, 1]$ in Section 2.4, we inspect the set of physical properties dependent on s. We are interested in the structure factor $S_s(\nu)$ and the density of states $\rho_s(\nu)$. These are presented below.

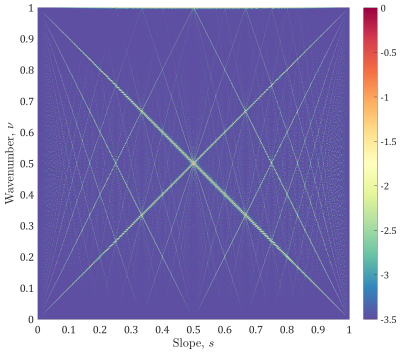

(a) Wannier diagram of the structure factor $S_s(\nu)$ (diffraction spectrum). The color bar represents the structure factor in a logarithmic scale.

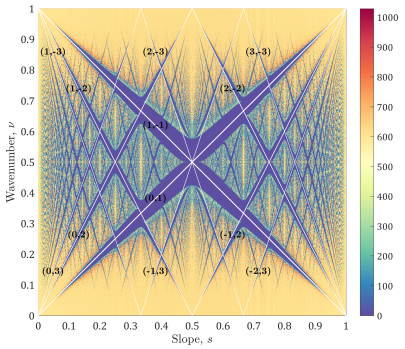

(b) Wannier diagram of the normalized density of states. The color bar represents the density of states value. The gaps for $|q| \leq 3$ are depicted by the white lines with their label (p, q) attached.

Figure 5.7: Wannier diagrams for the cut and project method using scattering matrix with $(n_A, n_B) = (1, \tau)$ and $(l_A, l_B) = (\tau, 1)$. The wavenumber ν and the slope s are supported on $[0, 1]$. (a) Diffraction spectrum. (b) Density of states. Wannier lines are given as $\nu = p + qs$.

5.B.1 Construction of Wannier Diagrams

Set $\nu = \xi / d_N \in [0, 1]$ as the physical wavenumber (normalized wavevector k). We plot the structure factor (Bragg peaks) $S_s(\nu)$ at all slopes $s \in [0, 1]$ calculated with the scattering matrix formalism (see [38, 68, 71] for details). The Bragg peaks are solutions of Diophantine equations, and thus are located at

$$\nu_{p,q} = p + qs \pmod 1, \tag{5.70}$$

which is exactly the Wannier diagram (see Figure 5.7a). Similarly, using the scattering matrix (see Section 3.4), one can plot the density of states (DOS) $\rho_s(\nu)$ instead of the diffraction spectrum [38, 68, 71]. The gaps are located at the same $\nu_{p,q}$ (see Figure 5.7b).

5.B.2 Topological Interpretation

For periodic systems, the numbers (p, q) in the Wannier diagram 5.7b are understood as Chern numbers [4, 95] (see [96–98] for review). In simple terms, a $2d$ periodic Hamiltonian $H(x, y)$ in a perpendicular magnetic field (in Landau gauge) exhibits a quantized Hall conductance [4]

$$\begin{aligned} \sigma_{\mathrm{H}} &= \frac{e^2}{h} \frac{\mathrm{i}}{2\pi} \int \mathrm{d}^2\boldsymbol{r} \int \mathrm{d}^2\boldsymbol{k} \left(\frac{\partial u^*}{\partial k_1} \frac{\partial u}{\partial k_2} - \frac{\partial u^*}{\partial k_2} \frac{\partial u}{\partial k_1} \right) \\ &= \frac{e^2}{h} \frac{\mathrm{i}}{4\pi} \int \mathrm{d}^2\boldsymbol{r} \oint \mathrm{d}k \left(u^* \frac{\partial u}{\partial k} - \frac{\partial u^*}{\partial k} u \right). \end{aligned} \tag{5.71}$$

Here $u_{\boldsymbol{k}}(\boldsymbol{r})$ is the Bloch function corresponding to the eigenfunctions of $H(x, y)$, and e^2/h is the natural conductance. The integral $\int \mathrm{d}^2\boldsymbol{k}$ can be interpreted as the Gauss-Bonnet-Chern curvature. Thus, σ_{H} is given in units of e^2/h of the *Chern number* [96, 97]. This gives them a topological aspect.

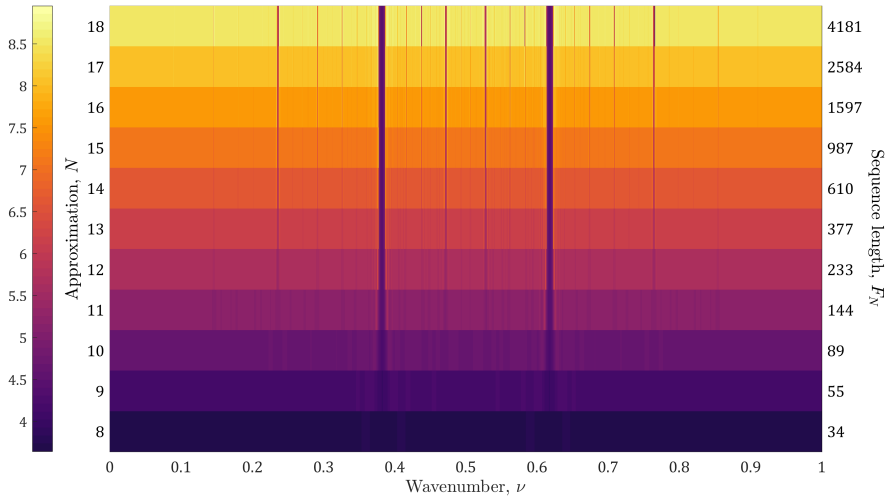

Figure 5.8: Approximations of the density of states $\rho_N(\nu)$ for the cut and project method using scattering matrix with $(n_A, n_B) = (1.9, 2)$ and $(l_A, l_B) = (2, 1.9)$. The color bar represents the values of $\rho_N(\nu)$ in a logarithmic scale.

The above description works for any $s \in \mathbb{Q}$ in the C&P scheme [98]. However, since the calculation of the Chern numbers relies on the periodicity of $H(x, y)$, it would not work for an irrational s nor for non-periodic boundary conditions. In the irrational case, the numbers (p, q) are understood as the image of the K_0 group under trace operation [27] (cf. Section 5.2.6). Their topological character is therefore differs from Chern.

In order to combine both views, we consider the sequence $s_N \to s$ with $s \in \mathbb{R} \setminus \mathbb{Q}$ as before. For any finite N, the density of states $\rho_N(\nu)$ exhibits gaps characterized by their Chern numbers. For each consecutive N, more and more gaps open. In the limit $N \to \infty$, we obtain an infinite amount of gaps, where each gap is given by trace of K_0. The opening of gaps is presented in Figure 5.8.

Another approach is to define Chern numbers in Figure 5.7b using K-theoretical arguments on quasiperiodic quantum systems [99, 100]. Accordingly, bulk-boundary correspondence is identified and generalized to many-body systems.

COMPLEMENT 5.C Conventional Topological Numbers

Examining topological quantities in periodic systems, two phases come to mind: the Berry phase [29] and the Zak phase [101]. From them, it is straightforward to calculate Chern numbers (only in periodic systems). In this section, we shall show their counterparts in quasiperiodic C&P systems.

5.C.1 Topological Phases of Periodic Systems Revised

Let us start with the Berry phase [29]. Consider a time-dependent Hamiltonian $\mathcal{H}(\boldsymbol{R}(t))$ subjected to a periodic varying parameter $\boldsymbol{R}(t)$ such that $\boldsymbol{R}(T) = \boldsymbol{R}(0)$ for

some path in the phase space of $\boldsymbol{R}(t)$. The system evolves naturally as

$$\mathcal{H}(\boldsymbol{R})|\psi_n(\boldsymbol{R})\rangle = E_n(\boldsymbol{R})|\psi_n(\boldsymbol{R})\rangle \tag{5.72}$$

Solving the Schrödinger equation for the evolution of some state $|\xi(t)\rangle$, a *geometrical phase* emerges. On a closed phase-space path C, its change is given by

$$\gamma_n(C) = \mathrm{i}\oint_C \langle\psi_n(\boldsymbol{R})|\boldsymbol{\nabla}_{\boldsymbol{R}}\psi_n(\boldsymbol{R})\rangle\cdot \mathrm{d}\boldsymbol{R}. \tag{5.73}$$

The evaluation of $\boldsymbol{\nabla}_{\boldsymbol{R}}\psi_n(\boldsymbol{R})$ requites some knowledge of the representation of $\psi_n(\boldsymbol{R})$, and might be inconvenient. Using Stokes' theorem, $\gamma_n(C)$ can be rewritten in a representation free form [29],

$$\gamma_n(C) = -\iint_C \mathrm{d}\boldsymbol{S}\cdot\boldsymbol{V}_n(\boldsymbol{R}), \tag{5.74}$$

where

$$\boldsymbol{V}_n(\boldsymbol{R}) \doteq \mathrm{Im}\sum_{m\neq n}\frac{\langle\psi_n(\boldsymbol{R})|\boldsymbol{\nabla}_{\boldsymbol{R}}\mathcal{H}(\boldsymbol{R})|\psi_m(\boldsymbol{R})\rangle\times\langle\psi_m(\boldsymbol{R})|\boldsymbol{\nabla}_{\boldsymbol{R}}\mathcal{H}(\boldsymbol{R})|\psi_n(\boldsymbol{R})\rangle}{(E_m(\boldsymbol{R})-E_n(\boldsymbol{R}))^2}. \tag{5.75}$$

In periodic lattices, the application is straightforward. For instance, in a $2d$ periodic system, one chooses $\boldsymbol{R} = (k_x, k_y)$ with k_i the Bloch quasi-momenta. Let us now try to apply this scheme to quasiperiodic lattices. For simplicity, inspect $2d \longrightarrow 1d$ C&P structures as in Figure 2.1. One might expect, that the $1d$ counterpart of the Berry phase, namely the Zak phase [101], should work,

$$\gamma_n = \mathrm{i}\int_{\mathrm{BZ}}\left\langle u_{nk}\left|\frac{\partial u_{nk}}{\partial k}\right.\right\rangle \mathrm{d}k. \tag{5.76}$$

However, Zak phase is not sensitive to the internal structure of the potential, which holds the entire quasiperiodic information. We thus need to examine different ways.

5.C.2 Chern Numbers of Quasiperiodic Approximations in $2d$ Hamiltonians

As discussed in the previous section, it is impossible to extract information from a simple $1d$ Hamiltonian. We need an additional degree of freedom – the phason ϕ – to see the topological information. There is one caveat though. We do not have a magnetic field in our system, and the Hamiltonian is commuting with the time-reversal operator. Thus, if our Hamiltonian is also simply-connected, then the only Zak/Berry phases we could get are $\{0, \pi\}$ (see [102]). This would contradict with the positive and negative numbers we saw in Figure 5.7b. Yet, as our topological space is not simply connected, we might get equivalence with magnetic field.

To calculate topological integers—Chern numbers, we shall use similar ideas to [34, 35], but emphasize the periodic and finite nature of the quasiperiodic approximants. For pedagogical reasons, we shall solve a $2d$ problem – Hamiltonian of an electron living on torus as in Figure 5.9. This is *not* the $1d$ problem experimented upon in [37], but it will give us some good intuition. The main difference is that in $1d$ the phason is a *phase* that cannot change any physical property of the system, whereas in $2d$ it is a *physical axis* on the torus. Additionally, we want a finite approximant to the

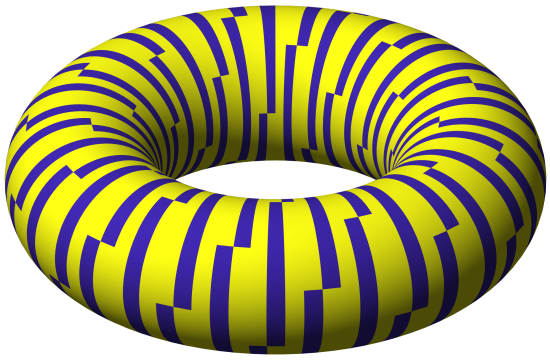

Figure 5.9: The quasiperiodic torus of the Fibonacci sequence with $d_N = 89$. The axes are x (large circle) and ϕ (small circle). The colors represent the potential with v_a on the yellow sites and v_b on the blue ones.

quasiperiodic system so that it becomes periodic. This can only happen for size d_N, where $s \to s_N = c_N/d_N$. This imposes an additional constraint, where both the real axis x and the phason axis ϕ become *discrete*. Let us see how it works.

Consider the following Hamiltonian,

$$\mathcal{H} = \frac{\boldsymbol{p}^2}{2\mu} + \mathcal{V}(x, \phi), \tag{5.77}$$

so that $\mathcal{V}(x + L, \phi) = \mathcal{V}(x, \phi + 2\pi) = \mathcal{V}(x, \phi)$. For $\mathcal{V}(x, 0)$, we consider a piecewise constant periodic potential of $L = d_N$ sites, where each site $\{a, b\}$ is $\{v_a, v_b\}$, respectively, of width $l_a = l_b = 1$ taken from the N^{th} approximant of some C&P slope s. The total function $\mathcal{V}(x, \phi)$ is a torus as in Figures 2.3 or 5.9. The potential thus reads,

$$\mathcal{V}(x, \phi) = \mathcal{T}_x^{m(\phi)} \mathcal{V}(x, 0) \mathcal{T}_x^{-m(\phi)}, \tag{5.78}$$

where

$$m(\phi) = \left(\frac{\phi}{2\pi} d_N \right) c_N^{-1} \pmod{d_N}, \tag{5.79}$$

similarly to Section 2.2.1. This means that $\mathcal{T}_\phi = \mathcal{T}_x^{m(\phi)}$, and we got a skew relation between x and ϕ instead of rotation. Thus, time-reversal symmetry is not broken.

Remark. The expression of $\mathcal{V}(x, \phi)$ is more restrictive than the general form in [32]. However, it has an explicit algebraic formula and relation to C&P procedure.

Not all hope is lost. Let us make a few observations. First, change variables from ϕ to $y = (\phi/2\pi)\, d_N$ so that

$$m(y) = y c_N^{-1} \pmod{d_N}, \tag{5.80}$$

and we have a torus of $d_N \times d_N$ as in Figure 5.9. The Hamiltonian thus reads

$$\mathcal{H} = \frac{\boldsymbol{p}^2}{2\mu} + \mathcal{V}(x, y). \tag{5.81}$$

Let $\psi_{n,\boldsymbol{k}}(\boldsymbol{r})$ be a solution to this equation with eigenenergy $E_{n,\boldsymbol{k}}$, with $\boldsymbol{r} = (x, \phi)$. Under Bloch's theorem, we inspect the periodic functions $u_{n\boldsymbol{k}} = \mathrm{e}^{-\mathrm{i}\boldsymbol{k}\cdot\boldsymbol{r}} \psi_{n\boldsymbol{k}}$, whose Hamiltonian reads

$$\mathcal{H} = \frac{(\boldsymbol{p} + \hbar\boldsymbol{k})^2}{2\mu} + \mathcal{V}(x, y). \tag{5.82}$$

The Berry phase is then given by

$$\gamma_n = \mathrm{Im} \int_{\mathrm{BZ}} \mathrm{d}^2\boldsymbol{k} \int_S \mathrm{d}^2\boldsymbol{r} \left(\frac{\partial u^*_{n\boldsymbol{k}}}{\partial k_x} \frac{\partial u_{n\boldsymbol{k}}}{\partial k_y} - \frac{\partial u^*_{n\boldsymbol{k}}}{\partial k_y} \frac{\partial u_{n\boldsymbol{k}}}{\partial k_x} \right). \tag{5.83}$$

According to [102], since there is time-reversal symmetry, the wavefunction could always be taken real so that the possible values of γ_n are $\{0, \pi\}$. Now we claim the following. Since $\mathcal{V}(x)$ has a period of d_N, there are exactly d_N *distinct* bands. Since they are all distinct, the Berry phase *must be* π for all of them. Now, we have a relation between ϕ and x. Since $\mathrm{d}\phi = \partial m(\phi)/\partial\phi \, \mathrm{d}x$ then $\mathrm{d}y = \partial m(y)/\partial y \, \mathrm{d}x = c_N^{-1} \, \mathrm{d}x$. This means that $\partial/\partial x = c_N^{-1} \partial/\partial y$. Thus, $k_x = c_N^{-1} k_y$ so that $\partial/\partial k_y = c_N^{-1} \partial/\partial k_x$. Using the Stokes theorem, the Berry phase is given by,

$$\gamma_n = c_N^{-1} \, \mathrm{Im} \oint_{\mathrm{BZ}} \mathrm{d}k \int_S \mathrm{d}^2\boldsymbol{r} \, \frac{\partial u^*_{nk}}{\partial k} u_{nk}. \tag{5.84}$$

By the previous discussion, the integrals amount to $\mathrm{i}\pi$. Hence, the Berry phase has a degeneracy of c_N^{-1},

$$\gamma_n = \pi c_N^{-1}. \tag{5.85}$$

The Chern number of the n^{th} band is given by

$$C_n \doteq \tfrac{1}{2\pi} \gamma_n = \tfrac{1}{2} c_N^{-1}, \tag{5.86}$$

and the winding of the edge state of the n^{th} gap is given by [95, 103],

$$W_n \doteq \sum_{i=1}^{n} C_n = \tfrac{1}{2} n c_N^{-1}, \tag{5.87}$$

or, equivalently,

$$C_n \doteq W_n - W_{n-1} = \tfrac{1}{2} c_N^{-1}. \tag{5.88}$$

Thus, for $n = q c_N$ one has

$$W_{n_q} = \tfrac{1}{2} q. \tag{5.89}$$

We should understand the $1/2$ factor here as follows. The edge state always winds twice around the Brillouin zone, when we change ϕ from 0 to 2π, because it travels from band n to band $n+1$ and back. However, when the Chern number is half-integer, it winds in the *same* direction [37] instead of flipping directions [102, 103]. This interpretation does not require external fields, and the ("molecular" [102]) Chern number is seen as an internal property of the crystal.

5.C.3 Chern Numbers and Chirality in 2*d* Hamiltonians

The main issue with the previous model is that the time-reversal symmetry is not broken. Thus, the topological numbers found are topologically trivial [102]. Consequently, the factor $1/2$ we have got has a shady interpretation. Below, we shall show a different approach.

We introduce twisted boundary conditions [104] similarly to [34]. This superficial condition is required in order to obtain Chern numbers [105] or to measure transport properties by using an effective Hamiltonian [70, 104]. Suppose that the N^{th} approximant is describing such a (x, y)-torus of size $d_N^2 = L^2$ (see Figure 5.9), and impose

chiral boundary conditions so that a full round-trip around the torus of x and y adds a phase of $e^{i\beta\phi}$. Specifically, if $\psi(x,\phi)$ is an eigenfunction of the Hamiltonian, then

$$\psi(x+d_N,\phi) = e^{i\beta\phi/2\pi}\,\psi(x,\phi)\,. \tag{5.90}$$

Thus, these boundary conditions can be incorporated into the Hamiltonian by [32, 104],

$$\mathcal{H} = \frac{\left(\boldsymbol{p}+\beta y L^{-2}\hat{x}\right)^2}{2\mu} + \mathcal{V}(x,y)\,, \tag{5.91}$$

These are exactly the equations of a magnetic field through a ring, where $\Phi_\beta = \beta/L$ plays the role of the Aharonov-Bohm flux in a Landau gauge. Note that the flux has a real physical interpretation only because we are in a $2d$ system.

The solution is now straightforward (see [106], for instance). We may use similar arguments to the Hofstadter solution to the Harper model [107, 108], with the following distinction. In [108], the flux can have any two integer numbers p/q; in the quasiperiodic case they are uniquely determined by c_N/d_N. The denominator is identified with the super-cell size, and it must coincide with the torus length d_N. Since we are in a quasiperiodic C&P approximant, for each d_N there is only one c_N, who governs the labeling order of the gaps (as will be shown below). The chirality β thus governs the winding of the edge state. Physically, since we are in a $1d$ system, we can only expect the trivial $\beta = 0$ or the topological $\beta = \pm 1$.

This Hamiltonian is already periodic in $2d$ (no need to add the k_x, k_y wavevectors). Thus, we can calculate the Berry phase. Similarly to the previous section, we have a relation between x and y, $\mathrm{d}y = c_N^{-1}\,\mathrm{d}x$ so that $\partial/\partial k_y = c_N^{-1}\partial/\partial k_x$. We use, as before, Stokes theorem, but now the integral is $2\pi i\beta$:

$$\gamma_n = c_N^{-1}\,\mathrm{Im}\oint_{\mathrm{BZ}}\mathrm{d}k\int_S \mathrm{d}^2\boldsymbol{r}\,\frac{\partial u_{nk}^*}{\partial k}u_{nk} = c_N^{-1}\,2\pi\beta \tag{5.92}$$

Therefore, the Berry phase is the chirality multiplied by c_N^{-1}. The latter factor gives the correct Chern number of the required band

$$C_n = \beta c_N^{-1}. \tag{5.93}$$

The winding of the edge state of the n^{th} gap is given by [95, 103],

$$W_n = \sum_{i=1}^{n} C_n = n\beta c_N^{-1}. \tag{5.94}$$

Thus, for $n = qc_N$ one has

$$W_{n_q} = \beta q. \tag{5.95}$$

Let us now connect to the chiral phase $\alpha(k,\phi)$ of (3.76) to the Chern numbers found above. In the experiments of [37], a structure and its reflection were concatenated to have a superstructure of double length. This corresponds to chirality of $\beta = +1$. An edge state always winds twice inside the gap [103], because it travels from band n to band $n+1$ and back. As the structure is one-dimensional with a given chirality, it winds in the same direction thus explaining the results of [37].

5.C.4 Discussion on the Chern Numbers in 2*d* Hamiltonians

The main arguments (ingredients) to obtain the Chern numbers in the approximants of quasiperiodic sequences are as follows.

i. The axes ϕ and x are connected by $m\,(\phi)$ calculated from the slope (and used to calculate the diffraction spectra).
ii. There are d_N distinct bands, where each one is topologically different from its neighbors below and above. This is a consequence of the gap labeling theorem.
iii. Each band has a degeneracy of $c_N^{-1} \pmod{d_N}$. This comes from the quasiperiodic approximant and $m\,(\phi)$.

Thus, the Chern number of the n^{th} gap for $n = qc_N$ is $nc_N^{-1} = q$. The first issue is the interpretation of the 3rd point. It is either (a) the non-trivial Berry phase for periodic lattice, or (b) the chiral number of the band. The second issue is the double winding in the same direction. It is either (a) a consequence of the π phase, or (b) the chirality.

The main advantage of the non-trivial Berry phase approach is the absence of a magnetic field. No additional conditions are imposed, and it is fully correlated with the structural approach. However, the interpretation of the $1/2$-integer Berry phase is a bit vague, as is the double winding in the same direction. The chiral boundary conditions are easier to calculate, but here the chirality is a superficial quantity that does not have physical interpretation (no physical quantity is dependent on it). It only acts as a mediator to calculate the Chern numbers.

5.C.5 Topological Numbers in 1*d* Dynamical Systems

Our physical system, as measured by [37], is 1*d*; the phason is just a phase that cannot change any physical quantity (e.g., IDOS, transport). We need to change the Hamiltonian accordingly. In the 2*d* case, we had a kinetic energy associated with the real axis ϕ, which does not happen in 1*d*. Thus, looking on a discrete periodic torus of size $d_N \times d_N$ (see Figure 5.9), each row is disconnected from the other.

Take a periodic 1*d* Hamiltonian of size d_N,

$$\mathcal{H}_\phi = \frac{p^2}{2\mu} + \mathcal{V}_\phi\,(x)\,. \tag{5.96}$$

Here both $\phi \in [0, 2\pi)$ and $x \in [0, d_N)$ are discrete with d_N sites each. For simplicity, rescale $y = d_N\phi/2\pi$ so that y is integer in $[0, d_N)$. Since we have a relation between different rows, we could treat this Hamiltonian as a dynamical system. Explicitly,

$$\mathcal{H}_{y'} = \mathcal{T}^{m(y'-y)}\mathcal{H}_y\mathcal{T}^{-m(y'-y)} = \frac{p^2}{2\mu} + \mathcal{V}_{y'}\,(x)\,, \tag{5.97}$$

where, as before $m\,(y) = yc_N^{-1} \pmod{d_N}$.

Let $\psi_n\,(x)$ be an eigenfunction with eigenenergy E_n. Since $\mathcal{H}_y$ is periodic, we use the Bloch theorem and write a Hamiltonian for the periodic $u_{nk}\,(x) = \mathrm{e}^{-\mathrm{i}kx}\,\psi_{nk}\,(x)$,

$$\mathcal{H}_y\,(k) = \frac{(p+\hbar k)^2}{2\mu} + \mathcal{V}_y\,(x)\,. \tag{5.98}$$

Calculating the Zak phase, we have

$$\gamma_n = \mathrm{i}\int_{\mathrm{BZ}} \left\langle u_{nk} \middle| \frac{\partial u_{nk}}{\partial k} \right\rangle \mathrm{d}k. \tag{5.99}$$

Now, since $\mathcal{H}_y(k)$ abides time-reversal symmetry, then $\gamma_n \in \{0, \pi\}$ [101, 102]. There are d_N distinct bands in C&P approximants of size d_N as a consequence of the Bloch theorem, since there are d_N different Bragg peaks per Brillouin zone. All of them are unique, and thus they get the phase $\gamma_n = \pi$.

So far, we have not used the information on the phason (ϕ or y). To do that make the following observation. $\mathcal{T}$ is the generator of translations in x, and its periodicity by d_N gives rise to k. Similarly, $\mathcal{T}^{m(y)}$ is the generator of translations in y and also has the periodicity of d_N. However, from the physical point of view, it acts on the *same* x axis, but with c_N^{-1} steps instead of 1. In C&P approximations, the translations $\mathcal{T}^{m(y)}$ are more natural than $\mathcal{T}$, as they are in the direction of the phason ϕ, thus converging with N. Henceforth, we shall use them.

The wavevector of y given by $k_y = c_N^{-1}k$. Rewriting Zak phase in terms of k_y, one has the same form as before, but the Brillouin zone is *inflated* by a factor of c_N^{-1},

$$\widetilde{\gamma_n} = \mathrm{i}\int_{\widetilde{\mathrm{BZ}}} \left\langle u_{nk_y} \middle| \frac{\partial u_{nk_y}}{\partial k_y} \right\rangle \mathrm{d}k_y = c_N^{-1}\gamma_n. \tag{5.100}$$

This can also be seen as a degeneracy. Define the Zak number of the n^{th} band by,

$$C_n = \tfrac{1}{2\pi}\,\widetilde{\gamma_n} = \tfrac{1}{2}\,c_N^{-1}. \tag{5.101}$$

Note the factor $\frac{1}{2}$ as before. Analogously to Chern numbers, the Zak number of the n^{th} gap is

$$W_n = \sum_{i=1}^{n} C_i = \tfrac{1}{2}\,nc_N^{-1}. \tag{5.102}$$

Thus, for the $n = qc_N$ gap, one has a topological integer

$$W_{n_q} = \tfrac{1}{2}\,q. \tag{5.103}$$

Claim. Note that the phason ϕ only comes to scale the integer number of the gaps. We have chosen $m(y) = c_N^{-1}y$, and thus the c_N^{-1} factor was brought to fruition. Should we select a different phase scale, the integer numbers would scale accordingly. Recall, however, that the c_N^{-1} factor comes from the C&P procedure, or, analogously, the characteristic function.

We have thus associated the gaps' integer labeling with winding numbers. However, edge states in the experiments of [37] wind *twice* inside each gap. This is not reflected in the current calculation, but rather it has the peculiar $\frac{1}{2}$ factor.

Remark. In [37] it was experimentally verified that

$$W_n = \sum_{i=1}^{n} C_n = 2nc_N^{-1}, \tag{5.104}$$

so that for $n_N = qc_N$ one has

$$W_q = \sum_{i=1}^{q} C_{n_N(q)} = 2q. \tag{5.105}$$

In other words, the topological number $W_q = 2q$ does not depend on the approximation N unlike the Chern numbers C_{n_N} inside. This is in contrast with periodic structures, where the Chern numbers are not dependent on system size.

Proposition. *Winding numbers W_q are topologically more resilient than Chern numbers C_n in C&P tilings. Moreover, their calculation is simpler as it does not require wavefunctions.*

Chapter 6

Fractals

This chapter is a bit special. Unlike the previous ones, where we have concentrated on simple tiling spaces [52], here we present a *discrete scale invariance* construction with a non-integer (Hausdorff) dimension. The avid reader is referred to [109] for a review on fractals in physics.

6.1 Introduction

Here we present a short introduction to the construction of fractals.

6.1.1 L-systems and Turtle Graphics

The L-systems, named after A. Lindenmayer, are a generalization of substitution systems [110, 111]. Formally, an L-system is the tuple

$$L \doteq (V, w_0, \pi)\,, \tag{6.1}$$

where V is the alphabet consisted of variables Γ changing under the rule π, and constants C that are not replaced; w_0 is the initial word (or an "axiom"); π are the production rules for all the variables, similar to substitution rules. One creates a word of order n via successive applications of π on w_0,

$$w_n \doteq \pi^n\,(w_0)\,. \tag{6.2}$$

We shall generally interpret the L-system as a drawing rule where we hold a pen (the "turtle"), and the letters in w_n tell it how to draw the fractal. Typically,

- $A, B, F, G \in \Gamma$: draw a line;
- $X, Y \in \Gamma$: involve but do not draw;
- $\pm \in C$: turn right $\pm\theta$ degrees;
- $[\,,\,] \in C$: push and pop positions into (respectively, from) the stack.

Let us inspect a few examples.

Example (Sierpiński Gasket)**.** Here, F, G is draw a line; $\pm$ turn right $\pm 120°$; $w_0 = F + G + G$; and

$$\pi_{\text{Sier}} : \begin{cases} F \mapsto F + G - F - G + F, \\ G \mapsto G\,G. \end{cases} \tag{6.3a}$$

Note that the angles $\pm$ do not need a rule.

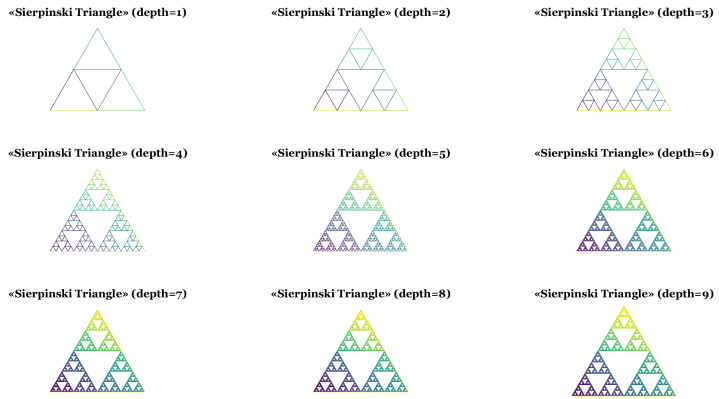

(a) Sierpiński Gasket for orders $n = 1–9$.

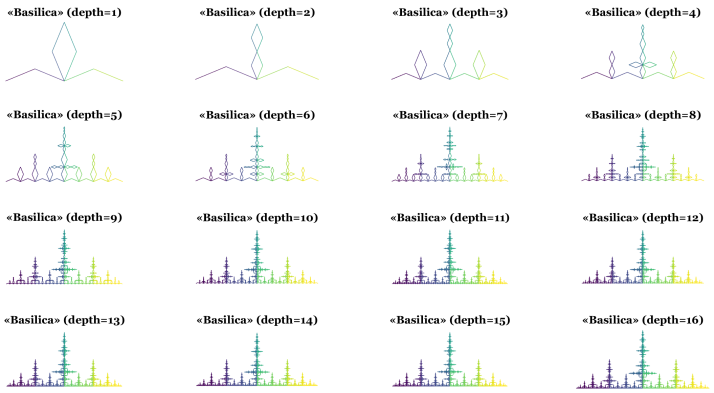

(b) Basilica for orders $n = 1–10$. Here, $w_0 = A$.

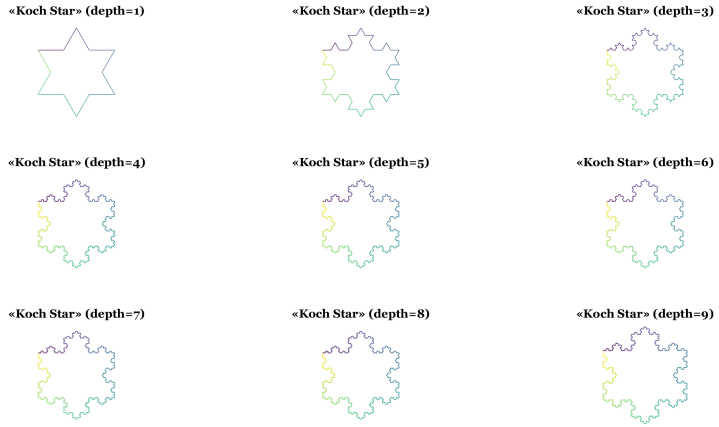

(c) Koch Star for orders $n = 1–9$.

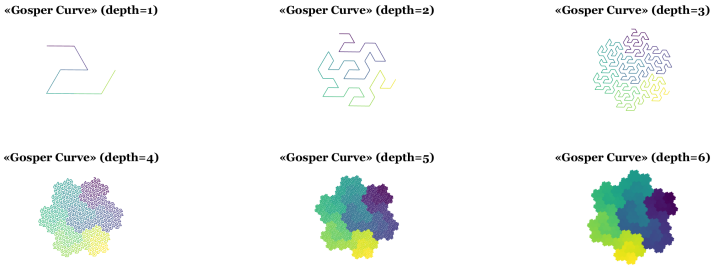

(d) Gosper Curve for orders $n = 1–6$.

Figure 6.1: Turtle Graphics Fractals. (a) Koch star; (b) Sierpiński Gasket; (c) Basilica; (d) Gosper Curve. The order n is shown at each fractal. The color code indicates the path the turtle makes.

Example (Basilica fractal)**.** Here A, B are curve leftwards, and C make a loop (facing backwards); $\pm$ turn right $\pm 90^\circ$; $w_0 = A{+}{+}A$; and

$$\pi_{\text{Bas}} : \begin{cases} A \mapsto B - C - B, \\ B \mapsto A, \\ C \mapsto B\,C\,B. \end{cases} \tag{6.3b}$$

Example (Koch curve)**.** Here, F is draw a line; $\pm$ turn right $\pm 60^\circ$; $w_0 = F{+}{+}F{+}{+}F$; and

$$\pi_{\text{Koch}} : F \mapsto F - F + + F - F. \tag{6.3c}$$

Example (Gosper curve)**.** Here, G, H is draw a line; $\pm$ turn right $\pm 60^\circ$; $w_0 = G$; and

$$\pi_{\text{Gos}} : \begin{cases} G \mapsto G + H + + H - G - - G\,G - H +, \\ H \mapsto \ - G + H\,H + + H + G - - G - H. \end{cases} \tag{6.3d}$$

These examples are presented in Figure 6.1.

6.1.2 Substitutions via L-systems

So far we have seen how L-systems generalize substitutions. Mainly, the constants and initial conditions enhance the capabilities of substitutions. Let us make the other direction, namely, restate L-systems in substitution language. This will allow us to use the many theorems and algorithms for substitutions we already know.

Let us make the following observation. The constants are letters in the substitution rule that map to themselves. Thus, we can simply rewrite the production rules of the L-systems as substitutions,

$$\sigma_{\text{Sier}} : \begin{cases} A \mapsto Ac\,BdAdB\,cA, \\ B \mapsto B\,B, \\ c \mapsto c, \\ d \mapsto d; \end{cases} \qquad (c, d) = (+, -)\,. \tag{6.4a}$$

$$\sigma_{\text{Bas}} : \begin{cases} A \mapsto B\,dCd\,B, \\ B \mapsto A, \\ C \mapsto BCB, \\ d \mapsto d; \end{cases} \qquad d = -. \tag{6.4b}$$

$$\sigma_{\text{Koch}} : \begin{cases} A \mapsto AcA\,bb\,AcA, \\ b \mapsto b, \\ c \mapsto c; \end{cases} \qquad (b, c) = (+, -)\,. \tag{6.4c}$$

$$\sigma_{\text{Gos}} : \begin{cases} A \mapsto Ac\,Bcc\,Bd\,Add\,A\,Ad\,Bc, \\ B \mapsto dA\,cB\,B\,ccB\,cA\,ddA\,dB, \\ c \mapsto c, \\ d \mapsto d; \end{cases} \qquad (c, d) = (+, -)\,. \tag{6.4d}$$

Here, the translation of the constant is explicitly stated. The constants are denoted by lower-case letters for visual aid only.

We observe here the crucial importance of the constants. Take, for example, the simple case of the Koch star. Without the constants, we have $F \mapsto FFFF$, which is simply a periodic structure. Similar argument transpires for all other presented cases.

Corollary. *The constants of a fractal substitution are essential for its algebraic properties.*

Let us focus on the initial condition w_0. We have considered thus far only *primitive* substitutions rules. The main mathematical idea was to create a *closed* tiling space Ω_T so that we can study its topology [52]. Technically, it means that we can recreate Ω_T starting with any tile $t \in T$. In fractals, this is not the case. The simplest example is the Cantor set,

$$\sigma_{\text{Cantor}} : \begin{cases} A \mapsto ABA, & A : \text{draw a line}, \\ B \mapsto BBB, & B : \text{skip drawing}. \end{cases} \tag{6.5}$$

Should we start with $w_0 = A$, we can safely recreate the fractal; starting with $w_0' = B$ results in an empty line. We can also view it from the non-primitive occurrence matrix $M_{\text{Cantor}} = \left(\begin{smallmatrix} 2 & 1 \\ 0 & 3 \end{smallmatrix}\right)$, which does not have strictly-positive leading eigenvector.

Corollary. *Primitivity implies insensitivity to initial conditions.*

Another problem is that now, when the associated occurrence matrix is non-primitive, one cannot use the Perron-Frobenius theorem. That means the definitions of the Čech cohomology $\check{H}^1(\Omega)$ do not hold, and one cannot apply anymore the gap-labeling theorem of [27]. Nonetheless, as we shall see below, the algorithm still holds.

6.2 Fractal Substitution Rules

In the previous section, we laid the groundwork of substitutions corresponding to fractals. In this section, we shall show the consequences of considering fractals in substitution language, and present new and interesting physics.

6.2.1 The Gap Labeling Conjecture for Fractals

We saw in the previous section how to construct a fractal with an L-system L (turtle graphics). Consider, for instance, the Sierpiński Gasket L_{Sier} shown in Figure 6.1a, or Basilica L_{Bas} whose half is shown in Figure 6.1b. Take each L-system and transform it into a planar graph G, where the edges are drawn by the turtle, and the nodes are their boundary. Then, to each graph assign a physical entity: a tight binding Hamiltonian. For planar graphs, it is simply the adjacency matrix [112] formally written as

$$H \doteq t \sum_{\langle i,j \rangle} c_i^\dagger c_j + \text{h.c.}, \tag{6.6}$$

where $\langle i, j \rangle$ are nearest neighbors $t \in \mathbb{R}$, and $c_i^\dagger c_j$ is the corresponding adjacency matrix element. For the rest of this section we set $t = 1$.

Next, calculate the IDOS by diagonalizing the Hamiltonian (6.6). We want to label the gaps similarly to the aperiodic tiling case. We saw earlier that the gap labeling theorem does not hold in fractal substitutions due to non-primitivity. Nevertheless, we shall apply it formally *in good faith* exactly as in [27]. In other words, for any fractal substitution σ_{Fr}, the gaps' locations are conjectured to be located at

$$\mathcal{N}_{\text{gap}}^{\text{Fr}} = \frac{1}{a} \frac{k}{\lambda_*^N} \pmod 1, \qquad a, k, N \in \mathbb{N}. \tag{6.7}$$

Here, λ_* is the leading (largest) eigenvalue of the associated occurrence matrix M_1^{Fr}, and a is deduced from its respective leading eigenvectors $\boldsymbol{v}_{1/2}^*$ in both M_1^{Fr} and M_2^{Fr}.

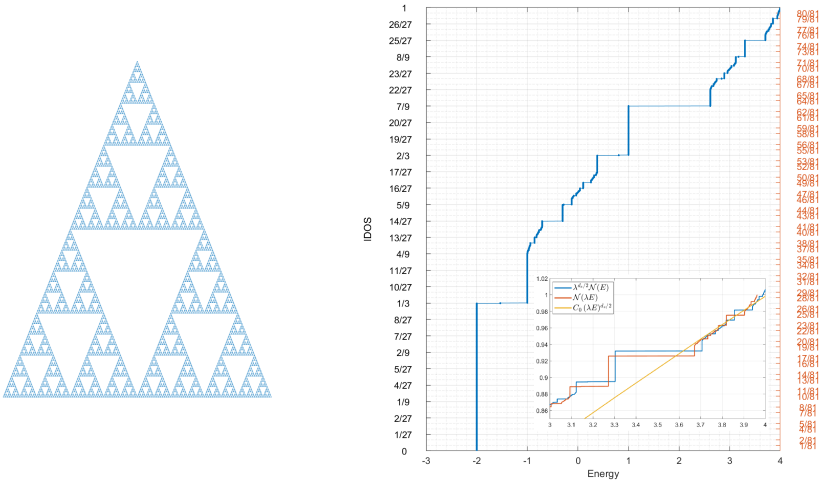

(a) Sierpiński Gasket of order $n = 7$. Inset: scaling at $\mathcal{N} \lesssim 1$ with $\lambda = 1.01$ and $d_s = \log_5 9$ (cf. (6.11)).

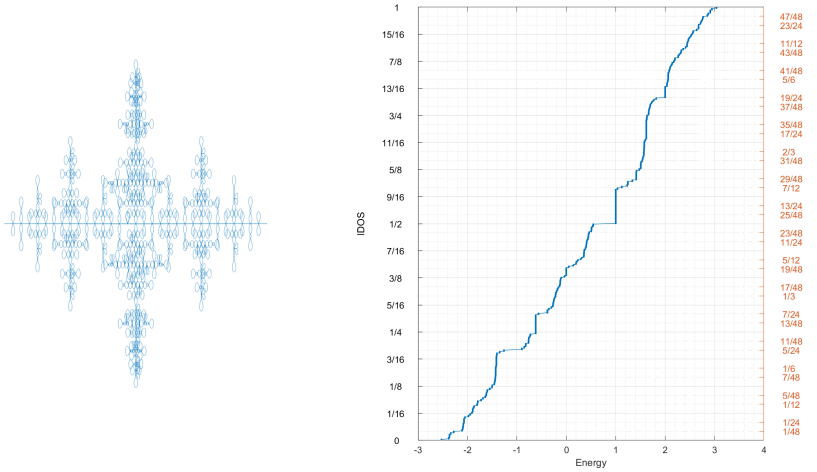

(b) Double Basilica with Loops of order $n = 9$.

Figure 6.2: IDOS vs. E of fractal planar graphs. (a) Sierpiński Gasket; (b) Double Basilica with Loops. Grid ticks are indicated on both sides for visual aid.

Claim. The only thing that matters for the gap labeling conjecture is the leading eigenvalue λ_* that represents the strongest frequency of the substitution. All other frequencies are washed away.

Remark (Perron-Frobenius Thm.). The primitivity requirement for $M_{1/2}$ ensures that (a) the leading eigenvalue λ_* is unique, real and positive; (b) the leading eigenvectors $\boldsymbol{v}^*$ have positive entries v_i. [59, 60]

These v_i are interpreted as corresponding letter l_i frequency in the infinite word w_∞ [43]. They are used as probability measures in the calculation of GLT [27].

Fact. *The Perron-Frobenius theorem above also holds for a general non-strictly-upper-triangular nonnegative matrix M (see Thm. 2.20 in [59]) up to the uniqueness of λ_*.*

Corollary. *Since this is the case in the presented fractal examples, the GLT combinatorics of [27] still holds.*

Example. The gap labeling for the Sierpiński Gasket and the Basilica fractals reads,

$$\mathcal{N}_{\text{gap}}^{\text{Sier}} = \tfrac{1}{10} k\, 3^{-N} \pmod 1, \quad k, N \in \mathbb{N}. \tag{6.8a}$$

$$\mathcal{N}_{\text{gap}}^{\text{Bas}} = \tfrac{1}{3} k\, 2^{-N} \pmod 1, \quad k, N \in \mathbb{N}. \tag{6.8b}$$

The good correspondence with the prediction is shown in Figures 6.2.

In planar graph fractals, we consider 3 different dimensions [109, 113–116]:

1. The Hausdorff dimension d_h corresponds to the geometric dimension.
2. The Walk dimension d_w corresponds to random walks $\langle r^2(t)\rangle \propto t^{2/d_w}$ [114].
3. The Spectral dimension d_s corresponds to the Heat kernel [114].

For planar graphs G_n at iteration n with N_n sites, L_n length and diffusion time T_n, these 3 dimensions are written as [113]

$$\begin{aligned} d_h &= \log N_n \,/\, \log L_n; \\ d_w &= \log T_n \,/\, \log L_n; \\ d_s/2 &= \log N_n \,/\, \log T_n. \end{aligned} \tag{6.9}$$

Thus, they are related by

$$d_s/2 = d_h \,/\, d_w. \tag{6.10}$$

The governing scaling dimension for the IDOS is the spectral dimension,

$$\mathcal{N}(\lambda E) = \lambda^{d_s/2} \mathcal{N}(E)\,. \tag{6.11}$$

In the Sierpiński Gasket, $d_s/2 = \ln 3 \,/\, \ln 5$ [113]. One can readily check in Figure 6.2a that this is indeed the scaling in case.

6.2.2 Topological Phase Transitions

Thus far, we have shown that the gap labeling conjecture works for the planar fractal graphs. Now, let us show how magnetic fluxes interact with the fractals. These questions were considered before by means of renormalization group approach [117, 118], but we shall seek a different—simpler—path.

Consider the Sierpiński Gasket above in a perpendicular magnetic flux. By means of Peierls substitution, we assign phases to each edge of the graph,

$$H_P \doteq t \sum_{\langle i,j\rangle} \mathrm{e}^{\mathrm{i}\alpha_{ij}}\, c_i^\dagger c_j + \text{h.c.} \tag{6.12}$$

This magnetic phase α_{ij} is given by means of Peierls substitution,

$$\alpha_{ij} \doteq \Phi_0^{-1} \int \boldsymbol{A} \cdot \mathrm{d}\boldsymbol{l}_{ij}. \tag{6.13}$$

where $\boldsymbol{A}$ is the gauge field vector potential, and $\boldsymbol{l}_{ij}$ is the path between nodes i and j, and $\Phi_0 = h/e$ the flux quantum.

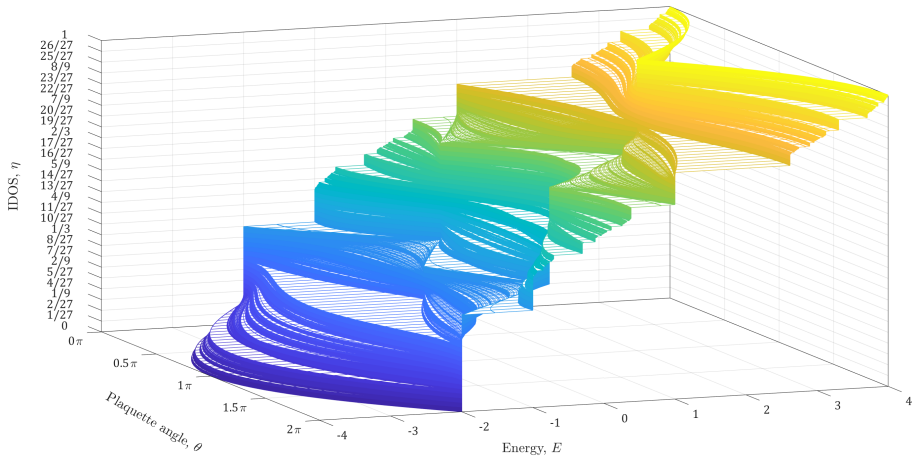

Figure 6.3: IDOS of the Sierpiński Gasket in a magnetic flux (linear model).

Consider an Aharonov-Bohm setup: a flux $\Phi_\triangle$ threading all the smallest plaquettes $\triangle$ in G_n with $\boldsymbol{B} = 0$ on their edges. We set a symmetric gauge $\boldsymbol{A} = B\,(x\hat{y} - y\hat{x})\,/2$, and integrate with respect to $\triangle$ so that $(0,0)$ is in its center. A short calculation yields,

$$\alpha_{ij} = \frac{BS_\triangle}{\Phi_0} \times \begin{cases} +1/3 & \text{for } \gamma_{ij} = \{2\pi/3,\ 0,\ -2\pi/3\} \quad \text{(anticlockwise)}, \\ -1/3 & \text{for } \gamma_{ij} = \{\ \pi/3,\ \pi,\ -\pi/3\} \quad \text{(clockwise)}, \end{cases} \tag{6.14}$$

where $S_\triangle$ is the plaquette area, and γ_{ij} is the the angle between nodes i and j,

$$\gamma_{ij} \doteq \tan^{-1}\!\big(r_{ij}^{y} \,/\, r_{ij}^{x}\big), \qquad \boldsymbol{r}_{ij} \doteq \boldsymbol{r}_j - \boldsymbol{r}_i. \tag{6.15}$$

Therefore, we only need a single parameter—the phase difference per plaquette,

$$\theta \doteq \theta_\triangle = \Phi_0^{-1} \oint_\triangle \boldsymbol{A} \cdot \mathrm{d}\boldsymbol{l} = BS_\triangle/\Phi_0 = \Phi_\triangle/\Phi_0. \tag{6.16}$$

The phase $\theta \in [0, 2\pi)$ is well-defined in the limit of infinite fractal order $n \to \infty$. Note that $B, S_\triangle, \Phi_\triangle$ are fictitious and can be dropped. The Hamiltonian in the "linear model" thus reads,

$$H_L = t \sum_{\langle i,j \rangle} \mathrm{e}^{\mathrm{i}\theta/3}\, c_i^\dagger c_j + \text{h.c.} \tag{6.17}$$

The results of the calculation of IDOS for the Sierpiński Gasket in a magnetic flux are given in Figure 6.3. One can readily see that gaps open and close with respect to θ. However, all of them reside on the gap labeling conjectured $\mathcal{N}_{\text{gap}}^{\text{Sier}}\,(E,\theta) = a^{-1}k/3^N$ as in (6.7). We thus have topological phase transitions on fractals.

Corollary. *The gap labeling conjecture persists in a magnetic flux. All of the gaps of the fractal—open or closed—must obey this gap labeling rule.*

Conjecture. *The main frequency λ_* is all that matters for IDOS calculations. Magnetic flux or other short-range interactions may only open or close gaps in the module of λ_*.*

Fact. *These L-systems are one-dimensional words in the sense of dynamical systems (though the fractals themselves are not).*

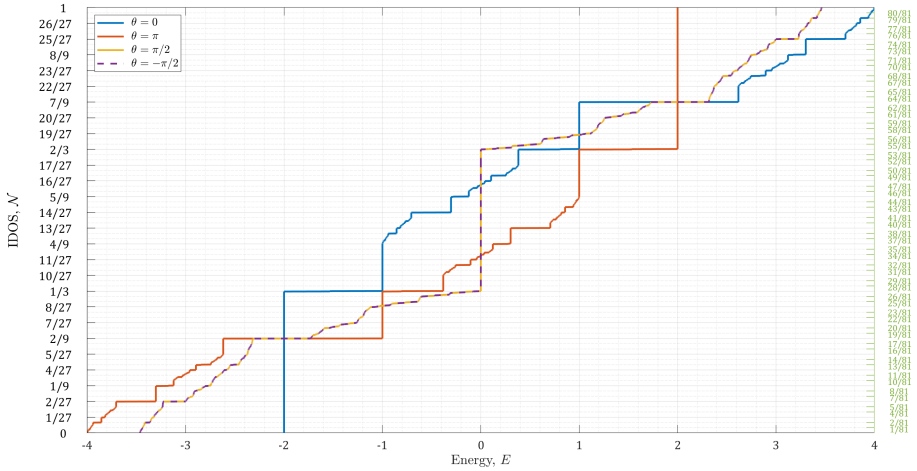

Figure 6.4: IDOS of the Sierpiński Gasket for chosen angles θ (linear model).

Claim. Gaps open and close only at $\theta = 0, \pi, \pm\pi/2$. The respective Hamiltonians exhibit high symmetry with high spectral degeneracy.

Corollary. *We got topological phase transitions with a simple gauge field in* 1*d systems.*

6.2.3 Analysis of Sierpiński IDOS

The Hamiltonian (6.17) is dependent only on a single parameter θ, the total angle per plaquette. Let us make a unitary transformation keeping θ,

$$H_L(\theta) \mapsto \tilde{H}_L(\theta) = t \sum_{\langle i,j \rangle} \mathrm{e}^{\mathrm{i}\tilde{\alpha}_{ij}} c_i^\dagger c_j + \text{h.c.}, \tag{6.18}$$

where

$$\tilde{\alpha}_{ij} = \theta \times \begin{cases} \{\ 1, -1,\ \ 1\} & \text{for } \gamma_{ij} = \{2\pi/3,\ 0,\ -2\pi/3\} \ \text{ (anticlockwise)}, \\ \{-1,\ \ 1, -1\} & \text{for } \gamma_{ij} = \{\ \pi/3,\ \pi,\ \ -\pi/3\} \ \text{ (clockwise)}. \end{cases} \tag{6.19}$$

Notice that $\mathrm{e}^{\pm(\theta+\pi)} = -\mathrm{e}^{\pm\theta}$. Therefore,

$$\tilde{H}_L(\theta) = -\tilde{H}_L(\theta + \pi)\,. \tag{6.20}$$

But since $\operatorname{spec} H_L(\theta) = \operatorname{spec} \tilde{H}_L(\theta)$, we have

$$E(\theta) = -E(\theta + \pi)\,. \tag{6.21}$$

Hence, the IDOS flips 180°,

$$\mathcal{N}(E, \theta) = 1 - \mathcal{N}(-E, \theta + \pi)\,. \tag{6.22}$$

Note that the gap labeling rule $\mathcal{N} = a^{-1}k/3^N$ as in (6.7) is unaffected. Additionally, since $\operatorname{spec} H_L(\theta) = \operatorname{spec} H_L^*(\theta) = \operatorname{spec} H_L(-\theta)$, then

$$\begin{aligned} \mathcal{N}(E, \theta) &= \mathcal{N}(E, -\theta)\,, \\ \mathcal{N}(E, \pi + \theta) &= \mathcal{N}(E, \pi - \theta)\,. \end{aligned} \tag{6.23}$$

This implies reflection of the IDOS around $\theta = 0$ and $\theta = \pi$. These two inversion (6.22) and reflection (6.23) symmetries are well seen in Figure 6.3.

There are 2 special cases to consider.

1. $\theta = 0$. Since $\mathcal{N}(E, 0)$ is asymmetric with respect to E (cf. Figure 6.2a), then (6.22) implies that there *must* be gaps that open and close.

   Corollary. *Topological phase transitions are unavoidable.*

2. $\theta = \pi/2$. From (6.23), one has $\mathcal{N}\left(E, \frac{\pi}{2}\right) = \mathcal{N}\left(E, -\frac{\pi}{2}\right)$. Together with (6.22), we have $\mathcal{N}\left(E, \frac{\pi}{2}\right) + \mathcal{N}\left(-E, \frac{\pi}{2}\right) = 1$.

   Corollary. $\mathcal{N}\left(E, \frac{\pi}{2}\right)$ *is symmetric with respect to* E, *and* $\mathcal{N}\left(E, \frac{\pi}{2}\right) = \mathcal{N}\left(E, -\frac{\pi}{2}\right)$.

These cases are presented in Figure 6.4.

Let us consider the change of the Sierpiński magnetic Hamiltonian with θ,

$$\begin{aligned}\partial_\theta H_L(\theta) &= \frac{t}{3}\sum_{\langle i,j\rangle}\left(\mathrm{i}\,\mathrm{e}^{\mathrm{i}\theta/3}\,c_i^\dagger c_j - \mathrm{i}\,\mathrm{e}^{-\mathrm{i}\theta/3}\,c_j^\dagger c_i\right)\\ &= \frac{t}{3}\sum_{\langle i,j\rangle}\left(\mathrm{e}^{\mathrm{i}(\theta+3\pi/2)/3}\,c_i^\dagger c_j + \mathrm{e}^{-\mathrm{i}(\theta+3\pi/2)/3}\,c_j^\dagger c_i\right)\\ &= \frac{1}{3}H_L(\theta + 3\pi/2)\,. \end{aligned} \tag{6.24}$$

A complementary approach is to rewrite (6.12) as

$$H_L(\theta) = \cos(\theta/3)\,H_0 + \sin(\theta/3)\,H_{3\pi/2}, \tag{6.25}$$

where $H_\theta \doteq H_L(\theta)$. Note that although $H_0 \neq H_{2\pi}$, one has $\mathrm{spec}(H_0) = \mathrm{spec}(H_{2\pi})$.

It is tempting to compare this Hamiltonian to a Zeeman interaction $\boldsymbol{B}\cdot\boldsymbol{\sigma}$, where $H_0 \sim \sigma_x$ and $H_{3\pi/2} \sim \sigma_y$. There are, however, two main differences. First, the spectrum of H_0 and $H_{3\pi/2}$ is different (cf. Figure 6.4) whereas $\mathrm{spec}(\sigma_i) = \pm 1$. Second, their commutation relations are not SU(2). Explicitly,

$$\left[H_0, H_{3\pi/2}\right] = -2\mathrm{i}\sum_{\langle\langle i,j\rangle\rangle}\left(c_i^\dagger c_j - c_j^\dagger c_i\right)\ \text{s.t.}\ (i,j) \in \left(\nabla_N^{(k)}, \nabla_N^{(l)}\right),\ k \neq l. \tag{6.26}$$

Thus, the next-nearest-neighbors $\langle\langle i, j\rangle\rangle$ belong to different highest-depth triangles ∇_N.

6.2.4 Sierpiński L-system and Tight Binding Correspondence

Let us reinspect the Sierpiński L-system with a slight change,

$$\pi_{\mathrm{Sier}^*}: \begin{cases} F \mapsto F + G - F - H + F, \\ G \mapsto G\,G, \\ H \mapsto H\,H, \end{cases} \tag{6.27}$$

so that F, G, H is draw a line; $\pm$ turn right $\pm 120^\circ$; $w_0 = F + G + H$. Note that all the F-s are pointing to the same direction, and similarly for G and H. As before, we translate it

to the substitution rule σ_{Sier^*} to create $1d$ words w_N. Applying formally the procedure of [27], we get the same gap labeling rule,

$$\mathcal{N}_{\text{Sier}^*} = \frac{1}{10}\frac{k}{3^N} \pmod 1, \quad k, N \in \mathbb{Z}. \tag{6.28}$$

Additionally, calculating the ζ-function using formally the procedure in Section 3.1.4, we have

$$\zeta_{\text{Sier}^*}(z) = \frac{1-z}{(1-3z)(1-2z)^2(1-z)}. \tag{6.29}$$

Hence, the Čech cohomologies read

$$\begin{aligned} \check{H}^0(\Omega_{\text{Sier}^*}, \mathbb{Z}) &= \mathbb{Z}, \\ \check{H}^1(\Omega_{\text{Sier}^*}, \mathbb{Z}) &= \mathbb{Z}[1/3] \oplus \mathbb{Z}[1/2]^2 \oplus \mathbb{Z}. \end{aligned} \tag{6.30}$$

Notice that $\check{H}^0 \cong \mathbb{Z}$ because the Sierpiński fractal is path connected. Additionally, $\check{H}^1 \supset \mathbb{Z}[1/3]$ as expected.

We saw that (6.27) gives rise to the tight binding Hamiltonian (6.6). Let us add the phase θ. Change $\pi_{\text{Sier}^*} \mapsto \pi_{\text{Sier}^*}(\theta)$ so that the rule stays the same, but F, G, H are now reinterpreted as "draw a line acquiring a phase of $e^{i\theta/3}$." The tight binding Hamiltonian for $\pi_{\text{Sier}^*}(\theta)$ changes to (6.12). It is well-defined, since each of F, G, H has the same γ_{ij}.

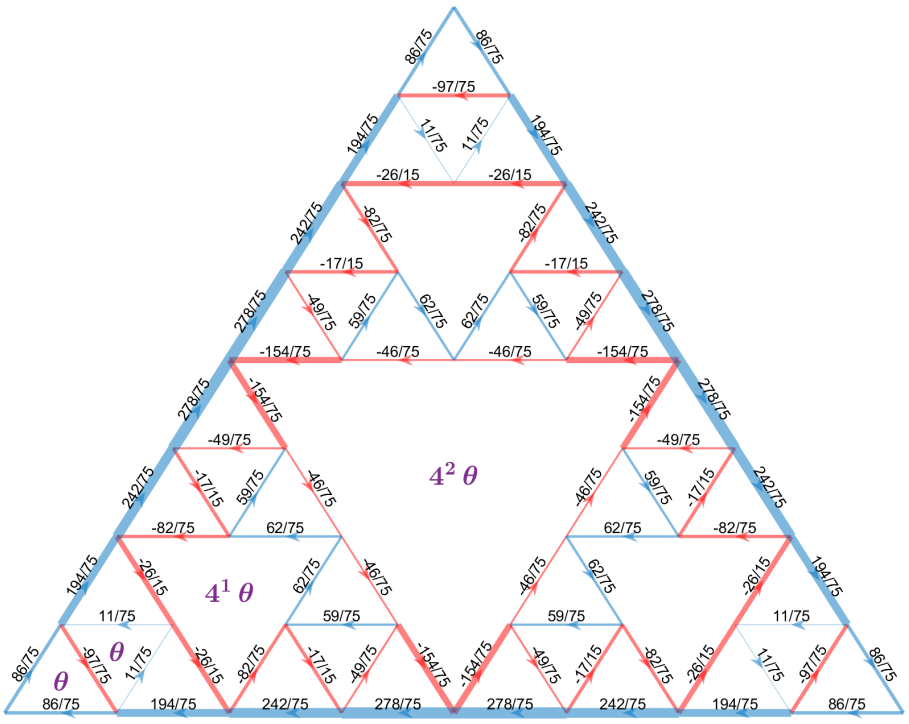

Figure 6.5: The angles $\alpha_{ij}^{\text{area}}/\theta$ for the Sierpiński Gasket of order $n = 3$. The values are shown above each edge and illustrated by its width. Blue and red edges indicate positive and negative values, respectively, with respect to the angles γ_{ij} indicated by the arrows. The flux inside each triangle representative is presented in purple.

As we have only reinterpreted the drawing rule, the substitution system is unchanged, namely, $\sigma_{\text{Sier}^*} = \sigma_{\text{Sier}^*}(\theta)$. Thus, $w_N = w_N(\theta)$ and the combinatorics are unaffected. Therefore, the gap labeling rule, ζ-function and Čech cohomologies remain unaltered.

Corollary. *The gap labeling rule of the magnetic Sierpiński Hamiltonian (6.12) is independent of θ. Namely, all gaps—opened or closed—must reside on $k/3^N$.*

Remark. The factor of $1/10$ in (6.28) comes from the combinatorics of the $1d$ chain. It is not seen in the tight binding calculation (cf. Figure 6.3).

6.2.5 Flux Penetrating the Entire Gasket

In Section 6.2.2, we have considered a linear flux penetrating the Gasket. The results were staggering—quantum phase transition have appeared. However, such a flux is either non-physical or difficult to realize experimentally at best. We shall follow the ideas of S. Alexander [118–120] immersing the whole Gasket in a magnetic field.

Consider a Sierpiński Gasket immerged entirely in a perpendicular magnetic flux. We shall call it the "area model." By means of Peierls substitution, assign phases to each edge of the graph as in (6.12). However, unlike the previous case in (6.14), the phases α_{ij} are not all equal. They obey the following criteria.

1. The phases surrounding a triangle sum up to the flux inside that triangle,

$$\begin{cases} \sum_{\nabla_m} \alpha_{ij} = 4^{m-1}\theta, \\ \sum_{\triangle} \alpha_{ij} = \theta. \end{cases} \tag{6.31a}$$

   Here, ∇_m is the downward triangle of the m^{th} depth, $\triangle$ is the upward (smallest) triangle. As before, θ is the total angle (normalized flux) through the smallest plaquette $\triangle$. See Figure 6.5 for illustration.

2. We enforce a Kirchhoff-like condition by applying the London gauge [118, 120]. Namely, the total of phases through a node i must vanish,

$$\sum_j \alpha_{ij} = 0, \quad \forall i. \tag{6.31b}$$

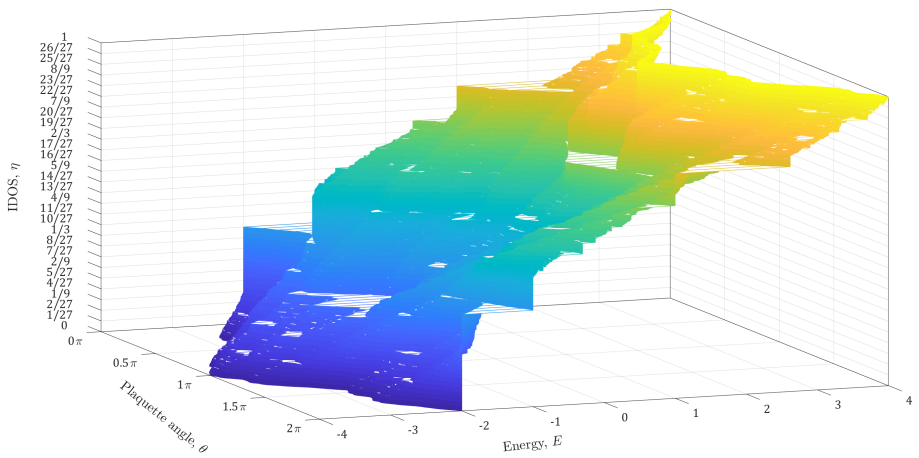

Figure 6.6: IDOS of the Sierpiński Gasket in a magnetic flux (area model).

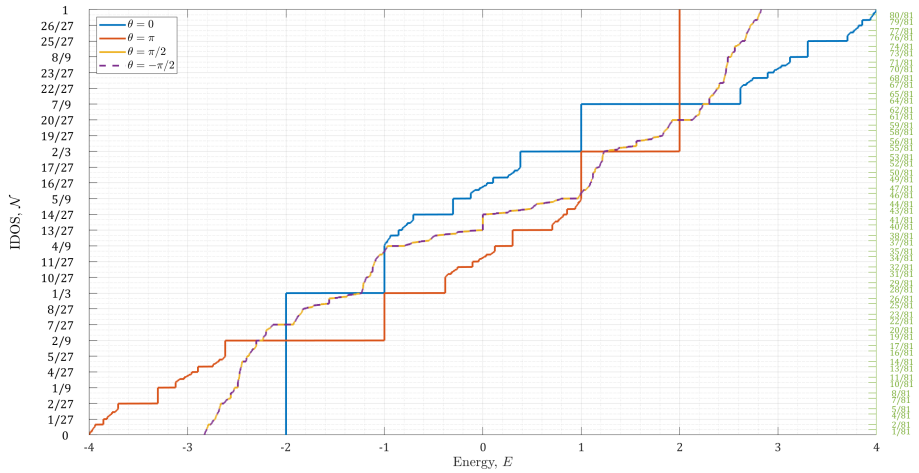

Figure 6.7: IDOS of the Sierpiński Gasket for chosen angles θ (area model).

We need to solve 3^{n+1} equations to obtain uniquely all the angles α_{ij} for the n^{th} order of the Sierpiński Gasket. By Euler's formula, criteria (6.31) above give us $3^{n+1}+1$ conditions (for depths $m = 1 \dots n$). Changing the gauge (6.31b) to $\sum_j \alpha_{ij} = v_i$ implies $\sum_i v_i = 0$ (since $\alpha_{ij} = -\alpha_{ji}$), thus removing one condition on the nodes.

Claim. If we, alternatively, change condition (6.31a) for the *downward triangles* to $\sum_{\nabla_m} \alpha_{ij} = -2^{m-1}\theta$, we are back in the linear model of Section 6.2.2.

Problem. Unlike (6.14), no closed form for $\alpha_{ij}^{\text{area}}$ has been found thus far. Their values are computed by solving equations (6.31).

Solving (6.12) in the area model, we have a similar picture of gaps appearing and disappearing, as seen in Figure 6.6. Moreover, looking closely (as in Figure 6.7), the gaps still reside on the same $\mathcal{N}_{\text{Sier}}^{\text{area}} = k\,3^{-N}$ as before (see Figure 6.4); only their locations in E have changed.

Corollary. *The IDOS condition $\mathcal{N}_{\text{Sier}} = k\,3^{-N}$ is a property of the L-system combinatorics rather than the model's flux conditions.*

Inspecting closer the angles α_{ij} in the area model (see Figure 6.5), we have a surprising result. Their values at the n^{th} order are rationals following the rule,

$$\frac{\alpha_{ij}^{\text{area}}}{\theta} = \frac{k_{ij}}{3 \times 5^{n-1}}, \quad k_{ij} \in \mathbb{Z}. \tag{6.32}$$

In other words, we have retrieved the factor 5 of d_s without any approximations. Note that these values can be negative, namely, in the opposite direction of γ_{ij}. Recall that in the linear model, $\alpha_{ij} = 1/3$ as in (6.14).

Corollary. *The dimension d_s can be inferred from the consistency conditions for α_{ij} with magnetic flux. No Hamiltonian needs to be solved.*

Remark. In [118, 119], the Hamiltonian (6.12) is not solved, but rather,

$$H_A \psi_k = \tfrac{1}{4} Z\, E_k \psi_k, \tag{6.33}$$

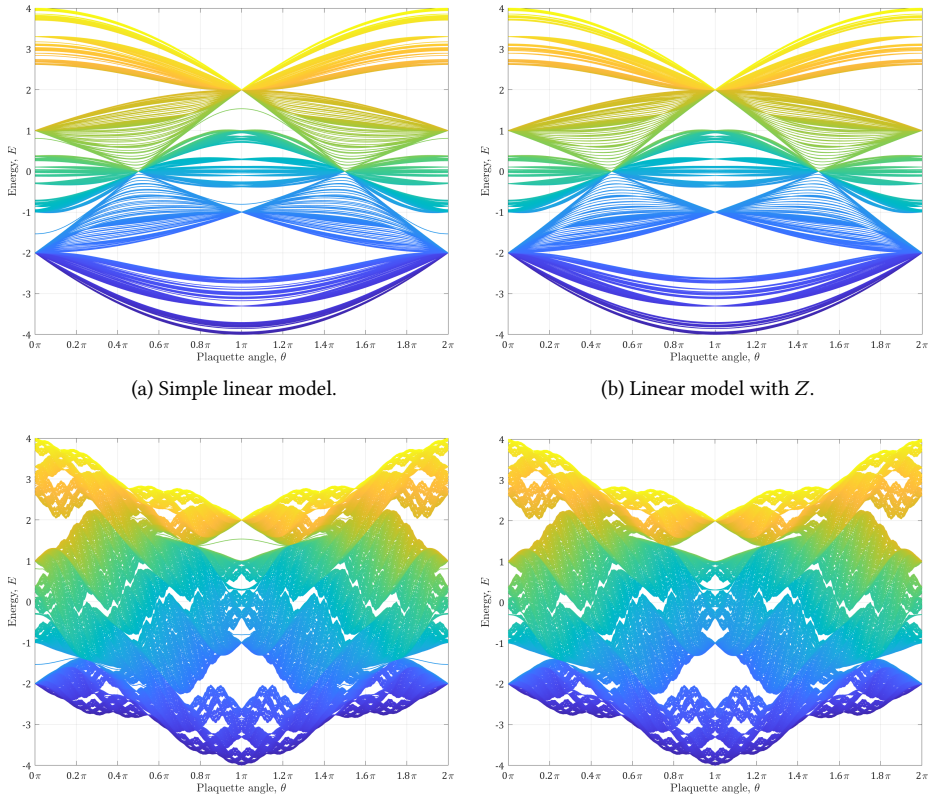

(a) Simple linear model.

(b) Linear model with Z.

(c) Simple area model.

(d) Area model with Z.

Figure 6.8: The spectrum of $H_P(\theta)$ with respect to Z in different flux models. Colors represent band index. (a) Simple linear model; (b) linear model with Z; (c) simple area model; (d) area model with Z.

where Z is a diagonal matrix of the number of neighbors of each node. Since all but the 3 head nodes have 4 neighbors, Z is expected to have a negligible effect on the results. However, its absence produces edge modes both in the linear and the area model, as presented in Figure 6.8. It also affects the eigenfunctions, which are imperative in Section 6.3, although the main results do not change.

Claim. The gaps in the area model open and close only at $\theta = 0, \pi, \pm\pi/2$ as before. Thus, the area model also exhibits topological phase transitions.

Remark. Making Peierls approximation (6.33) to the free-particle Schrödinger equation $(\mathrm{i}\boldsymbol{\nabla} - \boldsymbol{A}/\Phi_0)^2 \psi = q^2\psi$, obtain $q = \ell^{-1} \arccos E/4$ (see Appendix 6.A.1 and [118–120]). Being a monotonically decreasing function, the IDOS rule $\mathcal{N}_{\text{Sier}} = k\, 3^{-N}$ persists.

6.2.6 Flux Conditions

Adding a magnetic flux to the Sierpiński Gasket may change the topological group of the system. Take, for instance, the Hofstadter model [108]. Without a magnetic field, the system is boring with a single gap (so that $\check{H}^1 \cong \mathbb{Z}$); after adding a magnetic field with an irrational flux ($\Phi/\Phi_0 \notin \mathbb{Q}$) there appear an infinite amount of gaps ($\check{H}^1 \cong \mathbb{Z}^2$).

The resulting Wannier butterfly [121, 122] is very reminiscent of the one created in $1d$ C&P system (cf. Figure 5.7b). It can be shown that these two systems exhibit the same tiling rule. In the Sierpiński Gasket, however, we cannot utilize such methods. It was created by a $1d$ rule (e.g., (6.27)), but any flux condition (6.31a) is $2d$ by default. As we add a dimension instead of reducing one, we cannot use the construction of [45]. We thus need to describe the topological group in a different way.

Let us inspect (6.31a) and generalize it. Consider how the *flux* changes after application of the inflation (6.27), namely, use the tiling procedure on the magnetic fluxes. Let A be the flux though an upward plaquette $\triangle$, and B_m the flux though the downward plaquette of m^{th} depth $\triangledown_m$. Then,

$$\sigma^{\Phi}_{\text{Sier}}:\begin{cases} A \mapsto 3A + rB_1 \\ B_1 \mapsto bB_2 \\ B_2 \mapsto bB_3 \\ \quad\vdots \end{cases} \iff M^{\Phi}_{\text{Sier}} = \begin{pmatrix} 3 & r & & \\ & 0 & b & \\ & & 0 & b \\ & & & \ddots & \ddots \end{pmatrix}. \tag{6.34}$$

Here r is the ratio between the fluxes in $\triangle$ and $\triangledown_1$, and b is the basis of growth (inflation). In the area model $(b, r) = (4, +1)$, whereas in the linear model $(b, r) = (2, -1)$. This is an infinite inflation rule, which resembles a C&P scheme represented in a substitution language. Additionally, (6.31a) is rephrased as

$$\begin{cases} \sum_{\triangledown_m} \alpha_{ij} = rb^{m-1}\theta, \\ \sum_{\triangle} \alpha_{ij} = \theta. \end{cases} \tag{6.35}$$

We now have two knobs to probe. When $\theta = 0$, all the spectra are the same for any value of (b, r). However, when $\theta = \pi/2$, the spectra are different between the linear $(2, -1)$ and area $(4, +1)$ models (cf. Figures 6.4 and 6.7). Take a path between the linear and area models, say $(2, -1) \to (2, 0) = (4, 0) \to (4, +1)$. Note that the middle point is equivalent in any basis (no flux penetrating any of the $\triangledown_m$). Gaps that open or close in this path imply a different magnetic character between both end points. This is readily seen in Figure 6.9. The gaps retain the IDOS rule $\mathcal{N}_{\text{Sier}} = k\, 3^{-N}$.

The numerical calculation shows indeed a different character between $b = 2$ and $b = 4$. Yet, we cannot characterize it with (6.34), since the emerging tiling is infinite and our current tools do not support such tilings. This is reminiscent of the pinwheel tiling having an irrational rotation and thus an infinite number of tiles. In that case, *rotations* were added to the tiling space resulting in two types of tiles only (see Chap. 4 of [52]). Using these ideas, add *flux growth* to the tiling space so that (6.34) changes to

$$\sigma^{\Phi}_{\text{Sier}}:\begin{cases} A \mapsto 3A + rB \\ B \mapsto bB \end{cases} \iff M^{\Phi}_{\text{Sier}} = \begin{pmatrix} 3 & r \\ 0 & b \end{pmatrix}. \tag{6.36}$$

This substitution rule works with our established machinery. Since we deal with $2d$ tilings (since flux corresponds to area), the corresponding Čech cohomology is $\check{H}^2$ [45]. However, since we do not deal with a proper tiling space, the cohomology group is not $\check{H}^2$ by definition. That being said, we nonetheless call this group $\check{H}^2$ due to the similarities between tiling and flux spaces.

Calculating the $\check{H}^2$ group (similarly to $\check{H}^1$ in Section 3.1.4), one obtains,

$$\check{H}^2\left(\Omega^{\Phi}_{\text{g}}, \mathbb{Z}\right) \cong \mathbb{Z}\left[3^{-1}\right] \oplus \mathbb{Z}\left[b^{-1}\right], \tag{6.37}$$

where Ω^{Φ}_{g} is the new flux tiling space containing growth. Note that the ratio r does not play a role in the group characterization.

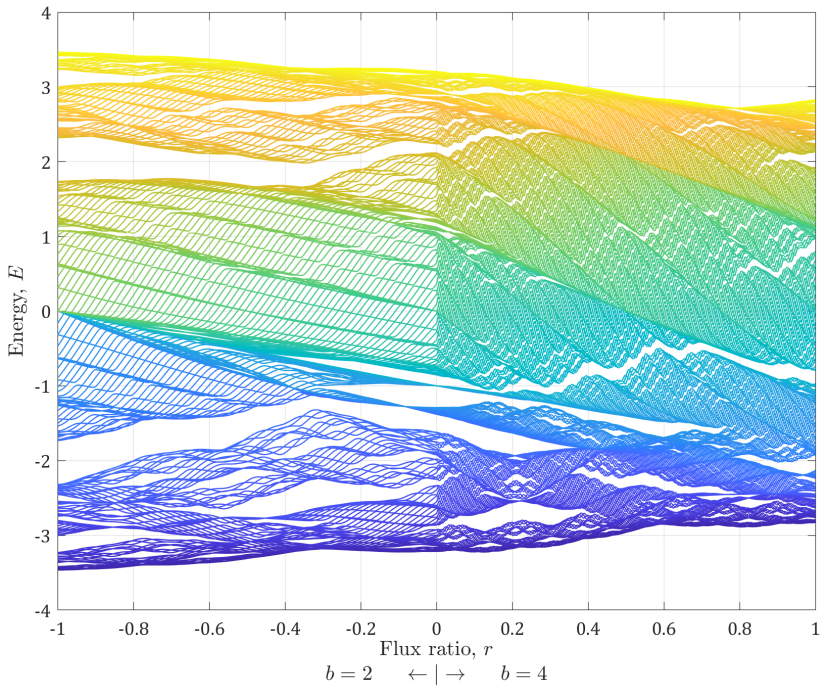

Figure 6.9: Spectrum of H_P with generalized flux conditions for $\theta = \pi/2$ and order $n = 5$. Negative r spectra are calculated in the linear model ($b = 2$); positive r spectra are in the area model ($b = 4$).

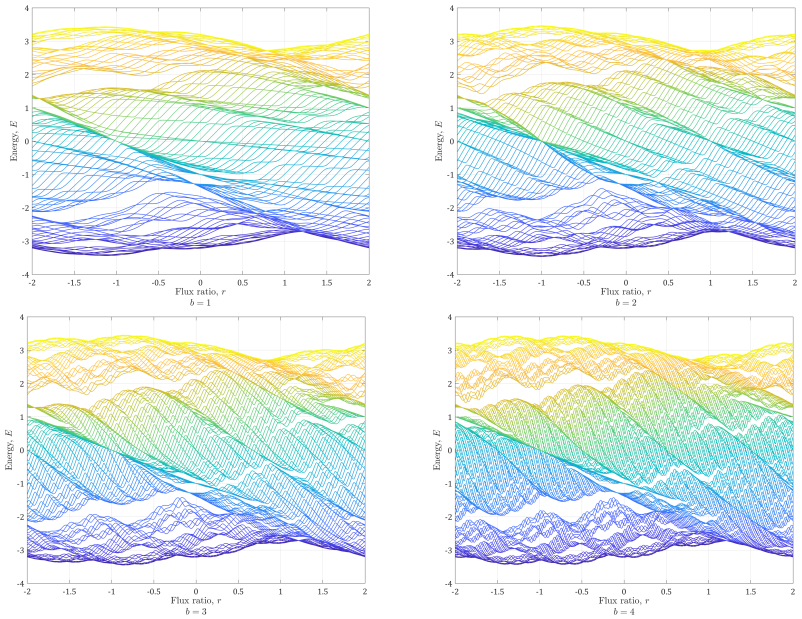

Figure 6.10: Spectrum of H_P with generalized flux conditions in different bases for $\theta = \pi/2$ and order $n = 5$. (a–d) $b = (1, 2, 3, 4)$, respectively, for a full spectral period.

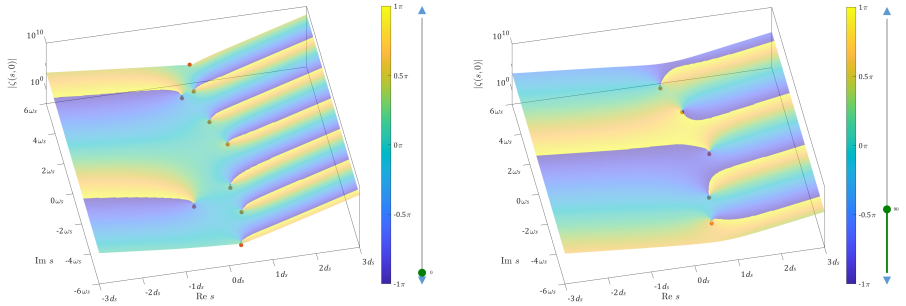

(a) ζ-function at $\theta = 0$. (b) ζ-function at $\theta = \pi/2$.

Figure 6.11: $\zeta_0(s;\theta)$ on a Sierpiński Gasket of order $n = 5$. (a) $\theta = 0$; (b) $\theta = \pi/2$. The amplitude is represented by height (logarithmic scale) and the phase by coloring (scale on the right). The zeros of $\zeta_0(s;\theta)$ are shown by red dots.

Corollary. *The linear and area models have different topological $\check{H}^2$ groups, namely, $\mathbb{Z}\left[\frac{1}{3}\right] \oplus \mathbb{Z}\left[\frac{1}{2}\right]$ and $\mathbb{Z}\left[\frac{1}{3}\right] \oplus \mathbb{Z}\left[\frac{1}{4}\right]$, respectively.*

The $\check{H}^2$ group does not add to the GLT, which stems from $\check{H}^1 \cong \mathbb{Z}\left[\frac{1}{3}\right] \oplus \mathbb{Z}\left[\frac{1}{2}\right]^2$. However, it changes the spectrum and its characteristics as shown in Figure 6.9. For instance, the positive and negative slopes of $b = 2$ in Figure 6.9 appear also in $b = 4$ (with larger values), but the latter has an additional set of negative slopes resulting in a "denser" pattern. A comparison of different bases is shown in Figure 6.10. The spectra of $H_P(\theta;\ b, r)$ are periodic so that

$$\operatorname{spec} H_P(2\pi/R;\ b, r) = \operatorname{spec} H_P(2\pi/R;\ b, r+R). \tag{6.38}$$

6.2.7 Spectral Zeta Function

Another way to characterize fractal systems is by the associated ζ-function [109, 113, 114]. This opens the path for thermodynamics, spectral dimensions and other physical properties. On the Sierpiński Gasket, the ζ-function has been considered thus far only for the Laplacian in zero flux [123, 124]. Let us extend these results.

The ζ-function is defined as [113]

$$\zeta(s,\gamma) \doteq \sum_k \frac{g_k}{(E_k+\gamma)^s}, \tag{6.39}$$

where g_k is the degeneracy of E_k and $s, \gamma \in \mathbb{C}$. It is the Mellin-Laplace transform of the heat kernel $Z(t)$,

$$\zeta(s,\gamma) = \Gamma(s)^{-1} \int_0^\infty \mathrm{d}t\, t^{s-1} Z(t)\, \mathrm{e}^{-\gamma t}, \tag{6.40}$$

where $\Gamma(s)$ is the gamma function and

$$Z(t) \doteq \sum_k g_k\, \mathrm{e}^{-E_k t}. \tag{6.41}$$

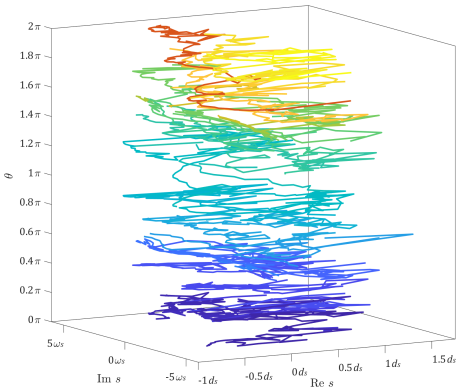

Figure 6.12: The location of $\zeta_0(s;\theta)$ zeros with respect to θ. Line colors represent contiguous zero change. The red line is emphasized for clarity.

For our purposes, we calculate the poles and zeros of the Sierpiński Gasket with respect to the magnetic flux at $\gamma = 0$,

$$\zeta_0(s;\theta) \doteq \zeta_{H_P(\theta)}(s,0)\Big|_{E_k\neq 0} = \sum_{k,E_k\neq 0} \frac{g_k}{(E_k(\theta))^s}. \tag{6.42}$$

The condition $E_k \neq 0$ is required to avoid infinities [123]. The poles of $\zeta_0(s;0)$ are located at $\{i\omega_s n, d_s + i\omega_s n : n \in \mathbb{Z}\}$ (see [123, 124]), where $d_s = \ln 9/\ln 5$ and $\omega_s = 2\pi/\ln 5$ for the Sierpiński Gasket. Figure 6.11 shows a calculation of $\zeta_0(s;\theta)$ for fluxes $\theta = (0, \pi/2)$.

We are left with the task of identifying the poles and zeros of $\zeta_0(s;\theta)$. Numerically, it is a challenging task, since we might never compute a pole or zero s_0 but rather points in its neighborhood. However, we can use a property of meromorphic functions $f(s)$: that $\arg f(s)$ winds around a pole or a zero s_0. Define the curl of $\zeta_0(s;\theta)$ by

$$C(s;\theta) = \partial_x \operatorname{Im}\zeta_0(s;\theta) - \partial_y \operatorname{Re}\zeta_0(s;\theta), \quad s = x + iy. \tag{6.43}$$

The zeros and poles are identified when $C(s_0;\theta) \geq C_0$, where $C_0 = 2\pi$. We may lower a bit C_0 to increase sensitivity. Figure 6.12 shows the variation of the zeros of $\zeta_0(s;\theta)$ using this method.

6.3 Eigenfunctions on Fractals

Thus far, we have analyzed the structural properties and the distribution of energies on fractals—with and without magnetic flux. These all were static properties of the system. Next, we would like to inspect the eigenfunctions on fractals to infer some winding and transport properties of fractals, as will be shown below.

6.3.1 Sierpiński Eigenfunctions

Consider the Hamiltonian (6.33) in the area model, and calculate its eigenfunctions ψ_k,

$$H_A(\theta)\psi_k = \tfrac{1}{4} Z E_k \psi_k. \tag{6.44}$$

These eigenfunctions must retain the Sierpiński C_3 symmetry [118]. For degenerate ψ_k, the numerical solver typically finds non-C_3-symmetric solutions. Yet, there always exists a C_3-symmetric linear combination of these states.

Remark. To force C_3-symmetric solutions ψ_k, one may add a small regularization mass term $|\mu| \ll |t|$ to (6.12) using $\mu \sum_i c_i^\dagger c_i$. However, since $\arg \psi_k$ is numerically susceptible to such changes, we drop it for now.

In some parameter combinations, the eigenfunctions obtain a very special shape: they exist only on a single depth $\triangledown_m$. The case of the boundary $\triangle_0$ and the first depth $\triangledown_1$ is shown in Figure 6.13. To quantify this, we define the overlap for the m^{th} depth as

$$O_k^m = \langle \psi_k | \mathbb{1}_m | \psi_k \rangle \, / \langle \psi_k | \psi_k \rangle \,, \tag{6.45}$$

where $\mathbb{1}_m$ is the indicator function on $\triangle_0$ or $\triangledown_{m>0}$, respectively. The results for O^0 and O^1 are presented in Figure 6.14 as a function of the flux θ and the IDOS $\mathcal{N}$ (since $\mathcal{N}$ has a linear scale whereas E does not). We have several immediate results.

1. The large overlaps are located in distinct bands.
2. Overlaps of different depths come consecutively (checker-board band pattern).
3. Jumps in overlaps occur near the gaps $\mathcal{N} = k\, 3^{-N}$.
4. The deeper the depth is, the less distinct the overlap becomes. The boundary (depth 0) has the highest overlap.

6.3.2 Sierpiński Eigenfunction Windings

Since the eigenfunctions are vectors $\psi_k \in \mathbb{C}^{N_n}$ (with N_n the number of nodes), they have an amplitude $|\psi_k|^2$ and a phase

$$\vartheta_k = \arg \psi_k. \tag{6.46}$$

Similarly to the quasiperiodic case, we inquire whether this phase winds with respect to some φ. Let us define this new phason φ. For each triangle $\triangledown_m$, define its center $\boldsymbol{r}_c^m$.

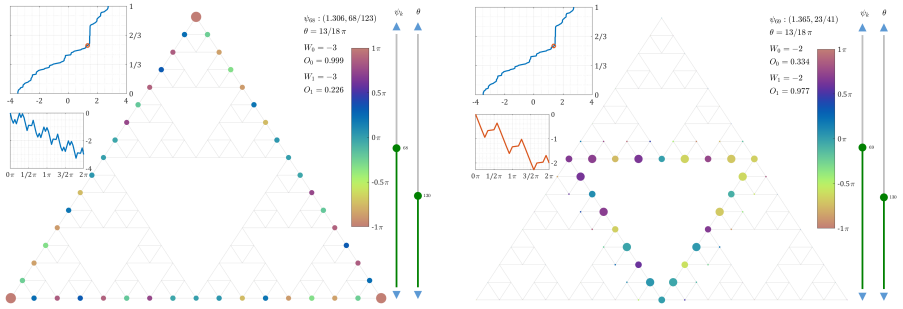

(a) An eigenfunction on the boundary $\triangle_0$.

(b) An eigenfunction on $\triangledown_1$.

Figure 6.13: Eigenfunctions on a Sierpiński Gasket of order $n = 4$. (a) The 68^{th} eigenfunction; (b) the 69^{th} eigenfunction. The flux is $\theta = 13\pi/18$ for both cases. The amplitude is indicated by circle radius and the phase by a cyclic color map (right). Top-left inset: the IDOS for the current flux with the energy shown by the red circle. Middle-left inset: winding of the phase ϑ_k with respect to φ.

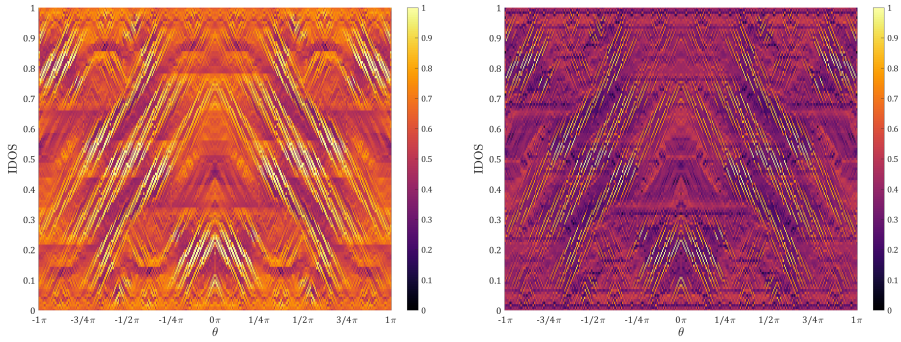

(a) Overlap of $\triangle_0$. (b) Overlap of $\triangledown_1$.

Figure 6.14: Overlaps of $\triangle_0$ and $\triangledown_1$ vs. IDOS $\mathcal{N}$ and flux θ for order $n = 4$.

It is unambiguous for $\triangle_0$ and $\triangledown_1$ lying in the center of the Gasket (we shall not deal with $m \geq 2$ for now). The phase $\tilde{\varphi}$, defined on the whole Gasket, is then

$$\tilde{\varphi}^m_{ij} \doteq \tan^{-1}\left(\bar{r}^y_{ij} \,/\, \bar{r}^x_{ij}\right), \quad \bar{\boldsymbol{r}}_{ij} \doteq \boldsymbol{r}_{ij} - \boldsymbol{r}^m_c. \tag{6.47}$$

Restricting $\tilde{\varphi}^m$ on its m^{th} triangle, we have a well-defined phase $\varphi^m \in [0, 2\pi]$,

$$\varphi^m_l \doteq \tilde{\varphi}^m_{ij}\big|_{\substack{\triangle_0 \text{ for } m=0\,, \\ \triangledown_1 \text{ for } m=1}} \quad \varphi^m_l < \varphi^m_{l+1}. \tag{6.48}$$

The winding W^m_k is then just the winding of ϑ_k with respect to φ^m defined as,

$$W^m_k \doteq \frac{1}{2\pi} \sum_l \frac{\delta \vartheta_k}{\delta \varphi^m_l} \Delta\varphi^m_l \doteq \frac{1}{2\pi} \sum_l \delta\vartheta^m_{k,l}. \tag{6.49}$$

The winding W^m_k is well-defined only on the wavefunctions ψ_k with $O^0_k = 1$ or $O^1_k = 1$. To be less strict, we define a threshold ε so that W^m_k is well-defined for $O^n_k > 1 - \varepsilon$ and 0 otherwise. To avoid abrupt changes, we use a threshold function f_ϵ instead. Figure 6.15 shows the winding with respect to this threshold.

Unfortunately, the winding W^m_k is not well-behaved while increasing the fractal order n. The general shape (and overlap) of the eigenfunction retains, but the winding value may change. This is unlike the quasiperiodic case, where the phase Θ and its winding converge well with n. It might be numerical diagonalization issues, degeneracy, or an ambiguous definition of phase. Either way, we cannot currently use the eigenfunction winding as a tool.

6.3.3 Sierpiński Currents

We use the spatial locations of the eigenstates in order to construct some interesting phenomena. Consider, for instance, an eigenstate $\psi_0 = \psi\left(\mathcal{N}^0, \theta\right)$ living on the boundary $\triangle_0$ only, namely, $O^0\left(\psi_0\right) \simeq 1$. We set the IDOS to $\mathcal{N}^0$, the flux to θ, and inject a thermodynamic current into one of the Gasket's head nodes. Since the corresponding state is ψ_0, the current I will stay on the boundary $\triangle_0$.

Now, suppose we want the current to flow on the first-depth triangle $\triangledown_1$. We need an eigenstate $\psi_1 = \psi\left(\mathcal{N}^1, \theta\right)$ with $O^1\left(\psi_1\right) \simeq 1$. However, since $O^1\left(\psi_0\right) \simeq O^0\left(\psi_1\right) \simeq 0$,

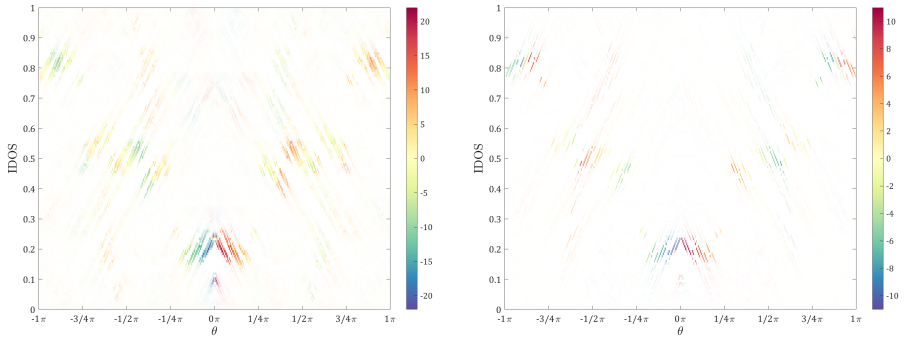

(a) Winding at $\triangle_0$. (b) Winding at $\triangledown_1$.

Figure 6.15: Windings at $\triangle_0$ and $\triangledown_1$ vs. IDOS $\mathcal{N}$ and flux θ for order $n = 4$. The threshold is $\varepsilon = 0.05$ with a threshold function (white saturation) $f_\varepsilon = \tan^{-1}(8\pi(O^m - (1-\varepsilon)))$.

we cannot just change $\mathcal{N}$ and θ to transfer between ψ_0 and ψ_1; we need an intermediate state ψ_{01} that has a large overlap with both $\triangle_0$ and $\triangledown_1$, that is $O^0(\psi_{01}) \simeq O^1(\psi_{01}) \simeq 0.7$. Luckily, we have such a state as presented in Figure 6.16. All we need to do is to change $\mathcal{N}$ and θ to their respective values in $\psi_0 \to \psi_{01} \to \psi_1$ consecutively. The current I_1 will persist on $\triangledown_1$ as it has no channels of decay.

Suppose one desires a persistent current I_2 on $\triangledown_2$. Similarly to the discussion above, find ψ_{12} and ψ_2 to transfer the current to $\triangledown_2$ using $\psi_0 \to \psi_{01} \to \psi_1 \to \psi_{12} \to \psi_2$. Generalizing this approach, one can continue up to a desirable I_m on $\triangledown_m$ by

$$\psi_0 \to \psi_{01} \to \psi_1 \to \cdots \to \psi_{m-1,m} \to \psi_m. \tag{6.50}$$

Corollary. *We have defined a* topological storage *or* memory *with respect to the persistent current I_m at depth m. Keeping the system in the eigenstate ψ_m, the current will stay on $\triangledown_m$ and will not leak to other triangles. In particular, there is no interaction with the Sierpiński Gasket boundary $\triangle_0$ where the current is probed.*

Remark. Triangles of depth $\triangledown_m$ are adjacent to all triangles of depth $\triangledown_{m+1}$, but not to those of depth $\triangledown_{m+2}$ and above. Thus, we need to make the sequence (6.50) consecutive through all depths. Remarkably, since $\triangle_0$ touches all $\triangledown_1$, $\triangledown_2$ and $\triangledown_3$, we can make a shortcut at these stages.

6.4 Index Theorems on Fractals

Thus far, we have observed that L-system fractals encompass integer numbers corresponding to a labeling of the gaps. We have also shown that these gaps open and close with respect to an external order parameter—the magnetic flux θ. To finish our discussion, we attempt to give them a topological nature by matching gap numbers with a certain operator's index

The topology of fractals is different than the usual condensed matter systems in which the underlying lattice of the Hamiltonian is periodic. Thus, the application of the common formulae (as presented in Section 6.4.1) is not expected to work. Additionally, these index formulae require two continuous symmetries, whereas we have only the magnetic flux and no Brillouin zone. Finally, any index defined by means of projection

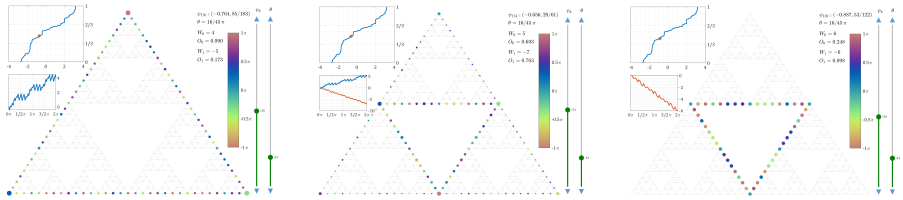

(a) Eigenstate at $\triangle_0$. (b) Eigenstate at both $\triangle_0$ and $\triangledown_1$. (c) Eigenstate at $\triangledown_1$.

Figure 6.16: Persistent current protocol on order $n = 5$ Sierpiński Gasket: start at $\psi_0 = \psi(\mathcal{N}_a, \theta)$, proceed to $\psi_{01} = \psi(\mathcal{N}_b, \theta)$ and finish with $\psi_1 = \psi(\mathcal{N}_c, \theta)$. (a) Eigenstate at $\triangle_0$ with $\mathcal{N}_a = 170/366$; (b) eigenstate at $\triangle_0$ and $\triangledown_1$ with $\mathcal{N}_b = 174/366$; (c) eigenstate at $\triangledown_1$ with $\mathcal{N}_c = 159/366$. The flux is $\theta = 16\pi/45$ in all three cases.

P_F requires a contiguous gap at E_F throughout the entire range of the flux. This is not the case in the Sierpiński Gasket, as presented in Figure 6.3.

6.4.1 Common Index Formulae

In this section, we present some unsuccessful tries to apply some index formula on the Sierpiński Gasket. In [125, 126], an attempt was made to apply an index to a band in the Sierpiński Gasket and carpet by means of a Chern number. The formula in question was given by [127],

$$\nu(P) = 12\pi \mathrm{i} \sum_{\substack{j\in B, i\in A \\ k\in C}} \left(P_{ij}P_{jk}P_{ki} - P_{ik}P_{kj}P_{ji}\right), \tag{6.51}$$

where A, B, C are regions dividing the space (see Figure 6.17), and P_{ij} are projections onto the l^{th} band given by

$$P_{ij} = \sum_{l\in\text{band}} \psi_l(i)\,\psi_l^*(j), \tag{6.52}$$

with $\psi_l(i)$ an eigenfunction of H_P on site i.

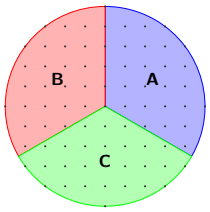

Figure 6.17: Kitaev's division of space.

The main issue with the application of (6.51) in [125, 126] is that a *local index formula* was used. Namely, the patches A, B, C were taken on a *finite patch* inside the Gasket rather than the entire fractal. Thus the boundary of the patch had a great effect, and non-integer numbers were obtained. Another issue is that Kitaev mainly deals with a *bipartite lattice* [127], which is not the case in the Sierpiński Gasket. Moreover, Kitaev required an infinite planar Bravais lattice. Thus, we need a different approach more suitable to the fractal case.

Another version of the index formula given by [127] is

$$\nu(P) = 2\pi \mathrm{i}\,\mathrm{Tr}\Big(P\left[[X,P],[Y,P]\right]\Big), \tag{6.53}$$

with P the projection onto the l^{th} band, and $[\cdot,\cdot]$ is a commutator. Note that this is a *continuous* version of (6.51), which is set on a lattice. This formula first appeared in the context of the quantum Hall conductance [4, 95, 96],

$$\mathrm{Ch}(P_F) = \int_{\mathbb{T}^2} \frac{\mathrm{d}^2\boldsymbol{k}}{2\pi\mathrm{i}}\,\mathrm{Tr}\big(P_F(\boldsymbol{k})\left[\partial_1 P_F(\boldsymbol{k}), \partial_2 P_F(\boldsymbol{k})\right]\big)$$

$$= \frac{1}{\pi}\int_0^{2\pi} \mathrm{d}k_1 \int_0^{2\pi} \mathrm{d}k_2 \ \mathrm{Im}\left\langle \partial_1 \xi\left(\boldsymbol{k}\right) | \partial_2 \xi\left(\boldsymbol{k}\right)\right\rangle, \tag{6.54}$$

for, $\partial_i = \partial/\partial k_i$ and $P_F\left(\boldsymbol{k}\right)\xi\left(\boldsymbol{k}\right) = \xi\left(\boldsymbol{k}\right)$ with $P_F\left(\boldsymbol{k}\right)$ a projection on all energies smaller than the Fermi energy E_F, namely, $E \leq E_F$. Another version of this formula appears in [128], where the index of a continuous quasiperiodic acoustic structure is taken to be

$$\mathrm{Ch}\left(P_F\right) = \mathrm{Tr}_L\Big(P_F\left[\partial_\phi P_F, \left[Z, P_F\right]\right]\Big), \tag{6.55}$$

where Tr_L is trace per unit length, ϕ the phason degree of freedom, and Z the coordinate along the structure. Note that the derivative with respect to ϕ is explicit.

Since we deal with the Sierpiński Gasket, we must find a set of periodic operators representing the symmetries of the Gasket. Because it has a natural C_3 symmetry, we choose the rotation $R_{2\pi/3}$ and the reflection Π around one of the Gasket's (triangle's) symmetry axes. The relevant index formula reads

$$\nu\left(P\right) = \mathrm{Tr}\Big(P\left[\left[R_{2\pi/3}, P\right], \left[\Pi, P\right]\right]\Big). \tag{6.56}$$

Unfortunately, this formula works only for the highly symmetric H_0 and $H_{\pi/2}$; other values of θ do not display meaningful results. That being said, since the numbers $\nu\left(P\right)$ are integers corresponding to a band, this approach has some promise.

Another symmetry presented is the periodicity of the eigenenergies in the flux $\theta \mapsto \theta + 2\pi$. Therefore we need to seek some magnetic group. We shall use the fact that—independently on the flux model—gaps open close at those fluxes θ_d at which $\mathrm{spec}\left[H\left(\theta_d\right)\right]$ is degenerate. In the first order (low Fractal depth n), $\theta_d^{(1)} = d\,\pi/2$ with $d \in \mathbb{Z}$; second order goes as $\theta_d^{(2)} = d\,\pi/2^2$; generally, $\theta_d^{(r)} = d\,\pi/2^r$. The degeneracy is more prominent in the linear flux model. Therefore, we cannot follow the bands uniquely. Denote, as before, $P_F\left(\theta\right)$ the projection on all energies $E \leq E_F$ of $H_P\left(\theta\right)$. However, generally, the gap does not persist with E_F as we change θ. Thus, a Chern number calculation [34, 95, 105] (similarly to (6.54)),

$$\mathrm{Ch}\left(P_F\right) = \frac{1}{2\pi\mathrm{i}}\int_{\mathbb{T}^2} \mathrm{d}\theta\,\mathrm{d}\phi\,\mathrm{Tr}\Big(P_F\left[\partial_\theta P_F, \partial_\phi P_F\right]\Big), \tag{6.57}$$

would not work.

6.4.2 Multiplicity and Index

Let us analyze the possible index from the Hamiltonian multiplicity considerations. The Linear Hamiltonian reads

$$H_L\left(\theta\right) = \sum_{\langle i,j\rangle} \exp\left(\mathrm{i}\alpha_{ij}\right) c_i^\dagger c_j + \mathrm{h.c.}, \quad \alpha_{ij} = \theta/3, \tag{6.58}$$

where α_{ij}^P is specified in the counter-clockwise direction. This implies, on the one hand, that $H_L\left(\theta\right) = H_L\left(\theta + 2\pi a \times 3\right)$ with $a \in \mathbb{Z}$. On the other hand, we saw that $\mathrm{spec}\left[H_L\left(\theta\right)\right] = \mathrm{spec}\left[H_L\left(\theta + 2\pi b\right)\right]$ with $b \in \mathbb{Z}$. Thus we have a 3-fold multiplicity in the solutions. This can also be seen from (6.25).

In the area model (of n^{th} order),

$$H_A^n\left(\theta\right) = \sum_{\langle i,j\rangle} \exp\left(\mathrm{i}\alpha_{ij}^n\right) c_i^\dagger c_j + \mathrm{h.c.}, \quad \alpha_{ij}^n = \theta\,\frac{k_{ij}}{3\cdot 5^{n-1}},\ k_{ij} \in \mathbb{Z}. \tag{6.59}$$

Similarly to the linear model, this implies $H_A^n(\theta) = H_A^n\left(\theta + 2\pi a \times 3 \cdot 5^{n-1}\right)$ together with spec $[H_A^n(\theta)]$ = spec $[H_A^n(\theta + 2\pi b)]$ with $a, b \in \mathbb{Z}$. Thus a $3{\cdot}5^{n-1}$-fold degeneracy unravels.

Corollary. *Any flux model with $\alpha_{ij}^n/\theta = k_{ij}/q_n$, where q_n is the least common multiplier of all the denominators, will have an q_n-fold multiplicity.*

Remark. The degeneracy does not prove the existence of a topological index, but rather implies its possibility.

After finding the multiplicity, let us check the corresponding degeneracy of the energy. For each flux change of 2π, define the degeneracy of the l^{th} band as

$$g_l = |\{E_l(\theta) \mid E_l(\theta) \text{ is degenerate at } \theta \in [-\pi q_n, \pi q_n)\}|. \tag{6.60}$$

Highly degenerate spectra appear at fluxes θ_d. Note that this definition of g_l is insensitive to sign, which has to be calculated otherwise.

6.4.3 The Zak Phase

Let us now inspect the Zak phase (5.76). Although there is no Brillouin zone to speak of, there exists a coordinate θ by which the Hamiltonian is periodic. It differs from the Berry phase case, which requires at least 2 periodic coordinates. In our case, the Zak phase is written as an integral over the Berry connection,

$$\gamma_l = \mathrm{i}\int_C \mathrm{d}\theta \left\langle \psi_l(\theta) \middle| \frac{\partial}{\partial\theta}\psi_l(\theta) \right\rangle, \tag{6.61}$$

where $C \doteq C(\theta(t))$ denotes a path in θ such that $H(\theta(0)) = H(\theta(T))$. The $|\psi_l(\theta)\rangle$ are the eigenfunctions of $H(\theta)$, which are unique up to the eigenenergy degeneracy happening in θ_d. This degeneracy makes the calculation of the index rather cumbersome, as one cannot follow uniquely the eigenfunctions through the fluxes θ_d. Unfortunately, the simplifications of [29] would not work, as the problem is $1d$ and there is no simple closed formula for the solutions. A direct application of Berry's formula requires a second periodic continuous coordinate; it does not exist in the present case.

An important issue with (6.61) is that the phase of $|\psi_l(\theta)\rangle$ is not unique. To deal with it, a phase independent formula was derived in [29]. However, it is not applicable in a single periodic coordinate. An attempt to align all eigenfunctions (by normalizing the total phase by the phase of the head node) produced inconclusive results. There is an apparent phase jump across a degeneracy point θ_d, which can be probed by a principle derivative,

$$\langle\psi_l^i|\mathrm{i}\partial_\theta^P|\psi_l^i\rangle \doteq \frac{\langle\psi_l^{i+1}| + \langle\psi_l^i|}{2}\,\mathrm{i}\frac{|\psi_l^{i+1}\rangle - |\psi_l^i\rangle}{\Delta\theta} = \frac{\mathrm{Im}\,\langle\psi_l^{i+1}|\psi_l^i\rangle}{\Delta\theta}, \tag{6.62}$$

where $\psi_l^i \doteq \psi_l(\theta_i)$ and $\Delta\theta = \theta_{i+1} - \theta_i$ choosing $\theta_i = \theta_d - \frac{1}{2}\Delta\theta$. However, there exist fictitious phase jumps far from θ_d, which make the calculation of the Zak phase (6.61) inconsistent. In total, this method yields $\gamma_l \simeq 0$ for most l with some irregularities as described above.

Corollary. *Either the Zak phase nullifies for the Sierpiński Gasket, or we must directly probe the degeneracy fluxes θ_d.*

Another method to lift the degeneracy is to apply a small disorder as in (6.70) or (6.71) with $W \ll t$. However, this disorder does not preserve the Zak phase γ_l for different realizations. Thus it cannot be used to calculate the phase. It also suggests that the Zak phase of (6.61) is not topologically protected.

An alternative approach to disorder is to add a small on-site regularization mass term [6] that explicitly breaks the Sierpiński Gasket's symmetry. However, such attempts did not yield meaningful results. Similarly to the disordered case, the calculated phase was susceptible to abscissas' locations or amount, fractal order, and so on.

6.4.4 An Emergent Symmetry

Let us make an interesting observation. Since we built the Sierpiński Gasket using an L-system as in (6.27), we have a natural order to the edges (bonds) $\langle i, j\rangle \doteq e$ with $e = 1 \dots 3^{n+1}$ by tracing the drawing rules. Therefore, (6.12) can be written as

$$H_P \doteq t \sum_e \left(\mathrm{e}^{\mathrm{i}\alpha_e} \, c^\dagger_{s_e} c_{t_e} + \text{h.c.} \right), \tag{6.63}$$

where s_e and t_e denote the source and target nodes of edge $|e\rangle$, respectively. Define a translation operator T_e such that $T_e \, |e\rangle = |e+1\rangle$ with $T_e \, |3^{n+1}\rangle = |1\rangle$. In other words,

$$R_e H_P R_e^\dagger = t \sum_e \left(\mathrm{e}^{\mathrm{i}\alpha_{e-1}} \, c^\dagger_{s_e} c_{t_e} + \text{h.c.} \right). \tag{6.64}$$

We note that in the linear model (6.17), $\alpha_e = \theta/3$ for all e. Therefore,

$$T_e H_L T_e^\dagger = H_L. \tag{6.65}$$

Remark. This result is seemingly gauge dependent, because it would not work for $\tilde{H}_L$ in (6.18). However the only difference in α_e is for edges with different spatial orientations, which are labeled by the L-system's variables F, G, H in (6.27). Hence, we can always redefine T_e with respect to the gauge.

Now that we have a periodic coordinate, we may apply Bloch's theorem. If $\psi\,(e)$ is a mutual eigenstate of T_e and H_L, we may rewrite it in terms of $u_\kappa\,(e) = \mathrm{e}^{-\mathrm{i}\kappa e}\,\psi\,(e)$. These are the eigenstates of the Bloch Hamiltonian,

$$\hat{H}_L\,(\theta, \kappa) = t \sum_e \left(\mathrm{e}^{\mathrm{i}\,(\theta/3 - \kappa\ell)} \, c^\dagger_{s_e} c_{t_e} + \text{h.c.} \right), \tag{6.66}$$

where ℓ is the length of each edge, and $\hat{H}_L\,(\theta, \kappa)$ periodic in κ in the Brillouin zone $B_\kappa = 3^{-(n+1)}\,[-\pi/\ell, \pi/\ell]$.

As there are two periodic coordinates, the flux θ and Bloch's wavevector κ, we can calculate Berry's curvature [29]. We must pay attention to the following.

1. The number of nodes $N_n = \left(3^{n+1} + 3\right)/2$ and the number of edges $N_e = 3^{n+1}$ is not equal. Thus, we mush carefully rephrase (6.63) in the basis of $|e\rangle$.

2. The flux θ and Bloch's wavevector κ may be replaced by a single coordinate in Hamiltonian (6.66). Thus, the degeneracies cannot be avoided. A careful derivation of the Peierls substitution (see Appendix 6.A.1) implies that the approximation $\ell^2 \partial_s \xi_{ij} \ll 1$ does not change under the transformation $\xi \to \xi - \kappa$ in (6.73).

Let us return to the gauge and probe carefully the degrees of freedom. Denote by $\alpha_e^{F,G,H}$ the phase for edge $|e\rangle$ that lies in direction F, G, H, respectively. Let us assume that the phase α_e does not depend on the index e, namely,

$$\alpha_e^{F,G,H} = \alpha^{F,G,H}, \quad \forall e. \tag{6.67}$$

Then condition (6.31a) (phase per plaquette applied to the linear model) leads to

$$\alpha^F + \alpha^G + \alpha^H = \theta; \tag{6.68a}$$

and condition (6.31b) (London gauge) to

$$\begin{cases} \alpha^F - \alpha^G = 0 \\ \alpha^G - \alpha^H = 0 \\ \alpha^H - \alpha^F = 0 \end{cases} \implies \alpha^F = \alpha^G = \alpha^H. \tag{6.68b}$$

Together, these conditions imply that

$$\alpha^{F,G,H} = \theta/3. \tag{6.69}$$

Corollary. *Conditions (6.68) in the linear model are equivalent to assumption (6.67). This is the analogue of the Landau gauge on a square net as in [120].*

Let us make the following observation. There exists a periodic coordinate $|e\rangle$ containing non-trivial connections between non-neighboring edges. Thus there are *long-range correlations*, which summarize to the non-trivial spectrum in Figure 6.3. This is very reminiscent of the quasiperiodic lattice, which carries long-range correlations resulting in an interesting spectrum as well. Additionally, aperiodic tilings admit an extraordinary metric connecting spatially distant patches (see (3.1) and [52, 54]) similarly to the connections between edges on the Sierpiński Gasket.

6.4.5 Disorder

A natural thing to investigate when discussing a (topological) index is the response of the system to disorder. Effects of disorder on the Sierpiński Gasket and carpet were considered in [125, 126, 129–131]. For our purposes, any index formula working on the unperturbed system must also work after applying a small disorder.

We shall model the disorder by an on-site random potential as follows,

$$H_W^V(\theta) = H_P(\theta) + V_W \doteq t \sum_{\langle i,j \rangle} \left(\mathrm{e}^{\mathrm{i}\alpha_{ij}} c_i^\dagger c_j + \text{h.c.} \right) + \sum_i w_i c_i^\dagger c_i, \tag{6.70}$$

where $H_P(\theta)$ is the Hamiltonian (6.12), $w_i \in [-W, W]$ is taken from a constant distribution, and W defines the disorder strength. The disorder does not open and close gaps, but rather washes up distinct features of the IDOS. This can be seen in Figures 6.18 showing the IDOS of (6.70) with respect to W averaged over N_W realizations. We see that the gaps weaken as we increase W. We also observe that the energy degeneracy is lifted by disorder. Similar results are seen in Figures 6.19 shown IDOS of (6.70) versus the flux θ. The area model exhibits identical behavior.

A complementary approach is to add disorder to the edges by

$$H_W^E(\theta) \doteq t \sum_{\langle i,j \rangle} \left(e_{ij}\, \mathrm{e}^{\mathrm{i}\alpha_{ij}} c_i^\dagger c_j + \text{h.c.} \right), \tag{6.71}$$

with $e_{ij} = l_{ij}/\ell \in [1 - W, 1 + W]$ is the relative edge length. In this procedure, the disorder must be small ($W \ll t$) in order to make the approximations in (6.79) valid, and to leave the degree matrix Z in (6.33) unchanged (see [119, 120] and Appendix 6.A.1).

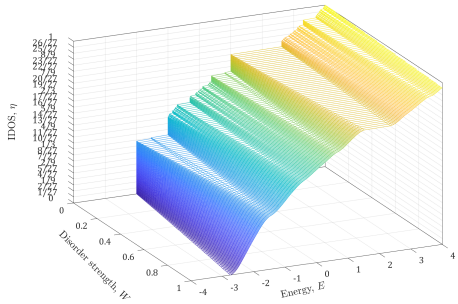

(a) Mean IDOS of H_W $(\theta = 0)$.

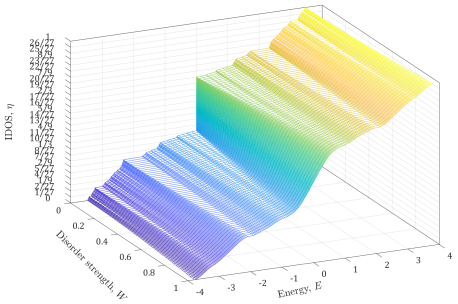

(b) Mean IDOS of H_W $(\theta = \pi/2)$.

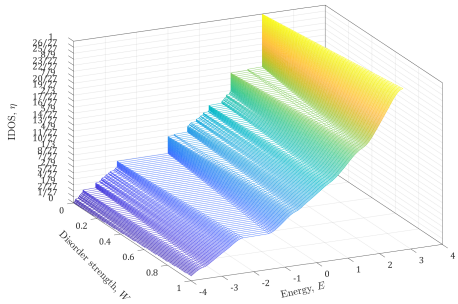

(c) Mean IDOS of H_W $(\theta = \pi)$.

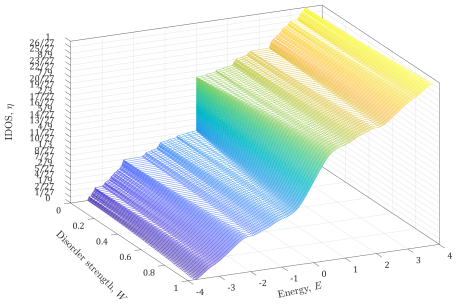

(d) Mean IDOS of H_W $(\theta = 3\pi/2)$.

Figure 6.18: Average integrated density of states of H_W (θ) with respect to disorder strength W. The spectrum was averaged over $N_W = 121$ realizations. (a–d) $\theta = (0, \pi/2, \pi, 3\pi/2)$, respectively.

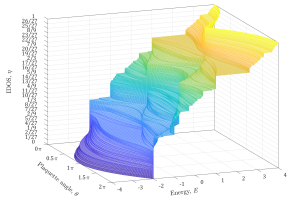

(a) Mean IDOS of $H_{W=0}$ (θ).

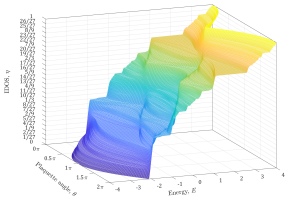

(b) Mean IDOS of $H_{W=0.2}$ (θ).

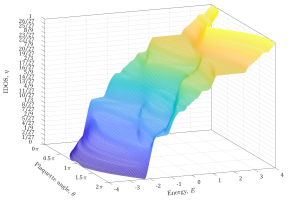

(c) Mean IDOS of $H_{W=0.4}$ (θ).

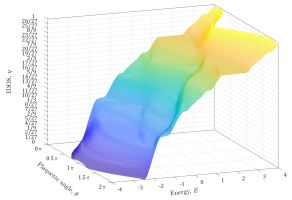

(d) Mean IDOS of $H_{W=0.6}$ (θ).

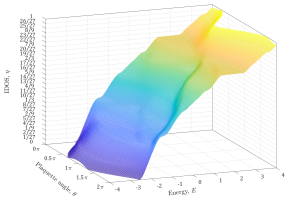

(e) Mean IDOS of $H_{W=0.8}$ (θ).

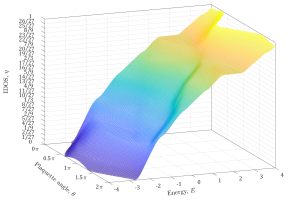

(f) Mean IDOS of $H_{W=1}$ (θ).

Figure 6.19: Average integrated density of states of H_W (θ) with respect to θ. The spectrum was averaged over $N_W = 121$ realizations. (a–f) $W = (0, 0.2, 0.4, 0.6, 0.8, 1)$, respectively.

COMPLEMENT 6.A Derivations

6.A.1 Peierls Approximation Derivation in Alexander's Model

In this section, we show a short derivation of (6.33) based on [118–120]. Start with the free particle Schrödinger equation in a magnetic field,

$$\left(\mathrm{i}\boldsymbol{\nabla} - \boldsymbol{A}/\Phi_0\right)^2 \psi = q^2\psi, \tag{6.72}$$

where $\Phi_0 = \hbar c/e$ is the flux quantum and $q^2 = 2m\epsilon/\hbar^2$. Next, set this equation on a thin-wire network resulting in

$$\left(\mathrm{i}\partial/\partial s - \xi\right)^2 \psi = q^2\psi, \tag{6.73}$$

using $s \doteq \hat{u}\cdot\boldsymbol{r}$ and $\xi \doteq \hat{u}\cdot\boldsymbol{A}/\Phi_0$, where $\hat{u}$ is the direction of a bond. The continuity of ψ on the edges of each bond requires that

$$\psi_{ij}\left(s_i\right) = \psi_i, \quad \psi_{ij}\left(s_j\right) = \psi_j, \tag{6.74}$$

for nodes i and j. On the derivatives of ψ impose a Kirchhoff-like condition [132],

$$\sum_j \left[\left(\mathrm{i}\partial_s - \xi\right)\psi_{ij}\left(s\right)\right]_{s_i} = 0, \tag{6.75}$$

taking the derivatives in the outgoing direction relative to the node.

The formal solution of (6.73) reads

$$\psi_{ij}\left(s\right) = C_1\,\mathrm{e}^{-\mathrm{i}\left(\alpha_{ij}+sq\right)} + C_2\,\mathrm{e}^{-\mathrm{i}\left(\alpha_{ij}-sq\right)}, \tag{6.76}$$

with $\alpha_{ij} \doteq \int_i^j \xi_{ij}\left(s\right)\,\mathrm{d}s$. Apply conditions (6.74) for $s_i = 0$ and $s_j = l_{ij}$,

$$\begin{cases} \psi_i = C_1 + C_2 \\ \psi_j = \left(C_1\,\mathrm{e}^{-\mathrm{i}\vartheta_{ij}} + C_2\,\mathrm{e}^{+\mathrm{i}\vartheta_{ij}}\right)\mathrm{e}^{-\mathrm{i}\alpha_{ij}}, \end{cases} \tag{6.77}$$

where $\vartheta_{ij} \doteq l_{ij}q$, and with $\alpha_{ij} \simeq \xi_{ij}l_{ij}$ assuming $l_{ij}^2\,\partial_s\xi_{ij} \ll 1$. This surmounts to

$$\psi_{ij}\left(s\right) = \frac{\mathrm{e}^{-\mathrm{i}s\xi_{ij}}}{\sin\vartheta_{ij}}\left[\psi_i \sin\left(q\left(l_{ij}-s\right)\right) + \mathrm{e}^{\mathrm{i}\alpha_{ij}}\,\psi_j \sin\left(qs\right)\right]. \tag{6.78}$$

Next, apply conditions (6.75) to have

$$-\sum_j \frac{q\cos\vartheta_{ij}}{\sin\vartheta_{ij}}\,\psi_i + \sum_j \frac{q\,\mathrm{e}^{\mathrm{i}\alpha_{ij}}}{\sin\vartheta_{ij}}\,\psi_j = 0. \tag{6.79}$$

Let all bonds be the same length $l_{ij} = \ell$, and assume small nets $\ell q \ll 1$. Hence,

$$-\sum_j \psi_i \cos\left(\ell q\right) + \sum_j \mathrm{e}^{\mathrm{i}\alpha_{ij}}\,\psi_j = 0. \tag{6.80}$$

Set $\cos\left(\ell q\right) = E/4$ and obtain (6.33) as required.

Another useful form of (6.79) is

$$m_i q^2 \psi_i + \sum_j d_{ij}\left(\mathrm{e}^{\mathrm{i}\alpha_{ij}}\,\psi_j - \psi_i\right) = 0, \tag{6.81}$$

where the "bond diffusivity" $d_{ij} = q/\sin\vartheta_{ij} \simeq l_{ij}^{-1}$ corresponds to conductance, and a mass term $m_i = q^{-1}\sum_j \tan\left(\vartheta_{ij}/2\right) \simeq \sum_j l_{ij}/2$.

COMPLEMENT 6.B Laplacian Spectrum in the Sierpiński Gasket

In this Appendix, we show that the spectrum of the Hamiltonian (6.6) on the Sierpiński Gasket equals to the spectrum of the Laplacian on it up to a linear transformation. We shall follow [133] throughout the Appendix.

6.B.1 Laplacian on the Sierpiński Gasket

Let Γ_n be the Sierpiński graph of order n and V_n be its vertices. We define the graph Laplacian by

$$\Delta_n u(x) \doteq \sum_{x \overset{n}{\sim} y} (u(y) - u(x)), \quad x \in V_n \setminus V_0, \tag{6.82}$$

for $u(x)$ a function on Γ_n, and $x \overset{n}{\sim} y$ denote the neighbors of n^{th} order. The Laplacian on the infinite Gasket is then defined by

$$\Delta u(x) \doteq \frac{3}{2} \lim_{n\to\infty} 5^n \Delta_n u(x). \tag{6.83}$$

The origin of the factors $3/2$ and 5^n comes from the measure and energy regularization,

$$\Delta u(x) = \lim_{n\to\infty} \left(\frac{2}{3}\frac{1}{3^n}\right)^{-1} \left(\frac{3}{5}\right)^{-n} \Delta_n u(x). \tag{6.84}$$

We present below the details behind these factors.

6.B.1.1 Energy Regularization

We define the energy E_n of the graph Γ_n by

$$E_n(u) = \sum_{x \overset{n}{\sim} y} (u(y) - u(x))^2. \tag{6.85}$$

For self-similar graphs, we need to renormalize the energies by

$$\mathcal{E}_n(u) = r^{-n} E_n(u), \quad 0 < r < 1. \tag{6.86}$$

For the Sierpiński Gasket, $r = 3/5$. The infinite graph energy is then

$$\mathcal{E}(u) = \lim_{n\to\infty} \mathcal{E}_n(u). \tag{6.87}$$

Additionally, $E_n(u)$ can be rewritten as

$$\begin{aligned} \mathcal{E}_n(u) &= -r^{-n} \sum_{x\in V_n\setminus V_0} u(x) \sum_{x \overset{n}{\sim} y} (u(y) - u(x)) \\ &= -r^{-n} \sum_{x\in V_n\setminus V_0} u(x)\, \Delta_n u(x). \end{aligned} \tag{6.88}$$

We identify the regularized energies with the corresponding Laplacian. The renormalized energies are depicted in Figure 6.20a.

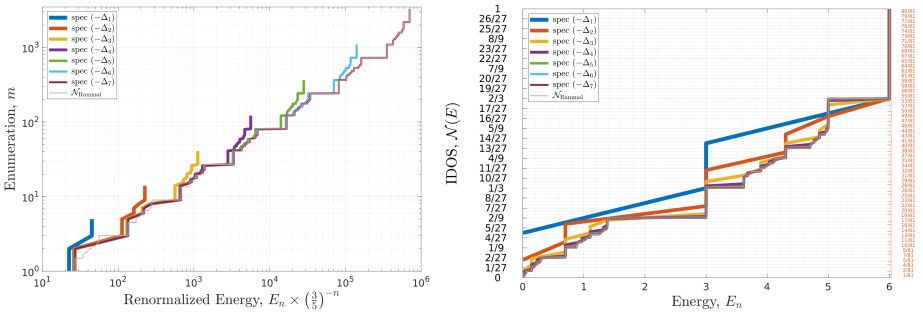

Figure 6.20: The spectrum of the Sierpiński Gasket Laplacian for increasing order n. The gray line is the normalized infinite energy calculated with (6.96). (a) Renormalized energy $\mathcal{E}_n$ with respect to μ_0. (b) The IDOS $\mathcal{N}(E)$ with respect to W.

6.B.1.2 Measures and Weights

The standard measure on the Sierpiński Gasket of order n is defined by

$$\mu_0 = 3^{-n} \begin{cases} 2/3 & x \in V_n \setminus V_0 \\ 1/3 & x \in V_0\,, \end{cases} \tag{6.89}$$

where V_0 are the 3 head nodes and V_n denote all other nodes. The weights used in the diagonalization of (6.6) are given by

$$W = \frac{Z}{4} = \begin{cases} 1 & x \in V_n \setminus V_0 \\ 1/2 & x \in V_0\,, \end{cases} \tag{6.90}$$

where $Z(x)$ is the number of neighbors of node x (see [118]). In the Gasket, all the nodes have 4 neighbors except the head nodes having 2. Therefore,

$$\mu_0 = \frac{1}{2}\frac{1}{3^{n+1}} Z = \frac{2}{3^{n+1}} W. \tag{6.91}$$

6.B.1.3 Adjacency Matrix

The Hamiltonian (6.6) is represented by the adjacency matrix given by

$$A\,u(x) \doteq \sum_{x \overset{n}{\sim} y} u(y) = (\Delta_n + Z)\,u(x)\,. \tag{6.92}$$

The generalized spectrum $\{\lambda_i, v_i\}$ of A with respect to weights W reads

$$A v_i = \lambda_i W v_i\,. \tag{6.93}$$

Therefore,

$$\begin{aligned} \Delta_n v_i &= (A - Z)\,v_i = \lambda_i W v_i - 4 W v_i \\ &= \tfrac{1}{2} 3^{n+1} (\lambda_i - 4)\,\mu_0 v_i. \end{aligned} \tag{6.94}$$

Thus, spec $\Delta_n^{\mu_0} = \left\{\frac{1}{2}3^{n+1}(\lambda_i - 4), v_i\right\}$. Hence, we have a linear correspondence between the spectrum of Δ^{μ_0} and the spectrum of A^W.

The spectrum of A^W is bounded in $[-2, 4]$ for any order n; moreover, the spectrum of the magnetic Hamiltonian (6.12) is bounded in $[-4, 4]$. Therefore, they are better suited for comparison purposes.

6.B.2 Sierpiński IDOS Formula

For Sierpiński Gaskets of dimension d, the functional iterative equation for the IDOS is given by [134],

$$\mathcal{N}_d(E) = \begin{cases} 0, & E \le 0 \\ \dfrac{\mathcal{N}_d(\phi_d(E)) - \frac{d-1}{d+1}\,\Theta(E-2)}{d+1}, & 0 < E \le \dfrac{d+3}{2} \\ \dfrac{2 - \mathcal{N}_d(\phi_d(E)) - \frac{d-1}{d+1}\big(\Theta(E-2) - \Theta(E-d-3)\big)}{d+1}, & \dfrac{d+3}{2} < E < 2d+2 \\ 1, & 2d+2 \le E, \end{cases} \tag{6.95}$$

with $\Theta(x)$ the step function, and $\phi_d(E) = E(d+3-E)$ the renormalization function. For the triangular $d = 2$ gasket embedded in the $2d$ plane, (6.95) reduces to

$$\mathcal{N}(E) = \begin{cases} 0, & E \le 0 \\ \dfrac{1}{3}\mathcal{N}(\phi(E)) - \dfrac{1}{9}\,\Theta(E-2), & 0 < E \le \dfrac{5}{2} \\ \dfrac{2}{3} - \dfrac{1}{3}\mathcal{N}(\phi(E)) - \dfrac{1}{9}(\Theta(E-2) - \Theta(E-5)), & \dfrac{5}{2} < E < 6 \\ 1, & 6 \le E, \end{cases} \tag{6.96}$$

with $\phi(E) = E(5-E)$.

These equations are solved by an iterative process. Numerical calculations show a complete match with the spectrum of (6.6) (see Figure 6.20b). Moreover, since the denominators in (6.96) are 3 and 9 only, the values $\mathcal{N}(E)$ gets during the iterations are of the form $k/3^N$. This infers the gap labeling formula (6.28).

Chapter 7

Topological Phase Transitions

Thus far, we have seen that different structures—C&P or substitution—have topological character exhibited in their Čech cohomology. It can be manifested experimentally by means of winding numbers. The next natural question is whether one can continuously transform between two structures of *different* topological character. If so, then one has a topological phase transition (TPT) in a *classical* system reminiscent of the structural phase transitions of [135, 136]. In the following chapter, we shall explore such transitions.

7.1 Random Substitution Tilings

In this section, we shall explore substitution tilings with an explicit randomization built-in.

7.1.1 Introduction

The field of random tilings starts with Godrèche and Luck [137]. They have considered a transition between two equivalent Fibonacci substitution rules,

$$\sigma_{\text{Fib}}^{\text{Fib}}(p) = \begin{cases} \sigma_0 : \begin{cases} A \mapsto AB \\ B \mapsto A \end{cases} & \text{with probability } 1-p, \\ \sigma_1 : \begin{cases} A \mapsto BA \\ B \mapsto A \end{cases} & \text{with probability } p. \end{cases} \tag{7.1}$$

The creation of words w_N by consecutive application of $\sigma_{\text{Fib}}^{\text{Fib}}(p)$ is similar to the regular case, but at each step we apply *either* σ_0 or σ_1 with their respective probabilities. Note that $\sigma_{\text{Fib}}^{\text{Fib}}(0) = \sigma_0$ and, likewise, $\sigma_{\text{Fib}}^{\text{Fib}}(1) = \sigma_1$.

To quantify the randomness, we can inspect the topological entropy [138] (structural entropy per letter),

$$S = \lim_{N\to\infty} \frac{\log c_N}{L_N}. \tag{7.2}$$

where c_N is the complexity defined in Section 3.1.5 and $L_N = |W_N|$ (note that since the substitutions are of the same length, it is well-defined). For $\sigma_{\text{Fib}}^{\text{Fib}}(p)$ above, it was found that [137]

$$S\left(\sigma_{\text{Fib}}^{\text{Fib}}\right) = \sum_{m=2}^{\infty} \frac{\log m}{\tau^{m+2}} \simeq 0.444399. \tag{7.3}$$

Note that for all deterministic substitutions, $S(\sigma_{\text{deter}}) = 0$.

Families of random noble mean substitutions were considered in [138, 139],

$$\sigma_m : \begin{cases} A \mapsto \begin{cases} BA^m & \text{with probability } p_0 \\ ABA^{m-1} & \text{with probability } p_1 \\ \vdots & \\ A^m B & \text{with probability } p_m \end{cases} \\ B \mapsto A. \end{cases} \tag{7.4}$$

The ideas of mixed substitution tiling spaces were rigorously defined and constructed by Gähler and Maloney [140], based on the AP complexes [45], and the Čech cohomology was computed. We shall not repeat it here.

7.1.2 Phase Transitions

With these definitions, we can consider the probability p as an *order parameter* to transform between different spaces. Consider, for instance

$$\sigma_{\text{TM}}^{\text{Per}}(p) = \begin{cases} \sigma_{\text{Per}} : \begin{cases} A \mapsto AB \\ B \mapsto AB \end{cases} & \text{with probability } 1-p, \\ \sigma_{\text{TM}} : \begin{cases} A \mapsto AB \\ B \mapsto BA \end{cases} & \text{with probability } p, \end{cases} \tag{7.5}$$

which interpolates between the periodic and Thue-Morse substitutions. Now, since $\check{H}^1(\Omega_{\text{Per}}) \cong \mathbb{Z}$ and $\check{H}^1(\Omega_{\text{TM}}) \cong \mathbb{Z} \oplus \mathbb{Z}\left[\frac{1}{2}\right]$, we have two very different topologies and thus a topological phase transition. Several problems immediately arise.

1. How to measure this topology?
2. We are dealing with finite sequences only and the definitions work for the infinite case.
3. How to physically construct such a substitution?

The main point to consider is the first – how to probe the topology with a simple procedure. We have already dealt with finite approximations and stated that they reconstruct well the properties of the infinite case. An experimental work is still too far beyond the horizon.

To tackle these problems, we introduce a statistical physics approach.

a) Take some $\sigma(p)$ for a given p, and fix the iteration number N.
b) Construct many realizations of words $w_N^r(p)$ for $r = 1 \dots R$ with large R.
c) Take the average of $f\left(w_N^r\right)$. There is no sense of inspecting an average word $\bar{w}_N$, but we can look on *some function* (say, IDOS) of w_N^r, namely, $f\left(w_N^r\right)$. Take its average w.r.t. realizations,

$$\bar{f}_N(p) \doteq \left\langle f\left(w_N^r(p)\right)\right\rangle_r. \tag{7.6}$$

d) Calculate the variance of $f\left(w_N^r\right)$,

$$(\Delta f_N)^2 \doteq \left\langle f^2\left(w_N^r\right)\right\rangle_r - \left\langle f\left(w_N^r\right)\right\rangle_r^2. \tag{7.7}$$

One may consider higher cumulants as well.

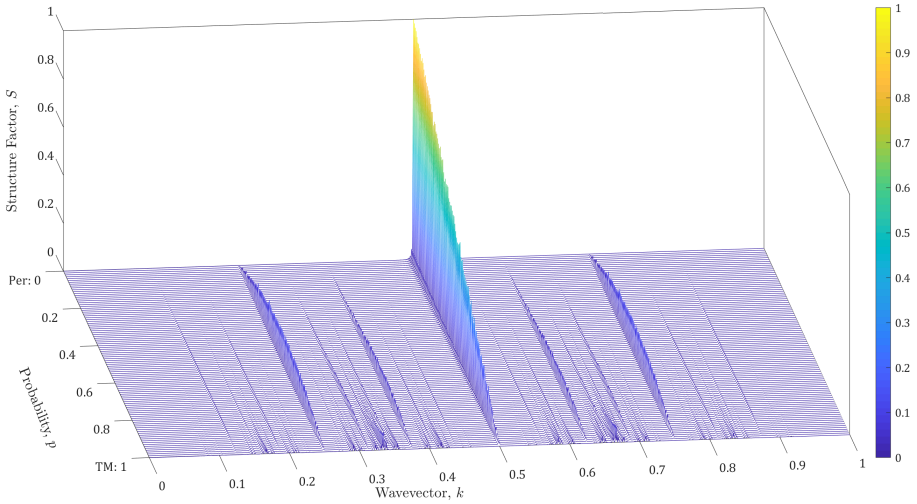

(a) Periodic–Thue-Morse.

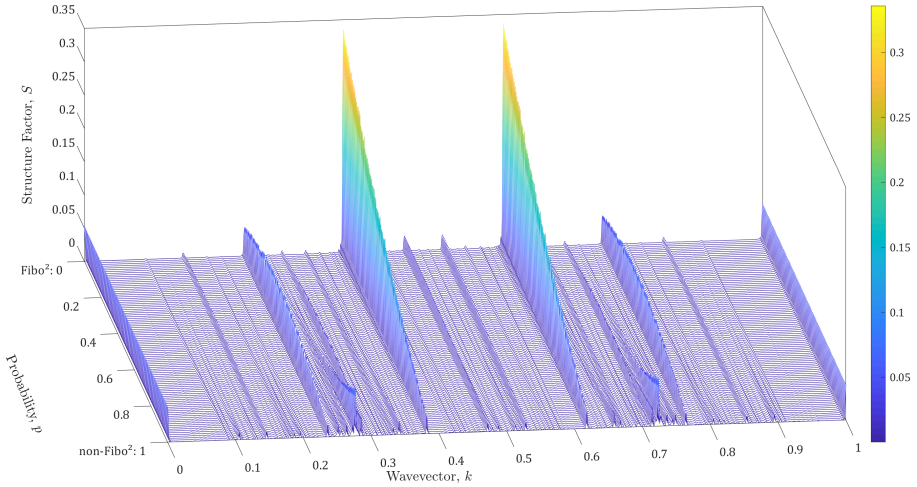

(b) Fibonacci²–non-Fibonacci².

Figure 7.1: Structure factor $S(k)$ for random substitutions. (a) Periodic–Thue-Morse with $R = 1255$ and $F_N = 512$; (b) Fibonacci²–non-Fibonacci² with $R = 1255$ and $F_N = 377$.

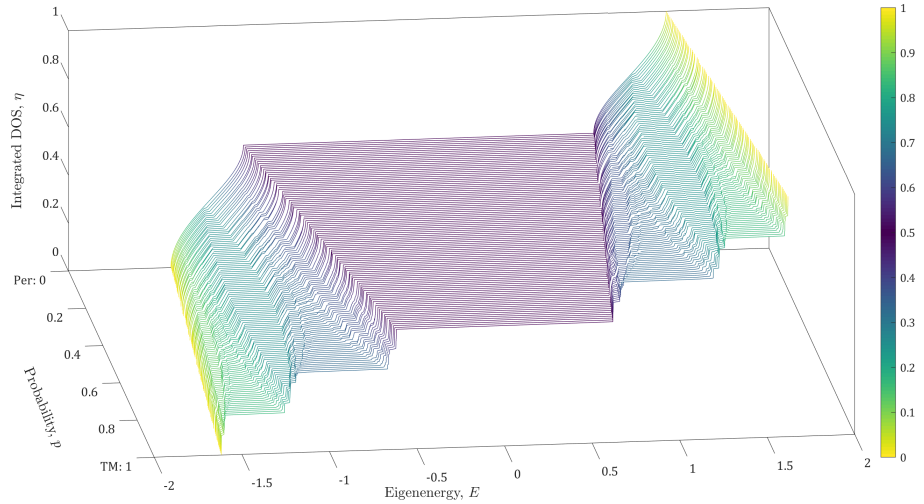

(a) Periodic–Thue-Morse.

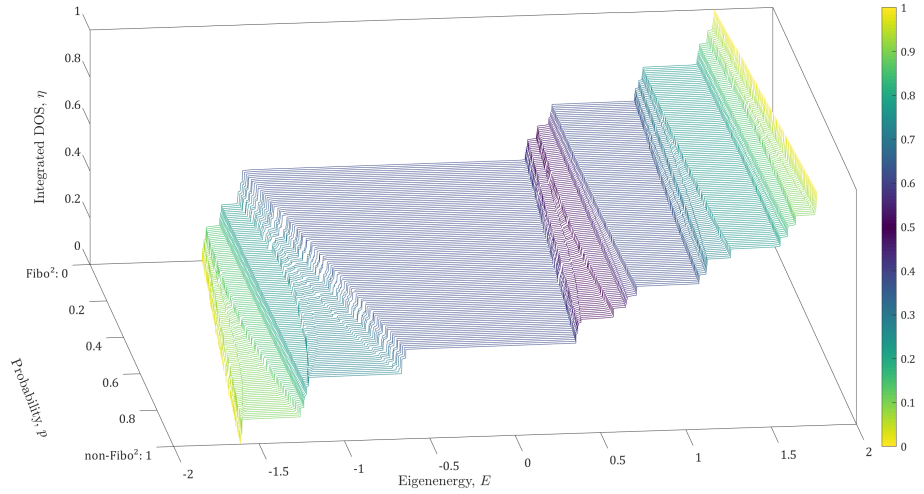

(b) Fibonacci²–non-Fibonacci².

Figure 7.2: Integrated density of states $\eta(E)$ for random substitutions. (a) Periodic–Thue-Morse with $R = 1255$ and $F_N = 512$; (b) Fibonacci²–non-Fibonacci² with $R = 1255$ and $F_N = 377$.

e) Repeat the calculation for each $p \in [0,1]$.

This procedure can be well simulated on a computer in a reasonable time as seen in Figures 7.1 and 7.2. A physical construct is also possible.

Remark. The simulations above in Figures 7.1 and 7.2 are done using the tight binding rather than scattering matrix formalism due to two main reasons. First, it is much faster, as one only needs to diagonalize an $F_N \times F_N$ matrix instead of a large mesh in the k-space. Second, in scattering matrix approach one needs to refine the mesh near gap edges due to numerical instabilities. As it is unknown *a priori* where are the gaps and which of them need refining for each realization, the simulation slows considerably, and the final—combined—mesh is rather large with more inaccuracies.

7.1.2.1 Inverse Participation Ratio

We have many gaps located at different energies and it is hard to quantify the amount of "gapness" in the sequence. The usual suspect to quantify the spatial localization is the inverse participation ratio defined by [141],

$$I \doteq \int |\psi(x)|^4 \, \mathrm{d}x, \tag{7.8}$$

where $\psi(x)$ is the normalized wavefunction so that $|\psi(x)|^2$ is the probability to find a particle at location x. Setting $\psi = \hat{\rho}(k)$ the Fourier transform of the atomic density so that $|\hat{\rho}(k)|^2 = S(k)$ is the structure factor, one has

$$\bar{I}(p) \doteq \int \bar{S}^2(k;p) \, \mathrm{d}k, \tag{7.9}$$

where the structure factor normalized such that $\int S(k) \, \mathrm{d}k = 1$. More general definitions are in [96, 142].

Unfortunately, numerical analysis does not show any significant change of $\bar{I}(p)$ from Periodic–Thue-Morse or Fibonacci²–non-Fibonacci² substitutions (as in Figures 7.1). Thus, we need a different approach.

7.2 Thermodynamics of Random Substitutions

As stated in the previous section, the main problem is how to measure the topology. What we want, in simple words, is some functional of the IDOS $\eta(E,p)$ that gives us a number quantifying the topology with respect to p. Ideally, for $p = 0, 1$ it would restore the Čech cohomology $\check{H}^1(\Omega)$ or some characteristic of it. In the following, we present a thermodynamic approach to quantify the topology.

7.2.1 Heat Kernel

Let us define the heat kernel $Z(t)$ by [68, 70],

$$Z(t) \doteq \mathrm{Tr}\left[\mathrm{e}^{-tH}\right], \tag{7.10}$$

with H the Hamiltonian of the system. Explicitly, in terms of the density of states $\varrho(E)$,

$$Z(t) = \int \mathrm{e}^{-tE} \varrho(E) \, \mathrm{d}E. \tag{7.11}$$

Note that $\mathrm{d}\eta(E) = \varrho(E) \, \mathrm{d}E$ is a well-defined Lebesgue measure (see, e.g., [28, 44]).

Since we calculate the IDOS $\eta(E)$ rather than $\varrho(E)$, and since derivatives are numerically inaccurate, we would like to rephrase $Z(t)$ in terms of $\eta(E)$. Integrating by parts, we have

$$\begin{aligned} Z(t) &= \mathrm{e}^{-tE}\,\eta(E)\Big|_{E_{\min}}^{E_{\max}} + \int_{E_{\min}}^{E_{\max}} t\,\mathrm{e}^{-tE}\,\eta(E)\;\mathrm{d}E \\ &= \mathrm{e}^{-tE_{\max}} + t\int_{E_{\min}}^{E_{\max}} \mathrm{e}^{-tE}\,\eta(E)\;\mathrm{d}E, \end{aligned} \tag{7.12}$$

where $[E_{\min}, E_{\max}]$ is the support of $\eta(E)$ with $\eta(E_{\min}) = 0$ and $\eta(E_{\max}) = 1$. Now, since E might be negative (depending on the values of the potential in H), we rescale $Z(t)$ to

$$Z(t) = \mathrm{e}^{-t(E_{\max}-\mu)} + t\int_{E_{\min}}^{E_{\max}} \mathrm{e}^{-t(E-\mu)}\,\eta(E)\;\mathrm{d}E, \tag{7.13}$$

where $\mu = E_{\min}$. Thus $Z(t)$ is a good Laplace transform.

Now, let us return to the random substitutions. We set

$$Z(t,p) = \mathrm{e}^{-t(E_{\max}-E_{\min})} + t\int_{E_{\min}}^{E_{\max}} \mathrm{e}^{-t(E-E_{\min})}\,\eta(E,p)\;\mathrm{d}E, \tag{7.14}$$

where $E_{\max}$, $E_{\min}$, η and Z are all implicitly functions of p averaged over the realizations (thus, $Z(t,p) = \bar{Z}_N(t;p)$, etc.). Identifying the heat kernel over t with the partition function over β, we define the following thermodynamic functions:

$$U(t,p) = -\frac{\partial \log Z(t,p)}{\partial t} \qquad \text{“Internal energy;”} \tag{7.15a}$$

$$C(t,p) = t^2\,\frac{\partial^2 \log Z(t,p)}{\partial t^2} \qquad \text{“Heat capacity;”} \tag{7.15b}$$

$$F(t,p) = -\frac{\log Z(t,p)}{t} \qquad \text{“Free energy;”} \tag{7.15c}$$

$$S(t,p) = t^2\,\frac{\partial F(t,p)}{\partial t} \qquad \text{“Entropy.”} \tag{7.15d}$$

The interpretation as thermodynamic quantities should not be taken at face value (thus the quotation marks).

Similarly, one can calculate the zeta function [68],

$$\zeta_H(s) \doteq \mathrm{Tr}\left[H^{-s}\right], \quad s \in \mathbb{C}. \tag{7.16}$$

Explicitly,

$$\zeta_H(s) = \int E^{-s}\varrho(E)\;\mathrm{d}E. \tag{7.17}$$

Repeating the steps as in the heat kernel calculation above, one obtains,

$$\zeta_H(s,p) = (E_{\max}-E_{\min})^{-s} + \begin{cases} \dfrac{1}{s-1}\displaystyle\int_{E_{\min}}^{E_{\max}} (E-E_{\min})^{1-s}\,\eta(E,p)\;\mathrm{d}E, & s \neq 1; \\ \displaystyle\int_{E_{\min}}^{E_{\max}} \log(E-E_{\min})\,\eta(E,p)\;\mathrm{d}E, & s = 1. \end{cases} \tag{7.18}$$

Heat capacity calculations are shown in Figures 7.3, as $C(t,p)$ is the most pronounced thermodynamic quantity. The periodic sequences in Figure 7.3a do not show any special behavior, whereas the aperiodic Thue-Morse heat capacity changes sign and oscillates. Things are even more violent in Fibonacci[2] vs. non-Fibonacci[2] sequences as in Figure 7.3b.

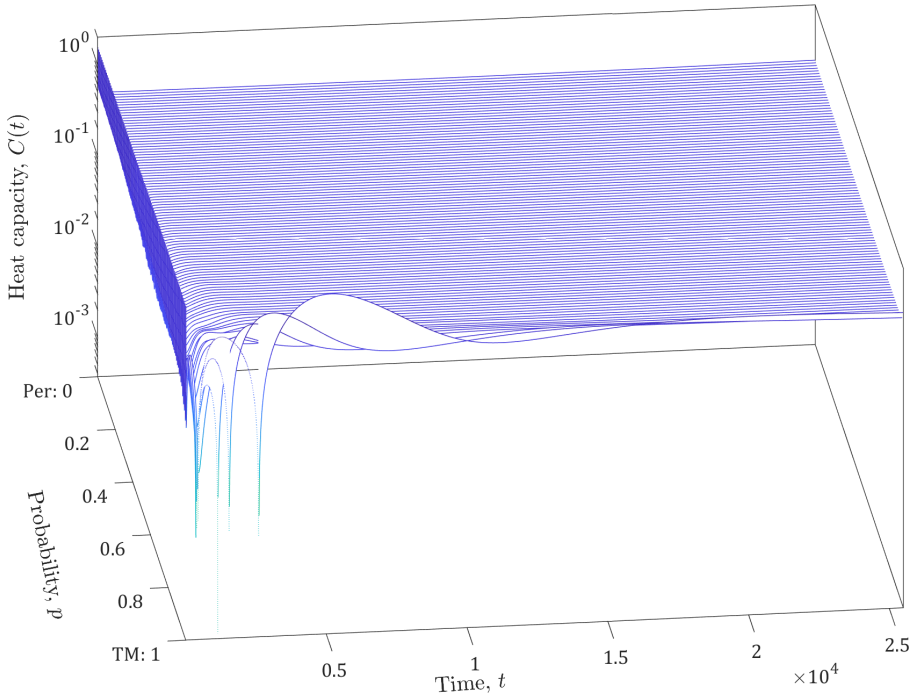

(a) Periodic–Thue-Morse.

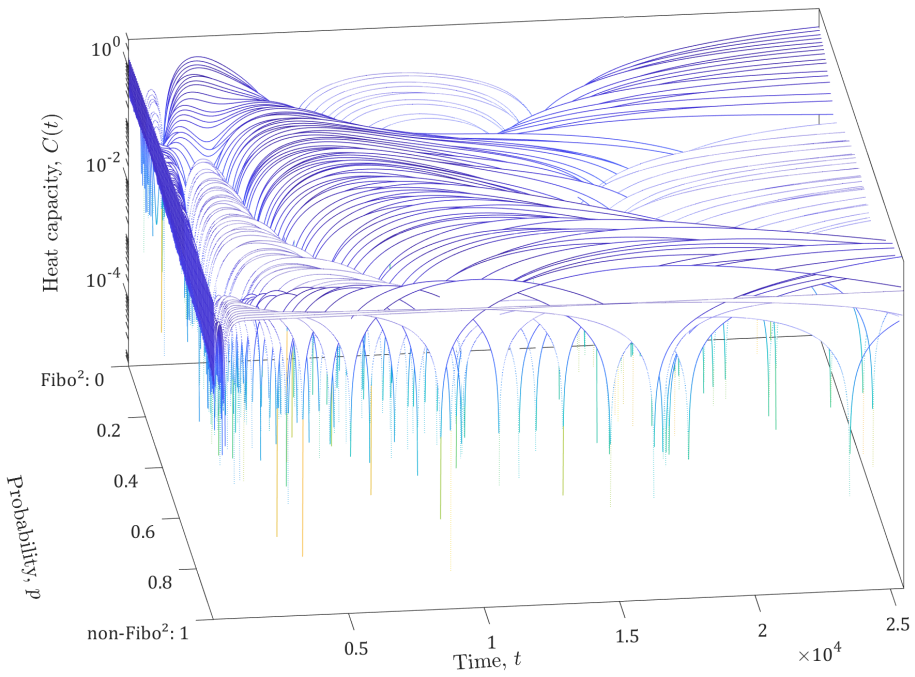

(b) Fibonacci^2–non-Fibonacci^2.

Figure 7.3: Heat capacity $C(t, p)$ for random substitutions in logarithmic scale. Solid lines are positive values of $C(t, p)$, and dashed lines are negative values. (a) Periodic–Thue-Morse with $R = 1255$ and $F_N = 512$; (b) Fibonacci^2–non-Fibonacci^2 with $R = 1255$ and $F_N = 377$.

7.2.1.1 Phase Transitions

Unfortunately, as seen in Figures 7.3, it is quite difficult to identify TPTs in these structures. The heat capacity changes violently, and does not follow any "n^{th}-order phase transition" rule. Most probably, a different definition of thermodynamic quantities is required for aperiodic tilings, which makes use of the tiling's combinatorics. Thus far, it has not been found.

7.2.2 Probability Measures

In the previous section, we have described the thermodynamics of the spectral part. Can we do the same for the structural part? To succeed, we need a probability measure similarly to $\mathrm{d}\eta(E)$. Luckily, $\mathrm{d}\mu = S\,\mathrm{d}k$ is a good Lebesgue measure [23, 73]. Thus, we have structural and spectral measures,

$$\mathrm{d}\mu(k) \doteq S(k)\ \mathrm{d}k, \tag{7.19a}$$
$$\mathrm{d}\eta(E) \doteq \varrho(E)\ \mathrm{d}E. \tag{7.19b}$$

Both $\mu(k)$ and $\eta(E)$ have the same algebraic properties thus obtained from $\check{H}^1(\Omega)$. Therefore, we need to repeat the procedure of the previous section but with $S(k)$ instead of $\varrho(E)$.

Problem. Unlike the spectral case where $E \in [E_{\min}, E_{\max}]$, in the structural case $k \in (-\infty, \infty)$. To make $Z_{\text{struct}}(t)$ finite, we confine the integration to the first quasi-Brillouin zone, namely, $k \in [0, k_0]$.

Since $\eta(E)$ is derived from the scattering matrix $\mathcal{S}(E)$, we propose deriving $\mu(k)$ in a similar manner, namely, find $\mathcal{T}(k)$ such that

$$\mu(k) = c\,\mathrm{Tr}\log\mathcal{T}(k), \tag{7.20a}$$
$$\eta(E) = c\,\mathrm{Tr}\log\mathcal{S}(E). \tag{7.20b}$$

Here, $c = -\mathrm{i}/\pi$ a constant. The operator $\mathcal{T}(k)$ is new. It can be found by reverse engineering via comparison to the derivation of $\mathcal{S}(E)$ from $\mathcal{G}(E)$ as in Section 3.4.3.

Let us now combine the probability measures to the topological language of $\check{H}^1$ and K_0. Recall that the gap labels are given by the trace on the K_0 group. This is the reason behind the Tr in (7.20). Similarly, the trace $\tau_*^{\check{H}}$ (or Ruelle-Sullivan current) that gives the Bragg locations of $S(k)$ is a trace. We combine both and (7.20) to

$$\mu(k) = \tau_*^{\check{H}}\left(\check{H}^1(\Omega)\right) \doteq \mathrm{Tr}_\perp\,\check{H}^1(\Omega), \tag{7.21a}$$
$$\eta(E) = \tau_*^{K}\left(K_0(\mathcal{B})\right) \doteq \mathrm{Tr}_\parallel\,K_0(\mathcal{B}). \tag{7.21b}$$

The parallel and perpendicular subscripts are given a physical interpretation. In the parallel case $\mathrm{Tr}_\parallel$, one considers a scattering experiment parallel to a $1d$ structure of thin films. The scattering matrix gives $\eta(E = k)$ as in (3.73). The perpendicular case $\mathrm{Tr}_\perp$ implies a transmission experiment perpendicular to the same structure—a phase mask. In the far-field one gets the structure factor $S(k)$. Thus, $\mu(k)$ and $\eta(E)$ are different points of view of the same phenomenon.

Chapter 8

Summary

In this chapter, we summarize our work and explore future endeavors.

8.1 Contribution

In this work, we reviewed the topological behavior of many families of aperiodic tilings. In $1d$ C&P tilings, we defined winding numbers using the phason as a gauge field. The phason gives rise to the permuted tiling Σ_1, whose Fourier transform argument indicates the windings on Bragg peak locations with the ubiquitous $p + qs$ formula. This works for any $2d \to 1d$ C&P tiling with slope s, where the best rational approximations to $s \notin \mathbb{Q}$ are in terms of continued fractions. Constructing Wannier diagrams, we conclude that spectral gaps (of the wave equation) and diffraction peak are in 1-to-1 correspondence, with the slope in the $s{-}\nu$ plane coincides with the aforementioned q. Identifying quasiperiodic tilings with C&P ones, we extended our definition for quasiperiodicity to a condition on fluctuations around the mean tiling. We demonstrated that this condition also holds for certain classes of substitution tilings, thus establishing them as quasiperiodic.

We then presented a more general mathematical treatment of tiling combinatorics using Bratteli diagrams, complexity trees, Čech cohomology $\check{H}^1$ and zeta functions. We explained the GLT and the explicit calculations of its formula. Next, we illustrated how this treatment explains the intricate nature of dual aperiodic tilings. Simply put, the construction of alphabets of n-letters (or tiles for $d > 1$) contains all the information required to construct dual tilings. After that, we combined general aperiodic tilings with quasiperiodic ones showing that several aspects pertain (such as the basic windings in the non-Fibonacci^2 tiling), but many more features appear (more windings for non-Fibonacci^2, etc.). These features were analyzed by means of Čech cohomology establishing that when it changes, the aspects of a tiling also change. However, in some cases it is not enough, and we must calculate additional properties of the tiling such as the Bratteli diagrams or the atomic surface. We ended the chapter by presenting scattering theory and how we can calculate some tiling properties from it. We demonstrated that winding numbers can be written in terms of $\mathcal{S}$-matrix related quantity akin to the Krein-Schwinger formula.

Next, we showed an important aspect of aperiodic tilings – their diffraction patterns. Emphasizing the Thue-Morse tiling, we analyzed its peaks and compared them to known experimental results. Whereas in quasiperiodic tilings the peaks are Bragg,

easily discernible and enumerable, the singularly-continuous peaks of the Thue-Morse tiling pose a difficulty to distinguish between different families, and a proper identification experiment – of plotting the diffraction intensity of a peak with respect to the tiling order N – has not been realized. This makes the nature of Thue-Morse diffraction peaks at finite order an open question. We then illustrated how to calculate diffraction peaks for some tilings using autocorrelation between tiles. Finally, we introduced a novel idea to calculate the diffraction of tilings with Bragg spectrum using the Bratteli diagrams we discussed earlier. We demonstrated it in a periodic, C&P quasiperiodic and aperiodic (Period Doubling) cases. We showed how in each case we can identify a phason and calculate winding number. We summarized by mentioning additional tilings without complete Bragg spectrum like Thue-Morse. Therefore, Čech cohomology—or, more accurately, the sequence of Bratteli diagrams converging to it—can be utilized to calculate diffraction spectra of tilings.

We moved on to connect the diffraction and energy spectra of aperiodic tilings by means of an extension of Bloch theory. We showed how to construct quasiperiodic Bloch Hamiltonians and identified its symmetries using operators. We extended the Hamiltonians to be continuous and connected their eigenfunctions to pattern equivariant functions. Then we numerically validated all our constructions above. Putting our attention to general aperiodic tilings in $1d$, we used our previous work [58] to connect the traces of $\check{H}^1$ and K_0, where $\check{H}^1$ is on the structural (diffraction) side and K_0 on the spectral one. The connection between $\tau_*^{\check{H}}(\check{H}^1)$ and the structure factor $S(k)$ is only valid in C&P tilings, whereas the GLT corresponds to the spectral gaps $\mathcal{N}_{\text{gap}}(E)$ for all tilings. We then conjectured that a similar relation exists between $\check{H}^1$ and the structural winding's group, and between K_0 and the spectral winding group in $1d$ C&P tilings. Altogether, since the diagrams (5.47) and (5.52) commute, we can omit K_0 and focus on $\check{H}^1$ only. We finished this chapter by analyzing conventional topological numbers, such as Chern number, in quasiperiodic systems using the Zak and Berry phases.

Straying from FLC tilings, we explored the world of fractals. We introduced L-systems and reverted them to substitution rules. We then demonstrated the GLT on the Sierpiński gasket with and without magnetic flux pierce the fractal. Analyzing the spectrum led us to deduce topological phase transitions in this setup. We furthermore examined different flux conditions and showed that the flux itself acts as an order parameter, and new topological phase transitions in terms of $\check{H}^2_\Phi$ have arisen. We continued to explore more properties, such as windings and currents, on magnetic Sierpiński gaskets. We ended the section checking various index formulae on the gasket but to no avail.

It the last part, we return to FLC tilings and searched for topological phase transitions therein. Employing the idea of random substitution rule between two $1d$ tilings, we found phase transitions between the topological groups $\check{H}^1$ of each tiling. We also introduced thermodynamic potentials in this scheme.

8.2 Outlook

In this work, we focused our attention to $1d$ tilings leaving $2d$ and $3d$ tilings unexplored (with the exception of dual tilings, and the flux in the Sierpiński gasket). This is a rich environment where some of our results can be readily generalized. For instance, the Penrose and Octanacci C&P tilings both admit 2 distinct phasons in the internal space $E_\perp$ together with the $2d$ physical space $E_\parallel$. Note that in the Penrose case, although

$\dim E_\perp = 3$, one of the dimensions is degenerate to obtain the "regular" Penrose tiling [15, 17, 18]. These two phasons together thus imply a phase akin to Berry's phase indicating new and exciting topological numbers unlike the $1d$ windings. In $3d$ icosahedral quasicrystals, there are 3 distinct phasons implying exotic behavior such as braiding or knotting.

Although we explained how to compute diffraction spectra using Bratteli diagrams, we found it only in tilings containing Bragg peaks. In periodic tilings it could be calculated using standard descriptions. In the quasiperiodic case, however, we needed the combinatorics developed in Chapter 2. In the Period Doubling example, we closely analyzed Bratteli diagrams to deduce the diffraction. This leaves the question of general tilings open—why does the Thue-Morse tiling have (mostly) a singularly-continuous diffraction, and the Rudin-Shapiro tiling an absolutely continuous one? Can we give a general statement on any $1d$ tilling just by looking on its Bratteli diagrams (of the proper orders)? This question can be generalized even to higher dimensions to probe the diffraction of the Penrose, Octanacci and Chair tilings by means of their Bratteli diagrams.

As proven in Theorem 5.1, the traces of both $\check{H}^1$ and K_0 groups are identical. This leaves the relation between $\check{H}^1$ and diffraction in $1d$ open apart from quasiperiodic tilings. Since we saw that $S(k)$ can be computed in some cases using Bratteli diagrams, then there must be a mapping $\varpi(\check{H}^1) = \{k_B^i\} \cup \{k_0^j\}$ for Bragg peaks k_B and singularly-continuous peaks k_0. Additionally, there must be a mapping to the winding groups $\upsilon^\Theta(\check{H}^1) = \mathcal{W}_\phi[\Theta]$ and $\upsilon^\alpha(\check{H}^1) = \mathcal{W}_\phi[\alpha]$ as in (5.52), and an isomorphism ψ between both winding groups.

The GLT for fractals is very tailored to the Sierpiński case, as the substitution is $1d$ whilst the fractal is embedded in $2d$. There are complicated links, which are seen only in the $2d$ perspective. Moreover, the GLT is defined with respect to the substitution, and thus is insensitive to the $2d$ links. Yet it matches the calculated data impeccably. Better means of correlation between $1d$ and $2d$ ought to be made. In addition, the conventional index theorems do not work for fractals despite numerous attempts, and a suitable one is in order to capture gap locations, windings, and so forth.

The main issue with topological phase transitions on FLC tilings, is that we could not identify a proper observable of $\check{H}^1$ of this transition. Naturally, gaps open and close, but it happens with even slightest randomization and goes only one way (unlike the Sierpiński case, where the same gap opens and closes periodically). Similar phenomenon happens in the diffraction case. Finding such observable opens path to experiments to measure and validate it.

Bibliography

[1] N. W. Ashcroft and N. D. Mermin, *Solid State Physics*, HRW international editions (Cengage Learning, Inc, 1976).

[2] P. Y. Yu and M. Cardona, *Fundamentals of Semiconductors*, 4th ed. (Springer-Verlag GmbH, 2010).

[3] E. Fradkin, *Field Theories of Condensed Matter Physics*, 2nd ed. (Cambridge University Press, 2013).

[4] D. J. Thouless, M. Kohmoto, M. P. Nightingale, and M. den Nijs, "Quantized hall conductance in a two-dimensional periodic potential," Phys. Rev. Lett. **49**, 405–408 (1982).

[5] O. Ovdat, J. Mao, Y. Jiang, E. Y. Andrei, and E. Akkermans, "Observing a scale anomaly and a universal quantum phase transition in graphene," Nat. Commun. **8**, 1–6 (2017).

[6] O. Ovdat, Y. Don, and E. Akkermans, "Vacancies in graphene: Dirac physics and fractional vacuum charges," Phys. Rev. B **102**, 075109 (2020).

[7] R. Schirhagl, K. Chang, M. Loretz, and C. L. Degen, "Nitrogen-Vacancy Centers in Diamond: Nanoscale Sensors for Physics and Biology," Annu. Rev. Phys. Chem. **65**, 83–105 (2014).

[8] P. London, R. Fischer, I. Alvizu, J. R. Maze, and D. Gershoni, "Local probing of nuclear bath polarization with a single electronic spin," Phys. Rev. B **92**, 241117 (2015).

[9] L. S. Froufe-Pérez, M. Engel, P. F. Damasceno, N. Muller, J. Haberko, S. C. Glotzer, and F. Scheffold, "Role of Short-Range Order and Hyperuniformity in the Formation of Band Gaps in Disordered Photonic Materials," Phys. Rev. Lett. **117**, 053902 (2016).

[10] D. Chen and S. Torquato, "Designing disordered hyperuniform two-phase materials with novel physical properties," Acta Mater. **142**, 152–161 (2018).

[11] H. Wang, "Proving theorems by pattern recognition—II," Bell Sys. Tech. J. **40**, 1–41 (1961).

[12] R. Berger, "The undecidability of the domino problem," Mem. Amer. Math. Soc. **66**, 72 (1966).

[13] R. Penrose, "The Rôle of Aesthetics in Pure and Applied Mathematical Research," Bull. Inst. Math. Appl. **10**, 266–271 (1974).

[14] M. Gardner, *Penrose Tiles to Trapdoor Ciphers ... and the return of Dr. Matrix*, MAA Spectrum (The Mathematical Association of America, 1997).

[15] M. Senechal, *Quasicrystals and Geometry* (Cambridge University Press, 1996).

[16] S. Mozes, "Tilings, substitution systems and dynamical systems generated by them," J. Anal. Math. **53**, 139–186 (1989).

[17] N. G. de Bruijn, "Algebraic theory of Penrose's non-periodic tilings of the plane. I," Indag. Math. Proc. **84**, 39–52 (1981).

[18] N. G. de Bruijn, "Algebraic theory of Penrose's non-periodic tilings of the plane. II," Indag. Math. Proc. **84**, 53–66 (1981).

[19] C. Janot, *Quasicrystals: A Primer*, 2nd ed., Monographs on the Physics and Chemistry of Materials (Oxford University Press, 1995).

[20] D. Levine and P. J. Steinhardt, "Quasicrystals: A new class of ordered structures," Phys. Rev. Lett. **53**, 2477–2480 (1984).

[21] D. Levine and P. J. Steinhardt, "Quasicrystals. i. definition and structure," Phys. Rev. B **34**, 596–616 (1986).

[22] D. Shechtman, I. Blech, D. Gratias, and J. W. Cahn, "Metallic phase with long-range orientational order and no translational symmetry," Phys. Rev. Lett. **53**, 1951–1953 (1984).

[23] J. M. Luck, "Cantor spectra and scaling of gap widths in deterministic aperiodic systems," Phys. Rev. B **39**, 5834–5849 (1989).

[24] D. Damanik, M. Embree, A. Gorodetski, and S. Tcheremchantsev, "The fractal dimension of the spectrum of the fibonacci hamiltonian," Commun. Math. Phys. **280**, 499–516 (2008).

[25] D. Tanese, E. Gurevich, F. Baboux, T. Jacqmin, A. Lemaître, E. Galopin, I. Sagnes, A. Amo, J. Bloch, and E. Akkermans, "Fractal energy spectrum of a polariton gas in a fibonacci quasiperiodic potential," Phys. Rev. Lett. **112**, 146404 (2014).

[26] B. Sutherland, "Self-similar ground-state wave function for electrons on a two-dimensional penrose lattice," Phys. Rev. B **34**, 3904–3909 (1986).

[27] J. Bellissard, A. Bovier, and J.-M. Ghez, "Gap labelling theorems for one dimensional discrete Schrödinger operators," Rev. Math. Phys. **04**, 1–37 (1992).

[28] J. Bellissard, "Gap Labelling Theorems for Schrödinger Operators," in *From Number Theory to Physics*, Les Houches March '89, edited by M. Waldschmidt, P. Moussa, J.-M. Luck, and C. Itzykson (Springer Berlin Heidelberg, 1992) pp. 538–630.

[29] M. V. Berry, "Quantal phase factors accompanying adiabatic changes," Proc. R. Soc. Lond. A **392**, 45–57 (1984).

[30] D. J. Thouless, "Quantization of particle transport," Phys. Rev. B **27**, 6083–6087 (1983).

[31] D. Xiao, M.-C. Chang, and Q. Niu, "Berry phase effects on electronic properties," Rev. Mod. Phys. **82**, 1959–2007 (2010).

[32] H. Kunz, "Quantized currents and topological invariants for electrons in incommensurate potentials," Phys. Rev. Lett. **57**, 1095–1097 (1986).

[33] A. Poddubny and E. Ivchenko, "Photonic quasicrystalline and aperiodic structures," Physica E **42**, 1871–1895 (2010).

[34] Y. E. Kraus, Y. Lahini, Z. Ringel, M. Verbin, and O. Zilberberg, "Topological states and adiabatic pumping in quasicrystals," Phys. Rev. Lett. **109**, 106402 (2012).

[35] Y. E. Kraus and O. Zilberberg, "Topological equivalence between the fibonacci quasicrystal and the harper model," Phys. Rev. Lett. **109**, 116404 (2012).

[36] M. A. Bandres, M. C. Rechtsman, and M. Segev, "Topological Photonic Quasicrystals: Fractal Topological Spectrum and Protected Transport," Phys. Rev. X **6**, 011016 (2016).

[37] F. Baboux, E. Levy, A. Lemaître, C. Gómez, E. Galopin, L. L. Gratiet, I. Sagnes, A. Amo, J. Bloch, and E. Akkermans, "Measuring topological invariants from generalized edge states in polaritonic quasicrystals," Phys. Rev. B **95**, 161114 (2017).

[38] A. Dareau, E. Levy, M. B. Aguilera, R. Bouganne, E. Akkermans, F. Gerbier, and J. Beugnon, "Revealing the topology of quasicrystals with a diffraction experiment," Phys. Rev. Lett. **119**, 215304 (2017).

[39] I. Dana, "Topologically universal spectral hierarchies of quasiperiodic systems," Phys. Rev. B **89**, 205111 (2014).

[40] K. A. Madsen, E. J. Bergholtz, and P. W. Brouwer, "Topological equivalence of crystal and quasicrystal band structures," Phys. Rev. B **88**, 125118 (2013).

[41] A. V. Poshakinskiy, A. N. Poddubny, and M. Hafezi, "Phase spectroscopy of topological invariants in photonic crystals," Phys. Rev. A **91**, 043830 (2015).

[42] M. Duneau and A. Katz, "Quasiperiodic patterns," Phys. Rev. Lett. **54**, 2688–2691 (1985).

[43] J. M. Luck, C. Godrèche, A. Janner, and T. Janssen, "The nature of the atomic surfaces of quasiperiodic self-similar structures," J. Phys. A **26**, 1951–1999 (1993).

[44] J. M. Luck, "Aperiodic structures: Geometry, diffraction spectra, and physical properties," in *Fundamental Problems in Statistical Mechanics, VIII*, edited by M. H. Ernst and H. van Beijeren (Elsevier, 1994) pp. 127–167.

[45] J. E. Anderson and I. F. Putnam, "Topological invariants for substitution tilings and their associated C^*-algebras," Ergod. Th. Dynam. Sys. **18**, 509–537 (1998).

[46] J. Bellissard, B. Iochum, E. Scoppola, and D. Testard, "Spectral properties of one dimensional quasi-crystals," Commun. Math. Phys. **125**, 527–543 (1989).

[47] J. Bellissard, "Renormalization group analysis and quasicrystals," in *Ideas and Methods in Quantum and Statistical Physics*, In Memory of Raphael Høegh-Krohn (1938–1988), Vol. 2, edited by S. Albeverio, J. E. Fenstad, H. Holden, and T. Lindstrøm (Cambridge University Press, 1992) Chap. 4, pp. 118–148.

[48] W. B. Jones and W. J. Thron, *Continued Fractions: Analytic Theory and Applications*, Encyclopedia of Mathematics and its Applications, Vol. 11 (Cambridge University Press, 2008).

[49] E. Arthur Robinson, Jr., "Symbolic dynamics and tilings of $\mathbb{R}^d$," in *Symbolic dynamics and its applications*, Proceedings of Symposia in Applied Mathematics, Vol. 60, edited by S. Williams (American Mathematical Society, 2004) pp. 81–120.

[50] M. Queffélec, *Substitution Dynamical Systems – Spectral Analysis*, 2nd ed., Lecture Notes in Mathematics, Vol. 1294 (Springer Berlin Heidelberg, 2010).

[51] T. I. Andress and E. Arthur Robinson, Jr., "The Čech cohomology and the spectrum for 1-dimensional tiling systems," in *Ergodic Theory, Dynamical Systems, and the Continuing Influence of John C. Oxtoby*, Contemporary Mathematics, Vol. 678, edited by J. Auslander, A. Johnson, and C. E. Silva (American Mathematical Society, 2016) pp. 53–71.

[52] L. A. Sadun, *Topology of Tiling Spaces*, University Lecture Series, Vol. 46 (American Mathematical Society, 2008).

[53] L. Sadun, "Cohomology of Hierarchical Tilings," in *Mathematics of Aperiodic Order*, Progress in Mathematics, Vol. 309, edited by J. Kellendonk, D. Lenz, and J. Savinien (Springer Basel, Birkhäuser, Basel, 2015) pp. 73–104.

[54] J. Kellendonk, "Pattern-equivariant functions and cohomology," J. Phys. A: Math. Gen. **36**, 5765 (2003).

[55] M. Baake and U. Grimm, *Aperiodic Order*, Encyclopedia of Mathematics and its Applications, Vol. 2: Crystallography and Almost Periodicity (Cambridge University Press, 2018).

[56] S. Kakutani, "A problem of equidistribution on the unit interval $[0, 1]$," in *Measure Theory*, Lecture Notes in Mathematics, Vol. 541, edited by A. Bellow and D. Kölzow (Springer Berlin Heidelberg, 1976) pp. 369–375.

[57] Y. Smilansky, "Uniform distribution of Kakutani partitions generated by substitution schemes," Isr. J. Math. **240**, 667–710 (2020).

[58] E. Akkermans, Y. Don, J. Rosenberg, and C. L. Schochet, "Relating Diffraction and Spectral Data of Aperiodic Tilings: Towards a Bloch theorem," (accepted, 2021), arXiv:2007.15961 [math-ph] .

[59] R. S. Varga, *Matrix Iterative Analysis*, 2nd ed. (Springer Berlin Heidelberg, 2000).

[60] E. Seneta, *Non-negative Matrices and Markov Chains*, Rev. Print. ed., Springer series in statistics (Springer New York, 2006).

[61] S. Eilenberg and N. Steenrod, *Foundations of Algebraic Topology* (Princeton University Press, 1952).

[62] J. M. Franks, *Homology and Dynamical Systems*, CBMS Regional Conference Series in Mathematics No. 49 (American Mathematical Sciences for the Conference Board of the Mathematical Sciences, 1982).

[63] M. Baake and U. Grimm, "Combinatorial problems of (quasi-)crystallography," in *Quasicrystals*, edited by H.-R. Trebin (John Wiley & Sons, Ltd, 2006) Chap. 2, Structure and Mathematical Modelling, pp. 160–171.

[64] M. Barge and B. Diamond, "Cohomology in one-dimensional substitution tiling spaces," Proc. Amer. Math. Soc. **136**, 2183–2191 (2008).

[65] A. Julien, "Complexity and cohomology for cut-and-projection tilings," Ergod. Th. Dynam. Sys. **30**, 489–523 (2009).

[66] B. Grünbaum and G. C. Shephard, *Tilings and Patterns* (W. H. Freeman, New York, 1987).

[67] C. Skau, "Ordered K-theory and minimal symbolic dynamical systems," Colloq. Math. **84/85**, 203–227 (2000).

[68] E. Akkermans, G. V. Dunne, and E. Levy, "Wave Propagation in One Dimension," in *Optics of Aperiodic Structures: Fundamentals and Device Applications*, edited by L. Dal Negro (Pan Stanford Publishing, 2013) pp. 407–449.

[69] E. Levy and E. Akkermans, "Topological boundary states in 1D: An effective Fabry-Perot model," Eur. Phys. J. Special Topics **226**, 1563–1582 (2017).

[70] E. Akkermans and G. Montambaux, *Mesoscopic Physics of Electrons and Photons* (Cambridge University Press, 2011).

[71] E. Levy, *Topological properties of quasiperiodic chains: structural and spectral analysis*, PhD Thesis, Technion – Israel Institute of Technology (2016).

[72] Z. Cheng, R. Savit, and R. Merlin, "Structure and electronic properties of Thue-Morse lattices," Phys. Rev. B **37**, 4375–4382 (1988).

[73] M. Baake and U. Grimm, *Aperiodic Order*, Encyclopedia of Mathematics and its Applications, Vol. 1: A Mathematical Invitation (Cambridge University Press, 2013).

[74] M. Baake, F. Gähler, and U. Grimm, "Spectral and topological properties of a family of generalised Thue-Morse sequences," J. Math. Phys. **53**, 032701 (2012).

[75] F. Axel and H. Terauchi, "High-resolution x-ray-diffraction spectra of Thue-Morse GaAs-AlAs heterostructures: Towards a novel description of disorder," Phys. Rev. Lett. **66**, 2223–2226 (1991).

[76] M. Kolář, B. Iochum, and L. Raymond, "Structure factor of 1D systems (superlattices) based on two-letter substitution rules. I. delta (Bragg) peaks," J. Phys. A: Math. Gen. **26**, 7343–7366 (1993).

[77] J. Peyrière, E. Cockayne, and F. Axel, "Line-Shape Analysis of High Resolution X-Ray Diffraction Spectra of Finite Size Thue-Morse GaAs-AlAs Multilayer Heterostructures," J. Phys. I **5**, 111–127 (1995).

[78] F. Gähler and R. Klitzing, "The diffraction pattern of self-similar tilings," in *The Mathematics of Long-Range Aperiodic Order* (Springer Netherlands, 1997) pp. 141–174.

[79] S. Aubry, C. Godrèche, and J. M. Luck, "A structure intermediate between quasiperiodic and random," Europhys. Lett. **4**, 639–643 (1987).

[80] S. Aubry, C. Godrèche, and J. M. Luck, "Scaling properties of a structure intermediate between quasiperiodic and random," J. Stat. Phys. **51**, 1033–1075 (1988).

[81] J.-P. Gazeau and J.-L. Verger-Gaugry, "On the spectrum of the Thue-Morse quasicrystal and the rarefaction phenomenon," J. Théor. Nr. Bordx. **20**, 673–705 (2008).

[82] J. Wolny, A. Wnęk, J.-L. Verger-Gaugry, and L. Pytlik, "Average unit-cell approach to diffraction on Thue–Morse sequence and decorated quasicrystals," Mater. Sci. Eng. A **294-296**, 381–384 (2000).

[83] J. Wolny, A. Wnęk, and J.-L. Verger-Gaugry, "Fractal Behaviour of Diffraction Pattern of Thue–Morse Sequence," J. Comput. Phys. **163**, 313–327 (2000).

[84] M. Baake, U. Grimm, and J. Nilsson, "Scaling of the Thue-Morse Diffraction Measure," Acta Phys. Pol. A **126**, 431–434 (2014).

[85] M. Queffélec, "Spectral study of automatic and substitutive sequences," in *Beyond Quasicrystals*, edited by F. Axel and D. Gratias (Springer Berlin Heidelberg, 1995) Chap. 12, pp. 369–414.

[86] S. Kakutani, "Strictly ergodic symbolic dynamical systems," in *Proceedings of the Sixth Berkeley Symposium on Mathematical Statistics and Probability (Univ. California, Berkeley, Calif., 1970/1971), Vol. II: Probability theory* (1972) pp. 319–326.

[87] A. Hof, "On diffraction by aperiodic structures," Commun. Math. Phys. **169**, 25–43 (1995).

[88] A. Hof, "On a "structure intermediate between quasiperiodic and random"," J. Stat. Phys. **84**, 309–320 (1996).

[89] M. Barge, J. Kellendonk, and S. Schmieding, "Maximal equicontinuous factors and cohomology for tiling spaces," Fundam. Math. **218**, 243–267 (2012).

[90] J. Bellissard, D. J. L. Herrmann, and M. Zarrouati, "Hull of Aperiodic Solids and Gap Labelling Theorems," in *Directions in Mathematical Quasicrystals*, CRM Monograph Series, Vol. 13, edited by M. Baake and R. V. Moody (American Mathematical Society, 2000) pp. 207–259.

[91] A. Forrest, J. Hunton, and J. Kellendonk, *Topological Invariants for Projection Method Patterns*, Memoirs AMS 758 (American Mathematical Society, 2002).

[92] J. Kellendonk and I. F. Putnam, "Tilings, C^*-algebras and K-theory," in *Directions in Mathematical Quasicrystals*, CRM Monograph Series, Vol. 13, edited by M. Baake and R. V. Moody (American Mathematical Society, 2000) pp. 186–215.

[93] C. C. Moore and C. L. Schochet, *Global Analysis on Foliated Spaces*, 2nd ed. (Cambridge University Press, 2005).

[94] J. Kellendonk and I. F. Putnam, "The Ruelle-Sullivan map for actions of $\mathbb{R}^n$," Math. Ann. **334**, 693–711 (2006).

[95] J. E. Avron, R. Seiler, and B. Simon, "Homotopy and quantization in condensed matter physics," Phys. Rev. Lett. **51**, 51–53 (1983).

[96] J. Bellissard, A. van Elst, and H. Schulz-Baldes, "The noncommutative geometry of the quantum Hall effect," J. Math. Phys. **35**, 5373–5451 (1994).

[97] J. E. Avron, D. Osadchy, and R. Seiler, "A Topological Look at the Quantum Hall Effect," Phys. Today **56**, 38–42 (2003).

[98] G. G. Naumis, "Topological map of the Hofstadter butterfly: Fine structure of Chern numbers and Van Hove singularities," Phys. Lett. A **380**, 1772–1780 (2016).

[99] Y. Liu, L. F. Santos, and E. Prodan, "Topological Gaps in Quasi-Periodic Spin Chains: A Numerical and K-Theoretic Analysis," (2020), arXiv:2009.03752 [cond-mat.str-el] .

[100] Y. Liu and E. Prodan, "Mapping Chern numbers in quasi-periodic interacting spin chains," (2020), arXiv:2010.06171 [cond-mat.mes-hall] .

[101] J. Zak, "Berry's phase for energy bands in solids," Phys. Rev. Lett. **62**, 2747–2750 (1989).

[102] R. Resta, "Manifestations of Berry's phase in molecules and condensed matter," J. Phys.: Condens. Matter **12**, R107–R143 (2000).

[103] Y. Hatsugai, "Chern number and edge states in the integer quantum Hall effect," Phys. Rev. Lett. **71**, 3697–3700 (1993).

[104] E. Akkermans, "Twisted boundary conditions and transport in disordered systems," J. Math. Phys. **38**, 1781–1793 (1997).

[105] Q. Niu and D. J. Thouless, "Quantum Hall effect with realistic boundary conditions," Phys. Rev. B **35**, 2188–2197 (1987).

[106] M. Kohmoto, "Topological invariant and the quantization of the Hall conductance," Ann. Phys. **160**, 343–354 (1985).

[107] P. G. Harper, "Single band motion of conduction electrons in a uniform magnetic field," Proc. Phys. Soc. London, Sect. A **68**, 874 (1955).

[108] D. R. Hofstadter, "Energy levels and wave functions of Bloch electrons in rational and irrational magnetic fields," Phys. Rev. B **14**, 2239–2249 (1976).

[109] E. Akkermans, "Statistical Mechanics and Quantum Fields on Fractals," in *Fractal Geometry and Dynamical Systems in Pure and Applied Mathematics II: Fractals in Applied Mathematics*, Contemporary Mathematics, Vol. 601, edited by D. Carfì, M. L. Lapidus, E. P. J. Pearse, and M. van Frankenhuijsen (American Mathematical Society, 2013) pp. 1–21.

[110] A. Lindenmayer, "Mathematical models for cellular interactions in development. I. Filaments with one-sided inputs," J. Theor. Biol. **18**, 280–299 (1968).

[111] A. Lindenmayer, "Mathematical models for cellular interactions in development. II. Simple and branching filaments with two-sided inputs," J. Theor. Biol. **18**, 300–315 (1968).

[112] E. Akkermans, A. Comtet, J. Desbois, G. Montambaux, and C. Texier, "Spectral Determinant on Quantum Graphs," Ann. Phys. **284**, 10–51 (2000).

[113] E. Akkermans, G. V. Dunne, and A. Teplyaev, "Physical consequences of complex dimensions of fractals," EPL (Europhys. Lett.) **88**, 40007 (2009).

[114] E. Akkermans, G. V. Dunne, and A. Teplyaev, "Thermodynamics of Photons on Fractals," Phys. Rev. Lett. **105**, (2010).

[115] E. Akkermans, O. Benichou, G. V. Dunne, A. Teplyaev, and R. Voituriez, "Spatial log-periodic oscillations of first-passage observables in fractals," Phys. Rev. E **86**, (2012).

[116] E. Akkermans and E. Gurevich, "Spontaneous emission from a fractal vacuum," EPL (Europhys. Lett.) **103**, 30009 (2013).

[117] J. M. Ghez, Y. Y. Wang, R. Rammal, B. Pannetier, and J. Bellissard, "Band spectrum for an electron on a Sierpinski gasket in a magnetic field," Solid State Commun. **64**, 1291–1294 (1987).

[118] S. Alexander, "Some properties of the spectrum of the Sierpinski gasket in a magnetic field," Phys. Rev. B **29**, 5504–5508 (1984).

[119] S. Alexander, "Superconductivity of networks. A percolation approach to the effects of disorder," Phys. Rev. B **27**, 1541–1557 (1983).

[120] S. Alexander and E. Halevi, "Superconductivity on networks : II. The London approach," J. Phys. **44**, 805–817 (1983).

[121] G. H. Wannier, "A Result Not Dependent on Rationality for Bloch Electrons in a Magnetic Field," Phys. Stat. Sol. (b) **88**, 757–765 (1978).

[122] D. Osadchy and J. E. Avron, "Hofstadter butterfly as quantum phase diagram," J. Math. Phys. **42**, 5665–5671 (2001).

[123] A. Teplyaev, "Spectral zeta functions of fractals and the complex dynamics of polynomials," Trans. Amer. Math. Soc. **359**, 4339–4359 (2007).

[124] G. Derfel, P. J. Grabner, and F. Vogl, "The zeta function of the Laplacian on certain fractals," Trans. Amer. Math. Soc **360**, 881–898 (2008).

[125] M. Brzezińska, A. M. Cook, and T. Neupert, "Topology in the Sierpiński-Hofstadter problem," Phys. Rev. B **98**, 205116 (2018).

[126] S. Pai and A. Prem, "Topological states on fractal lattices," Phys. Rev. B **100**, 115135 (2019).

[127] A. Kitaev, "Anyons in an exactly solved model and beyond," Ann. Phys. **321**, 2–111 (2006).

[128] D. J. Apigo, W. Cheng, K. F. Dobiszewski, E. Prodan, and C. Prodan, "Observation of Topological Edge Modes in a Quasiperiodic Acoustic Waveguide," Phys. Rev. Lett. **122**, (2019).

[129] G. N. Katomeris and S. N. Evangelou, "Level statistics for electronic states in a disordered fractal," J. Phys. A: Math. Gen. **29**, 2379–2387 (1996).

[130] E. van Veen, S. Yuan, M. I. Katsnelson, M. Polini, and A. Tomadin, "Quantum transport in Sierpinski carpets," Phys. Rev. B **93**, (2016).

[131] M. Fremling, M. van Hooft, C. M. Smith, and L. Fritz, "Existence of robust edge currents in Sierpiński fractals," Phys. Rev. Res. **2**, 013044 (2020).

[132] P.-G. de Gennes, "Champ critique d'une boucle supraconductrice ramefiée," C. R. Acad. Sci. II **292**, 279–282 (1981).

[133] R. S. Strichartz, *Differential Equations on Fractals* (Princeton University Press, 2006).

[134] R. Rammal, "Spectrum of harmonic excitations on fractals," J. Phys. **45**, 191–206 (1984).

[135] G. Montambaux, F. Piéchon, J.-N. Fuchs, and M. O. Goerbig, "A universal Hamiltonian for motion and merging of Dirac points in a two-dimensional crystal," Eur. Phys. J. B **72**, 509 (2009).

[136] G. Montambaux, F. Piéchon, J.-N. Fuchs, and M. O. Goerbig, "Merging of Dirac points in a two-dimensional crystal," Phys. Rev. B **80**, 153412 (2009).

[137] C. Godrèche and J. M. Luck, "Quasiperiodicity and randomness in tilings of the plane," J. Stat. Phys. **55**, 1–28 (1989).

[138] M. Baake and M. Moll, "Random Noble Means Substitutions," in *Aperiodic Crystals*, edited by S. Schmid, R. L. Withers, and R. Lifshitz (Springer Netherlands, Dordrecht, 2013) pp. 19–27.

[139] F. Gähler and E. Miro, "Topology of the Random Fibonacci Tiling Space," Acta Phys. Pol. A **126**, 564–567 (2014).

[140] F. Gähler and G. R. Maloney, "Cohomology of one-dimensional mixed substitution tiling spaces," Topol. Appl. **160**, 703–719 (2013).

[141] R. Wang, M. Röntgen, C. V. Morfonios, F. A. Pinheiro, P. Schmelcher, and L. Dal Negro, "Edge modes of scattering chains with aperiodic order," Opt. Lett. **43**, 1986–1989 (2018).

[142] J. M. Luck and D. Petritis, "Phonon spectra in one-dimensional quasicrystals," J. Stat. Phys. **42**, 289–310 (1986).

ריצופים לא־מחזוריים, מושפעים משינוי זה של הקומבינטוריקה גם כן. אנחנו נציג את הכלים המתמטיים העיקריים הדרושים כדי לזהות ולתאר ריצופים לא־מחזוריים בדגש על קוהומולוגיית צ׳ך. אנחנו נראה את ההשלכות הפיזיקליות, ונציג חישובים חדשים בעזרת תיאור זה.

אחת התכונות העיקריות של ריצופים היא תמונת העקיפה שלהם המתארת את התכונות המבניות שלהם. ניסוי עקיפה בריצוף מחזורי מניב תמונה של שיאי בראג בלבד במרחב ההופכי, המרמזת על מִתאם (קורלציה) ארוכת־טווח. בדומה לכך, ריצופים קוואזי־מחזוריים מניבים שיאי בראג במרחב ההופכי, אבל תמונת העקיפה של השיאים צפופה ואין אזור בְּרִילוּאֶן (Brillouin). מנקודת מבט פיזיקלית, הקיום של שיאי בראג הוא תנאי הכרחי (אבל לא מספיק) עבור ריצוף להיות קוואזי־מחזורי. באופן כללי, תמונת העקיפה מופרדת לשלושה חלקים לפי משפט לֶבֶג (Lebesgue): נקודתי טהור (כלומר, בראג), רציף בהחלט ורציף סינגולרית. דוגמאות ראויות לציון הן ריצוף רוּדִין־שָׁפִּירוֹ (Rudin-Shapiro) בעל תמונת עקיפה רציפה בהחלט בלבד, וריצוף תוּאֶה־מוֹרְס (Thue-Morse), שלו תמונת עקיפה רציפה סינגולרית. אנחנו ננתח את החלקים הללו של תמונת העקיפה, ונראה כיצד לחשבה במקרים מסוימים עם כלים הנגזרים מתוך חישוב קוהומולוגיית צ׳ך.

אם משפט בלוך הוא נדבך מרכזי בריצופים מחזוריים המקשר את מיקום שיאי עקיפת בראג לפערי אנרגיה ספקטרליים, כיצד הוא מופגן בריצופים לא־מחזוריים? ידוע, כי משפט בלוך מתקיים בריצופים קוואזי־מחזוריים בדומה לריצופים מחזוריים. ברם, בריצופים לא־מחזוריים זהו לא המקרה בדרך כלל. קודם כל, אנחנו ננסח את משפט בלוך לריצופים קוואזי־מחזוריים. בנוסף נראה, שב־$1d$ יש קשר בין הליפופים המבניים של מופע (פאזת) שיאי בראג לליפופים הספקטרליים של המופע הכיראלי של מטריצת הפיזור. לבסוף נראה, שבמקרה הכללי של ריצופים בעלי סיבוכיות מקומית סופית בממדים $d \geq 3$, רק העקבות של קוהומולוגיית צ׳ך ושל חבורת K_0 נשארות זהות. העקבות הללו מתארות את השוויון בין תכונות מבניות וספקטרליות, בהתאמה.

ביססנו את קוהומולוגיית צ׳ך כשמורה הטופולוגית העיקרית בריצופים לא־מחזוריים בממדים נמוכים. לכן מעבר בין שני ריצופים עם קוהומולוגיות צ׳ך שונות לכל אחד מתאר מעבר פאזה טופולוגי. להראות זאת לא פשוט כלל וכלל. בגישה אחת, אנחנו נעזר בפרקטלים כדי להראות, שלמשולש סֶרְפִּינְסְקִי (Sierpiński) המשוקע בשטח מגנטי יש מעבר פאזה טופולוגי כתלות בשטף. נציג תכונות הולכה ומשפטי אינדקס על פרקטלים אלו. בגישה אחרת. נשתמש בחוקי החלפה אקראיים כדי לקבל מעבר פאזה טופולוגי בין ריצופים לא־מחזוריים מצויים, ונציג בהם תכונות תרמודינמיות תואמות.

תקציר

למערכות מחזוריות חשיבות מרכזית בפיזיקה. הן מאפשרות מגוון תופעות בממד אחד, בשניים ובשלושה ממדים. חלקן מבניות כגון סידור גבישי, עקיפה (דיפרקציה), קשיות החומר וכו׳; אחרות ספקטרליות כגון פערי אנרגיה, ניידות חשמלית, מספרי צֵ׳רְן (Chern) וכיוב׳. נוסף על כך, מחזוריות בזמן מובילה לתופעות כמו המילטוניאן פְלוֹקֶה (Floquet) או גבישי זמן. השילוב של תכונות מבניות וספקטרליות מוביל למשפט בְלוֹךְ (Bloch) המפורסם, המקשר סימטריות מבניות עם סימטריות פונקציות־הגל של המילטוניאן מחזורי.

כאשר יוצאים מתחום המערכות המחזוריות, מחפשים מערכות הקרובות להיות מחזוריות. אפשרות אחת היא להכניס הפרעה למערכת מחזורית בצורת אי־סדר; אחרת היא להכניס פגם במערכת כמו מגרעת (vacancy), מרכז צבע או שבר; רעיון אחר הוא חומרים היפר־אחידים, שהם לא מסודרים אבל בעלי תכונות משותפות עם מערכות מחזוריות. אנחנו מחפשים מערכות כמעט־מחזוריות, אשר מצד אחד דטרמיניסטיות ללא הפרעות או אי־סדר, ומצד שני אינן מחזוריות למרות תכונות משותפות עם מערכות כאלו. הפתרון נעוץ בריצופים לא־מחזוריים, שבהם נתמקד בתזה זו – ובעיקר בריצופים בחד־ממד.

ריצופים לא־מחזוריים מופיעים בתחומים רבים בפיזיקה של חומר מעובה, במערכות דינמיות, במכניקה סטטיסטית, במדע של חומרים, באופטיקה וכו׳. הם התשובה לשאלה: "האם קיים ריצוף דטרמיניסטי אבל לא־מחזורי של המישור בעזרת קבוצה סופית של מרצפות?". התשובה שוערה לחיוב ע״י וַאנְג (Wang), ומאוחר יותר הוכחה בהתאם ע״י בֶּרְגֶר (Berger) בעזרת מרצפות וואנג. שיטה זו הוכללה בהמשך ל"חוקי התאמה מקומיים". כך נפתח הצוהר לריצופים לא־מחזוריים נוספים. פֶּנְרוֹז (Penrose) הראה ריצוף בעל סימטריה מחומשת, הידוע כיום כ"ריצוף פנרוז", בעזרת חוקי החלפה. בממד אחד חוקי ההחלפה שקולים לסידור מרחבי של אותיות מעל אלף־בית מסוים. מאוחר יותר דֶה־בְּרוּיִן (de Bruijn) הסביר כיצד לקבל ריצוף לא־מחזורי באמצעות הטלה ממרחב ממד גבוה, מה שמוכר כיום כשיטת "גזור־והטל" (Cut and Project). כיום שלוש השיטות הללו, חוקי התאמה מקומיים, חוקי החלפה וגזור־והטל, הן הכלים העיקריים ליצור ריצופים לא־מחזוריים.

משפחה מפורסמת של ריצופים לא־מחזוריים היא של ריצופים קוואזי־מחזוריים, אשר הקרובים ביותר ("כמעט") למחזוריים. לריצופים ממשפחה זו יש עקיפת בְּרַאג (Bragg); התכונות הספקטרליות שלהם (של גלים מתקדמים או של המילטוניאנים בקשירה־הדוקה) הן של מקשתת (ספקטרום) פרקטלית עם אינסוף פערי אנרגיה. משפט כינוי הפער (Gap labeling theorem) מאפשר לסווג את פערי האנרגיה הללו בעזרת מספרים שלמים, ששונים מהסיווג הסטנדרטי של מערכות מחזוריות בעזרת מספרי צ׳רן המובעים באמצעות עקמומיות בֶּרִי (Berry). כלומר, לא ניתן לרשום את המספרים השלמים הללו בעזרת עקמומיות של גאומטריה חילופית (קומוטטיבית). ניתן לצקת למספרים השלמים הללו תוכן טופולוגי ותכונות שמורות (אינווריאנטיות) דרך קוהומולוגיית צֶ׳ךְ (Čech). יחד עם זאת, רוב התכונות הללו לא ממופות ולא ניתנות לווידוא ניסיוני פרט למספר יוצאים מן־הכלל. לכן התוכן הטופולוגי של ריצופים לא־מחזוריים, כלומר, המספרים השלמים המוכרים דלעיל, אינם מחושבים להיות בעלי חשיבות פיזיקלית. אנחנו נדגים כיצד לאפיין את המספרים הטופולוגיים הללו בריצופים קוואזי־מחזוריים בעזרת מספרי ליפוף (winding), ונקשר אותם לניסיונות ידועים.

ריצופים נעשים אקזוטיים מעבר לעולם הקוואזי־מחזורי. ריצופים קוואזי־מחזוריים מפגינים שיאי בראג בתמונת העקיפה, שאותם ניתן למספר במרחב ההופכי בדומה לאינדקסי מִילֶר (Miller) של ריצופים מחזוריים. יחד אם זאת, לריצופים לא־מחזוריים כלליים יש קומבינטוריקה שונה, ולכן לא ניתן למספרם באותו הסגנון. תכונות פיזיקליות נוספות, כמו המקשתת של המילטוניאנים המוגדרים על

לסבי המנוח,
אנצל פרידמן

רשימת פרסומים

חלק מן התוצאות בחיבור זה פורסמו כמאמרים מאת המחבר ושותפיו למחקר בכנסים ובכתבי־עת במהלך תקופת מחקר הדוקטורט של המחבר, אשר גרסאותיהם העדכניות ביותר מפורטות להלן.

[i] O. Shpielberg, Y. Don, and E. Akkermans, "Numerical study of continuous and discontinuous dynamical phase transitions for boundary-driven systems," Phys. Rev. E **95**, 032137 (2017).

[ii] E. Akkermans, Y. Don, E. Levy and D. Gitelman, "Topological properties of some quasi-periodic tilings – From structure to spectrum, in Spectral Structures and Topological Methods" in Mathematical Quasicrystals, Workshop ID: 1740, M. Baake, D. Damanik, J. Kellendonk and D. Lenz (eds.), Mathematisches Forschungsinstitut Oberwolfach (2017).

[iii] O. Ovdat, Y. Don and E. Akkermans, "Vacancies in graphene: Dirac physics and fractional vacuum charges," Phys. Rev. B **102**, 075109 (2020).

[iv] E. Akkermans, Y. Don, J. Rosenberg and C. L. Schochet, "Relating Diffraction and Spectral Data of Aperiodic Tilings: Towards a Bloch theorem," (accepted, 2021) arXiv: 2007.15961 [math-ph].

תודות

ברצוני להכיר את תודתי העמוקה למנחה שלי, פרופ׳ אריק אקרמן, על ההשראה לרדוף אחר מחקר אקדמי נקי ומדויק; על שלל הרעיונות והידע האינסופי – אידאל, שאליו אני שואף; ועל היותו יותר מרק מדריך וחבר.

אני מודה במיוחד לשותפי למחקר: אוהד שפילברג, אלי לוי, דור גיטלמן, עמרי עבדת, יונתן רוזנברג, חיים שוחט ואריק אקרמן, שעזרו לי לצקת את מחשבותיי ורעיונותיי ליצירות מוחשיות.

ברצוני להודות גם לעמיתים שלי, אוהד שפילברג, דור גיטלמן, עמרי עבדת, בוריס רוטשטיין, ברק קציר, תום שינדלמן ואריאן סורה על השעות הרבות של דיונים פורים ועל הרעיונות המעניינים.

לבסוף, אני מצדיע למשפחתי על הסבלנות המרובה ועל התמיכה.

המחקר בוצע בהנחייתו של פרופסור אריק אקרמן בפקולטה לפיזיקה

אני מודה לעמותת אירווין וג׳ואן ג׳ייקובס ולטכניון
על התמיכה הכספית הנדיבה בהשתלמותי

תכונות טופולוגיות של ריצופים לא־מחזוריים ושל פרקטלים

חיבור על מחקר

לשם מילוי חלקי של הדרישות
לקבלת התואר דוקטור לפילוסופיה

ירוסלב דון

הוגש לסנאט הטכניון – מכון טכנולוגי לישראל

מרץ, 2021 חיפה אדר, התשפ״א

תכונות טופולוגיות של ריצופים
לא־מחזוריים ושל פרקטלים

ירוסלב דון